CERN-THESIS-2014-027

Inaugural - Dissertation

zur
Erlangung der Doktorwürde
der
Naturwissenschaftlich-Mathematischen
Gesamtfakultät
der
Ruprecht-Karls-Universität
Heidelberg

vorgelegt von
Dipl.-Phys. Daniel Andreas Fink
aus Stuttgart-Bad Cannstatt

Tag der mündlichen Prüfung: 23. Januar 2014

Improving the Selectivity of the ISOLDE Resonance Ionization Laser Ion Source and In-Source Laser Spectroscopy of Polonium

Gutachter: Prof. Dr. Klaus Blaum

Prof. Dr. Selim Jochim

Zusammenfassung

Exotische Atomkerne weit ab der Stabilität sind faszinierende Studienobjekte in vielen wissenschaftlichen Feldern, wie zum Beispiel der Atom-, Kern- und Astrophysik. Da es sich bei diesen meist um kurzlebige Isotope handelt, ist es wichtig, deren Produktion mit der sofortigen Extraktion und Weiterleitung zu den Experimenten zu koppeln. Dies ist das Einsatzfeld des Isotopenseparators ISOLDE am CERN. Ein wichtiger Teil dieser Großforschungsanlage ist die Resonanzionisations-Laserionenquelle (RILIS), da diese ein schnelles und hochselektives Mittel zur Ionisation der Reaktionsprodukte darstellt. Zusätzlich dient diese Technik auch als empfindlicher Aufbau für die Entwicklung und Verbesserung von Elektronenanregungsschemata zur resonanten Laserphotoionisation und für die Laserspektroskopie zur Untersuchung der Kernstruktur oder fundamentaler atomphysikalischer Eigenschaften.
In der hier vorgelegten Arbeit werden alle diese verschiedenen Aspekte der RILIS behandelt: Ein neuartiges Gerät zur Unterdrückung von oberflächenionisierten Kontaminationen in RILIS Ionenstrahlen, bekannt als die Laserionenquelle und -falle (LIST), wurde an die ISOLDE angepasst, weiterentwickelt und charakterisiert; ein neues Elektronenanregungsschema zur Laserionisation von Kalzium wurde entwickelt; die Ionisationsenergie von Polonium wurde mittels Rydbergspektroskopie mit höchster Präzision gemessen; und schließlich führte die erste Anwendung der hochselektiven LIST zur Bestimmung von Kernstruktureigenschaften von ^{217}Po mittels der Resonanzionisationsspektroskopie in der Ionenquelle.

Abstract

Exotic atomic nuclei far away from stability are fascinating objects to be studied in many scientific fields such as atomic-, nuclear-, and astrophysics. Since these are often short-lived isotopes, it is necessary to couple their production with immediate extraction and delivery to an experiment. This is the purpose of the on-line isotope separator facility, ISOLDE, at CERN. An essential aspect of this laboratory is the Resonance Ionization Laser Ion Source (RILIS) because it provides a fast and highly selective means of ionizing the reaction products. This technique is also a sensitive laser-spectroscopy tool for the development and improvement of electron excitation schemes for the resonant laser photoionization and the study of the nuclear structure or fundamental atomic physics.
Each of these aspects of the RILIS applications are subjects of this thesis work: a new device for the suppression of unwanted surface ionized contaminants in RILIS ion beams, known as the Laser Ion Source and Trap (LIST), was implemented into the ISOLDE framework, further developed and characterized; a new electron-excitation scheme for the laser ionization of calcium was developed; the ionization energy of polonium was determined by high-precision Rydberg spectroscopy; and finally, the first ever on-line physics operation of the highly selective LIST enabled the study of nuclear structure properties of ^{217}Po by in-source resonance ionization spectroscopy.

Contents

List of figures

List of tables

Abbreviations and acronyms

AC ..... Alternating current
AIS ..... Auto-ionizing state
Al ..... Aluminium
At ..... Astatine
Au ..... Gold
Bi ..... Bismuth
BN ..... Boron nitride
Ca ..... Calcium
CERN .... European Organization for Nuclear Research
CPO ..... Charged Particle Optics©
Cs ..... Cesium
CW ..... Continuous wave (laser)
DAQ ..... Data-acquisition
DC ..... Direct current
DCM 4-dicyanomethylene-2-methyl-6-p-dimethylaminostyryl-4H-pyran
DM ..... Droplet model
EBIS ..... Electron beam ion sources
EOM ..... Equation of motion
FC ..... Faraday cup
FiS ..... Field shift
Fr ..... Francium
FS ..... Fine structure
GANIL ... Grand Accelélérateur National d'Ions Lourds, Caen, France
GPS ..... General Purpose Separator
GSI ..... Gesellschaft für Schwerionenforschung GmbH, Darmstadt, Germany
HFS ..... Hyperfine structure
Hg ..... Mercury
HRS ..... High Resolution Separator
HV ..... High voltage
IE ..... Ionization energy
IG ..... Ion guide
IP ..... Ionization potential
IR ..... Infrared
IRIS ..... Investigation of Radioactive Isotopes on Synchrocyclotron, Gatchina, Russia
IS ..... Isotope shift
ISOL ..... Isotope separator on-line
LC ..... Inductor-capacitor
LIST ..... Laser Ion Source and Trap

LLF ..... LIST loss factor
LQF ..... LIST quality factor
LSF ..... LIST suppression factor
MCP ..... Micro channel plate
Mg ..... Magnesium
MR-TOF . Multi-reflection time-of-flight
MS ..... Mass shift
Na ..... Sodium
NB ..... Narrow band
NBI ..... Niels Bohr Institute of Physics
Nd:YAG .. Neodymium-doped yttrium aluminum garnet
NMS ..... Normal mass shift
OBE ..... Optical Bloch equations
Pb ..... Lead
PIPS ..... Passivated implanted planar silicon
PNPI .... Petersburg Nuclear Physics Institute
Po ..... Polonium
pp ..... Peak to peak
PSB ..... Proton Synchrotron Booster
Pt ..... Platinum
R6G ..... Rhodamine 6G
RB ..... Rhodamin B
Re ..... Rhenium
RF ..... Radio-frequency
RFQ ..... Radio-frequency quadrupole
RIB ..... Radioactive ion beam
RIKEN ... Rikagaku Kenkyūjo; Japanese for: the institute of physical and chemical research
RILIS .... Resonance Ionization Laser Ion Source
Rn ..... Radon
S ..... Selectivity
S ..... Sulphur
SC ..... supercycle
Se ..... Selenium
SiC ..... Silicon carbide
SMS ..... Specific mass shift
Sn ..... Tin
Ta ..... Tantalum
Te ..... Tellurium
Ti ..... Titanium
Ti:Sa ..... Titanium:sapphire
TiO ..... Titanium oxide
Tl ..... Thallium
Tm ..... Thulium
TRIUMF . Tri University Meson Facility, National laboratory for particle and nuclear

	physics, Vancouver, Canada
UC_2	Uranium carbide
UV	Ultraviolet
W	Tungsten
WM	Wavemeter
Yb	Ytterbium

1 Introduction

From the perspective of our habitable corner of the universe, i.e. the Earth, matter seems to be fairly stable. Yet, our existence relies on so-called "exotic atomic nuclei", as these nuclei are often a stepping stone in the *nucleosynthesis processes*, responsible for the creation of the elements. Exotic nuclei are radioactive because they have an unusual ratio of protons and neutrons compared to that of the stable nuclei that surround us. Many of these exist only for a very short time in our sun or in extreme conditions far away in the universe such as neutron stars or supernovae. Besides their fundamental role in nature, they are extremely interesting objects to be studied in many fields from atomic to nuclear physics and from solid-state to medical and biophysics.

Very few exotic nuclei occur naturally and most of our knowledge about the properties of these short-lived and volatile objects stems from their artificial production. To date more than 3000 nuclei have been discovered of which, to put this into a context, only 284 are stable. They can be illustrated in the *chart of nuclei*, as shown in Figure 1.1, where each combination of a number Z of protons with a number N of neutrons represents one specific nucleus. The nuclear and atomic properties of these isotopes* may vary greatly and their theoretical description still remains an extremely challenging task in nuclear physics, despite the power of modern computers. Nuclei, heaver than the lightest hydrogen isotope ^{1}H, are many-body systems, and except for the very lightest nuclei, an *ab initio* calculation, i.e. a calculation relying on the fundamental forces, is impossible. It is therefore a common approach to search for macroscopic trends and patterns across the nuclear chart. The most obvious observation is the line of stable nuclei, known as the *valley of stability*. Another macroscopic observation is the unusual stability of nuclei consisting of certain numbers of protons or neutrons, known as the *magic numbers*: 2, 8, 20, 28, 50, 82 and 126 (see Figure 1.1). A microscopic model that is able to reproduce the magic numbers is the nuclear shell model [73], which, in a simplified picture, assumes the nucleons (protons and neutrons) to be arranged into energy shells within the nucleus, analogous to the concept of electron shells in atomic physics. Nevertheless, it is now clear that these concepts need to be refined for isotopes far away from stability. Magic numbers, for instance, are known to disappear for imbalanced proton and neutron numbers, while new ones may appear[82, 174]. The recently discovered new magic number at $N = 34$ in the neutron-rich isotope ^{54}Ca is a good example [165]. However, the study of these exotic nuclei is an experimental challenge due to their short half-lives of typically of the order of seconds to milliseconds. A high production yield and fast separation, extraction and transport to the experimental setup is therefore essential.

*Isotopes are atoms of the same element (same proton number, Z), but different number of neutrons (neutron number, N).

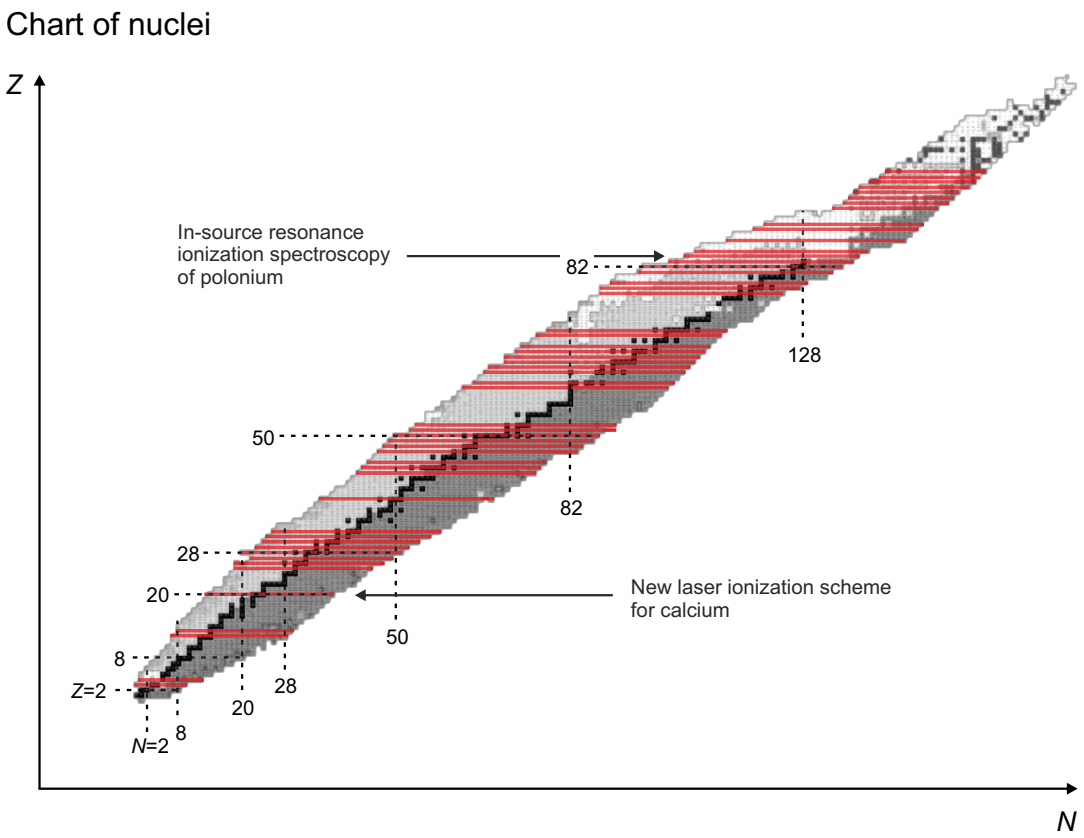

Figure 1.1: The chart of nuclei (x-axis neutron number N, y-axis proton number P) and the regions of interest for this thesis. The red solid lines indicate elements, for which RILIS laser ionization schemes exist, while magic numbers are indicated with the dashed lines. Different tones of gray correspond to different radioactive decay channels.

One type of apparatus that is able to address all these demands is the "radioactive ion beam facility" [75], whose proof of principle was demonstrated at the *Niels Bohr Institute of Physics* (NBI) in Copenhagen, Denmark [91]. One prominent example is the *ISOLDE* facility [85] at the *European Organization for Nuclear Research* (CERN) in Switzerland, where the results, reported in this thesis, were obtained. The ISOLDE radioactive ion beam facility is based on the *Isotope Separator On-Line* (ISOL) process, where an accelerator is combined with a mass separator to irradiate a suitable target material with a high-energy driver beam to produce a multitude of different nuclei of all kinds and masses. These are almost instantly released from the target, ionized and mass separated by magnets to be sent as ion beams to the experiments. In the fastest cases, all these events are happening in a time-span of only a few milliseconds, as it was for instance demonstrated for ^{14}Be, which has a half-life of only 4.35 ms [84]. For radioactive ion beam production, one of the most important and difficult aspects is the ionization process as all experiments on exotic nuclei often rely on highest beam purity and intensity.

The ion source, which most closely meets these requirements is the *Resonance Ionization Laser Ion Source* (RILIS). First design studies were presented by *V.S. Letokhov and V.I. Mishin* [103] in 1984 and by *H.-J. Kluge et al.* in 1985 [90] and for the first time operated by *Alkhazov et al.* [1, 2] at the IRIS* facility at the Petersburg Nuclear Physics Institute (PNPI) in Gatchina, Russia in 1989. The RILIS is based on the principle of the selective laser photoionization [102], where several lasers are wavelength-tuned to the element-unique electron transitions of the atom for the stepwise excitation of the weakest bound electron above the ionization threshold. By principle, this technique is absolutely element-selective and ionization efficiencies of more than 10 % are possible. The RILIS at ISOLDE [57] was operated for the first time in 1992 [119] and has now become the most often used ion source at ISOLDE. In total, laser ionization schemes for more than 30 elements were developed and RILIS installations are operated at many radioactive ion beam facilities worldwide. For a comprehensive discussion of the developments in this field during the last decades, I refer to the review article of *V.N. Fedosseev, Yu. Kudryavtsev and V.I. Mishin* [58]. The regions on the nuclear chart, which are currently accessible by the RILIS technique are indicated by the red bars in Figure 1.1 and the expansion of the available elements is subject to ongoing research.

Despite the element-selective principle of the RILIS, the beam purity may be reduced due to ionization processes which take place in parallel. This is especially the case for the ISOLDE RILIS, where the laser photoionization takes place in a hot metallic cavity. The hot cavity also provides the conditions for the process of *surface ionization*, where an atom may lose an electron during the contact with a hot surface. This process can be very efficient for elements with low ionization energies, such as alkali or alkaline earth metals. The resolution of the separator magnets is not sufficient to efficiently suppress *isobars* (i.e. isotopes of the same mass, but from different elements) and thus, the *selectivity* of the RILIS, defined as the ratio of the ion beam intensity of the isotope of interest over the ion beam intensity of the isobaric contaminants, may be greatly reduced. In some cases, the contamination is so strong that foreseen experiments are hampered or may even be harmed. An important aspect of the technical developments for the RILIS are therefore aimed at improving the selectivity.

In addition to providing radioactive ion beams with high intensities and high purity to the experiments at ISOLDE, the RILIS is also a powerful and sensitive resonance ionization spectroscopy tool for ionization scheme development, fundamental atomic physics experiments and nuclear structure studies [1].

In this thesis all of these aspects of RILIS operation are performed: improvement of the selectivity of the RILIS by implementing a new device, the Ion Source and Trap (LIST), into the ISOLDE framework; laser ionization scheme development for calcium; determination of the ionization energy for polonium; and in-source resonance ionization spectroscopy of neutron-rich polonium.

*IRIS is the abbreviation for "Investigation of Radioactive Isotopes on Synchrocyclotron".

The outline of the thesis is as follows:
Part I, "Theory and Methods", aims at introducing all theoretical and experimental aspects necessary for the understanding of the experiments and results reported in this thesis. Chapter 2, "Interaction of light with atoms", describes the electronic structure of the atoms as well as different aspects of laser spectroscopy. In Chapter 3, the relevant theoretical and experimental principles of the "Radioactive ion beam production" are introduced: the ISOL process, the ionization processes, the RILIS setup and ion detection methods, and the principles of radiofrequency ion guides.
Part II, "Improvement of the selectivity of the resonance ionization laser ion source", describes two approaches for the improvement of the selectivity. Chapter 4 reports on the technical implementation into the ISOLDE framework, development work and experimental characterization of a device known as the *Laser Ion Source and Trap* (LIST). The LIST is a novel type of ion source for ISOLDE and was proposed by *H.-J. Kluge* and first described by *K. Blaum et al.* in 2003 [14, 176]. It consists in its present form of an electrostatic surface ion repelling electrode and a radiofrequency quadrupole (RFQ) ion guide located immediately downstream of the cavity. The problem of the unwanted isobaric contamination in RILIS beams is tackled directly as ions created before the LIST structure are blocked by the positively charged repeller electrode whilst neutral atoms may enter the laser/atom interaction region inside the RFQ, where the element-selective resonance ionization takes place. After development work at the Mainz University [14, 74, 152, 176, 178] prior to the work described in this thesis, extensive off-line tests and the first two on-line runs at ISOLDE allowed the characterization and the improvement of the performance in terms of selectivity and ionization efficiency. Following these, a first on-line physics experiment to use the LIST took place at ISOLDE/CERN in September 2012.
In Chapter 5, a new laser ionization scheme for calcium will be introduced that increases the laser ionization efficiency by a factor of about 20 compared to the previous existing laser ionization scheme. During the on-line period in 2012, the new laser ionization scheme for calcium was in use for two experiments [11, 96] and enabled the study of the exotic ^{53,54}Ca isotopes for the first time by the ISOLTRAP experiment [177].
Part III, "In-source laser spectroscopy of polonium", covers fundamental atomic and nuclear structure studies of polonium isotopes. Chapter 6, is about the "precision measurement of the ionization energy of polonium". Laser scans over the ionization energy of polonium revealed a rich spectrum with many *Rydberg states* (highly excited electron states), which enabled the determination of the ionization energy with more than 50 times higher precision than the value known from literature [149]. Chapter 7 is devoted to the in-source laser spectroscopy of polonium isotopes using the RILIS. This is a fitting conclusion to the work described in this thesis since the isotope of interest, ^{217}Po, was only accessible due to the strong suppression of francium isotopes achieved by using the LIST. The results obtained give a valuable insight into the evolution of nuclear structure for this region of the nuclear chart, whilst the success of the experiment is a demonstration of the LIST as a viable ion source option for high purity ion beam production and in-source resonance ionization spectroscopy.

Part I

Theory and methods

2 Interaction of light with atoms

This chapter describes the basic principles of the interactions between light and atoms, which are essential to understand the experimental methods and physics described in this thesis. The basic concept of atomic physics is briefly introduced by the most simple atomic structure, the one-electron systems. A similar behavior of the energy levels is observed in so-called *Rydberg-atoms*, whose spectra can be described by the *Rydberg-Ritz formula*. It will be used to determine the ionization potential of polonium later in this work. Building upon the discussion of the one-electron system, the fine-structure of multi-electron atoms and important parameters such as the quantum numbers that describe the atomic structure are summarized. One important part of this work is the observation and description of the *hyperfine-structures* and *isotope shifts* of exotic polonium nuclei. These phenomena are described in the last part of Section 2.1, which deals with atomic spectra. In Section 2.3, the fundamental principles of the emission and absorption of light are discussed since they are essential to the understanding of the technique of laser spectroscopy. The chapter ends with the fundamental formulae which describe the atomic spectral lineshapes and widths. The discussion follows the descriptions given in [42, 48, 164, 167], if not otherwise identified.

2.1 Electronic structure of atoms

2.1.1 One-electron systems

The precise calculation of the discrete energy levels of the two body system of one-electron atoms, such as the hydrogen atom (H) and hydrogen-like atoms (He^{+}, Li^{++}, etc.), is one of the greatest achievements of quantum physics theory. In fact, these are the only atomic systems in non-relativistic quantum theory, which have an exact solution and they therefore serve as an important basis for the further understanding of the electron-structure of multi-electron atoms.
A one-electron atom consists of an electron with charge $-e$ and mass m_e and an atomic nucleus with charge Ze and mass M. Its stationary states are solutions of the *time-independent Schrödinger equation*:

$$\mathcal{H}\,\Psi(\boldsymbol{r}) = E\,\Psi(\boldsymbol{r})\,, \tag{2.1}$$

where $\mathcal{H} = \mathcal{H}_{kin} + \mathcal{H}_{Coulomb}$ is the *Hamilton energy operator* and $\Psi(\boldsymbol{r})$ the eigenfunction of the one-electron atom as a function of the position variable $\boldsymbol{r}$*. The calculation can be simplified by placing the nucleus into the origin of the two-body system and by replacing m_e with the reduced mass $\mu = m_e M/(m_e + M)$ to study the relative motion of the electron to the nucleus. Then, the Schrödinger equation of the one-electron atom writes

*In this work, vectors are denoted in bold letters for improved readability.

as follows:

$$\left(-\frac{\hbar^2}{2\mu}\nabla^2 - \frac{Ze^2}{4\pi\epsilon_0 r}\right)\Psi(\boldsymbol{r}) = E\,\Psi(\boldsymbol{r})\,. \tag{2.2}$$

The spherical symmetry of the *Coulomb potential* suggests the use of spherical coordinates (r, θ, and ϕ), which leads after transformation of the Laplace operator ∇^2 to a separation ansatz since the Coulomb potential depends solely on r:

$$\Psi\left(r,\theta,\phi\right) = R(r)\,Y(\theta,\phi)\,. \tag{2.3}$$

Solutions to the separable terms in Equation. 2.3 are the *radial eigenfunctions* $R_{n,l}$ and the *spherical harmonics* Y_l^m, which introduce the quantum numbers: *principal quantum number n*, *angular momentum l* and *magnetic quantum number m*. The *energy eigenvalues* E_n are then given by

$$E_n = -\frac{1}{2}\frac{e^4\mu}{\left(4\pi\epsilon_0\right)^2\hbar^2}\frac{Z^2}{n} \equiv -R_M\frac{Z^2}{n^2}\,, \tag{2.4}$$

where R_M is the *Rydberg constant* of the one-electron system with reduced mass μ. R_M can also be rewritten as

$$R_M = R_\infty\frac{\mu}{m_e} = R_\infty\frac{M}{M+m_e} \tag{2.5}$$

where R_M is the fundamental Rydberg constant $R_\infty = 109737.32\,\mathrm{cm}^{-1}$. E_n is the energy of the excited state with principal quantum number n below the ionization limit, defined by $E_{\mathrm{lim}} = 0\,\mathrm{cm}^{-1}$. The resulting energy levels are therefore negative. In atomic spectroscopy however, it is common practice to note the electron levels as the excitation energy W_n, defined as the energy of the excited level to the ground state, $W_n = E_n - E_{\mathrm{lim}}$. The minimum energy that is required to remove one electron from the atom with respect to the lowest energy configuration of the electrons (the *atomic ground-state*) is given by $W_{\mathrm{lim}} = IE = E_{\mathrm{lim}} - E_0 = |E_0| = e\phi_1$ and is called the *first ionization energy* (IE) and ϕ_1 the *first ionization potential* (IP)*. This work mainly discusses the case, when one electron is removed from the neutral atom. Therefore, these measures are simply called the ionization energy and the ionization potential in the following.
The energy eigenvalues E_n describe the *gross structure* of the one-electron system and do not depend on the quantum numbers l and m. The energy level E_n of the one-electron system is therefore n^2-fold degenerate. For a full description of the one-electron system, Equation (2.2) needs to be further corrected for relativistic effects (*fine structure*, FS and the interaction of the electron with the nucleus (*hyperfine structure*, HFS, which leads to a splitting and shifting of the degenerate states. These effects are discussed for multi-electron atoms later in this chapter.

2.1.2 Rydberg atoms

In the first order for any multi-electron atom, the distribution of the states with a high principal quantum number, n is analogous to that of the one electron atom. The energy of

*In literature, the usage of these terms is not always consistent and often the term ionization potential refers to the ionization energy. In this work, the term ionization energy is used.

these so-called *Rydberg states* converge to the ionization limit or to *ionic states* similarly to the excited states of the one-electron atom described by Equation (2.4).
This similarity can be qualitatively explained by the screening of the total nuclear charge Z by the $N-1$ inner electrons ($N = Z$ for neutral atoms, $N-1$ for a singly ionized ion, etc.) of the atom. Thus, the effective charge acting on the highly excited outer electron is $\zeta = Z - (N-1)$ and the energy of the excited state can be calculated in first order by

$$E_n = -\frac{R_M \zeta^2}{n^2}\,. \tag{2.6}$$

However, there is a non-negligible probability that the electron penetrates the inner core of the electron shell. In this case, screening is not complete and the outer electron interacts with the larger charge of the nucleus and the inner $N-1$ electrons. The shift of the energy levels compared to the one-electron atom can be described by correcting the principal quantum number n through the use of the *quantum defect* $\delta_{n,l}$ and an *effective quantum number* $n^* = n - \delta_{n,l}$. The energy levels in the Equation (2.6) are then given by

$$E_n = -\frac{R_M \zeta^2}{(n-\delta_{n,l})^2} = -\frac{R_M \zeta^2}{(n^*)^2}\,. \tag{2.7}$$

The quantum effect varies with the angular momentum l due to the l-dependent penetration of the inner core. The probability to find an s-electron ($l = 0$) close to the inner core is higher than for electrons with larger l and thus, the s-electron will experience a nuclear potential that shows a stronger deviation from the point-like Coulomb potential of the one-electron atom.
The quantum defect δ is constant for high principal quantum numbers n and Equation (2.7) is a good approximation of the highly excited Rydberg states close to the ionization potential. However, the quantum defect shows also a small dependency on the principal quantum number n, which gets stronger for smaller n. These higher order effects can be described by the *Ritz expansion*:

$$\delta = \delta_0 + \frac{\delta_1}{n^*} + \frac{\delta_2}{(n^*)^2} + \cdots\,, \tag{2.8}$$

which can be approximated in the second order to

$$\delta(n) = A + \frac{B}{(n-A)^2}\,, \tag{2.9}$$

where A and B are newly introduced constants to take account for the n-dependency of $\delta(n)$.
Combining Equation (2.7) and Equation (2.9) leads to the the Rydberg-Ritz formula [83]:

$$E_n = -\frac{R_M \zeta^2}{\left(n - A + \frac{B}{(n-A)^2}\right)^2}\,. \tag{2.10}$$

The Rydberg formula and Rydberg-Ritz formula (Equations 2.7 and 2.10) can be used to determine the ionization energy of an element very precisely, provided that the energies of several members of a *Rydberg series* (Energy levels E_n with same quantum defect $\delta_{n,l}$) are known.

2.1.3 Multi-electron atoms

The Hamilton operator of a multi-electron atom with N electrons and a nuclear charge of Ze takes the form

$$\mathcal{H} = \sum_{i=1}^{N} \left(-\frac{\hbar}{2m}\nabla_i^2 - \frac{Ze^2}{4\pi\epsilon_0 r_i} \right) + \sum_{i<j=1}^{N} \frac{e^2}{4\pi\epsilon_0 r_{ij}} + \sum_{i=1}^{N} \xi(r_i)\,(\boldsymbol{l}_i \cdot \boldsymbol{s}_i)\ . \tag{2.11}$$

The first term in Equation (2.11) describes the kinetic energy and interaction of each electron with the Coulomb potential of the nucleus. The second term describes the contribution to the potential energy from the electrostatic repulsion between the electrons. The third term is due to the interaction of the intrinsic *electron spin* $\boldsymbol{s}$ (quantum numbers $s = \pm\frac{1}{2}$) with the dipole moment due to its orbital angular momentum $\boldsymbol{l}$ and is known as the *spin-orbit interaction*.
There exists no exact solution for the Schrödinger equation of multi-electron atoms and the wave-functions have to be approximated. However, it turns out that the non-central electrostatic interaction depends on the *total orbital angular momentum* $\boldsymbol{L} = \sum_i^N = l_i$ and the *total spin* $\boldsymbol{S} = \sum_i^N = s_i$. Their associated quantum numbers L, S, M_L, and M_S replace the individual quantum numbers m_l and m_s of each electron
The spin-orbit interaction leads to a splitting of the formerly degenerate gross-structure into separated energy-levels, called the *fine structure*. The appropriate method of evaluating the spin-orbit interaction depends on the relative interaction strength of the individual electron spin with its own magnetic dipole moment. Two limiting cases can be distinguished: the pure ***LS**-coupling*, which is a good description for light atoms and the ***jj***-coupling, which occurs in heavier atoms.

***LS*-coupling**

In case of ***LS***-coupling, the interaction between the orbital moments $W_{l_i,lj} = a_{ij}\boldsymbol{l}_i\boldsymbol{l}_j$ and between the spin magnetic moments $W_{s_i,sj} = b_{ij}\boldsymbol{s}_i\boldsymbol{s}_j$ are strong compared to the interaction between the orbital magnetic moment and the spin magnetic moment of the same electron e_i: $W_{l_i,si} = c_{ii}\boldsymbol{l}_i\boldsymbol{s}_i$. Then, the orbital magnetic moments and spin magnetic moments couple to the *total angular momentum* $\boldsymbol{J} = \boldsymbol{L} + \boldsymbol{S}$. It has the corresponding quantum number J with values of

$$J = L + S,\ L + S - 1,\ \cdots,\ |L - S|\ . \tag{2.12}$$

The value of $\boldsymbol{J}$ is then given by $|\boldsymbol{J}| = \hbar\sqrt{J\,(J+1)}$. Pure ***LS***-coupling results in a well separated fine splitting of the energy levels of the one-electron energies $E(n, L, S)$, for which the individual fine structure component is then denoted as $n^{2S+1}L_J$.

jj-coupling

The pure jj-coupling is the opposite extreme, where the interaction between the orbital magnetic moment and the spin magnetic moment of the same electron $W_{l_i,si}$ is dominating. Then the angular momentum $\boldsymbol{l_i}$ and spin $\boldsymbol{s_i}$ of each electron couple to the *resultant angular momentum* $\boldsymbol{j_i} = \boldsymbol{l_i} + \boldsymbol{s_i}$ and form the total angular momentum $\boldsymbol{J} = \sum_{i=1}^{N} \boldsymbol{j_i}$. In this case, the fine splitting is no longer well resolved in the spectrum and L and S cannot be treated as a "good" quantum number. The only remaining "strong" quantum number to describe the spectrum is the total angular momentum J.

2.2 The influence of the nucleus on the atomic structure

Such is the precision of laser spectroscopy measurements that perturbations or splittings of the atomic energy levels due to the non-point like nature of the nucleus may be resolved, even though the correction on the energy levels are orders of magnitudes smaller than the contributions of the gross and fine structure. Two effects are of importance in this work: a small shift of the fine structure energy levels for different isotopes of the same element, called the *isotope shift* (IS), and a further splitting of the fine structure into the so-called *hyperfine structure*. The isotope shift is caused by the nuclear mass, volume and charge distribution. The hyperfine structure is the result of the interaction of the higher order components of the electromagnetic multipole field with the electrons.
The measurement of the isotope shift and the hyperfine structure are important observables in laser spectroscopy because they contain information related to the nuclear charge distribution and moments.

2.2.1 Isotope shift

The mass and the charge distribution inside the nucleus changes along an isotope chain due to the different number of neutrons. This shifts the energy levels of the atom, as the interaction between the electrons and the nucleus is affected. The total shift of one fine structure energy level E_{i} between two isotopes with mass mass M^A and $M^{A'}$ is called the isotope shift and is defined as

$$\Delta E_{\mathrm{IS},i} = E_i^{A'} - E_{\mathrm{i}}^{A} \,. \tag{2.13}$$

Two effects are responsible for the isotope shift: the change of the kinetic energy of the electrons due to the change of the finite nuclear mass (*mass shift*, MS) and the change of the Coulomb potential due the non-point-like structure of nucleus, which changes volume and shape (*field shift*, FiS):

$$\Delta E_{\mathrm{IS,i}}^{AA'} = \Delta E_{\mathrm{MS,i}}^{A'} + \Delta E_{\mathrm{FiS,i}}^{A'} \,. \tag{2.14}$$

Mass shift

The mass shift, which dominates the isotope shift of light nuclei ($Z < 30$), is caused by the difference in kinetic energy $\Delta E_{\mathrm{kin}}^{AA'}$ of the electrons of two isotopes with mass number

A and mass number A', respectively. It can be calculated by

$$\Delta E^{AA'}_{\mathrm{kin,i}} = E^{A'}_{\mathrm{kin,i}} - E^{A}_{\mathrm{kin,i}} = \frac{1}{2}\frac{M^{A'} - M^{A}}{M^{A'}M^{A'}} \sum_{i=1}^{N} \boldsymbol{p}_i^2 + \sum_{i>j}^{N} \boldsymbol{p}_i \boldsymbol{p}_j \,, \tag{2.15}$$

where $\boldsymbol{p}$ is the momentum of the electrons. The two terms in Equation (2.15) can be treated separately: term one describes the sum over the change in the single electron energies due to the change in mass and is called the *normal mass shift* (NMS), while the second term describes the changes in the electron-electron correlations and is called the *specific mass shift* (SMS). It follows that NMS and SMS have the same mass dependency and the total mass shift can be written as:

$$\Delta E^{AA'}_{\mathrm{MS,i}} = \Delta E^{AA'}_{\mathrm{NMS,i}} + \Delta E^{AA'}_{\mathrm{SMS,i}} = (K_{\mathrm{NMS,i}} + K_{\mathrm{SMS,i}}) \frac{M^{A'} - M^{A}}{M^{A}M^{A'}} \,, \tag{2.16}$$

where $K_{\mathrm{NMS},i}$ is calculated easily by $m_e \cdot E_{\mathrm{FiS},i}$. $K_{\mathrm{SMS},i}$ is not analytically solvable for multi-electron systems and have to be derived by theoretical calculations [33]. However, the calculations are very difficult to obtain and therefore limit the accuracy of the information derived from the isotope-shift measurements.

Field shift

The field shift $\Delta E^{A'}_{\mathrm{FiS}}$ dominates the isotope shift of heavier elements since the mass shift is approximately inversely proportional to $M^A M^{A'}$. It can be written as

$$\Delta E^{AA'}_{FiS} = F_i \cdot \lambda^{AA'} = E_i \cdot f(Z) \cdot \lambda^{AA'}, \tag{2.17}$$

where E_i is the *electronic factor*, $f(Z)$ is a function which takes into account the finite size of the nucleus and $\lambda^{AA'}$ is the change of the *nuclear charge parameter*. The electronic factor is proportional to the change of the total non-relativistic electron-charge density at the nucleus $\Delta\left|\Psi(0)\right|^2$ and is given by

$$\Delta E^{AA'}_{FiS} = \frac{\pi a_0}{Z} \Delta\left|\Psi(0)\right|^2 \,. \tag{2.18}$$

The determination of the electronic factor E for heavier isotopes relies on empirical data, since its precise calculation, based only on fundamental interactions, is only possible for atomic systems with up to three electrons [65, 76]. The function $f(Z)$ increases with Z and takes into account the finite nuclear charge distribution and corrects the electronic factor E_i for relativistic effects. The nuclear charge parameter $\lambda^{AA'}$ can be expressed as a power series of the changes in the mean charge radius $\delta\langle r^{2i}\rangle^{AA'}$:

$$\lambda^{AA'} = \delta\langle r^2\rangle^{AA'} + \sum_{i=2}^{\infty} \frac{C_i}{C_1} \langle r^{2i}\rangle^{AA'} \,, \tag{2.19}$$

where C_i are the *Seltzer-coefficients*. They can be found in literature for most elements together with the relations between the higher order of the changes in the mean square charge radius $\delta\langle r^{2i}\rangle^{AA'}$ and the mean square charge radius $\langle r^2\rangle^{AA'}$ [161]. The Seltzer coefficients are decreasing rapidly with higher orders and thus, higher powers of the mean square radii do not contribute much. In case of polonium, literature values for C_i and $\frac{\delta\langle r^{2i}\rangle^{AA'}}{\delta\langle r^2\rangle^{AA'}}$ lead to $\lambda^{AA'} \approx 0.932 \cdot \delta\langle r^2\rangle^{AA'}$.

Obtaining nuclear properties from isotope shift measurements

A careful analysis of the isotope shift gives access to the changes in the mean-square charge radius $\delta\langle r^2\rangle^{AA'}$. Its accuracy is limited by the precision of the determination of the constants K_{NMS}, K_{SMS}, E, and $f(Z)$. As has been discussed, the electronic factor and the value of K_{SMS} rely on atomic calculations or supplementary experimental data. In heavier nuclei, the mass shift becomes less important since it is proportional to $\frac{1}{AA'}$. On the other hand, the field shift is proportional to Z, which makes the determination of the changes in the mean square charge radius $\delta\langle r^2\rangle^{AA'}$ easier for heavier nuclei such as polonium. However, an alternative way to determine the electronic factor E and the specific mass constant K_{SMS} is the so-called *King plot*, if additional independent information (e.g. from e^- scattering, muonic decay, or K x-ray experiments) about isotope shifts in other transitions is available [88]. It allows a separation of the field and mass shifts and gives information about the consistency of the data. In preparing a King plot, the isotope shifts of a measured transition and a reference transition are put into relation by introducing the *modified isotope shift* defined by

$$\Delta E_{\mathrm{IS,i}}^{\mathrm{mod}} = \left(\Delta E_{\mathrm{IS,i}} - \Delta E_{\mathrm{NMS,i}}\right) \frac{AA'}{A' - A} \tag{2.20}$$

to remove its mass dependency. The modified isotope shift of the reference transition becomes the x-axis and the modified isotope shift of the measured optical transition becomes the y-axis of the King plot. Then, the pairs of the modified isotope shifts fall on a straight line, where the slope is the ratio between the two electronic factors E of the transitions and the interception with the y-axis is the difference of the mass-shift factors. For a detailed description of this procedure, I refer to [76, 88, 128]. A King plot using recent data for the even-even polonium isotopes can be found in [39].

2.2.2 Hyperfine structure

On smaller energy scales, a further splitting of the fine-structure becomes visible. This so-called *hyperfine structure* is caused by the interaction of the higher order electromagnetic multipoles of the non-point-like nucleus with the electrons. When the electromagnetic potential of the nucleus, V_{em}, is written as a multipole expansion one gets:

$$V_{\mathrm{em}} = V_{\mathrm{Coulomb}}\left(\mathcal{O}(\mathcal{R}^{-1})\right) + V_{\mathrm{Dipole}}\left(\mathcal{O}(\mathcal{R}^{-3})\right) + V_{\mathrm{Quadrupole}}\left(\mathcal{O}(\mathcal{R}^{-5})\right) + \cdots . \tag{2.21}$$

In general, the effect on the energy levels gets weaker with higher multipole orders and thus, only the first three leading terms are of practical relevance in laser spectroscopy. The first term is the Coulomb-potential of the nucleus and causes the gross structure as discussed previously. The second and third terms, responsible for the hyperfine structure, are the *magnetic dipole moment* and the *electric quadrupole moment*, respectively. A schematic of the hyperfine structure of an atomic level with nuclear spins $I = 3/2$ and total angular momentum $J = 2$ can be found in Figure 2.1.
Similar to the total angular momentum $\boldsymbol{J}$ of the electrons, a total nuclear spin $\boldsymbol{I} = \sum_{n=1}^{A}(\boldsymbol{s}_n + \boldsymbol{l}_n)$ can be assigned to the nucleus as the sum over all spins and angular momenta of the protons and neutrons. $\boldsymbol{I}$ and $\boldsymbol{J}$ couple to give the total angular momentum $\boldsymbol{F} = \boldsymbol{I} + \boldsymbol{J}$ of the atom, where F takes values from $|I - J|$ to $|I + J|$. A hyperfine level with total atomic angular momentum F is then shifted relative to the energy of a fine

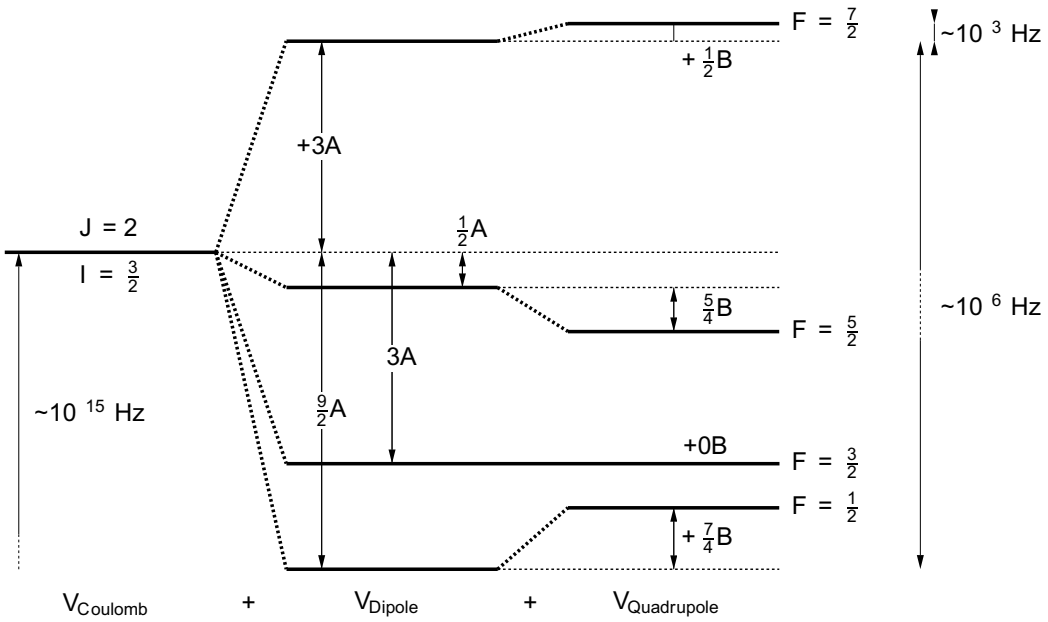

Figure 2.1: Schematic of the hyperfine structure of an electronic level with $I = 3/2$ and $J = 2$ [36]. Only the dipole interaction and the quadrupole interaction are considered. The level splitting is not to scale.

structure energy level $n^{2S+1}L_J$ by

$$\Delta E_F = \frac{A}{2} \cdot C + B \cdot \frac{\frac{3}{4}C\,(C+1) - I\,(I+1)\,J\,(J+1)}{2\,(2I-1)\,(2J-1)\,I \cdot J}\,, \tag{2.22}$$

where $C = F\,(F+1) - J\,(J+1) - I\,(I+1)$ is the *Casimir factor* [28].
A is the *magnetic dipole constant* and describes the interaction of the nuclear magnetic moment μ_I with the magnetic field at the nucleus caused by the total angular momentum J of the electrons $H_J(0)$:

$$A = \frac{\mu_I H_J(0)}{I \cdot J}\,. \tag{2.23}$$

Note that the nuclear magnetic moment, given by $\mu_I = g_I \frac{e}{2m_p}\boldsymbol{I}$ is smaller than the magnetic moment of the electron spin $\mu_S = g_S \frac{e}{2m_e}\boldsymbol{S}$ by the factor of $\frac{m_e}{m_p} \approx \frac{1}{1836}$. This is the reason why the hyperfine structure splittings is typically 3 orders of magnitude smaller than the fine structure splitting. Furthermore, the nuclear spin of ground state nuclei with even numbers of protons and neutrons (*ee*-nuclei) is $\boldsymbol{I} = 0$ (except for very few light nuclei) and thus, the magnetic dipole interaction is only observed for nuclei with either an odd number of nucleons (*eo*-, or *oe*-nuclei, where I is a half-integer) or an odd number of proton and neutron (*oo*-nuclei, where I is an integer).
B is the *electric-quadrupole coupling constant* and describes the interaction of the electric field gradient $\partial^2 V/\partial^2 z|_{z=0}$ at the nucleus with the *spectroscopic quadrupole moment* Q_s:

$$B = \left(\frac{\partial^2 V}{\partial^2 z}\right)\Bigg|_{z=0} eQ_s\,. \tag{2.24}$$

Q_s is usually expressed in terms of the *deformation parameter*, β, and is a measure of the deviation of the nuclear charge distribution from a spherical distribution. The electric-quadrupole interaction is therefore strongest for deformed nuclei and its sign depends on the deformation of the nucleus: $Q > 0$, if the nucleus is elongated along the direction of $\boldsymbol{I}$ (prolate shape) and $Q < 0$, if the nucleus is flattened (oblate shape). The shift due to the electric quadrupole requires a non-zero Q and a non-zero electrical field gradient at the nucleus, which leads to $I, J \geq 1$.
Higher order components of the HFS are beyond the resolution power of the techniques used in this work and are therefore neglected in the following. For further reading, I refer to the literature [19].

2.3 Absorption and emission of light

Valence (or outer shell) electrons can interact with photons in various ways. Essential for laser spectroscopy is the absorption and emission of photons, whereby an electron undergoes a transition between two energy levels E_i and E_j (with $i < j$). Energy must be conserved and thus, the energy of the photon is $E_{ij} = E_i - E_j$. A photon which fulfills this criteria is then called resonant with this transition. E_{ij} is directly proportional to the *frequency* ν and inversely proportional to the *wavelength* in vacuum $E_{12} = h\nu_{12} = hc/\lambda$. In optical spectroscopy however, it is common practice to note a transition by its wavenumber defined by $\tilde{\nu} = \nu/c = 1/\lambda$.
In the following, the basic principles of absorption and emission of light are described first by the *Einstein coefficients*. The spectral linewidth, lifetime and broadening mechanisms of a transition between two atomic states are then discussed.

2.3.1 The Einstein probability coefficients

The processes involved in a transition of one electron between two energy levels E_i and E_j ($i < j$) were first described by Albert Einstein [54]. Einstein identified three fundamental processes, which govern the emission and absorption of light and assigned each of them an intrinsic probability coefficient: *resonant absorption* (Einstein coefficient B_{ij}), *stimulated emission* (Einstein coefficient B_{ji}), and *spontaneous emission* (Einstein coefficient A_{ji}).
In the following discussion of the Einstein coefficients, an ensemble of idealized non-degenerated two-level atoms with energy states $E_2 > E_1$ is assumed as shown in Figure 2.2. First we can state that secondary transition channels are absent and that the total occupation N_{tot} of the energy states should then be constant:

$$N_1 + N_2 = N_{\mathrm{tot}} = \text{const.}\,, \tag{2.25}$$

where N_1 and N_2 are numbers of electrons in the lower and upper level, respectively.

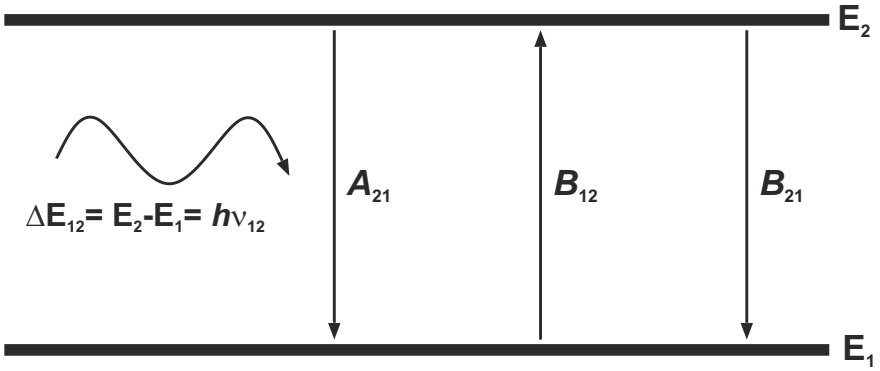

Figure 2.2: An illustration of the three possible processes involved in a transition of an electron between two electron levels with their corresponding Einstein probability coefficients: spontaneous emission (A_{21}), absorption (B_{12}), and stimulated emission (B_{21}).

Resonant absorption

Resonant absorption occurs, when a resonant photon with frequency ν_{12} excites an electron from the lower state to the upper state. If the ensemble is exposed to a radiation field with density $\rho(\nu)$, the number of electrons in the lower state N_1 is then reduced with a rate $\dot{N}_1$ proportionally to the amount of photons with ν_{12}:

$$\dot{N_1} \equiv \frac{\partial N_1}{\partial t} = -B_{12}\rho(\nu_{12})\, N_1 \,. \tag{2.26}$$

Stimulated emission

In the stimulated absorption, electrons in the excited state may jump with probability (B_{12}) to the lower state in the presence of a radiation field $\rho(\nu_{12})$:

$$\dot{N_2} = -B_{21}\rho(\nu_{12})\, N_2 \,. \tag{2.27}$$

Spontaneous emission

While the former two effects only occur in a radiation field, spontaneous emission is purely statistical and may occur also without the presence of a radiation field. An electron in the excited state releases its energy with probability A_{21}. The rate of this process is then given by:

$$\dot{N_2} = -A_{21} N_2 \,. \tag{2.28}$$

Spontaneous emission defines the natural lifetime of an excited atomic and can be observed, for instance, in an excited medium as fluorescence.

Einstein's relations

While absorption and stimulated emission can in principle be explained by a semiclassical approach using time-dependent quantum mechanic wavefunctions and classical electromagnetic theory, spontaneous emission cannot be explained this way, because it involves statistical processes. It therefore requires the theory of quantum electrodynamics (QED) for a full description. Luckily no knowledge about wavefunctions is necessary to derive the relations between the different Einstein coefficients. In fact, Einstein derived the relations between the probability coefficients from considerations based entirely on the principles of thermodynamics by describing the processes for an idealized two-level atom in a blackbody enclosure.
The ensemble is then exposed to a radiation field, which follows the Planck relation:

$$\rho(\nu, T)\, d\nu = \frac{8\pi\nu^2}{c^3} d\nu \frac{1}{e^{h\nu/kT} - 1} h\nu \,, \tag{2.29}$$

where k is the *Boltzmann constant*.

The population ratio is given by the Boltzmann relation if the ensemble is in thermal equilibrium with an environment with temperature T:

$$\frac{N_2}{N_1} = \frac{g_2}{g_1} e^{-\frac{h\nu_{12}}{kT}} , \tag{2.30}$$

where g_2/g_1 is the degeneracy of the energy levels E_2. For the idealized non degenerate system, the ratio becomes E_1. $g_2/g_1 = 1$. In addition, the population of the lower and excited state is constant ($\dot{N}_1 = \dot{N}_2 = 0$) in thermal equilibrium and the total rate of resonant absorption must equal the rate of emission:

$$A_{21} N_2 + B_{21} \rho\left(\nu_{12}\right) N_2 = B_{12} \rho\left(\nu_{12}\right) N_1 . \tag{2.31}$$

Rearranging Equation (2.31) and using the Boltzmann relation in Equation (2.30) leads to

$$\rho\left(\nu_{12}\right) = \frac{A_{21}}{B_{12}\left(g_1/g_2\right) e^{h\nu_{12}/kT} - B_{21}} . \tag{2.32}$$

This must be equal to the Planck relation given in Equation (2.29) and by comparison one obtains the Einstein relations for the Einstein probability coefficients

$$g_1 B_{12} = g_2 B_{21} \quad \text{and} \quad A_{21} = \frac{8\pi h \nu_{12}^3}{c^3} B_{21} . \tag{2.33}$$

2.3.2 Resonance excitation of atoms

The Einstein probability coefficients for the transition between two states are intrinsic properties of the atom. They are thus also valid for atoms, which are taken out of the ideal blackbody enclosure and exposed to a photon flux Φ $\left[\mathrm{cm^2 s^{-1}}\right]$ (for example from a laser). Instead of using the absorption coefficient B_{12} it is more common to use the evidently related *absorption cross section* σ_{12} of the transition. The rate of the absorption is then given by

$$\dot{N}_2 = \Phi \sigma_{12} . \tag{2.34}$$

In a many-level atom, higher levels can then be successively populated from the excited level by the same principle using several light sources, which match the energy of the higher-lying transitions. The overall process is then governed by the probabilities (or cross-sections) for absorption and emission of all involved transitions and will eventually reach an equilibrium, where the rates of absorption and emission are equal. This is the underlying mechanism of resonance laser ionization and in-source laser spectroscopy.

2.3.3 Spectral linewidth

An elegant way to describe the interaction of electromagnetic waves with the electrons of an atom, involving statistical processes such as spontaneous emission, is the *density matrix formalism*, which leads to the *optical Bloch equations* (OBE). A thorough treatment of this approach is given in [16, 162]. In short, the solutions of the OBEs for a two-level transition between two states E_i and E_j (with $i < j$) lead to the *saturation parameter*,

S, and the *resonant saturation parameter*, S_0, given by:

$$S = \frac{S_0}{1 + \frac{4\delta^2}{\gamma^2}}, \quad \text{and} \quad S_0 = \frac{I}{I_{\text{sat}}} \quad \text{with} \quad I_{\text{sat}} = \frac{\pi hc}{3\lambda^2}\gamma, \tag{2.35}$$

where γ is the *damping parameter*. In the simple two-level atom, this can be interpreted as the spontaneous emission $\gamma = A$. δ is the detuning of the frequency with respect to the resonance frequency of the transition. I is the intensity of the laser radiation of wavelength λ. I_{sat} is the *saturation intensity* at which a population of the excited state E_j reaches its maximum of 50%, provided that $g_1 = g_2$. An excited state population of more than 50% is called a *population inversion* and is only possible for excitation schemes with more than two levels.
The lineshape of a transition has a *Lorentzian* form with a linewidth (FWHM*) of

$$\delta\nu_{\text{p}} = \frac{\gamma}{2\pi}\sqrt{1 + S_0}. \tag{2.36}$$

The *natural linewidth* observed, if the transition is not saturated ($I < I_{\text{p}}$). In this case, the linewidth is given by the damping parameter γ or by the inverse of the lifetime τ of the transition†:

$$\delta\nu_{\text{nat}} = \frac{\gamma}{2\pi} = \frac{1}{2\pi\tau}. \tag{2.37}$$

For a two-level atom, the natural linewidth is simply the Einstein coefficient A_{21} of the transition and its lifetime $\tau = \frac{1}{A_{21}}$ by its inverse. For more realistic multi-level atoms, the lifetime has to be corrected for the additional lower states, to which the excited electron with E_j can decay. Then, the total decay probability to all $N = k$ lower levels is the sum of the corresponding Einstein coefficients and the total lifetime calculates to:

$$\tau_j = \frac{1}{\sum_{k=1}^{k} A_{jk}}. \tag{2.38}$$

The line profile of the lower state E_i is also *naturally broadened* due to contribution of the line profiles of all transitions to the total linewidth. This leads in turn to a Lorentzian shape with an overall natural linewidth of this transition of

$$\delta\nu_{\text{nat,ij}} = \delta\nu_{\text{nat,j}} + \delta\nu_{\text{nat,i}} = \frac{1}{2\pi\tau_j} + \frac{1}{2\pi\tau_i}. \tag{2.39}$$

Typical lifetimes of non-metastable excited states are of the order of 10^{-8} s with corresponding typical natural linewidths of 100 MHz. The resolution of these narrow transitions by laser spectroscopy is very complicated and requires special Doppler-free or Doppler-reduced techniques such as collinear laser spectroscopy [13, 87] and collinear resonance ionization spectroscopy [135]. For in-source laser spectroscopy as used in this work, the natural linewidth cannot be resolved since the other broadening mechanisms dominate the

*Full width at half maximum

†The natural linewidth of a transition can be obtained alternatively by the *Heisenberg uncertainty principle* ($\Delta E \cdot \Delta t \geq \frac{\hbar}{2}$).

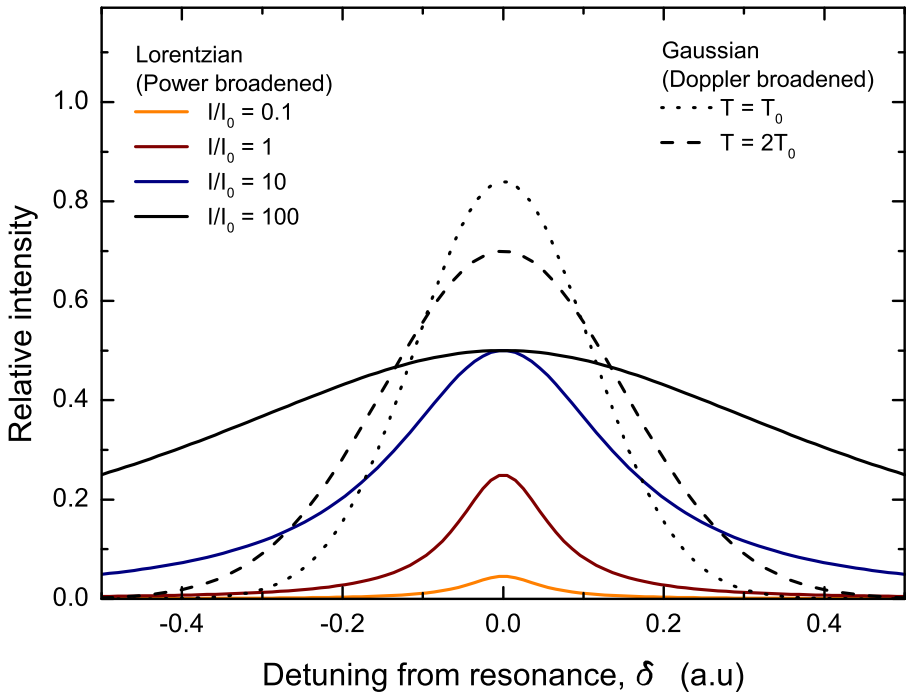

Figure 2.3: Lineshapes of power or Doppler broadened transitions. The power broadened transitions have a Lorentzian shape with intensity dependent widths. In contrast, the Doppler broadened transitions are Gaussian and depend on the temperature of the atomic vapour.

spectral lineshape. The most important of these are *power broadening*, *Doppler broadening*, and *pressure broadening*, which will be discussed in the following.

Power broadening

If the laser intensity I approaches or exceeds the saturation intensity I_{sat}, the lineshape still remains Lorentzian, but a broadening of the natural linewidth is observed. This can be understood by looking at the formula for the linewidth in Equation (2.36): if the laser frequency is in resonance with the transition ($\nu = \nu_0$, $\delta = 0$), the population of the excited state cannot exceed 50%. On the other hand, if the laser frequency is off resonance ($\nu \neq \nu_0$, $\delta \neq 0$), the population maximum is not yet reached and the population can thus further increase with increasing laser intensity resulting in a flatter slope of the Lorentzian lineshape.

Pressure broadening

If ionization takes place in a buffer gas, in a dense vapour, or in the presence of charged particles such as ions and electrons, the energy and lifetime of an excited state can be altered. A shifting, broadening, and mixing of the energy levels can therefore occur. These effects are due to interactions between the excited atom and the buffer gas atoms. For

example, collisions of the excited atom with particles may reduce the lifetime of a state and thus broaden the lineshape (*collisional broadening*). Additionally, the *Stark effect*, which results in a shift of the resonance frequency, may be observed, if the excited atom is perturbed by an electric field of charged particles nearby. This effect can be significant in case the ionization takes place in gas cells, where the pressure is many orders of magnitude higher than in the hot cavity, which was used for the experiments described in this work. A full description of these effects is given in the reference [167].

Doppler broadening

For in-source laser spectroscopy in a hot cavity, the lineshape is dominated by Doppler broadening. This is due to the velocity distribution of a hot vapour with atomic mass m_A and temperature T, which follows the *Maxwell-Boltzmann distribution*:

$$\frac{\mathrm{d}N(v_x)}{N} = \frac{1}{\sqrt{\pi}} \exp\left(-v_x^2/v_0^2\right) \quad \text{with} \quad v_0 = \left(\frac{2k_bT}{m_A}\right)^{1/2}, \tag{2.40}$$

where v_x is the velocity of a single atom, v_0 is the "most probable velocity" and k_b is the Boltzmann constant. The transition frequency ν of a single atom which propagates with velocity v_z in opposite direction (z-direction) of the laser light becomes Doppler shifted to the transition frequency ν_0 at rest:

$$\nu = \nu_0 \left(1 + v_z/c\right) . \tag{2.41}$$

The overall lineshape follows the Maxwell-Boltzmann distribution from equation (2.40), which results in the Gaussian intensity profile

$$I(\nu) = I(\nu_0) \exp\left[-\left(\frac{c(\nu - \nu_0)}{\nu_0 v_0}\right)^2\right] \quad \text{with} \quad I(\nu_0) = \frac{c}{\sqrt{\pi}\nu_0 v_o} . \tag{2.42}$$

The contribution to the total broadening by the *Doppler broadening* $\delta\nu_{\mathrm{D}}$ is

$$\delta\nu_{\mathrm{D}} = 2\sqrt{\ln 2}\,\frac{\nu_0 v_0}{c} = \nu_0\sqrt{\frac{8k_bT\ln 2}{m_Ac^2}} . \tag{2.43}$$

In addition, the center frequency has to be corrected for the expected Doppler shift. This is especially the case for highly directional atomic flow jets.
For laser ionization in hot cavities as performed in this work, Doppler broadening can be of the order of several GHz. However, to account for a Gaussian and a Lorentzian contribution, one can use the so-called *Voigt function*, which is a convolution of a Gaussian $I_{\mathrm{G}}(\nu)$ and a Lorentzian line profile $I_{\mathrm{L}}(\nu)$:

$$I(\nu) = I_{\mathrm{G}}(\nu) * I_{\mathrm{L}}(\nu) = \int_{-\infty}^{\infty} d\nu' I_{\mathrm{G}}\left(\nu'\right) I_{\mathrm{L}}\left(\nu - \nu'\right) . \tag{2.44}$$

Although, the integral in Equation (2.44) cannot be solved analytically, modern computers and data analysis programs can generate Voigt functions and perform least-squares

fitting very rapidly. In case of in-source laser spectroscopy in hot cavities, a Gaussian approximation is often sufficient for determining the centroids of a transition due to the strong Doppler broadening.

2.3.4 Selection rules for allowed transitions

Not all transitions between atomic states show the same probability or are observed in nature. Whether a transition is *'allowed'* or *'forbidden'* is based on the rules of momentum conservation and symmetry (*parity* σ). To first order dipole approximation, the dipole operator only acts on the angular momentum and not on the electron spin. Therefore $\Delta l = \pm 1$, $\Delta s = 0$ and parity changes by $\sigma = \pm 1$. In case of $\boldsymbol{LS}$-coupling, where L, S, and J are good quantum numbers one gets the following rules for allowed dipole transitions:

$$\Delta S = 0, \Delta L = 0, \pm 1 \quad \text{and} \quad \Delta J = 0, \pm 1, \text{ where } J = 0 \not\Longrightarrow J = 0\,. \tag{2.45}$$

Similar expressions can be derived for transitions between hyperfine structure levels:

$$\Delta J = 0, \pm 1 \quad \text{and} \quad \Delta F = 0, \pm 1, \text{ where } F = 0 \not\Longrightarrow F = 0\,. \tag{2.46}$$

The word 'forbidden' is misleading as higher order multipole transitions may still occur, albeit with much smaller transition probabilities and cross-sections (several orders of magnitudes). Also, $\boldsymbol{LS}$-coupling is not always pure and lines and formerly forbidden dipole lines appear. Nevertheless, the selection rules given in Equation (2.45) and Equation (2.46) are good guides to analyze atomic spectra and for finding new laser excitation schemes.

3 Radioactive ion beam production

The production of exotic isotopes far away from stability enables the study of a large variety of phenomena in fields such as fundamental atomic-, astro-, nuclear-, and solid state physics. Some exotic nuclei are found to be deformed, decay in unexpected manner, or are suitable for medical applications. Determining their properties gives answers to questions such as the origin of elements (nucleosynthesis), nuclear structure and the chemistry of synthetic elements. It is also a very useful tool to explore new applications in fields such as nuclear medicine and material science.
Since the advent of radioactive ion beam (RIB) facilities in the 1950, more than 3000 isotopes have been discovered and studied [85] and many more isotopes are expected to be in reach.
Several concepts for the production of radioactive ion beams exist, but common for the majority of the techniques are a *driver (particle) beam* (also called *primary beam*), whose particles collide with the target material and cause nuclear reactions for the production of exotic nuclei, and a mass spectrometer to separate and select the reaction product of interest.
The production of nuclei far from stability comes with several difficulties:

- low production cross-sections and low ion yields of the isotope of interest.
- short half-lives of many isotopes.
- non-selective production inside the target and possible contamination with unwanted species.

Therefore, all types of RIB facilities require an efficient atom and ion release from the target, highly selective elements for beam purification, and efficient beam transportation. Most RIB facilities follow two fundamental concepts: the Isotope Separator On-Line (ISOL) technique and the In-Flight Fragment Separator technique. ISOL facilities can be further divided into two categories: those that use thick targets for production and *thermalization*[*] and rely on thermal motion for transport to the ion source; and facilities that use thin targets for production and gas catchers to stop the reaction products. An overview of the different types of RIB facilities is given in Figure 3.1 and in [18].
ISOL facilities are the most effective means of producing high intensity, low emittance beams of isotopes with a half-life greater than 10 - 100 ms. In contrast, the In-Flight Fragment Separator method uses heavy projectiles to react with a thin target. This process is extremely fast, chemistry independent and results in a high energy, high emittance beam of ions in a variety of charge states. Extremely exotic and short lived species are therefore

[*]Stopping and neutralization of the reaction products until the particles eventually reach thermal equilibrium with the target material.

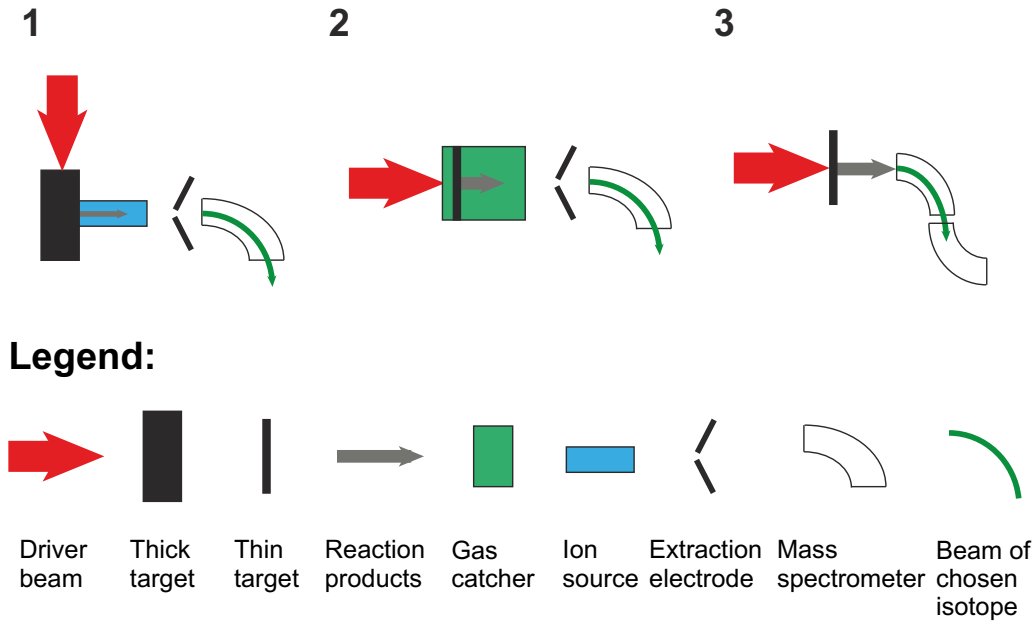

Figure 3.1: A sketch of the three different principles of radioactive ion beam facilities [113]: 1) ISOL method using a thick target and an ion source as used at ISOLDE/CERN, Meyrin, Switzerland. 2) ISOL facility with thin target plus gas catcher as used at IGISOL, Jyväskylä, Finland. 3) In-flight fragment separation method as used at GSI, Darmstadt, Germany.

accessible but the production yield of any chosen isotope is typically much lower than it can be achieved at an ISOL facility. Examples for ISOL facilities are ISOLDE at CERN, Switzerland, the RIB facility in Louvain-la-Neuve, Belgium and the IGISOL facility in Jyväskylä, Finland. In-Flight Fragment Separator facilities are found at the *Gesellschaft für Schwerionenforschung* (GSI) in Darmstadt, Germany, at the *Grand Accélérateur National d'Ions Lourds* (GANIL) in Caen, France and at the *the Japanese Institute of Physical and Chemical Research* (RIKEN*) in Wako, Japan. For further reading about the different facilities and methods, I refer to the several review papers [17, 18, 52].
Of the three different types of RIB facilities, only a thick target type ISOL facility requires necessarily a dedicated ion source for standard operation. Most commonly used are ion sources based on *surface ionization*, *resonance laser ionization*, *electron impact ionization* and *plasma ionization*. The right choice for the type of ion sources is crucial in planning an experiment and is made depending on the nuclear- (half-life), the atomic- (ionization energy, atomic levels, etc.) and the chemical properties of the element. The most important characteristics of an ion source at a RIB facility are the *ionization efficiency* ϵ_{ion} defined as

$$\epsilon_{\text{ion}} = \frac{\#\text{ of atoms ionized}}{\text{total }\#\text{ of atoms released from the target}} \tag{3.1}$$

*RIKEN is an abbreviation of Rikagaku Kenkyūjo, which translates from Japanese to English to "the institute of physical and chemical research".

and the *selectivity*, S, defined as

$$S = \frac{\text{Ion intensity of isotope of interest}}{\text{Total ion intensity on the given mass of contaminants and isotope of interest}} . \tag{3.2}$$

A lot of effort is continuously invested in the development of new techniques to improve these two parameters. One of the primary goals of the work described in this thesis was to improve the selectivity and efficiency of the Resonance Ionization Laser Ion Source (RILIS) at the ISOLDE facility.
This chapter will focus on the aspects of the radioactive ion beam production process at ISOLDE which are relevant to this work. A description of the ionization techniques with emphasis on resonance laser ionization is given. The status of the RILIS installation and its application as a spectroscopy tool is then discussed in the last part of the chapter.

3.1 The ISOL process at ISOLDE

This section discusses the ISOL process at ISOLDE, which includes the production of the exotic nuclei, the thermalization of the reaction products, the transport of the atoms to the ion source, the ionization, and the mass separation. The optional stages of ion beam cooling and bunching, charge-state breeding and post-acceleration were not used during this work and are therefore omitted. Figure 3.2 gives an overview of the different components and their location at ISOLDE: the driver beam enters ISOLDE through the proton beam line and impinges on the target installed at one of the target front-ends, where the exotic atoms are produced in nuclear reactions. The atoms are then transferred to an ion-source, extracted into the beam-line and mass separated by one of the separator magnets.

3.1.1 The driver beam

ISOLDE is integrated into the CERN accelerator complex as shown in Figure 3.3. It uses the bunched, 1.4 GeV proton beam from the CERN Proton Synchrotron Booster (PSB) as a driver beam, which is sent through the proton beam line towards the target front-end. PSB Proton bunches are of 1.66 µs length, contain up to $3 \cdot 10^{13}$ protons, and are separated by 1.2 s. The proton bunch distribution between the various users (ISOLDE, nTOF, LHC etc.), follows a repetitive sequence, known as the *super-cycle*, which typically contains of the order of 39 pulses. The maximum proton current that can be sent to ISOLDE is limited to 2 µA due to radio-protection constraints.

3.1.2 The target and front-end

A cross-section of a standard ISOLDE target unit for surface or resonance laser ionization is shown in Figure 3.4. It comprises a target cylinder filled with the target material, a transfer line for atom transport from the target to the source and a hot cavity, which serves as surface ion source or as the laser-atom interaction region for resonance laser

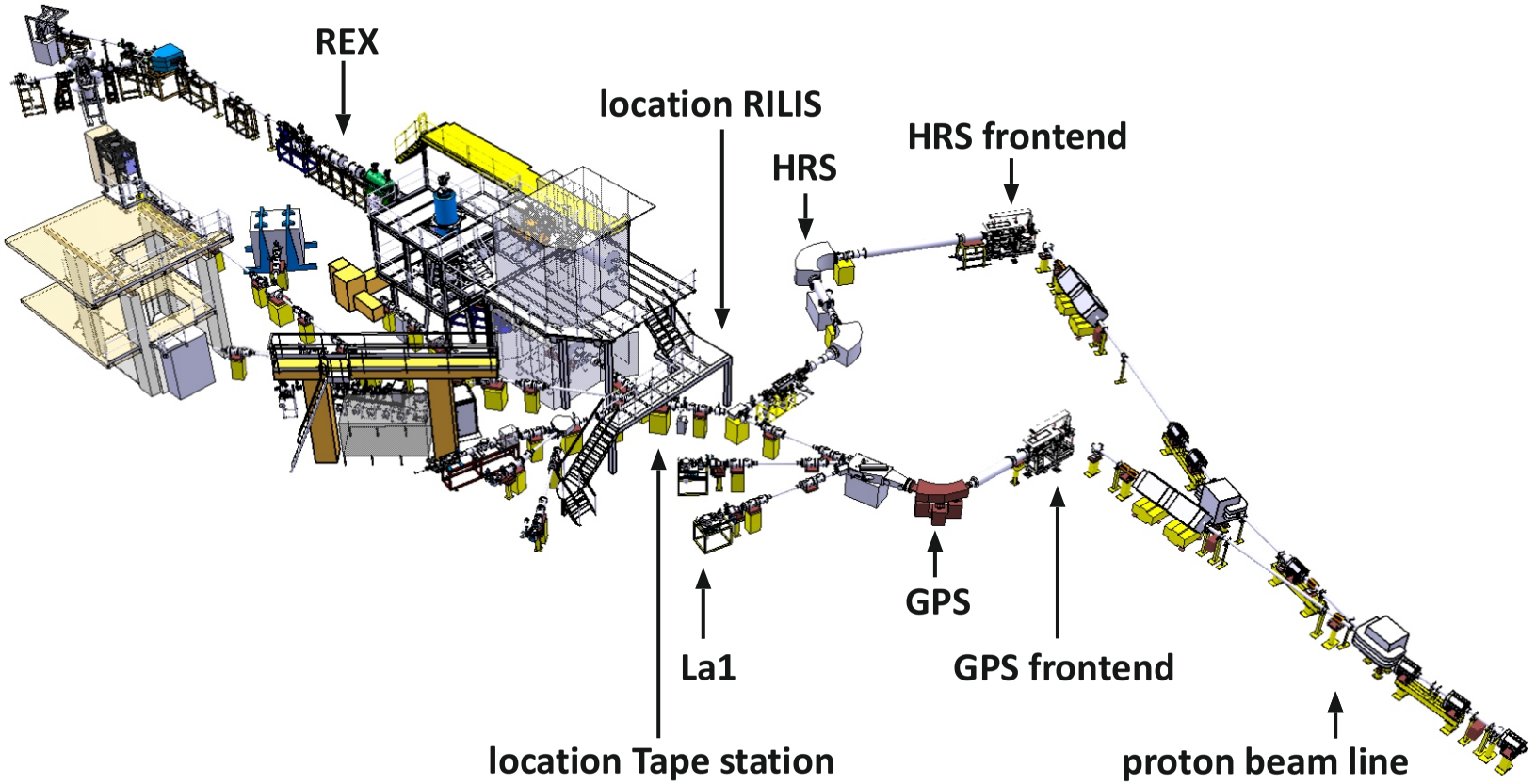

Figure 3.2: A drawing of the ISOLDE facility and its main components: 1.4 GeV proton driver beam, GPS- and HRS target front ends with target, transfer line, ion source and extraction electrode, and the two mass separators GPS and HRS. Optionally the beam from the HRS separator magnet can be further cooled and bunched, charge state bred, and post-accelerated to up to 3.1 MeV/u. Experiments are located at the end of the different beam-lines in the ISOLDE experimental hall. The RILIS ion source is located in the experimental hall above the HRS mass separator. Picture adapted from [21].

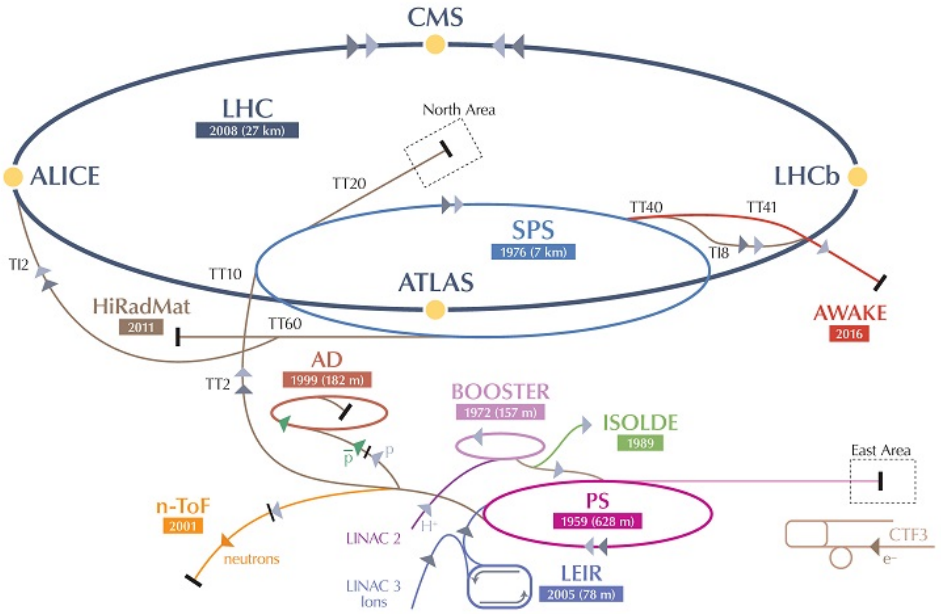

Figure 3.3: An illustration of the CERN accelerator complex with all major facilities. The proton bunches are accelerated by the LINCAC 2 and Booster (in the text referred to as the Proton Synchrotron Booster, PSB) to 1.4 GeV before they are sent to ISOLDE [30].

ionization. Resistive heating of the target container and the hot cavity to up to 2000 °C enables the transport and ionization of atoms.
The target can be installed at one of the two front-ends at ISOLDE (see Figure 3.2). These correspond to the beam-lines of the two mass separators *General Purpose Separator* (GPS) and *High Resolution Separator* (HRS). Ions are extracted from the hot cavity into the ISOLDE beam-line by a potential difference between the target and front-end on a high-voltage (+30 keV and +60 keV) and an extraction electrode on ground potential, which is installed approximately 60 mm away from the exit of the ion source.

3.1.3 The target materials

The choice of the correct target material is crucial for highest production rates of the isotope of interest. For the work described in this thesis, rolled foils of titanium (Ti) or pellets of uranium-carbide (UC_2) were used as a target material. As illustrated by Figure 3.5, a range of isotopes of many different elements are produced. The actual experimental cross-sections for each isotope are difficult to obtain, but can be calculated theoretically by the ABRABLA code [109]. These production cross-sections were verified at GSI, but are expected to be similar to the production cross-sections at ISOLDE. Due to the non-selective reaction reaction processes, a degree of selectivity must be thus introduced during the subsequent processes of atom transport, ionization, and ion transport to extract an isotopically pure beam.

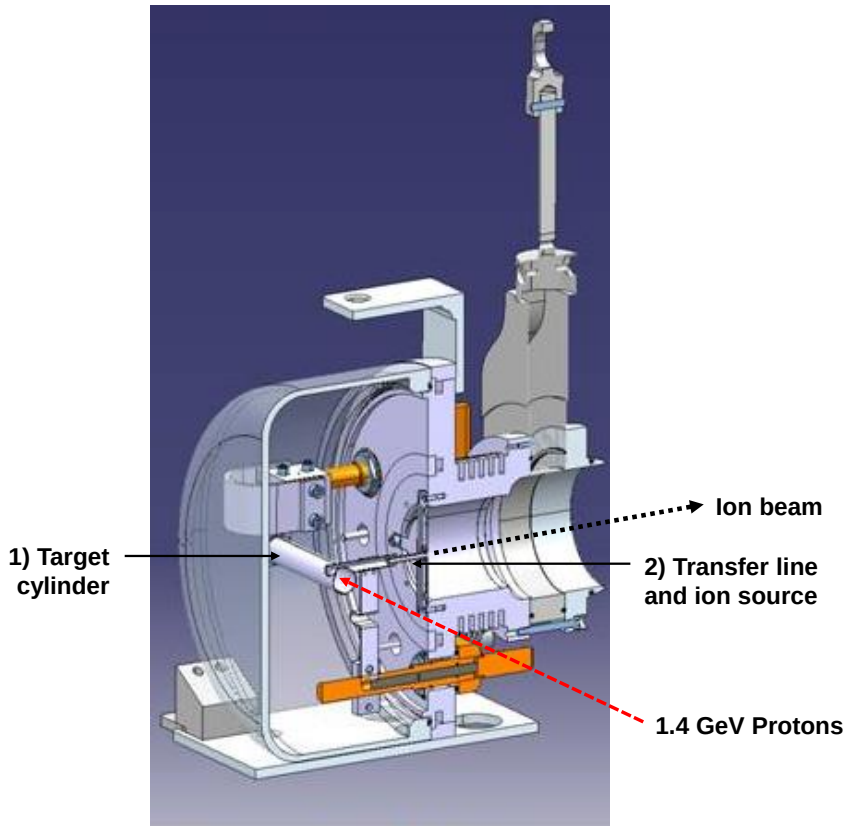

Figure 3.4: A cross-sectional drawing of an ISOLDE target unit equipped with a tantalum ionizer cavity for surface or laser ionization. The main elements are: 1) The thick target container filled with the target material. 2) The transfer line for atom transport and a hot cavity for surface ionization and laser ionization [117].

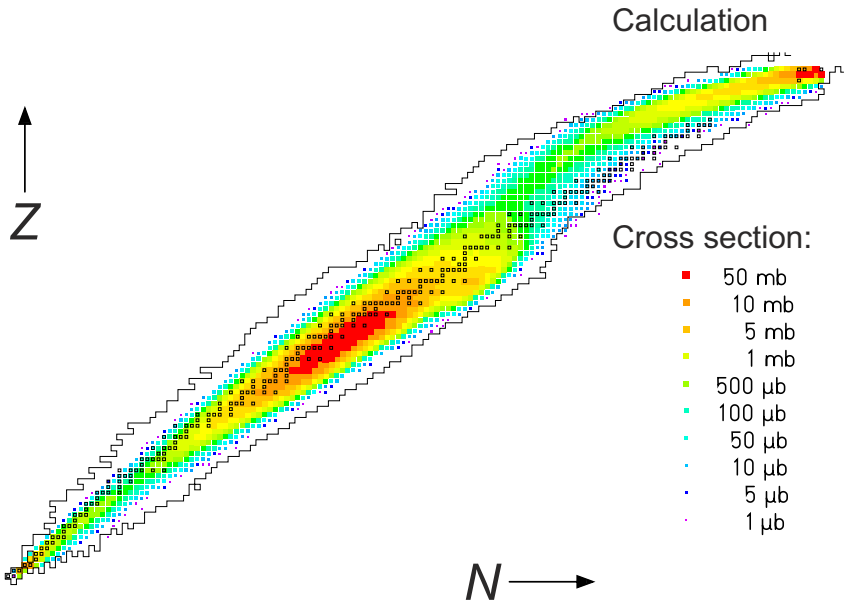

Figure 3.5: Theoretically expected production cross-sections at ISOLDE for 1 GeV protons on ^{238}U [109].

3.1.4 The reaction mechanisms

The 1.4 GeV proton beam from the PSB travels through the target cylinder as shown in Figure 3.4 and undergoes nuclear reactions with the target material. Three production channels are present: proton induced fragmentation, spallation, and fission. Fragmentation and spallation dominate the production at the neutron-deficient side of the nuclear chart and fission is mainly responsible for the production of neutron-rich nuclei. However, all channels are usually present and the exact production process is not always clearly distinguishable.
It is possible to give preference to the fission reaction channel by the use of a neutron converter [108]. This is a solid tungsten cylinder, positioned adjacent to the target. If the protons are directed onto the converter then a portion of the spallation neutrons are emitted into the target material and induce fission reactions.

3.1.5 Atom thermalization and transport

The initial kinetic energies of radioactive isotopes right after the production inside the target is in general quite high. Fission reaction products, for example, have kinetic energies of about 200 MeV. At ISOLDE, these atoms are stopped inside the target matrix itself and cooled down to the target temperature (typically $\approx 2000\,^{\circ}\mathrm{C}$), which corresponds to a kinetic energy of $\approx 300\,\mathrm{meV}$ [52]. Depending on the vapor pressure of the element, the atoms are able to diffuse through the porous target material and eventually reach the aperture to a transfer line, which guides the atoms to the ion source. The transfer line is the first opportunity to introduce chemical selectivity by inserting a quartz transfer line to delay alkali metals and thus reducing the contamination by decay [23].

3.1.6 Ionization processes

The ionization region is located immediately after the transfer line. Depending on the properties of the isotope of interest, one can choose between surface ionization, laser ionization, electron impact and plasma ionization. The first three of these ionization mechanisms that are relevant to the work described in here are discussed in more detail later in this chapter in section 3.2. After the ionization, the ions are then accelerated by the potential difference between the target assembly on a high-voltage (between -30 kV and -60 kV) and an extraction electrode on ground potential.

3.1.7 Mass separation

Each of the two ISOLDE target frontends has a corresponding dipole magnet mass spectrometer: the General Purpose Separator (GPS) and the High Resolution Separator (HRS), respectively. When the beam enters the dipole magnet, ions of a different mass-to-charge ratio are bent with different radii. For a mono-energetic beam with kinetic energy T, atomic mass m, and particle charge q in a magnetic dipole field with field strength B,

the bending radius ρ of the ion beam is given by:

$$\rho = \frac{1}{B} \cdot \sqrt{\frac{2mT}{q}} \,. \tag{3.3}$$

The overall *resolving power*, R, of such a mass separator for a given mass m is defined as

$$R = \frac{m}{\Delta m} \,, \tag{3.4}$$

where Δm is the FWHM of the ion beam with mass m in the focal plane of the separator. The resolving power of the GPS mass separator (singly staged 90° analyzing magnet) is $R \approx 2500$ and thus, is less strong than the resolving power of the HRS mass separator (two subsequent analyzing magnets with 90° and 60° respectively) with $R \approx 7000$, but can achieve higher transport efficiency and is easier and faster to tune. In addition, the GPS has the advantage that it can enable transmission of up to three masses simultaneously within a mass range of 15% (low mass, central mass, and high mass). The HRS beam-line, however, is also equipped with an RFQ ion cooler and buncher for further improvement of the beam quality/emittance.

3.1.8 Production rates and total transport efficiency

The intensity of a radioactive ion beam at an ISOL facility is given by

$$I = \sigma \cdot N_{\text{target}} \cdot \Phi \cdot \epsilon \,, \tag{3.5}$$

where σ is the cross-section of the relevant production process for the isotope of interest (see Figure 3.5), N the number of atoms inside the target material, Φ the flux of the driver beam, and ϵ the transport and ionization efficiency from the target to the experiment. The total transport and ionization efficiency consists of the transport efficiency from the target to the ion source $\epsilon_{\text{release}}$, the ionization efficiency $\epsilon_{\text{ionization}}$, and the transport efficiency through the analyzing magnets and the beam line to the experiments $\epsilon_{\text{transport}}$:

$$\epsilon = \epsilon_{\text{release}} \cdot \epsilon_{\text{ionization}} \cdot \epsilon_{\text{transport}} \,. \tag{3.6}$$

This work puts its emphasis on the improvement of the ionization efficiency of the ion sources.

3.2 Ionization mechanisms and ion sources at ISOLDE

An ion is defined as a nucleus with a number of shell-electrons N_e, which is smaller or greater than the number of protons $N_p = Z$, where Z is the atomic number. It is therefore either positively charged ($N_e < Z$, *"positive ions"*) or negatively charged ($N_e > Z$, *"negative ions"*). Almost all experiments at ISOLDE are performed with positive ions and thus, in the context of this work, the word "ion" is used to refer to a singly positively charged ion. The ionization methods described below are therefore techniques, which remove one electron from a neutral atom.
All ionization methods must provide a reaction energy which is at least greater than the ionization energy $E > IE = e\phi_1$, where ϕ_1 is the ionization potential, to remove one electron from the atomic shell (see Chapter 2.1). If this energy is supplied to a confined sample, then a plasma of electrons, ions and neutral atoms is generated. The ion source therefore needs to be optimized in terms of extraction and emittance of the ion beam to match the special requirements of the beam-line, of the post-accelerators, and the specific experiment.
The different ion sources at ISOLDE fall into four main categories: surface ionization*, resonance laser ionization, electron impact ionization and plasma ionization. Each type of ion source has advantages for specific elements in terms of efficiency and selectivity. Surface ionization is highly efficient for elements with low ionization energies such as alkali and alkaline-earth metals. Resonance laser ionization is highly efficient and element-selective, but requires good knowledge and extensive investigations about the atomic structure of the element as well as a series of transitions between atomic levels that are accessible with the available laser system. Electron impact ionization and plasma ionization are rather non-selective, but give access to elements with high ionization energies, such as noble gases, or to elements with an atomic structure that makes laser ionization impractical or inefficient, such as the halogens. In the following, the ionization mechanisms relevant to this thesis, surface, laser and electron impact ionization are discussed.

3.2.1 Surface ionization

Surface ion sources are the standard choice for elements with low ionization energies at ISOLDE. Surface ionization may occur when a neutral atom with ionization energy $IE = e\phi_i$ interacts with a surface of a material with a work function W. The least electron may then tunnel into the Fermi band of the material.
Following *Meghnad Saha*'s description of the ionization in hot gases, *Irving Langmuir* first described the relation between the ionization probability of a vapor by contact with a surface by considering the ratios between neutral atoms, ions, and electrons on the surface [98, 148]. The so-called *Langmuir-Saha* formula gives the ratio α_s between the number of ions N_i and number of neutral atoms N_0 with ionization energy $e\phi_i$ on the surface with temperature T and work function W in thermal-equilibrium:

$$\alpha_{\mathrm{s}} = \frac{N_i}{N_0} = \frac{g_i}{g_0} \exp\left(-\frac{e\phi - W}{kT}\right), \tag{3.7}$$

*Or *contact ionization*. The denotation depends on the literature.

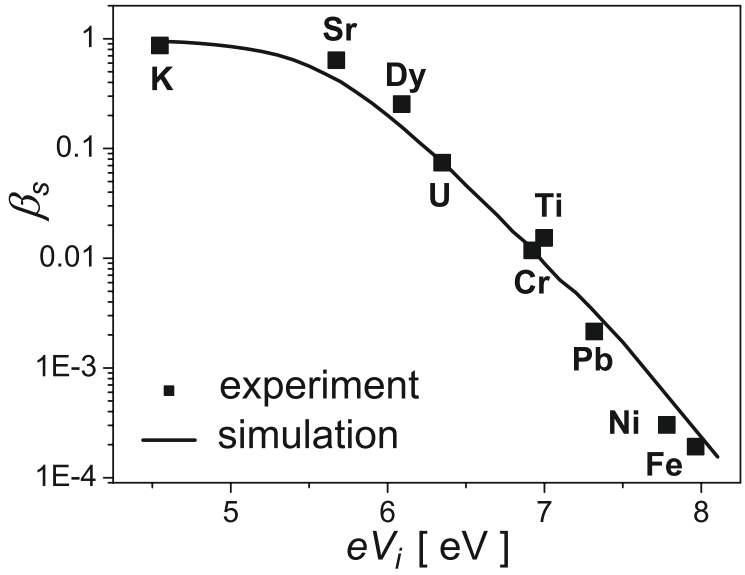

Figure 3.6: Surface ionization efficiencies in a hot cavity ion source obtained by experiments [89] and by simulations [170].

where g_i and g_0 are the *degeneracy of states** for the ions and neutral atoms, respectively. The probability to ionize one atom on the surface is then given by

$$\beta = \frac{N_i}{N_0 + N_i} = \alpha_s \left(\frac{1}{1 + \alpha_s} \right) . \tag{3.8}$$

As it follows from Equation (3.7), the surface ionization efficiency benefits from a high temperature, a low ionization energy and a high work function†. Therefore, the highest ionization efficiencies are obtained for alkaline metals with low ionization energies from 5.1 eV (sodium, Na) to 3.9 eV (cesium, Cs and francium, Fr) in combination with contact materials with high working functions such as tantalum, Ta (W=3.7−4.9 eV)‡, tungsten, W (W=4.5−4.8 eV) or rhenium, Re (W≈5 eV) [3, 4].
The ionization efficiency obtained by an ISOLDE-type hot-cavity surface ion source actually exceeds the value that is implied by Equation (3.7) [89]. This is due to a combination of effects: multiple atom-wall interactions per atom, a plasma potential, which is formed inside the hot cavity by the emitted electrons, and a penetrating extraction field. The plasma potential is neutral close to the axis of the source and positive towards the walls of the hot cavity. This leads to a confinement of the positive ions inside the hot cavity and to a reduced neutralization at the walls [100].
However, a quantity to describe the overall enhancement of the ionization efficiency β_s

*g is the degeneracy of states, given by $g = 2J + 1$, where J is the total angular momentum in the ground state of the atom or ion.

†For the production of negative ions, the opposite, high electron affinity and low work function, applies.

‡The work function depends on the surface orientation, in case of crystalline elements.

to the ionization probability β predicted in Equation (3.8) is given by the amplification factor η:

$$\eta = \frac{\beta_s}{\beta} \,. \tag{3.9}$$

Recently, the surface ionization efficiency for several elements has been successfully simulated and compared to experimental values [89, 170]. The experimental values and the results from the simulation are shown in Figure 3.6. As expected, the ionization efficiency depends strongly on the ionization energies. Ionization efficiencies of about 100 % are obtained for alkaline metals such as potassium, but decrease sharply for elements with higher ionization efficiencies.

3.2.2 Electron impact ionization

Electron impact ionization is the ionization principle of the plasma ion source, the electron beam ion sources (EBIS), and the electron beam ion traps. Free electrons with kinetic energies above the ionization potential ($E \geq IE$) may remove an electron from the electron cloud of an atom or an ion with a certain probability. This process is described by the following reaction:

$$e^- + A^{q+} \rightarrow A^{(q+1)+} + 2e^- \,, \tag{3.10}$$

where A is the atom with initial charge state q. The overall ionization rate R in a volume V with target particle (atoms or ions) densities N_i and electron densities N_e is given by

$$R = \int\int N_i N_e \sigma_i \left(v_{e,i}\right) dv_{e,i}\, dV \,, \tag{3.11}$$

where $v_{e,i}$ is the relative velocity between the electrons and the target particles and $\sigma_i \left(v_{e,i}\right)$ the velocity dependent cross-section of the process. In general, the reaction cross-section is zero for electron energies below the ionization threshold and reaches its maximum at electron energies at about three to four times the ionization energy. The cross-section as a function of the energy can be described by several semi-empirical formulas [107, 126], but close to the ionization-threshold, the cross-section can be approximated by

$$\sigma_i = \alpha \left(E_e - e\phi_i\right)^n \,, \tag{3.12}$$

where α is a constant and n depends on whether the target is an atom ($n = 1.1269$) or an ion ($n = 1.056$). The cross-section declines for higher electron energies since the interaction time gets shorter.
If the ionization takes place in a hot plasma, the velocity distribution of the electrons is given by the Maxwell distribution (Equation (2.40)). In this case, ionization occurs due interaction with the electrons in the higher energy tail of the velocity distribution. Using electron impact ion sources, the electron energy can be precisely tuned to the maximum of the cross section of the reaction. A suitable increase in the electron beam energy makes it possible to ionize the ions to higher charge states.
In contrast to surface ionization, electron impact ionization can be applied for elements

with high ionization potentials such as halogens or noble gases. However, the process is not selective since the maximum of the cross-section is rather broad and thus, isobaric contamination can be a problem in radioactive ion beams. Provided that the chosen isotope is a volatile element, a degree of selectivity can be achieved through the use of a cooled transfer line to transport the reaction products to the ion source.

3.2.3 Resonance laser ionization

A very efficient and element selective ionization technique is the resonance laser ionization [92, 102]. Here, electrons are excited from the ground state above the ionization energy using several subsequent electron transitions. These must be in reach of the tuning range of the available lasers. The final step of ionization can be achieved by either non-resonant excitation into the continuum, by an excitation to a so-called *auto-ionizing state* above the ionization energy or by an excitation to a highly excited Rydberg-state close to the ionization energy. In the latter, the atom can then be efficiently ionized by external effects such as a strong field gradient, blackbody radiation or collisions. An overview over the different ways to ionize an atom by resonance laser ionization is shown in Figure 3.7. These so-called *ionization schemes* are discussed in more detail later in this section.
The process of resonance laser ionization is completely element-selective due to the element-unique atomic structure. In some cases, even isotope or isomer selectivity is possible if the laser line-width is sufficiently narrow to resolve isotope- or isomer shifts. Moreover

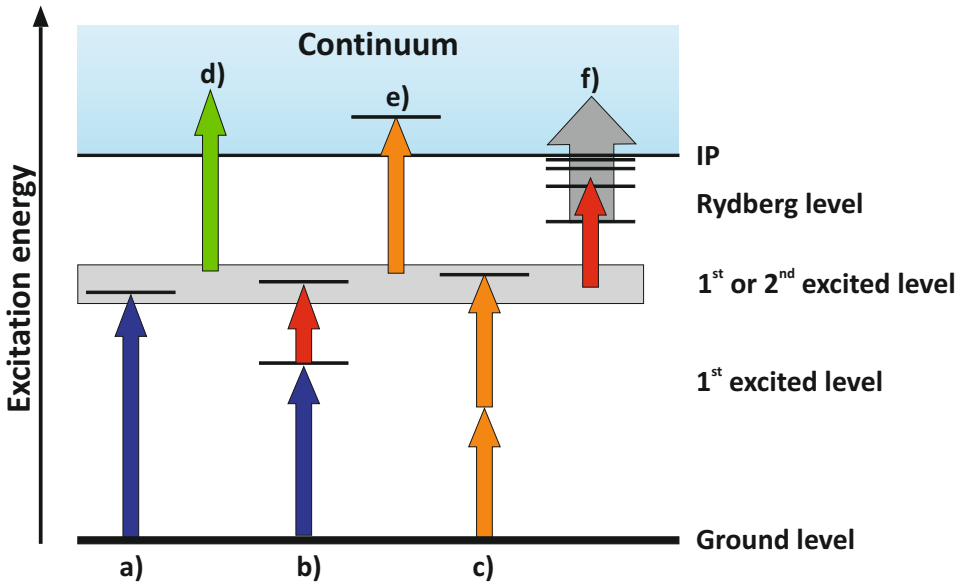

Figure 3.7: An illustration of different excitation schemes that may be applied for resonance laser ionization: intermediate states can be populated resonantly by a) one or b) two photons or by c) two-photon excitation through a virtual level. Ionization is possible by d) non-resonant ionization into the continuum or resonance excitation to e) auto-ionizing states or f) Rydberg levels followed by field or laser ionization.

high ionization efficiencies of up to 30 % can be achieved, and due to the very short ionization process, no additional significant delay is introduced into the production process. The resonance laser ionization is the technique of choice for most ion beams produced at ISOLDE [59] (see Figure 1.1).
In the following section, the principle and the basic requirements for an efficient laser ionization are discussed. For a thorough analysis of the laser ionization process, I refer to [81, 102]. The description below follows the discussion found in [51].

Laser ionization efficiency

For a given ionization scheme several conditions must be satisfied to maximize the ionization efficiency:

Minimum photon energy: The sum of all of the electron transition energies, E_i $(i = 1, \cdots, k)$, has to exceed the ionization energy:

$$\sum_{i=1}^{i=k} E_i \geq e\phi_i = IE\,. \tag{3.13}$$

The minimum photon energy required to ionize the elements with lowest ionization energies (cesium and francium) must be greater than $E \approx 3.9\,\mathrm{eV}$, which corresponds to ultraviolet light of about 320 nm. The expected efficiency in this case will be very low due to the low laser power available for UV light and the low cross-section for non-resonant ionization. Generally, two to four lasers are therefore used to provide a step-wise resonance ionization scheme.

Flux condition: the depopulation rate of the excited state due to resonant or non-resonant absorption, given by the product of the *photon flux*, Φ $\left[\mathrm{cm}^{-2}s^{-1}\right]$, and the cross-section, σ_{i}, has to be greater than the loss rate due to de-excitation β $\left[s^{-1}\right]$ of the level to meta-stable levels or energy levels that don't match part of the excitation scheme*. This is the so-called *flux condition* and can be expressed by

$$\sigma_i \cdot \Phi \gg \beta\,. \tag{3.14}$$

Fluence condition: For this discussion the *photon fluence* is calculated as the photon flux multiplied by the useful interaction time. For *continuous wave lasers* (CW lasers) the interaction time would be defined by the lifetime of the excited state. For efficient ionization for a given average laser power it is therefore preferable to use a laser with a pulse length that is less than the excited state lifetime. If this is the case then the useable photon fluence, ϕ $[\mathrm{cm}^{-2}]$ is simply the flux times the laser pulse length:

$$\phi = \Phi \cdot \tau_l\,. \tag{3.15}$$

*These levels are often colloquially referred to as "dark states" as they are "invisible" to the photons that are provided by the lasers.

To ensure that enough photons are delivered within the suitable time period to ionize all excited atoms, the *fluence condition* is then given by:

$$\sigma_i \cdot \phi \cdot \frac{g_2}{g_1 + g_2} \gg 1\,, \tag{3.16}$$

where g_1 and g_2 are the statistical weights of the ground and excited state of the atom, respectively.

A transition between two states is called *saturated*, if both, the flux condition and the fluence condition hold and in turn the maximum ionization rate is achieved if this is separately valid for each involved transition. Typical values for the spontaneous emission rate of $\beta = 10^{-6}\,\mathrm{s}^{-1}$ and for the cross-section of the weakest transition of $\sigma_i = 10^{-17}\mathrm{cm}^2$ require a photon flux of more than 10^{21} photons/s [51]. This corresponds to a 500 W CW laser power or to a pulsed laser with a pulse energy of much more than 5 µJ/pulse. At ISOL facilities, only the latter is practical.
The repetition rate of the pulsed lasers has to be chosen with respect to the average transport time of the atoms through the hot cavity of roughly 10 µs, which leads to a repetition rate of 10 kHz and in turn defines together with the flux and fluence condition the pulse energy. If any transition remains unsaturated, the achievable ionization efficiency is directly proportional to either the laser laser power or the cross-section for the transition. However, the ionization cross-section can vary by several orders of magnitude, depending on whether the ionization is non-resonant above the ionization energy or resonant to an auto-ionizing state or Rydberg-level.

Non-resonant laser photo-ionization

Non-resonant laser photo-ionization occurs, when an electron of an atom is excited above the ionization energy into the ionization continuum. This is illustrated in Figure 3.7d. It requires a photon energy, which is higher than the energy from the intermediate state to the ionization energy. The cross-section for non-resonant laser ionization is only $10^{-17}\mathrm{cm}^2$ to $10^{-19}\mathrm{cm}^2$. Although the maximum residual power of the non-tunable pump laser is usually used for a non-resonant ionization step, the transition is in most cases difficult to saturate.

Ionization via auto-ionizing states

Strong resonances with high cross-sections are observed above the ionization energy in the spectra of many elements. These cross-sections can be several orders of magnitudes higher than for non-resonant transitions to the continuum. In some cases (e.g. gadolinium [12, 24] and manganese [115]), the spectrum of bound states above the ionization energy can be extremely rich. These resonances can be interpreted as a resonant two-electron excitation, for which the combined excitation energies of both electrons exceeds the ionization energy. It is then possible that one electron decays back to a lower state, while the energy of this electron is transmitted directly to the other excited electron. In case of the latter, the excited electron has then enough energy to escape the atom. The process is known as *auto-ionization* and the corresponding bound state an *auto-ionizing state* (AIS).

The line-shape of such a transition can differ from resonances below the ionization energy. It can be rather asymmetric due to interference effects with the continuum and fits with a Voigt function (see Equation (2.44)) may not be suitable for fitting any more. A theory for the line-shape of these auto-ionizing states was first described by Ugo Fano [56]. Here, an auto-ionizing process is described by two scattering processes, which interfere with each other: the excitation to a discrete level (resonant scattering) and the scattering within a continuum of states (background scattering). If the excitation energy is varied around the central energy of the auto-ionizing resonance, the background process varies only slowly, while the amplitude and the phase of the resonant process changes rapidly. The variation of the phase leads to the asymmetric line-shape.
The total cross-section σ_{ai} follows a function of the *Fano factor* q and the so-called *reduced energy* ϵ:

$$\sigma_{\mathrm{ai}} = \sigma_{\mathrm{a}} \cdot F(q,\epsilon) + \sigma_{\mathrm{b}} \quad \text{with} \quad F(q,\epsilon) = \frac{(q+\epsilon)^2}{(1+\epsilon^2)} \quad \text{and} \quad \epsilon = \frac{E-E_0}{\Gamma/2}\,. \tag{3.17}$$

σ_{a} is the part of the continuum cross-section, which interacts with the discrete level, σ_{b} is the non-interacting constant background cross-section and Γ is the line-width of the resonance. The Fano factor q can then be interpreted as a quantity for the amplitudes of the resonant scattering and the background scattering and determines the shape of the resonance.
On resonance ($\epsilon = 1/q$), the amplitude is given by $\sigma_{\mathrm{ai,max}} = \sigma_{\mathrm{a}} \cdot \left(1+q^2\right) + \sigma_{\mathrm{b}}$, which leads in case of $q^2 \gg 1$ to

$$\sigma_{\mathrm{ai}} \approx q^2 \cdot \sigma_{\mathrm{a}}\,. \tag{3.18}$$

Typical values of σ_{a} are similar to the cross-sections of the non-resonant ionization ($10^{-17}\mathrm{cm}^2 - 10^{-19}\mathrm{cm}^2$). In combination with Equation (3.18), it is obvious that for high Fano factors q, the gain in laser ionization efficiency due to ionization through auto-ionizing states can be several orders of magnitudes compared to the non-resonant laser ionization. Line-widths of auto-ionizing states can vary strongly and resonances were observed with line-widths ranging from MHz to THz (see Chapter 5). However, in most cases, tunable lasers are needed to excite to auto-ionizing states. The higher cross section of transitions to an autoionizing state results in a reduced laser power requirement and, for the typical output power of a tunable laser of the laser ion source, this transition may be saturated. If this is not the benefit of using an autoionizing state, the usage of non-resonant ionization has to be carefully evaluated, taking into account the higher power and greater convenience of using a non-tunable laser for a transition to the continuum.

Ionization via Rydberg levels

It is possible to excite to high-lying Rydberg levels (see Chapter 2.1.2) for efficient ionization. The resonant photo-absorption cross-sections of these Rydberg states can be as high as $\approx 10^{-14}\,\mathrm{cm}^{-2}$. The binding energies of the electrons in these states is only of the order of meV. This is very small, when compared to the binding energy of the valence electron of typically several eV. In addition, the volume* of a Rydberg atom is large and their

*The radius increases approximately proportionally to the cube of the effective quantum number.

life-times can be very long (several μs) [68]. These properties make them very sensitive to ionization due to external disturbances:

Strong field gradients: Field ionization may occur when the Rydberg atom is exposed to a sufficiently strong field gradient.

Collision: The long life-time and large volume results in a high probability of collisions with other particles in the atomic vapour or plasma. Furthermore, the cross-section for ionization due to energy transfer during the collision is high because the electron is weakly bound.

Photo-ionization: In a hot cavity, the photon flux from the hot walls due to blackbody radiation can be high and can lead to an excitation of the electron from high-lying n-state into the continuum [9].

The study of a Rydberg series can be used to precisely determine the ionization energy of elements using the Rydberg-Ritz formula (Equation (2.10)). This has been recently demonstrated for astatine at ISOLDE [143, 144] and was performed as part of this thesis for polonium (see Chapter 6). The study of a Rydberg series can be used to precisely determine the ionization energy of elements using the Rydberg-Ritz formula (Equation (2.10)). This has been recently demonstrated for astatine at ISOLDE [143, 144] and was performed as part of this thesis for polonium (see Chapter 6).

3.3 The Resonance Ionization Laser Ion Source at ISOLDE

The Resonance Ionization Laser Ion Source (RILIS) has become the most often used ion source at ISOLDE. After first design studies were presented by *V.S. Lethokov and V.I. Mishin* [103] in 1984 and by *H.-J. Kluge et al.* in 1985 [90], the first ion source of this type at an ISOL facility was established at the IRIS facility at the Petersburg Nuclear Physics Institute (PNPI) in Gatchina, Russia in 1991 [1]. A similar installation was constructed at ISOLDE [57] and for the first time operated on-line by *Mishin, Fedosseev and colleagues* [119] in 1992.
Figure 3.8 is a schematic of the laser beam delivery to the ISOLDE target, taken from the first publication that referred to the ISOLDE RILIS [119]. Whilst the laser system has changed from that of the original RILIS, this figure is still representative of the ISOLDE setup, and closely matches the configuration methods used at several facilities worldwide. Mishin *et al.* reported laser ionization of ytterbium (Yb), thulium (Tm), and tin (Sn) with efficiencies of up to 10 % to 20 % [119].
In the standard configuration, the ISOLDE RILIS uses the hot cavity surface ion source as a laser/atom interaction region. The hot cavity has proven to be efficient and convenient for two reasons: 1) full overlap in time and space of the lasers with all atoms effusing from the target and 2) the cavity plasma potential that provides transverse confinement, and therefore enhances the survival of laser-ions during their drift towards the extraction region, as described in Section 3.2.1.
Many factors must be considered for the optimization of the geometry and characteristics of the hot-cavity:

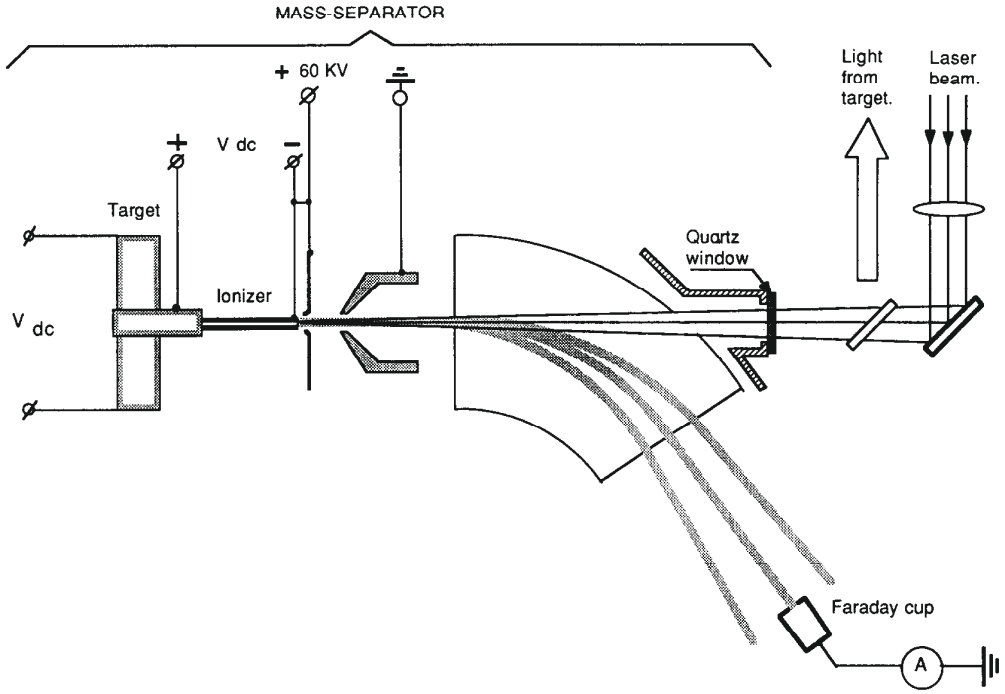

Figure 3.8: A schematic of the first RILIS setup at ISOLDE. Picture taken from [119]. Its basic principle is still valid for the RILIS at ISOLDE and exemplary for similar setups at RIB facilities with thick targets world-wide. Atoms released from the target are laser-ionized inside the hot cavity (here: the *ionizer*) extracted into the ISOLDE beam-line and mass separated by the separator magnets. Laser beams are sent through a quartz window and the magnet into the hot cavity.

Duty cycle: the cavity should provide confinement of the atoms long enough for each atom to be irradiated by at least one laser pulse. A long cavity therefore results in a lower repetition rate requirement for the laser system.

Decay losses: conversely, for short-lived isotopes, the effusion time should be minimized to avoid decay losses. In this case, the cavity length should be short. For the standard 30 mm cavity, the mean effusion time is about 100 µs, corresponding to a required repetition rate of 10 kHz

Diameter: to maximize the photon flux per unit area, the laser beams should be focused to a spot size as small as possible. In this case the atom confinement, or cavity diameter, should be equal to the laser spot diameter. For the long laser paths used at ISOLDE and, due to the inaccessibility of the optics outside of the laser installation, the typical laser focal spot diameter at the source is 3 mm.

Material and temperature: for maximum ionization efficiency, minimum effusion time and highest laser-ion survival, the cavity should be a high temperature material and a thermionic electron emitter. Refractory metals such as tungsten, tantalum, rhenium

are ideal in this respect.

The efficiency of the resonance laser ionization inside a hot cavity using a laser system with repetition rate f can be approximated by [119]

$$\epsilon_{\mathrm{RILIS}} = \frac{f\epsilon_{\mathrm{photo}}}{f\epsilon_{\mathrm{photo}} + \frac{dv}{4L^2}}, \tag{3.19}$$

where $\epsilon_{\mathrm{photo}}$ is the efficiency of the applied resonance laser ionization scheme, v is the thermal velocity of the atoms, and L and d are the length and the diameter of the hot cavity, respectively. The ISOLDE RILIS uses lasers with a repetition rate of $f = 10\,\mathrm{kHz}$ and the hot cavity dimensions are $L = 30\,\mathrm{mm}$ and $d = 3\,\mathrm{mm}$.
During the last 20 years, the RILIS was gradually upgraded to improve the stability, efficiency and reliability. Now, it operates more than 2000 hours/year and has delivered ion beams of 28 elements [113]. The current laser setup is described in the following section, followed by a description of the modes of operation that were used during the experiments described in this thesis.

3.3.1 The ISOLDE RILIS setup

A schematic of the current RILIS setup including the different detectors which were used during this work is shown in Figure 3.9. The laser setup went through two major upgrades during the last 5 years. First, the tunable dye-lasers and copper-vapor pump lasers (CVL) from the Russian Academy of Sciences were replaced by two commercial dye lasers from Credo© and two commercial neodymium-doped yttrium aluminum garnet (Nd:YAG) pump lasers from *Edgewave GmbH*. One tunable narrow band (NB) dye-laser remained in the system for spectroscopy purposes. A summary of these upgrades can be found in [115] and [59]. In the second stage, a complementary solid-state laser system, consisting of

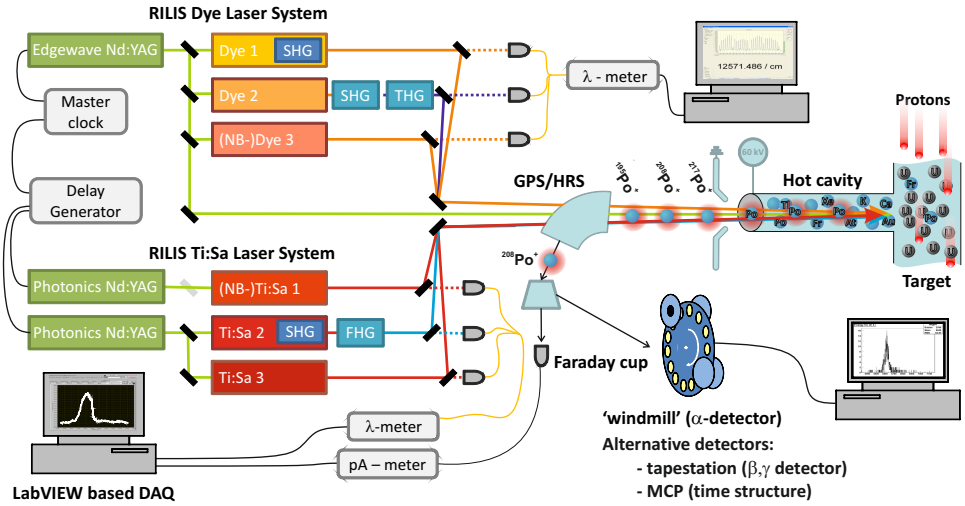

Figure 3.9: A schematic layout of the most important elements of the RILIS setup [143].

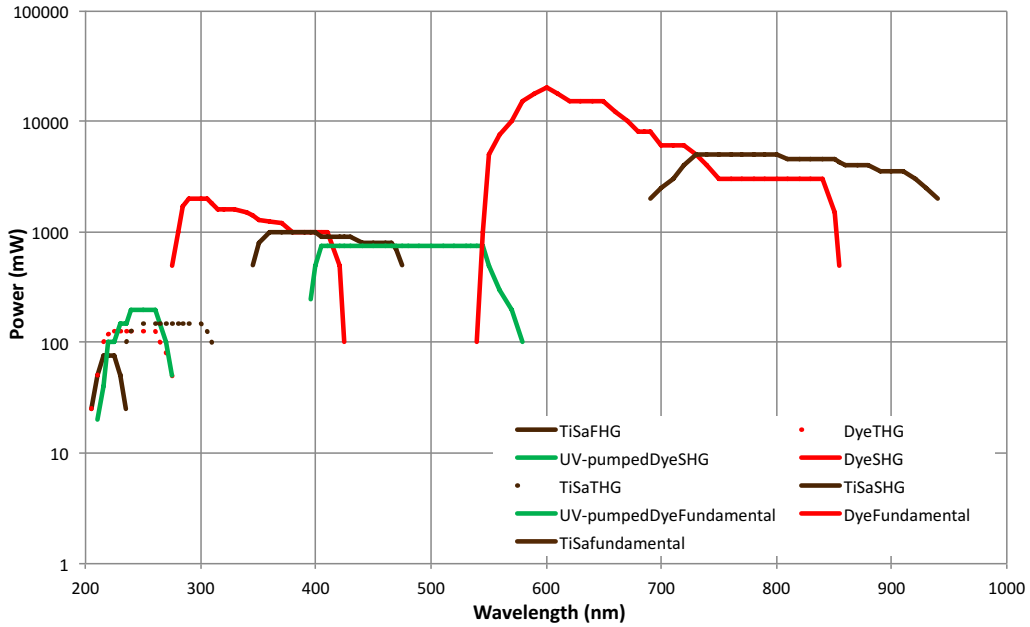

Figure 3.10: The wavelength tuning range after the dual RILIS upgrade, including all tunable dye and Ti:Sa lasers and second (SHG), third (THG), and fourth (FHG) harmonic generation [113].

three tunable Mainz design titanium:sapphire (Ti:Sa) lasers and two commercial Nd:YAG pump-lasers from *Photonics Industries* were installed [143, 145]. One of the Ti:Sa lasers was further modified for narrow-band operation [144] by inserting a second etalon into the Ti:Sa cavity to narrow the laser linewidth to below 1 GHz. Furthermore, the tuning of the NB-Ti:Sa was automatized and integrated into the RILIS control system [142].
If needed, non-linear crystals can be used for frequency multiplication of the fundamental beams of the lasers. Second, third and fourth harmonic generation can be achieved. The specifications of the pump and tunable lasers are given in Tables 3.1 and 3.2, respectively. Each tunable laser is coupled via fibers into wavemeters (WM) (*WS6* and *WS7* from *HighFinesse GmbH* [78, 79]) for wavelength measurement and data-acquisition (DAQ). Automatic scanning is possible for the dye lasers and the NB-Ti:Sa laser. The full tuning range of the RILIS lasers, including frequency-multiplication of the dye and Ti:Sa laser beams is shown in Figure 3.10.
A system of optical elements (mirrors, lenses, prisms, etc.) steers, converges and focuses the laser beams from the RILIS laser setup through the separator magnets into the cavity of the target. Due to the wide laser wavelength range and inaccessibility of the optics outside of the laser installation, broadband optics must be used for beam transport. For this uncoated quartz prisms, windows and reference plates are used for beam transport and sampling. The losses due to Fresnel reflections are therefore approximately 4 % for every optical surface in the beam path. Hence, the power delivered to the source is significantly lower than the measured power on the laser table. A commercial automatic beam stabilization unit (*Aligna®*, by *TEM Messtechnik GmbH*) was recently installed to im-

Table 3.1: Operating parameters of the RILIS pump lasers. Usually the dye lasers are pumped by different outputs (A, B, C) of one of the *Edgewave Nd:YAG* lasers. If needed, beam A can be directly sent to the ion source for non-resonant ionization.

laser	**Dye A**	**Dye B**	**Dye C**	**Ti:Sa 1**	**Ti:Sa 2**
Manufacturer	*Edgewave*	*Edgewave*	*Edgewave*	*Photonics*	*Photonics*
Harmonic Nd:YAG	2^{nd}	2^{nd}	3^{rd}	2^{nd}	2^{nd}
Wavelength (nm)	532 nm	532 nm	355 nm	532 nm	532 nm
Repetition rate (kHz)	10	10	10	10	10
Average power (W)	0 - 80	0 - 40	0 - 20	0 -74	0 - 72
Pulse duration (ns)	8	8	6	128	170
Pulse jitter (ns)	3	3	3	9.3	8
Divergence (mRad)	0.2	0.2	0.3	7.6	6.4
Beam quality (M^2)	< 1.3	-	-	≈ 30	≈ 30

Table 3.2: Typical parameters of the tunable RILIS lasers. In total two broadband (BB) Credo type dye lasers, one narrow band (NB) dye laser, two BB Ti:Sa laser, and one NB Ti:Sa laser are available.

laser	**Dye "Credo"**	**Dye NB**	**Ti:Sa**
Manufacturer	*Sirah GmbH*	*DMK*	*CERN / Mainz University*
Tuning range (nm)	$390 - 860$	$390 - 860$	$680 - 950$
Line-width BB/NB (GHz)	$9/-$	$15/0.8$	$5/0.8$
Maximal power (W)			
- Fundamental	20	10	6
- 2^{nd} harmonics	2.5	1	1
- 3^{rd} harmonics	0.2	0.2	0.15
- 4^{th} harmonics			0.15
Pulse duration (ns)	7	10	35
Divergence (mRad)	< 1	< 1	< 1

prove the stability of the ion beam production rate by correcting for any rapid or gradual drifts of the laser beam positions. For a full description of the RILIS setup it is referred to [113] and for a thorough description of the solid-state laser system it is referred to [143].

3.3.2 RILIS installations at off-line mass separators

The off-line* mass separators at ISOLDE and in Mainz can be equipped with temporary RILIS setups for ion source and ionization scheme tests [122, 153]. An all solid-state Ti:Sa based system is preferable for a temporary installation due to their smaller size and ease of use and cleanliness. A detailed description of the laser setup which was installed at the ISOLDE off-line mass separator will be given in Chapter 4.2.3.
Both off-line mass separators are very similar and differ only in terms of specific details of the electronics, the ion optics, and the control system and their design follows the principal setup shown in Figure 3.8. Their target frontends are compatible to the ISOLDE targets and therefore offer a realistic testing environment. Ions are usually extracted at 30 kV and the 60 ° magnets are used for mass separation.

3.4 Ion beam detection at ISOLDE

ISOLDE has a wide variety of different ion detection methods. Faraday cups (FC), wire scanners and wire grids are installed at several locations along the ISOLDE beam line [63]. These detectors are usually used for beam tuning with intense ion beams above the background noise of the detection electronics (≈ 0.2 pA), but can be also used for experiments with radioactive isotopes, if the ion beam intensities are high enough. Micro-channel plate (MCP) detectors are suitable for the detection of low intensity ion beams, particularly for stable or long lived isotopes whose activity is too low for detection at a decay station [180]. The fast response of MCP detectors makes them capable of measuring the time structure of laser-ion bunches with ns precision. These measurements are important for the understanding of the ion production process and optimization and development of ion sources.
However, in most cases, Faraday cups and MCPs are not suited for the characterization of radioactive ion beams due to their non-selective detection principles and particle identification is usually performed by the study of the radioactive decay channels. At ISOLDE, β-emitters can be studied by a *tape station* and α-emitters by a so-called *"Windmill"-detector* setup. Both detectors can be also used for γ-emitters.

3.4.1 The ISOLDE tape station detector for beta- and gamma-decaying isotopes

The local tape station detector at ISOLDE is a device for the detection of short-lived β- and γ-decaying nuclei. Its primary use at ISOLDE is the study of the radioactive ion yields and the measurement of the release times from the ISOLDE targets, but can be

*The term "off-line" setup refers to an experimental installation, which is not attached to a driver beam accelerator.

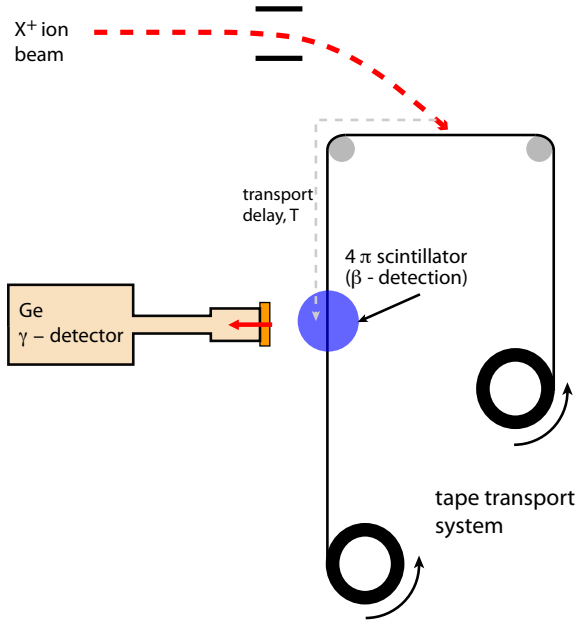

Figure 3.11: A schematic of the ISOLDE tape station, consisting of a beam gate, transport tape, and detectors for γ- and β-emitters.

also used for nuclear decay spectroscopy. An illustration of the tape station is shown in Figure 3.11. It consists of a beam gate, a transport tape (Mylar® with an aluminum layer), a 4π scintillator for β-detection, and a germanium (Ge) detector for γ-detection. After opening the beam gate, the ions with kinetic energies of up to 60 keV are implanted into the tape, which is then moved to the detectors. Measurements with the tape station are limited to nuclei with half-lives above the transport time of $\approx$ 100 ms. Clearly, the implantation of intense beams of long-lived isotopes (several hours or more) should be avoided to prevent long-term contamination.

The KU Leuven "Windmill" detector for α- and γ-decaying isotopes

The "Windmill" detector from the KU Leuven is a highly sensitive α- and γ-detector, which can be installed at one of the free ISOLDE beam lines [55]. For the experiments reported here, the "Windmill" setup was installed at the end of the LA1 beam line (see Figure 3.2) for the measurements of the HFS and IS of $^{216-219}$Po (see Chapter 7).
Figure 3.12 shows the main components of the windmill setup. The ions are implanted with up to 60 keV energy into one of the 10 carbon foils (10 mm diameter, 20 μg/cm^2, from the GSI target laboratory [106]), which is moved into the axis of the ion beam. Here, silicon detector system 1 (detectors C1 and C2 in Figure 3.12) surround the carbon foil. These are the detectors used for registering the alpha-emitting polonium isotopes that were studied as part of this thesis. Detector C1 is a passivated implanted planar silicon (PIPS) detector with 300 mm^2 active surface and is installed as close as possible behind

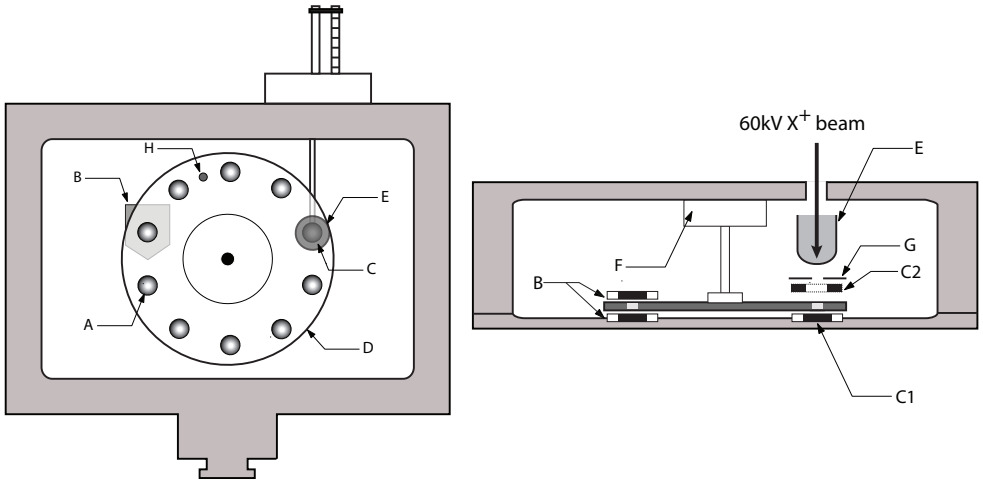

Figure 3.12: A schematic of the Windmill detector setup [37]. It consists of a rotating wheel (D), equipped with 10 thin carbon discs (A) rotatable by a stepping motor (F), Si α-detectors (C1, C2, and B), a collimator (G), a Faraday cup (E), and a ^{214}Am source (H).

the carbon foil. Detector C2 is a *cylindrical surface barrier detector* with 350 mm^2 surface and is placed in front of the foil. Its aperture of 6 mm diameter allows the ion beam to pass through the detector to the carbon foil for implantation. The best solid angle coverage ($\approx 51\%$) of the escaping α-particles is achieved if this detector is placed 4mm away from the carbon foil [36]. A collimator (element G in Figure 3.12) with an aperture of 5 mm protects the detector C2 from ions that diverge from the beam axis. After implantation of the ion beam and after finishing the data taking, the wheel can be rotated to move a clean carbon foil into the ion beam.
The alpha spectra recorded by C1 and C2 differ slightly due to the different geometry and location of the detectors, which needs to be considered during the analysis. The ions are implanted closer to the detector C2 than to detector C1. Therefore, the α-particles travel through more material to reach the detector C1 and thus, the observed α-energy peak at detector C1 is shifted and has a stronger tail towards lower energies. C2 gives a higher count rate because of the better solid angle coverage.
Silicon detector system 2 (detector pair B in Figure 3.12) is mainly used for background checks and decay-spectroscopy of isotopes with longer half-lives. This detector pair surrounds a different foil position on the windmill wheel and consists of two PIPS detectors similar to the PIPS detector C1.
It is further possible to move a Faraday cup in front of detector C2 for ease of stable beam tuning to the foil position. To calibrate and test the detectors, the rotating wheel is also equipped with a 30-50 Bq ^{241}Am source, which can be moved between the detectors. However, the α-calibration is slightly shifted because of the implantation depth of the ISOLDE beam. Therefore a calibration using an ion beam of an isotope with a well-known α-line is preferable.

3.5 Ion beam manipulation and transport using linear radiofrequency quadrupole ion guides

The concept of linear quadrupole ion guides is based upon the groundbreaking work of Wolfgang Paul, for which he received the Nobel Prize in Physics in 1989 [129]. Wolfgang Paul developed a technique to confine charged particles radially and to filter these depending on their mass to charge ratio by applying alternating electrical fields to four hyperbolic rods [130, 131, 132]. Later, this concept was extended to the trapping of charged particles in three dimensions [62].
Nowadays, these so-called radio-frequency quadrupole (RFQ) mass filters and ion guides are used in a wide range of research, e.g. mass spectrum analysis in chemistry or as an ion storage device for quantum computing. At ISOLDE and at RIB facilities, devices known as "ion cooler and buncher" combine an RFQ ion guide with segmented radio-frequency rods (RF-rods) and with injected buffer gas for the confinement in radial direction, bunching and cooling of the ion beams [77, 111]. Also the Laser Ion Source and Trap (LIST), which will be discussed in detail in Chapter 4, makes use of a linear RFQ structure to guide laser ionized ions. The basic principles of linear RFQ ion guides are therefore introduced in the following. In order to limit the discussion, only the two-dimensional confinement in radial direction is discussed. For further reading and a more fundamental mathematical treatment of the theory, I refer to the literature [15, 44, 69, 110, 129].

3.5.1 The ideal RFQ ion guide and mass filter

The general three-dimensional time-dependent quadrupole potential can be described in Cartesian coordinates* by:

$$\Phi(x, y, z, t) = \Phi_0(t) \cdot \left(ax^2 + by^2 + cz^2\right) , \tag{3.20}$$

where $\Phi_0(t)$ is the time-dependent voltage amplitude and a, b and c are geometrical parameters. Assuming that no space-charge effects disturb the pure quadrupole potential, the *Laplace-equation* $\Delta\Phi = 0$ leads to the condition $a + b + c = 0$. The solution for a confinement of charged particles in radial direction† is:

$$a = -c \quad \text{and} \quad b = 0 . \tag{3.21}$$

A possible geometry is a quadrupole, which consists of four hyperbolic rods with infinite length as shown in Figure 3.13 a. In this case, the coefficients can be normed to $a = -c = \frac{1}{r_0^2}$, where r_0 is the *free field radius*, defined as the distance from the longitudinal axis to the vertexes of the hyperbolic rods.
Confinement of ions, which are traveling through the RFQ, is achieved by applying an alternating potential, $\Phi_0(t)$, phase-shifted by 180° between neighboring rods. One general solution using sine-functions is of the form $\Phi_0(t) = U + V \cdot \cos(\omega t)$, where U is the static

*I follow the conventions for the Cartesian coordinates used in [129]: x and z are in radial direction, y is the axial direction. It may differ in alternative literature, where z is the axial direction.

†Confinement in all three dimensions is given, if the coefficients fulfill $a = b$ and $c = -2a$.

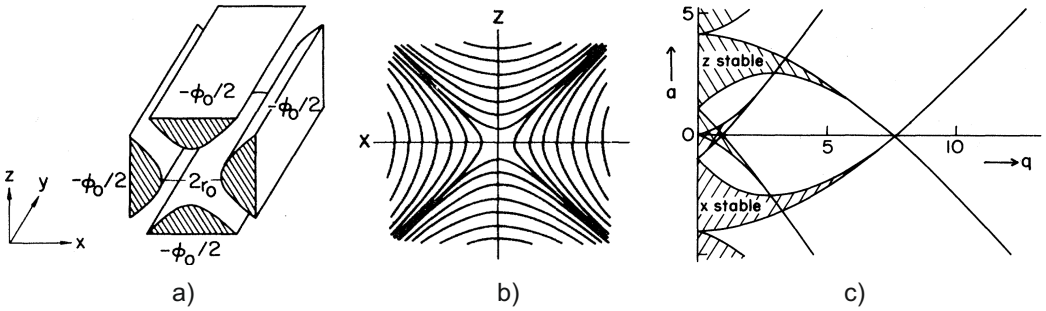

Figure 3.13: a) Geometry of the ideal, hyperbolic radiofrequency quadrupole. b) Equipotential lines in the x-z-plane. c) Areas of x- and z-stability. All figures were taken from [129]

direct-current (DC) potential, V the amplitude of the alternating-current (AC) potential and ω the frequency of the alternating potential.
Together with Equation (3.20), the overall potential of an RFQ with four hyperbolic RF-rods is then given by:

$$\Phi(x,z,t) = (U + V \cdot \cos(\omega t)) \cdot \frac{\left(x^2 - z^2\right)}{2r_0^2}\,. \tag{3.22}$$

The resulting equipotential lines in the x-z-plane are shown in Figure 3.13 b. The inhomogeneity of the quadrupole potential of Equation (3.22) leads to a weak net force towards the center of the RFQ, where the electrical field is the weakest. For certain applied voltages, U and V, the longitudinal motion becomes stable and the charged particle can travel through the RFQ without hitting the RF-rods. However, the resulting equation of motions (EOMs) of charged particles inside a linear RFQ are:

$$\begin{aligned} \ddot{x} + \frac{q}{mr_0^2}\left(U + V \cdot \cos(\omega t)\right) \cdot x &= 0 \\ \ddot{y} &= 0 \\ \ddot{z} - \frac{q}{mr_0^2}\left(U + V \cdot \cos(\omega t)\right) \cdot z &= 0\,, \end{aligned} \tag{3.23}$$

where $q = e$ for singly charged ions and m is the mass of the charged particle. The EOMs in x- and z-direction are types of *Mathieu equations* [118] and can be brought into the standardized form of

$$\begin{aligned} \frac{d^2x}{d\tau^2} + (a + 2q \cdot \cos(2\tau)) \cdot x &= 0 \\ \frac{d^2z}{d\tau^2} - (a + 2q \cdot \cos(2\tau)) \cdot z &= 0 \end{aligned} \tag{3.24}$$

by introducing dimensionless parameters $a = \frac{4qU}{mr_0^2\omega^2}$, $q = \frac{2qV}{mr_0^2\omega^2}$ and $\tau = \frac{\omega t}{2}$. The solution to the *Mathieu equations* is a superposition of two movements of the charged particle: a slow oscillating macro-movement and a faster micro-movement with a higher frequency but

smaller amplitude. Depending on the applied voltages, U and V, and the corresponding dimensionless parameters, a and q, respectively the EOMs have two types of solutions:

Unstable motion: the amplitudes of the oscillating charged particles grow exponentially and the particles will eventually get lost.

Stable motion: the amplitudes of the oscillations are limited and the charged particle travels through the RFQ.

Note that in case of the ideal RFQ the stability of the charged particle motion depends entirely on the value of a and q and not on the initial parameters, such as the velocity or the direction of the motion. The conditions for stable solutions can be illustrated in a *a-q stability diagram* as shown in Figure 3.13c, where the hashed areas mark the combinations of a- and q values for which x or z stability exists. However, only where the areas of x- and z- stability overlap with each other exists stability throughout the motion of the charged particle through the RFQ. The most important area of x-z-stability is shown in Figure 3.14, where stability is given for $0 < q < 0.92$ and corresponding a-values.
A so-called *operation line* for different masses, $m_1 < m_2 < m_3$, defined by $\frac{a}{q} = \frac{2U}{V} = \text{const.}$ and fixed r_0 and ω illustrates the operation principle of the linear RFQ mass filter. Only the masses m_1 and m_2 are inside the range of stability (range Δq in Figure 3.14) and have stable motions. A further improvement of the mass-resolution, R, of the linear mass filter is possible by steepening the operation line (e.g. increasing V).
The same principle is illustrated in Figure 3.15, where the stability diagram and the operation line is transformed into the V-U-space. In this case, the dimension of the area of stability depend on the mass of the charged particle and the operation line cuts through

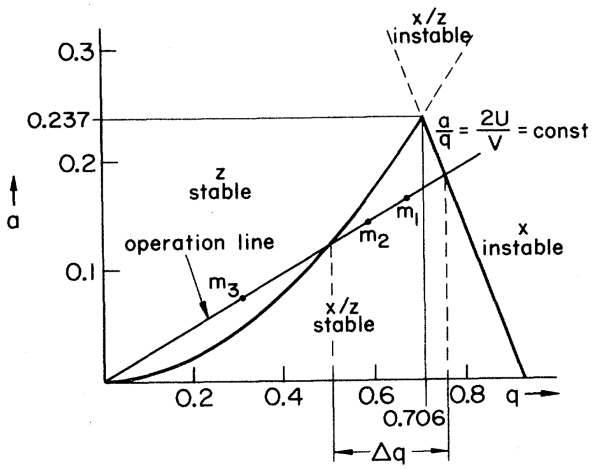

Figure 3.14: q-a area of stability of first order. For q-a pairs inside the area of stability, the motion is stable in x- and z-direction. For fixed values of r_0, ω, U, and V, different masses with $m_1 < m_2 < m_2$ lie on the operation line, of which only m_1 and m_2 are stable. Figure taken from [129].

the tips of the areas of stability. Figure 3.15b shows the corresponding mass spectra (filled areas). However, the only mode of operation of the LIST is the RF-only mode ($U = 0$) [43]. In this mode of operation, the RFQ works as an ion-guide for all masses $\frac{2eV}{qr_0^2\omega^2} < m < \infty$, which can be easily derived from the stability-condition $0 < q < 0.92$. The corresponding mass spectra is illustrated in Figure 3.15b by the empty areas. Both masses, m_1 and m_2, are transmitted until the maximum RF-amplitude V of the area of stability of m_1 (dashed line). For higher RF-amplitudes, only m_2 is transmitted, until the end of the area of stability of m_2 is reached.

3.5.2 The real RFQ ion guide and mass filter

The potential inside the real RFQ ion guide and mass filter differs from the ideal hyperbolic RFQ due to several reasons:

- Non-hyperbolic RF-rods.
- The RF-rods are of finite lengths.
- Slightly misaligned RF-rods.
- Field disturbances by external fields (e.g. nearby electrodes).
- Space charge effects due to the interaction between the stored charged particles.
- A disturbed RF-signal at the RF-rods.

The deviations from the ideal RFQ potential lead to so called *non-linear resonances*, which are unstable a-q-combinations inside the area of stability [45]. Usually, these non-linear resonances are observed as losses in the mass spectra for certain RF-voltage settings. However, in the experiments with the LIST, described in here, no such non-linear resonances were observed. Figure 3.15c shows a possible mass spectra without non-linear resonances of a real linear RFQ. In general, the mass peaks of a real RFQ mass filter show a decreased efficiency towards the limits of the RF-potential, V. In contrast, the mass peaks may tail over the limits of the RF-potential. This is due to the finite length, which only allows a certain number of oscillations. For charged particles with masses close to the area of stability, the defocusing effect may not be strong enough and the charged particles may eventually pass the RFQ without getting lost.

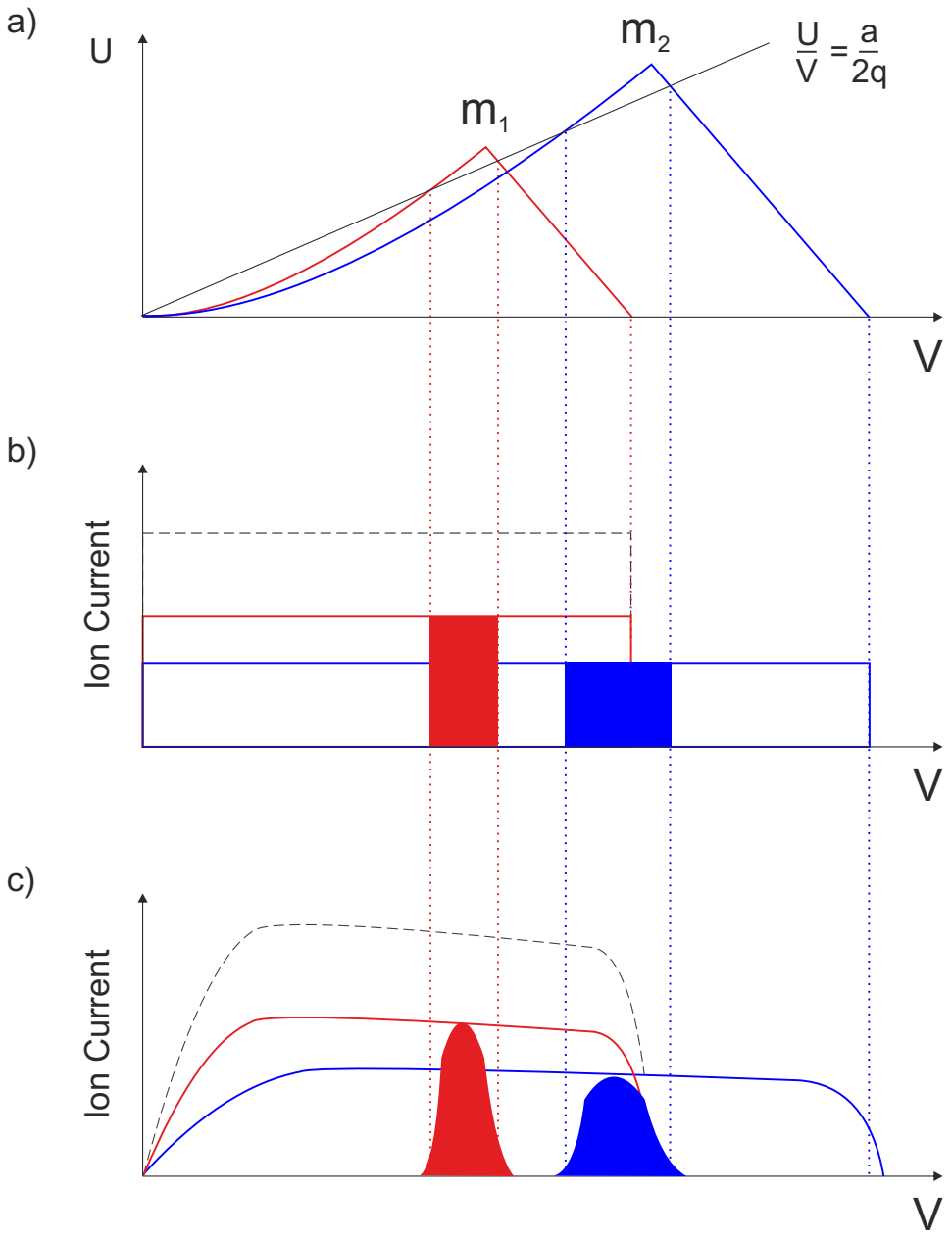

Figure 3.15: a) Areas of stability in the V-U-space. b) Ion signal as a function of the applied RF-voltage. The filled areas represent the mass spectra, when the RFQ is operated as a mass filter $U > 0$ and the empty areas represent the mass spectra of the ion guide mode of operation (RF-only, $U = 0$). In all figures, red lines belong to mass m_1 and blue lines belong to m_2. The dashed black line is the total ion current. c) Mass spectra of the real RFQ.

Part II

Improvement of the selectivity of the Resonance Ionization Laser Ion Source

4 The Laser Ion Source and Trap

The Laser Ion Source and Trap (LIST) is a novel approach to improve the selectivity of the RILIS. It combines the highly element-selective RILIS with an electrostatic repelling electrode that is installed shortly after the exit of the hot cavity to suppress surface ionized isobaric contaminants. Additionally, an RFQ ion guide (IG) is used to provide transverse confinement of ions inside the LIST as they drift towards the extraction region.
Figure 4.1 is an illustration of the LIST, combined with a typical target/ion source and mass separator configuration of ISOLDE. Two modes of operation can be distinguished: in *LIST mode*, a positive voltage is applied to the repeller electrode and thus, positive ions coming from the hot cavity are repelled and only neutral atoms are able to effuse into the RFQ ion guide, where the atoms of interest are subsequently ionized by the RILIS lasers. The ions are radially confined by the transverse RFQ potential and drift towards the aperture of the LIST end-electrode and the penetrating field of the high voltage (HV) extraction electrode. In *LIST mode* losses in efficiency compared to *standard RILIS operation* are expected, while the selectivity, i.e. the beam purity, is expected to improve strongly. Alternatively, the LIST can be operation in *ion guide mode*: in this mode of operation, a negative voltage is applied to the repeller electrode allowing all ions to pass the repeller electrode. This results in a lower selectivity, but allows for ionization efficiencies, comparable to *normal RILIS operation*, which is typically of the order of 10 % (Further explanations of the *LIST mode* and *ion guide mode* are given in Section 4.3.1).
The LIST was proposed as a new type of ion source for RIB facilities in 2003 [14, 176] and was built and designed at the University of Mainz [14, 74, 152, 176, 178]. The testing and development of the LIST was carried out as a collaboration between the University of Mainz and ISOLDE [150, 151].
This thesis describes the characterization and implementation of the LIST in the ISOLDE environment, further development work towards a higher selectivity and the first on-line applications of the LIST. The LIST was tested extensively at the off-line separators of ISOLDE and Mainz University [140] before it was further adapted and modified to match the special requirements of the on-line physics operation at ISOLDE. In May 2011, the LIST was for the first time operated with proton irradiation during an ISOLDE on-line target development run. This allowed for first studies of the LIST performance with radioactive isotopes.
Based on the results of these experiments, a new slightly modified LIST was designed to improve the ionization efficiency, and was tested off-line. The first on-line application of the LIST took place in September 2012. Its goal was the suppression of surface-ionized francium in polonium beams for the study of the hyperfine structure and isotope shifts of neutron-rich polonium isotopes. The results of this experiment are described in Chapter 7.
To put this doctoral work into context, this chapter starts with a short summary of the previous development stages and achievements. A detailed explanation of the final exper-

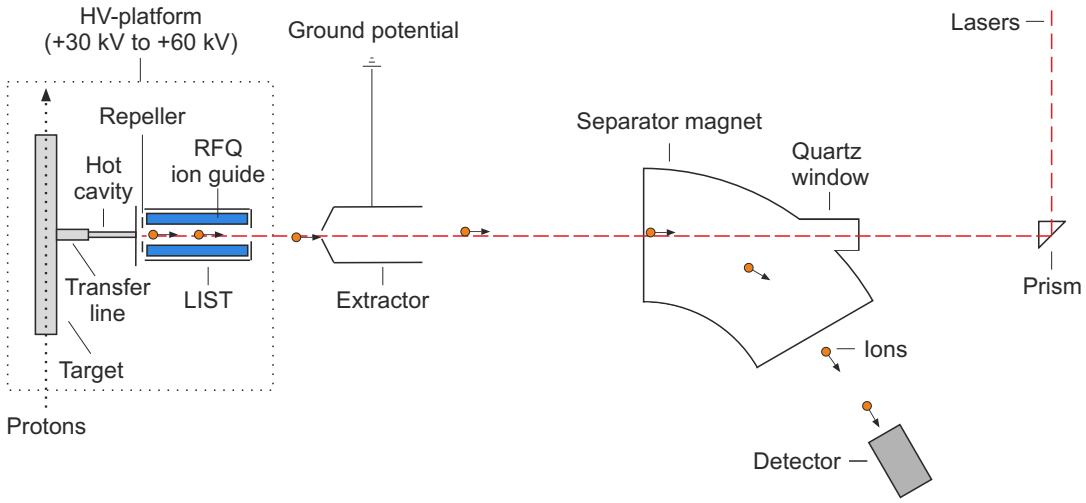

Figure 4.1: An illustration of the LIST target operated at the ISOLDE mass separator facility. The LIST (repeller electrode, RFQ) is attached to the target assembly (target container, transfer line, hot cavity). Protons are irradiate the target and the reaction products effuse through the target into the LIST RFQ, where the atoms are ionized by the lasers. After extraction by the extractor electrode, the ions are sent through the mass separator towards the detector or the experiment.

imental setup is then given together with the technical aspects, methods and parameters required to assess the LIST performance. A dedicated section addresses the different modifications of the LIST target-assembly and electronics, necessary for the implementation into the ISOLDE environment and for the preparation of the on-line runs. The results of the characterization of the performance from the ISOLDE off-line and on-line operation are given at the end of the chapter*.

4.1 LIST developments and achievements prior to this work

4.1.1 First proposal

The Laser Ion Source and Trap was first proposed by *H.-J. Kluge* and first described by *K. Blaum, C. Geppert, H.-J. Kluge, M. Mukherjee, S. Schwarz* and *K. Wendt* in 2003 [14]. Its initial design concept is illustrated in Figure 4.2. An ion-repelling electrode (colloquially called the *"repeller"* or the *"repeller electrode"*) is installed downstream of the exit of the transfer line of the target. Its function is to hinder the surface-ionized ions from entering the laser/atom interaction region behind the repeller electrode. The free atoms, which are able to pass the repelling potential undisturbed, interact with the RILIS laser beams which are tuned to ionize only the element of interest.
Without a shielding enclosure, the strong field gradient of several keV/cm towards the extraction electrode would lead to a wide energy spread of the ion beam and high losses

*This chapter comprises parts that were published in [60].

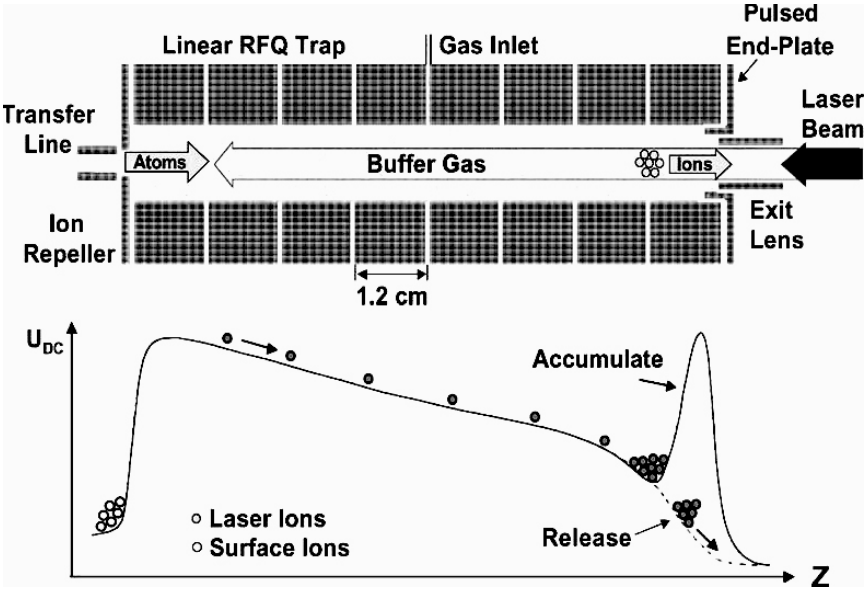

Figure 4.2: Top: schematic of the LIST, as proposed by [14]. This design comprises an ion-repeller electrode, a segmented linear RFQ ion trap, a gas inlet, a pulsed end-plate and an exit lens. Bottom: potential gradient along the ion beam axis, z.

in the magnet*. The laser ionization region is therefore enclosed by a cylindrical cavity. It surrounds a linear Paul trap with segmented RF-rods create a field gradient and potential well in the longitudinal direction. Simultaneously, it permits the confinement of the ions in radial direction by an RFQ quadrupole potential as well as the guidance to the exit of the source cavity. By injecting a buffer gas into the trap, the segmented linear RFQ can be operated as an RFQ ion cooler and buncher. The longitudinal trap potential is shown in the bottom part of Figure 4.2. The DC potential, which is superimposed on the RF signal of typically 1 MHz, lowers the potential towards the exit of the trap, where the ions are then cooled down from the initial thermal kinetic energy due to the collisions with the buffer gas and follow the declining potential energy. If the end-plate of the LIST is operated on the same potential as the repeller, the trap is closed and the ions eventually accumulate in a potential minimum next to the exit of the LIST. After a certain time of accumulation, the potential at the end-plate is lowered and the bunch of ions is released by the extraction electrode and sent towards the mass separator.
The sequence of ionizing, cooling, trapping and releasing is synchronized with the laser repetition rate of typically 10 kHz, and leads to a pulsed ion beam with pulses of only a few micro-seconds length.
The ionization efficiency of this first LIST design was simulated to be of the order of 20 % to 30 % of the total atom and the overall selectivity to be $\geq 10^6$ [14]. Furthermore, a beam emittance as low as 3π mm·mrad in the transverse direction and 10 eV · µs in the longitudinal direction was calculated.

*The acceptance of the GPS is approximately ±50 eV

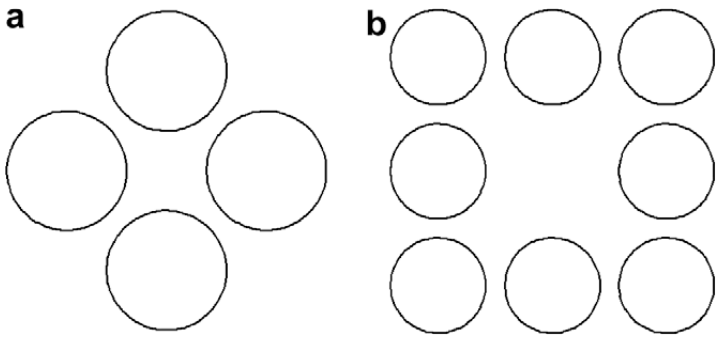

Figure 4.3: A transverse schematic [152] of the relative dimensions and alignments of the RF-rods of a) LIST A and b) LIST B. LIST A consisted of 4 segmented RF-rods with superimposed DC-potential (free field radius $r_0 = 0.6\,\text{cm}$; radius rods $R = 0.9\,\text{cm}$). LIST B consisted of 4 RF-rods and 4 segmented DC-rods ($r_0 = 1.05\,\text{cm}$, $R = 0.75\,\text{cm}$).

4.1.2 LIST A

Based upon the first proposal and preparatory studies by *M. Mukherjee* [125], a first prototype (LIST A*) was simulated, constructed and characterized by *K. Wies* as part of her dissertation [178] with support by *F. Schwellnus* [151, 152]. These first developments were carried out at the RISIKO mass separator in Mainz (see Chapter 3.3.2). The maximum trapping capacity of the LIST RFQ was determined to $4 \cdot 10^6$ ions and the beam emittance was simulated to be as low as $3\pi\,\text{mm}\cdot\text{mrad}$ in the transverse direction and $10\,\text{eV}\cdot\mu\text{s}$ in the longitudinal direction. Considering the limited trapping capacity, space charge effects and collisions with the buffer gas, the overall maximum ionization efficiency of the LIST was estimated to be $\leq 1\,‰$.

4.1.3 LIST B

An important aspect of designing an ion source at a RIB facility is to simplify the transport of electronic signals into the target. A second prototype (LIST B) was therefore constructed for which the RF-signal was decoupled from the superimposed DC-potential. This was done by applying the RF-signal to four non-segmented rods for radial confinement and adding four separate segmented rods for the longitudinal trapping [152]. A comparison of the spacing and alignment of the RF-rods between LIST A and LIST B is given in Figure 4.3.
Tests revealed that the ionization efficiency of the LIST scales to the distance of the repeller electrode to the hot cavity due to the divergence of the atomic beam. The total laser ionization efficiency in *ion guide mode* of the LIST B was determined to be $\geq 0.54‰$, which is slightly higher than obtained by LIST A. This improvement was achieved mainly

*In order to keep the discussion simple, the denotation for the different list devices is as follows: LIST prototypes, which were tested only at off-line facilities are denoted by capital letters; LIST devices, which were operated on-line, are denoted by numbers.

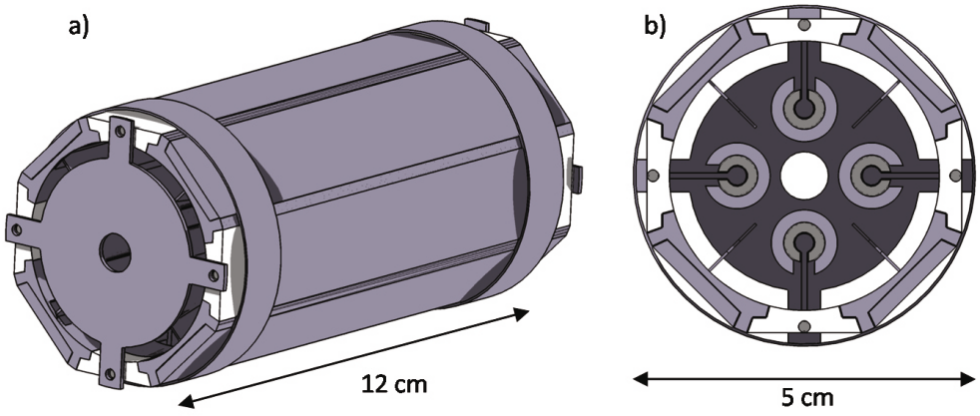

Figure 4.4: A schematic of the LIST C [150] in a) a sideways perspective, displaying the repeller electrode and enclosing cavity and b) plan view inside the LIST, displaying the four RF-rods.

by reducing the distance between the LIST and the exit of the hot cavity from 3 mm to 1 mm, which led to a greater overlap of the laser beam with the atoms.
During the diploma work of *T. Gottwald*, the RISIKO mass separator was equipped with an emittance meter for the study of the emittance of the LIST beam [74]. The experimentally determined beam emittance showed a surprisingly low emittance obtained without cooling and bunching of only $\approx 1\pi\,\text{mm}\cdot\text{mrad}$.

4.1.4 LIST C

The design of LIST B was modified and adapted for the special technical restrictions at the target fronted at ISOLDE during the dissertation of F. Schwellnus [150]. For this purpose, the complexity of the third LIST prototype (LIST C) was reduced for several reasons:

1. Limited available volume for the LIST inside the ISOLDE target.
2. Limited number of available vacuum feedthroughs for the transport of the electronic signals into the target.
3. Harsh conditions at the target front-end: radioactivity of up to kGy/h during operation and temperatures exceeding 2000°C.
4. Technical difficulties and safety considerations concerning the usage of buffer gas at the ISOLDE target front-end.

These restrictions, together with the promising results of the LIST B emittance without buffer gas, justified the reduction of the RFQ cooler and buncher to a linear RFQ ion guide without segmented rods and buffer gas cooling. A schematic of the LIST C design is shown in Figure 4.4. The LIST C was developed in a collaboration between the University of Mainz and ISOLDE and was successfully tested and operated at the ISOLDE off-line

mass separator under realistic conditions. It was then further simulated and characterized at the University of Mainz.
The minimum suppression of surface-ionized ions by the LIST C repeller electrode was of the order of 10^5, and the laser ionization efficiency could be increased to $\approx 0.14‰$*. Even without buffer gas, the LIST C pulse length of one laser pulse was smaller than 6 µs and the estimated transverse emittance was about 2π mm · mrad.
These promising results led to an ongoing continuation of the collaboration between the University of Mainz and ISOLDE for further development of the LIST, towards the first on-line test at ISOLDE. A first solution for the transport of the RF-signal into the target was proposed and additional tests of the resulting LIST D at the ISOLDE off-line mass separator were scheduled for October 2010.

4.1.5 Objective of this thesis

The work on this doctoral thesis started in September 2010, directly prior the scheduled off-line test of the LIST D at the ISOLDE off-line mass separator. It first aimed at characterizing the performance of the LIST at the off-line mass separator and then, if successful, eventually prepare and organize the first on-line test of the LIST at ISOLDE. The research work was carried out in a joint effort with *Sven Richter* (PhD student, University of Mainz [140]), within a collaboration between the RILIS group of *Dr. Valentin Fedosseev* and the target group of *Dr. Thierry Stora* at ISOLDE, the LARISSA working group of *Prof. Dr. Klaus Wendt* of Mainz University and the Division of *Prof. Dr. Klaus Blaum* at the Max-Planck Institut für Kernphysik in Heidelberg. This approach was compelled by the combined knowledge of design and construction in Mainz, and ISOLDE for the successful implementation of the LIST into the ISOLDE environment and the preparation of the off-line and on-line experiments. Additionally, the project benefited of complementary, independent tests at ISOLDE and at the RISIKO mass separator in Mainz. Based on the previous developments of the LIST described above, the objectives of this thesis are:

Establish a test setup at the ISOLDE off-line mass separator:
Setting-up a temporary RILIS installation at the ISOLDE off-line mass separator; setting up and testing the electronics and developing of a remote control program; the adaptation and modification of an ISOLDE target unit for the installation of the LIST.

Preparatory tests at the ISOLDE off-line mass separator:
Characterizing the LIST in terms of selectivity and ionization efficiency; testing an automatic RF-coupling system; commissioning of the ISOLDE target prior to the on-line target development test.

Implementation of the LIST into the ISOLDE environment
Constructing an on-line target; developing a technical solution for the transportation of an RF-signal into the target; installing the LIST power supplies and remote controls at the ISOLDE high voltage platform.

*Note that this increase was achieved in the *LIST mode* (repeller on positive potential), while the laser ionization efficiencies of LIST A and LIST B were obtained in *ion guide mode*.

On-line testing, optimization, further developments and operation of the LIST
Organizing a first on-line run; characterizing the LIST using radioactive nuclides; first on-line application of LIST for physics experiments at ISOLDE, in the case of a successful first on-line test.

4.2 The Laser Ion Source and Trap at ISOLDE

Three LIST devices were constructed and used for the experiments described here: LIST D for the initial tests at the ISOLDE off-line separator from October 2010 to February 2011, LIST 1 for the first on-line target development test at ISOLDE in May 2011 and LIST 2, which was used in September 2012 for the spectroscopy of neutron-rich polonium. All three LIST versions are based on the design of LIST C (repeller, RFQ ion guide, no cooling nor bunching), but were slightly altered between the different versions to optimize the performance. They were built at the workshop of the physics institute of the University of Mainz and the corresponding target assemblies were designed and constructed by the ISOLDE workshop.

4.2.1 Specifications of LIST D, LIST 1 and LIST 2

An illustration of the final LIST design is given in Figure 4.5 and photographs of the different stages of the assembling and installing of the LIST are shown in Figure 4.6. In order to improve the performance, the dimensions of some components were changed from LIST D to LIST 2. To simplify the description in the following, the LIST D values are used as default. For components that were modified for each LIST version, the dimensions are given in parenthesise with indexes referring to the specific LIST model. Further detailed technical drawings will be given in [140].
The LIST consists of two annular electrodes with an outer diameter of $d_{\mathrm{o}} = 35\,\mathrm{mm}$ and an aperture diameter of $d_{\mathrm{a}} = 7\,\mathrm{mm}$ ($d_{\mathrm{a},6} = 11\,\mathrm{mm}$) located at each end of a cylindrical chamber made of stainless steel with a length of $l_{\mathrm{c}} = 100\,\mathrm{mm}$ ($l_{\mathrm{c},5,6} = 90\,\mathrm{mm}$) and a diameter of $d_{\mathrm{c}} = 38\,\mathrm{mm}$. Four RF-rods of $l_{\mathrm{RF}} = 98\,\mathrm{mm}$ ($l_{\mathrm{RF},5,6} = 88\,\mathrm{mm}$ length) and $d_{\mathrm{RF}} = 10\,\mathrm{mm}$ diameter are fixed parallel with the axis of the LIST and equally spaced around a radius of $r_{\mathrm{RF}} = 15\,\mathrm{mm}$ from the center of the device to form the RFQ ion guide. Each of these elements are made of stainless steel and are separated by boron-nitride (BN) ceramic insulators, chosen for its high melting point of $T = 2973\,^{\circ}\mathrm{C}$ and its resistance against radioactivity.
The two electrodes (repeller and end-electrode) and the chamber shield the ionization region from the strong electric field of the ISOLDE extraction electrode; thereby providing a longitudinally field-free region, such that ions created inside the LIST will be extracted with a small energy spread.
A voltage of up to $V_{\mathrm{RF}} = \pm 500\,\mathrm{V}$ can be applied to the repeller electrode. The repeller voltage polarity determines the mode of operation of the LIST. A positive voltage repels ions that are created inside the hot cavity (*"LIST mode"*) permitting only neutral atoms to enter the LIST RFQ ion guide. A negative voltage enables passage of the hot cavity ions and the LIST RFQ acts as an ion guide only (*"ion guide mode"*). The RFQ ion guide

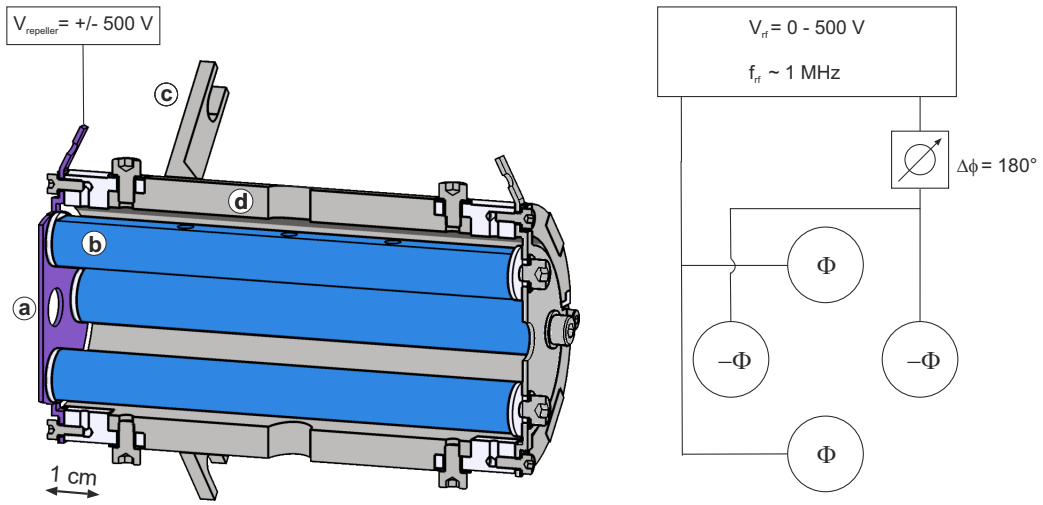

Figure 4.5: Left: a drawing of the LIST design and its most important parameters [140]: a) repeller, b) RF-rods, c) LIST holder and d) housing. A voltage of $V_{\text{repeller}} = \pm 500\,\text{V}$ can be applied to the repeller electrode. Right: the RF-signal ($V_{\text{RF}} = 0 - 500\,\text{V}$, $f_{\text{RF}} \approx 1\,\text{MHz}$) is applied to the RF-rods in opposite phase between neighboring rods.

is necessary for transverse confinement of ions within the LIST as they drift towards the extraction potential (see Chapter 3.5). A sinusoidal RF-signal with $f_{\text{RF}} = 1\,\text{MHz}$ frequency ($f_{\text{RF},5} = 1.2\,\text{MHz}$, $f_{\text{RF},6} = 1.15\,\text{MHz}$) and up to $V_{\text{RF}} = 500\,\text{V}_{\text{pp}}$ amplitude from peak to peak (pp) is applied to the RF-rods, in opposite phase between neighboring rods to generate a trapping potential.

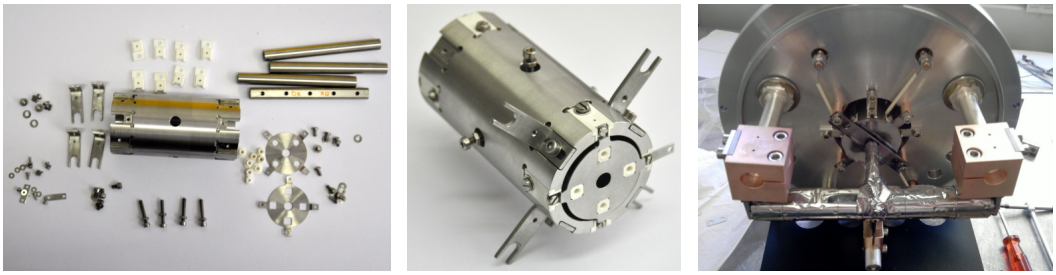

Figure 4.6: Left: Overview of the LIST 1 components. Center: assembled LIST. The repeller electrode, the LIST chamber, the LIST holder and the RF-contacts are visible. Right: LIST 1 installed into an ISOLDE target.

4.2.2 On-line runs and target specifications

One target was assembled for each on-line run and for the corresponding off-line test. Both were ISOLDE targets in standard configuration, as shown in Figure 3.4. They consisted of a target container ($l = 202\,\text{mm}$, $d = 20\,\text{mm}$), tantalum transfer line ($l = 41\,\text{mm}$ from target, $d = 5\,\text{mm}$) and a hot cavity ($l = 34\,\text{mm}$, $d = 3.1\,\text{mm}$ inner diameter). The individual target and operation parameters of the two LIST targets are given in Figure 4.7.

LIST target 1: off-line characterization October 2010 until May 2011 and on-line run May 2011

The first on-line target development run of the LIST was scheduled from May 5-7, 2011 at the beginning of the on-line period in 2011. The goal was the first on-line characterization of the LIST at ISOLDE, comprising measurements of the suppression and laser ionization efficiency of radioactive isotopes. Its long-term reliability under on-line conditions was also to be assessed. In addition, the feasibility of using the LIST to reduce contamination of surface ionized sodium and aluminium (Al) in magnesium (Mg) beams in the mass range from 21 u to 27 u was tested. For the production of these light exotic nuclei, the target (ISOLDE target #442) was filled with rolls of titanium-foils (25 µm thickness, 56 g total weight) as the target material.
The initial tests at the off-line separator were carried out with the LIST D. Due to space constrains inside the target, LIST 1 was built with a 1 cm shorter overall length. LIST D and LIST 1 were installed 5 mm downstream of the hot cavity. This was the closest possible position ascertaining that the LIST would not come into contact with the hot cavity or the protecting heat shields. An overview over the operating parameters of the LIST target 1 (ISOLDE target # 442) is given in Figure 4.7 a.

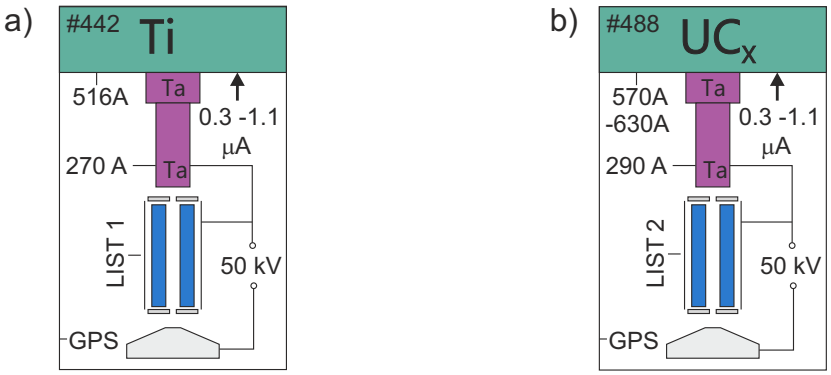

Figure 4.7: An illustration of the operating parameters of a) LIST target 1 and b) LIST target 2. From top to bottom: target number #, target material, typical target and hot cavity currents in A, proton intensities in µA, LIST symbol, extraction voltage and front-end. Design of schematics adopted from [143].

LIST target 2: off-line commissioning August 2012 and on-line run September 2012

The LIST was used for its first real on-line physics application in September 2012. The goal was suppression of surface ionized francium in polonium beams in order to subsequently perform laser spectroscopy on neutron-rich polonium isotopes (see Chapter 7). For this purpose a uranium-carbide UC_c was used. Due to a possible coating of the BN insulators because of the outgassing of material from the uranium-carbide target, the LIST was initially tested with silicon carbide (SiC) target to investigate this issue at the ISOLDE off-line mass separator.
A slightly altered design of the RF-rods insulators and the repeller electrode allowed for the LIST to be mounted 2.5 mm closer to the hot cavity than for the previous target, resulting in an overall distance of only 2.5 mm. This geometry leads to a greater overlap of the lasers with free atoms behind the repeller, possibly leading to a higher ionization efficiency. The operating parameters of the LIST target 2 (ISOLDE target #488) are given in Figure 4.7 b.

4.2.3 Implementation of the LIST at ISOLDE

The on-line operation of an electronic device such as the LIST in the ISOLDE environment required several technical modifications of the LIST, the target, and the GPS-front-end due to several constraints:

1. Previously there were no dedicated RF-feedthroughs or RF-cabling installed for transport of electronic signals over the distance of about 20 m from the high-voltage cage to the target. This necessitated:
   - → the installation of a new radiation-hard RF-coax line from the high-voltage cage to the target.
   - → the minimization of losses due to the transport of the RF-signal by sending a low-amplitude signal to the front-end as well as by transforming and splitting of the RF-signal into two RF-signals of opposite phase at the target using a transducer unit (*"transducer box"*).
   - → the minimization of losses due to the transport of the RF-signal by sending a low-amplitude signal to the front-end as well as by transforming and splitting of the RF-signal into two RF-signals of opposite phase at the target using a transducer unit (*"transducer box"*).
2. Harsh conditions during operation due to high radiation levels and high temperatures were overcome by:
   - → radiation hard insulators, cables and a transducer box.
3. Automatic handling of the targets by robots demanded:
   - → the design of the mount to hold the transducer box on the target assembly.
   - → the construction of an automatic RF-coupling from the front-end to the target.

4. No access to the target or to the front-end and only limited access to electronics on the high-voltage platform is possible during operation. This required a

   → remote control for the LIST operating parameters.

   → automatic data acquisition system.

Transport of the RF-signal

Due to the absence of a dedicated RF-cable and an RF-feedthrough to the target, several modifications to the GPS front-end and the target unit were necessary prior to the first on-line run. In order to avoid power losses during the transport of the RF-signal from the high-voltage cage to the target over a distance of about 20 m, a two-stage transport and transformation system was initially designed by K.-P. Höldtke from the University of Mainz [150]. The final design for the adaption to ISOLDE is shown schematically in Figure 4.8.
The RF-signal of about 1 MHz is generated by a function generator ("TTi", 0.001 Hz to 10 MHz, 0 V_{pp} to 7 V_{pp}) and amplified to up to 60 V by a pre-amplifier unit designed and built by the University of Mainz. The pre-amplifier can be tuned remotely by an analog 0 V to 10 V DC-voltage signal (*RF-control voltage*), provided by a *"Keithley 6487"* power supply.
The RF-signal was then sent down from the high-voltage cage to the target through a newly developed radiation hard coaxial line. It was designed in parallel for the first on-line test of a HELICON type ion source by Pekka Suominen from the ISOLDE target group and installed at the ISOLDE GPS front-end during the ISOLDE shutdown period in spring 2011 [97]. This line consisted of a 20 m radiation hard coaxial cable (50 Ω, 75.9 pF/m) of the company *Huber+Suhner*, a 0.7 m home-built coaxial copper line to bridge the high-radiation area close to the target, and an automatic RF-coupling to transport the signal to the target. This RF-coupling allows the automatic connection of the target to the coaxial

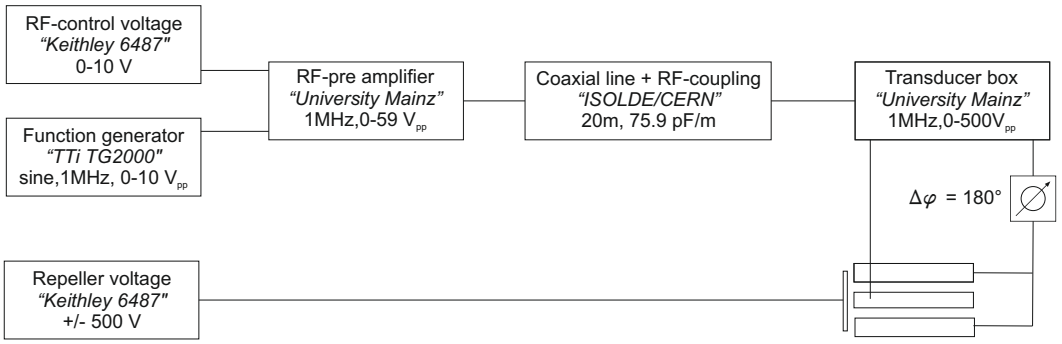

Figure 4.8: A schematic of the electronic supplies and the RF-transmission system from the high-voltage cage to the LIST. The RF-supply system consists of a function generator, a DC-control unit, a pre-amplifier, a radiation hard coaxial line including the RF-coupling and a transducer box. The DC-voltage for the repeller is provided by a power supply and transmitted through a standard feed-through to the target.

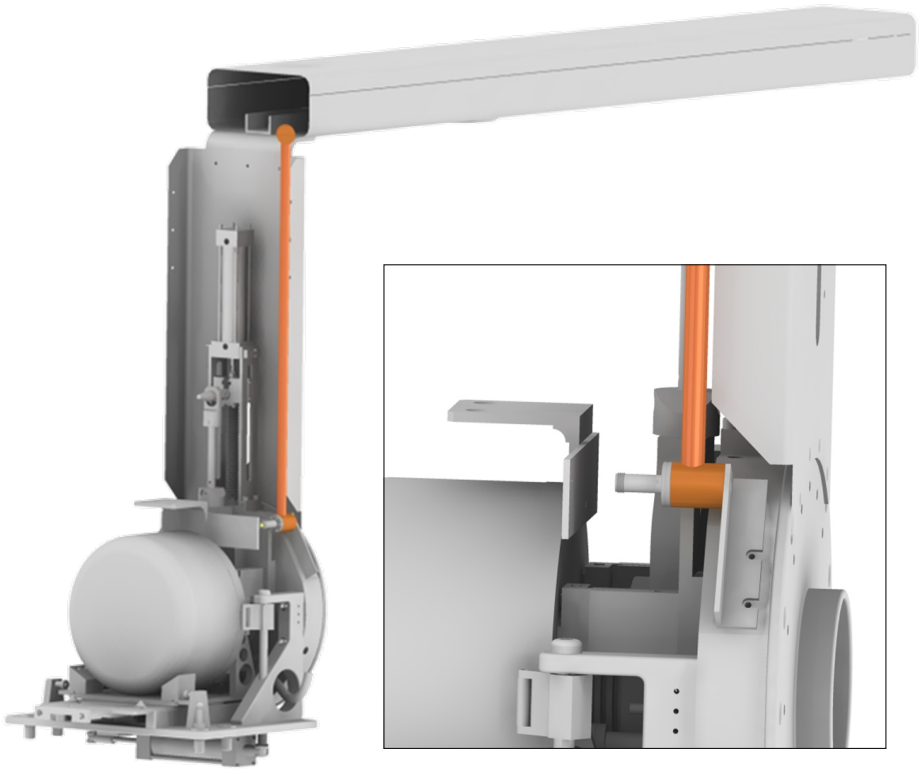

Figure 4.9: a) A picture of the radiation-hard coaxial copper line installed at the ISOLDE GPS front-end and a close-up of the RF-coupling [166].

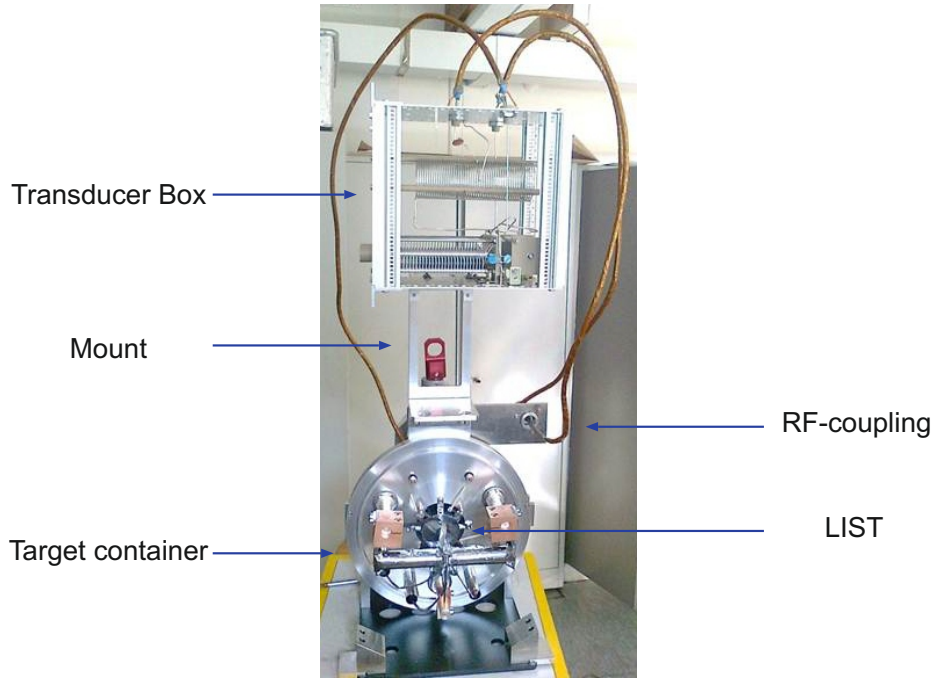

Figure 4.10: Target assembly 1 with LIST 1 before the first on-line run in May 2011. The transducer box, mount of transducer box, RF-coupling, LIST 1 and target container are visible.

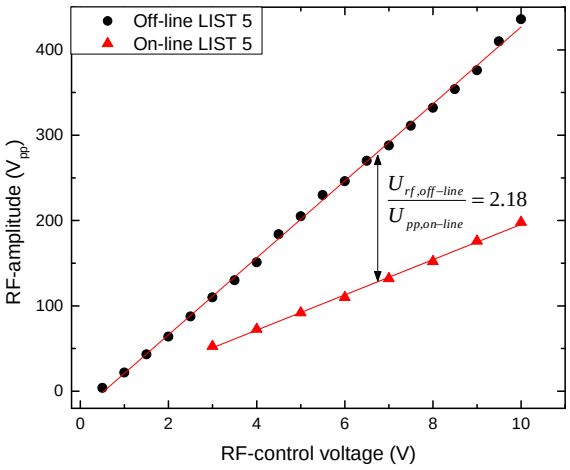

Figure 4.11: Calibration of the RF-amplitude as a function of the RF-control voltage at the off-line separator and at the GPS front-end before the on-line run 2011. The function generator was set to a sine-signal with an amplitude of 3 V_{pp}. The signal at the GPS front-end is reduced by a factor of 2.18.

copper line when the robot attaches the target to the front-end. A drawing of the coaxial copper line and the RF-coupling at the GPS front-end is given in Figure 4.9 [166].
After passing the RF-coupling, the RF-signal is transported to a transducer box, which is mounted above the target assembly. A technical drawing of the transducer box and further details can be found in [139, 140]. The transducer consists of an inductor-capacitor (LC) circuit with tunable capacitors to match the LC circuit to the 50 Ω coaxial line. All elements were made of radiation hard materials (PEEK) to protect the electrical components from the radioactive environment. If the frequency of the RF-signal is in resonance with the LC-circuit, the transducer transforms the signal to up to 500 V_{pp} to generate a sufficient trapping potential. The resonance frequency was 1.15 MHz for the transducer box of the LIST target 1 and 1.2ṀHz for the transducer box 2. The difference between these two transducer boxes was due to small differences of the LC-components.
Furthermore, the transducer box output is split into RF-signals of opposite phase for the neighboring rods of the RFQ (see Figure 4.5). The RF-signals are then transferred by standard vacuum feedthroughs from the transducer into the target continuing to the LIST. A picture of the final target assembly of the LIST 1 with transducer box and RF-coupling is shown in Figure 4.10.
After each attachment of the target assembly to the frontend, the RF-amplitudes at the LIST RF-rods need to be calibrated for the applied RF-control voltage. Figure 4.11 shows the calibration of the RF-control voltage to the RF-amplitude at the RF-rods of the of the LIST 1. The calibration at the ISOLDE off-line separator is compared to the calibration at the ISOLDE GPS front-end before the first on-line run in 2011. For each individual calibration, the RF-signal from the function generator was set to 3 V_{pp} and the tunable capacitors were set such that signal strength at neighboring rods was symmetrical. The dependency of the RF-amplitude to the RF-control voltage showed a linear behavior in both cases. However, a difference of the strengths of the RF-signals of a factor of 2.18 was observed between the off-line separator and the GPS front-end. For instance, at the off-line separator, the maximum obtained amplitude at 10 V RF-control voltage was 436_{pp}, while at the GPS frontend, the amplitude was only 198 V_{pp}. Despite the losses, the maximum RF-amplitude at the GPS front-end was believed to be enough to transport

all ions through the RFQ according to the preparatory tests performed at the off-line separator (see Chapter 4.3.3). If necessary, it would have been possible to increase the signal strength further by increasing the amplitude of the RF-function generator to 7 V_{pp}. The losses at the GPS front-end can be explained by the different RF-cables and RF-couplings, which were used at the off-line separator and the on-line separator. Since the LIST transducer box cannot be fine tuned at the front-end due to safety constraints, the transducer box could only be tuned at the off-line separator prior to the on-line run leading to a possible mismatch at the GPS-frontend. In order to limit the losses during the next LIST experiments, an identically constructed coaxial copper line and cable was installed at the off-line separator for a better matching of the transducer box prior to the second on-line run with the LIST 2 in 2012. The results of the calibration of the transducer box of the corresponding LIST target 2 are similar to the calibration line of the transducer box of LIST target 1 shown in Figure 4.11, but no direct measurements at the GPS frontend were possible prior the second on-line run due to safety constraints.

Handling and coupling of a target by robots

The modified LIST target assembly with the transducer box and the cabling adds space and weight to the standard ISOLDE target. Thus, the correct placement of the LIST transducer box and the automatic RF-coupling had to be investigated in order to balance the target during the transport by the robots, and to avoid contact with the elements of the target front-end. For this purpose, a mount for the LIST transducer box was designed. The handling of the target by the robot was successfully tested at the GPS front-end during the ISOLDE shutdown in April 2011. In addition, these tests provided important information about the correct placement of the transducer box on the mount with respect to the cabling at the front-end. Figure 4.12 gives an impression of the different stages of the handling phases by the robot: grabbing, transporting and attaching.

Remote control system

Remote control of the repeller voltage and the RF-settings is essential for optimizing the LIST operating parameters. To serve this purpose, a LabVIEW based control system for the LIST has been developed and integrated into the RILIS control system [142]. The system provided independent control of the RF-function generator *"TTi TG2000"* (RF-frequency), the RF-control voltage supply *"Keithley 6487"* (RF-amplitude) and the repeller voltage supply *"Keithley 6487"*. A schematic of the control system is shown in Figure 4.13.
Glass fibers were passed from the RILIS laboratory into the HV-cage to allow the remote control of the electronic units. RS232-to-ethernet and fiber-to-ethernet converters translated the signal from and to the HV-cage. The electronics were integrated into the CERN technical network as shown in Figure 4.13, which were in turn accessible by the RILIS control computer. Additionally, the Faraday cup signal could be accessed by the control system to allow for optimizing and scanning of the ion current as a function of the repeller voltage and the RF-amplitude.
This setup was also used during the preparatory tests of the LIST at the ISOLDE off-line

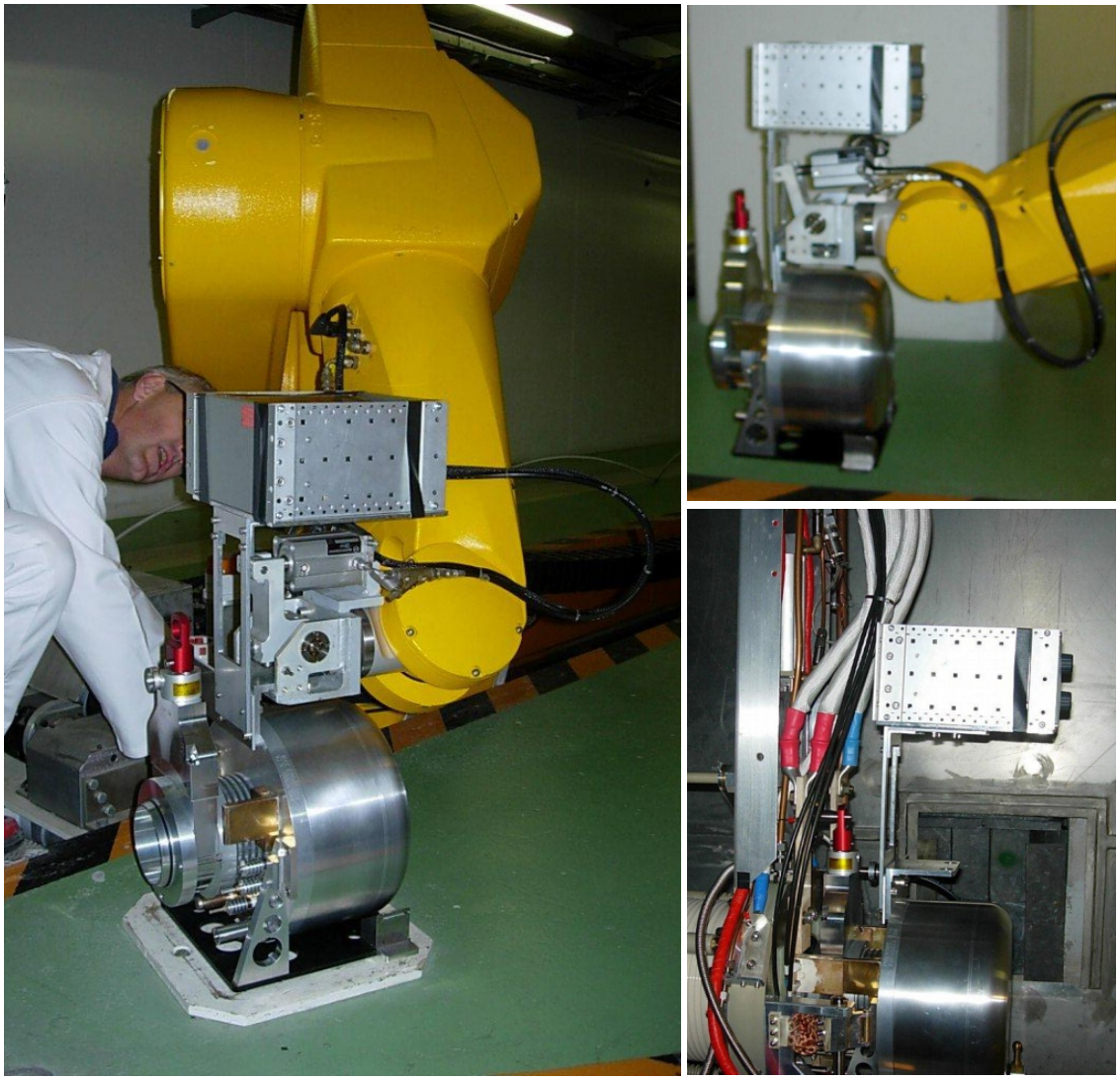

Figure 4.12: Photographs taken during the robot test of the LIST target 1 at the GPS front-end. Left: Richard Catherall controls the grabbing of the target by the robot arm. Location and balancing the weight of the transducer box is crucial. Right top: the robot lifts and moves the target towards the front-end. The design of the holder allows to move the robot freely. Bottom right: target attached to GPS front-end. Cabling of transducer box needs to be considered for the final placement of the the transducer box. It is noted that the transducer box was altered between this test and the on-line run (see Figure 4.10).

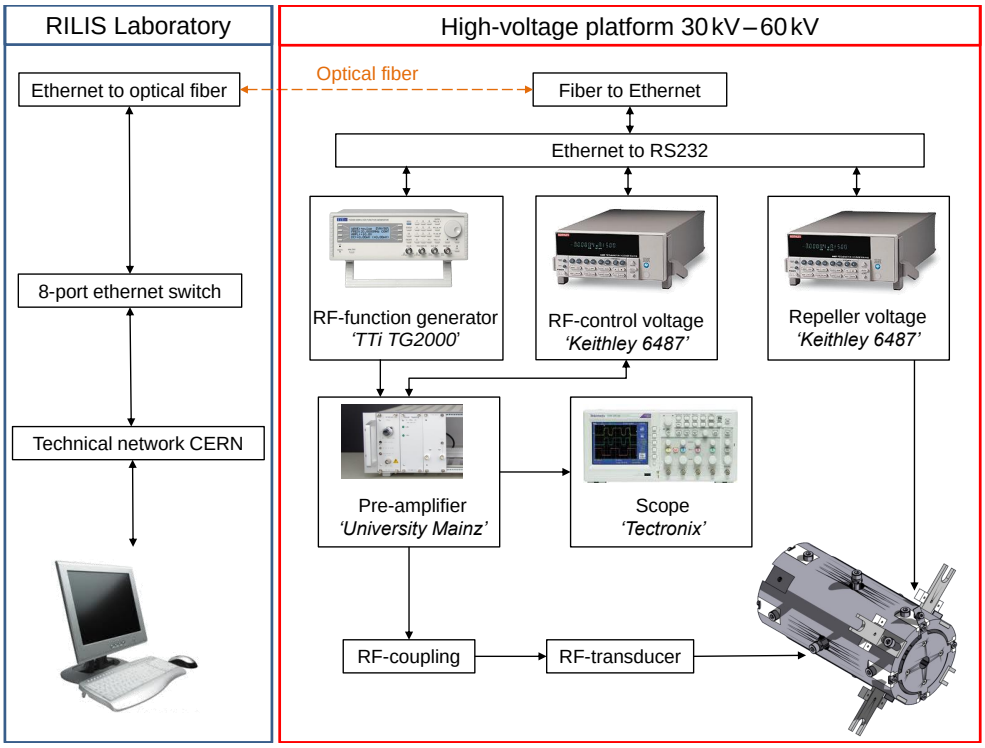

Figure 4.13: Illustration of the remote control system of the LIST. Glass fibers were passed from the RILIS laboratory to the HV-cage for remote control of the electronics. The RF-function generator, the RF-control supply and the repeller voltage supply are integrated and controlled via the technical network of CERN.

mass separator, except that the devices were not integrated into the technical network, but controlled via an USB-to-RS232 converter directly by the control computer.

Off-line laser system

A RILIS setup was installed at the ISOLDE off-line mass separator for the off-line tests. A sketch of the setup is shown in Figure 4.15. It consisted of two Ti:Sa solid-state lasers, which were pumped by a Nd:YAG 532 nm pump laser from *Photonics industry* and one frequency tripling unit. The pump laser beam was split by two tunable beam-splitters ($\lambda/2$-plate + beam-splitter cube), which allowed separate tuning of the pumping power of the two Ti:Sa lasers. A small fraction of the output from each of the Ti:Sa lasers was picked up by 4% beam splitters and sent to a wavemeter for monitoring. Laser optics for infrared (IR) and ultraviolet (UV) light - consisting of mirrors, telescopes and periscopes - guided and focused the laser beams through a metal tube and a quartz-window into the separator magnet and beam-line towards the LIST and the hot cavity.
The tests at the off-line mass separator were conducted with ytterbium (Yb) because of its efficient two-step laser ionization scheme, with wavelengths within the tuning range of the Ti:Sa lasers. The ionization scheme of ytterbium is shown in Figure 4.14a. Addition-

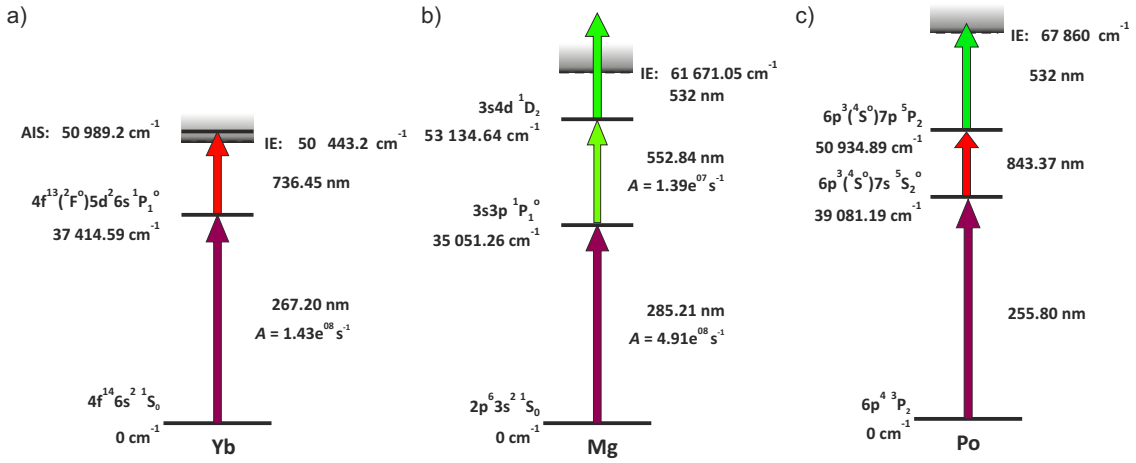

Figure 4.14: Laser ionization schemes for a) ytterbium (Yb), b) magnesium (Mg) and c) polonium (Po), as used during the experiments with the LIST. Ytterbium was ionized via an intermediate state to an autoionizing state. Magnesium and polonium were ionized via two intermediate transitions non-resonantly into the continuum. The second step of polonium was provided by a tunable NB Ti:Sa laser for the measurement of the HFS and the IS of that transition. Wavenumbers and configuration of the atomic levels and wavelengths and the transition probabilities are given if known from literature [94].

ally, ytterbium has a significant surface ionization efficiency, which allows to study the suppression of surface ionized ions and laser ionization efficiency in parallel.

On-line laser system

For the first on-line run, the RILIS laser system was tuned to the ionization scheme for magnesium, as shown in Figure 4.14b. A detailed description of the RILIS setup is given in Chapter 3.3.1. Two *Sirah Credo* dye lasers were used for the first two resonant transitions and the residual output power of the dye pump laser (frequency doubled *Edgewave* Nd:YAG) was used for the non-resonant ionization step. The target was prepared with one uncalibrated magnesium mass marker for initial testing and optimization of the laser beams and one calibrated magnesium mass marker (1100 nAh) for a laser ionization efficiency measurement.
During the first part of the 2012 run, the RILIS was tuned to magnesium to compare the LIST 2 to LIST 1 from the 2011 run. The setup of the RILIS was similar to the setup described above. In the second part of the 2012 on-line run, the setup was reconfigured to ionize polonium (Po) for the study of neutron-rich polonium isotopes (see Chapter 7). The laser ionization scheme [41] of polonium is shown in Figure 4.14c. The first resonant step was provided by the third harmonic of a Sirah dye laser, while the second step was provided by the fundamental of a tunable, narrow-band Ti:Sa laser for scanning of the spectroscopic transition. For the third transition above the ionization energy, the radiation of the frequency doubled *Edgewave* Nd:YAG dye pump-laser was used.

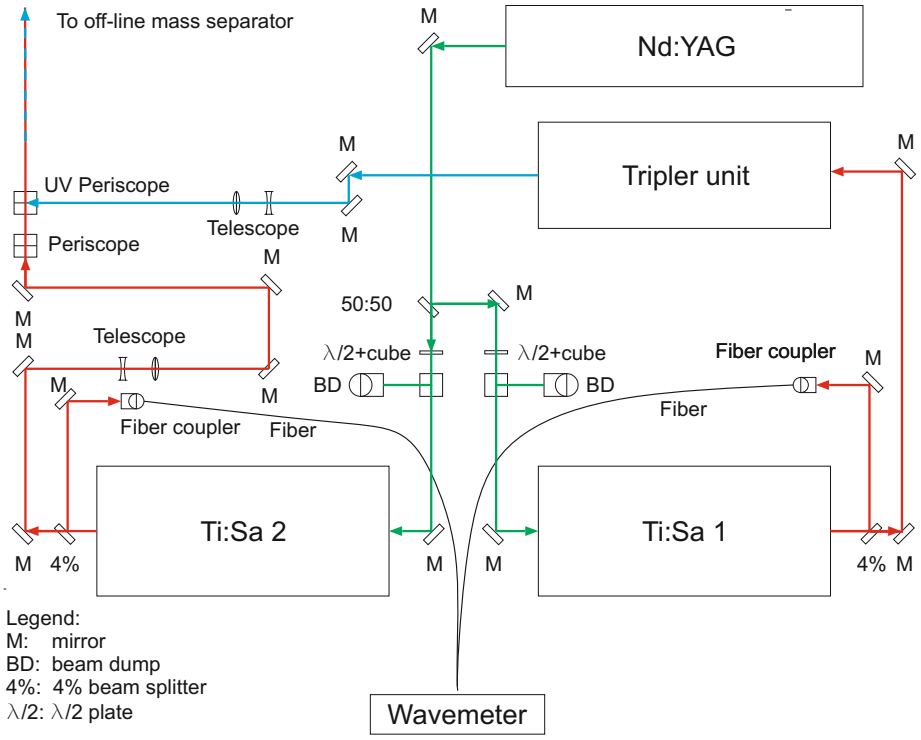

Figure 4.15: Schematic of the RILIS installation at the off-line mass separator for the testing and characterization of the LIST with ytterbium. The main components are a Nd:YAG 532 nm pump laser from *Photonics industries*, two Ti:Sa solid-state lasers, one tripler unit, a wavemeter and laser beam transport optics. The laser path is given by straight colored lines with arrows indicating the direction. The beams are finally mixed together at the last periscope and sent to the off-line separator.

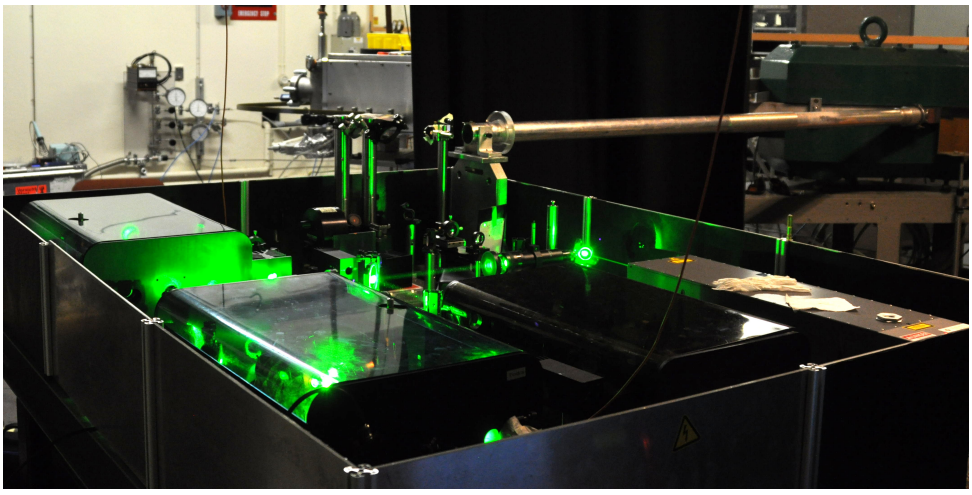

Figure 4.16: Photograph of the laser installation at the off-line mass separator (from the bottom right edge of the laser table in Figure 4.15). The two Ti:Sa lasers, the Nd:YAG pump laser and the optics are visible. The laser beams are transported by two periscopes into the metal beam pipe towards the quartz-window of the mass separator and the target.

4.3 Characterization of the performance of the LIST at ISOLDE

This section discusses the results of the two on-line runs and their preparatory tests at the off-line separator. Prior to the results, the most important terms, parameters and methods are defined to enable a better understanding. These are discussed with the help of Figure 4.17, which shows the different dependency of the ionization efficiency of laser ionized ^{174}Yb and surface ionized ^{174}Yb on the applied repeller voltage. For these measurements, the repeller voltage was scanned automatically from $U_{rep} = -215\,V$ to $U_{rep} = +215\,V$, while the ion current was measured by a Faraday cup. These so-called, *repeller scans*, were conducted with the LIST 1 at the ISOLDE off-line separator as part of the preparatory measurements for the first on-line run.

4.3.1 Different modes of operation

Depending on the repeller voltage setting, the LIST can be operated in the selective *LIST mode* or in the *ion guide mode* with a selectivity and efficiency similar to *normal RILIS operation*:

***LIST mode*:** In *LIST mode*, a positive repeller voltage is applied and surface ions are suppressed. Only laser-ions created inside the LIST are extracted. The repeller voltage setting in *LIST mode* is defined as the positive voltage for which maximum suppression of surface ions is achieved.
The effect of a positive repeller voltage to the ion current of ^{174}Yb is shown in Figure 4.17. When scanning across zero repeller voltage, the surface ion current decreases strongly and eventually reaches the background level of the Faraday cup at around $U_{rep} = +5\,V$. Despite of some fluctuations of the Faraday cup noise level, the surface ion current then remains indistinguishable from the Faraday cup background noise of 0.08 pA for higher repeller voltages, while the laser ion current remains well above the Faraday cup noise level. On the other hand, higher repeller voltages lead to the loss of laser ions due to an increased initial energy of ions created close to the repeller, which is detrimental for their transmission through the LIST. To take this effect into account, a range of suitable repeller voltages for the operation in *LIST mode* was determined from $U_{rep} = +7\,V$ to $U_{rep} = +12\,V$.

***Ion guide mode*:** In *ion guide mode* a negative voltage is applied to the repeller electrode and the positive ions, which were created in the hot cavity, may enter the LIST RFQ undisturbed. The overall extraction efficiency depends on the penetration of the negative repeller voltage into the source and thus, the *ion guide mode* is defined as the negative repeller voltage for which the laser ionization efficiency is highest.
In Figure 4.17, the *ion guide mode* for ^{174}Yb is between $U_{rep} = -25\,V$ to $U_{rep} = -55\,V$.

The exact values of the repeller voltage settings for *LIST mode* and *ion guide mode* need to be determined separately for each isotope and may differ, depending on the mass and

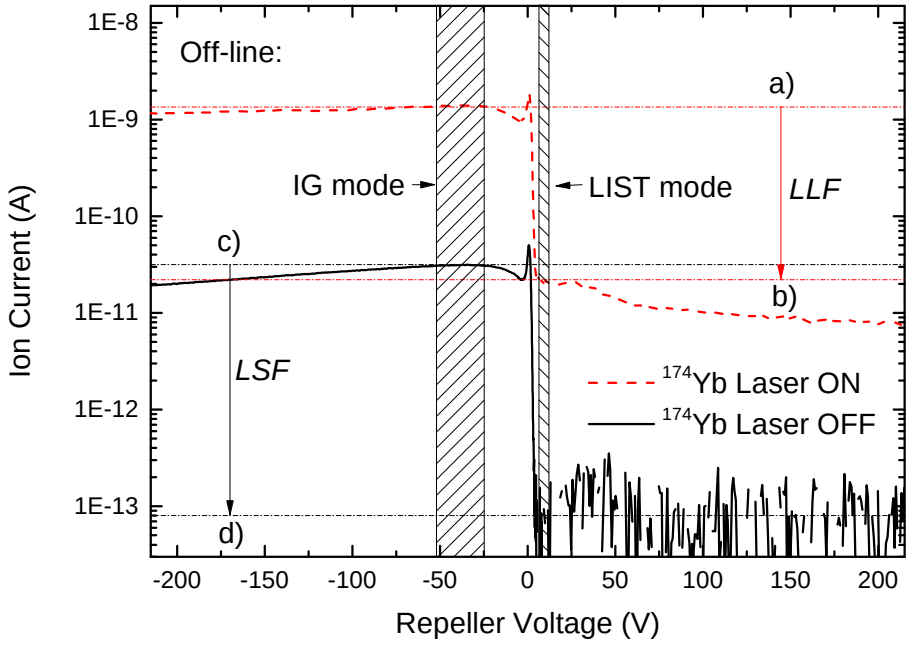

Figure 4.17: Ion current of laser ions (dashed red line, laser on) and surface ions (solid black line, laser off) of ^{174}Yb as a function of the repeller voltage, measured at the ISOLDE off-line separator with LIST 1. The hatched fields correspond to the repeller voltages for *ion guide mode* (IG) and *LIST mode*. The LIST loss factor, *LLF*, is indicated by the red arrow from the laser ion current in IG mode (a) and in *LIST mode* (b) and the LIST suppression factor, *LSF*, is indicated by the black arrow from the surface ion current in IG mode (c) and in *LIST mode* (d).

the level of contamination. However, in case of radioactive isotopes with low production yields a *repeller scan* is either impracticable or impossible. For these isotopes, the optimal LIST settings need to be extrapolated from the settings of stable isotopes.

4.3.2 Parameters of the LIST performance and measurement methods

The performance of the LIST can be characterized by five parameters: the *selectivity, S*, the *LIST suppression factor, LSF*, the *laser ionization efficiency* ϵ, the *LIST loss factor, LLF*, and the *LIST quality factor* LQF. Corresponding measurement methods, which were used throughout these experiments, are described when applicable.

Selectivity, *S*: The selectivity* is a measure of the purity of the ion beam and can be defined as:

$$S = \frac{\text{Ion intensity of isotope of interest}}{\text{Total ion intensity on the given mass of contaminants and isotope of interest}} . \tag{4.1}$$

*The selectivity has already been introduced in Equation 3.2 in Chapter 3 but is here given for completeness.

LIST suppression factor, *LSF*: The suppression in *LIST mode* can be described by the LIST suppression factor, *LSF*, which is given by:

$$LSF = \frac{\text{Ion intensity of contaminant in } \textit{ion guide mode}}{\text{Ion intensity of contaminant in } \textit{LIST mode}}. \tag{4.2}$$

If the ion intensity of the contaminant is above the detection limit of the Faraday cup, the LIST suppression factor can be determined by a *repeller scan* as demonstrated in Figure 4.17. It is calculated by comparing the maximum intensity in *ion guide mode* mode and the minimum intensity in *LIST mode*. For radioactive isotopes, for which a *repeller scan* is not easily achievable, the suppression factor is then derived by calculating the ratio between ion intensity in *ion guide mode* and in *LIST mode* using the predefined repeller settings for *LIST mode* and *ion guide mode*, which were obtained by extrapolation from the values of stable isotopes.
The *LSF* for ^{174}Yb, shown in Figure,4.17 has been determined to be ≈ 400 considering the background noise of 0.08 pA. Note that for this measurement, the Faraday cup noise was a lower limit and a measurement of the absolute *LSF* would require a detector with higher sensitivity (i.e. a SEM).

Laser ionization efficiency, ϵ_{ion}: The ionization efficiency, ϵ_{ion}, of an ion source can be defined as:

$$\epsilon_{\text{ion}} = \frac{\#\text{ atoms in sample ionized}}{\text{total }\#\text{ atoms in sample}}. \tag{4.3}$$

This is most reliably evaluated by measuring the integrated ion current after the total evaporation of a carefully calibrated sample of the element of interest. However, the absolute efficiency measurement is restricted to stable isotopes and is time consuming, which limits its applicability during on-line runs.

LIST loss factor, *LLF*: A more practical means of assessing the laser ionization efficiency of the LIST is to compare the *LIST mode* and *ion guide mode* ion intensity, using the predefined repeller voltage settings. The efficiency loss, *LLF*, due to the reduced atom/laser overlap in *LIST mode* is given by:

$$LLF = \frac{\text{Laser ion intensity in ion guide}}{\text{Laser ion intensity in } \textit{LIST mode}}. \tag{4.4}$$

As an example, Figure 4.17 shows a *LFF* value of ≈ 50 for ^{174}Yb with LIST 1.

LIST quality factor, *LQF*: Combining the LIST suppression factor, *LSF*, and the LIST loss factor, *LLF*, it is possible to characterize the LIST performance using the LIST quality factor, *LQF*, defined as:

$$LQF = \frac{LSF}{LLF}. \tag{4.5}$$

The value of *LQF* is intended as a guide to determine the typical LIST performance under standard conditions and is an important tool for comparing different LIST

units. For specific isotopes that suffer from poor isobaric suppression, due to isotope dependent sources of contamination, the target and LIST ion source assembly may be operated in non-standard conditions. In these cases, the LIST quality factor does not apply.
If the efficiency in *ion guide mode* is comparable to the efficiency of the normal RILIS operation, the LIST quality factor LQF is the gain in selectivity due to the use of the LIST compared to the RILIS.

4.3.3 Transmission through the RFQ ion guide

The RF amplitude at the rods, for which the transmission efficiency is highest, depends on the mass (see Chapter 3.5). This dependency was studied systematically at the ISOLDE off-line separator with several surface ionized isotopes, namely ^{23}Na, ^{40}Ca, ^{85}Rb and ^{133}Cs in *ion guide mode* with a repeller voltage settings of $U_{\mathrm{Rep}} = -43\,\mathrm{V}$. Laser ionized ^{174}Yb was studied in both, *LIST mode* and *ion guide mode* with repeller voltage settings of $U_{\mathrm{Rep}} = +7\,\mathrm{V}$ and $U_{\mathrm{Rep}} = -100\,\mathrm{V}$, respectively.
Figure 4.18 shows the normalized ion current of these isotopes as a function of the RF-amplitude obtained by LIST 2. In the left graph, the behavior of the surface ionized isotopes are shown. The transition curves of the different isotopes have similar shapes: a steep increase from $U_{\mathrm{RF}} = 0\,\mathrm{V_{pp}}$ to a mass-dependent maximum, from which the ion current slowly decreases to about a third of the maximum ion current and in case of the lightest studied isotope, ^{23}Na eventually drops to zero. This corresponds to the end of the stability diagram (see Figure 3.15 in Chapter 3.5). An approximate proportionality of the RF amplitudes for which the ion current is highest to the mass can be observed. For

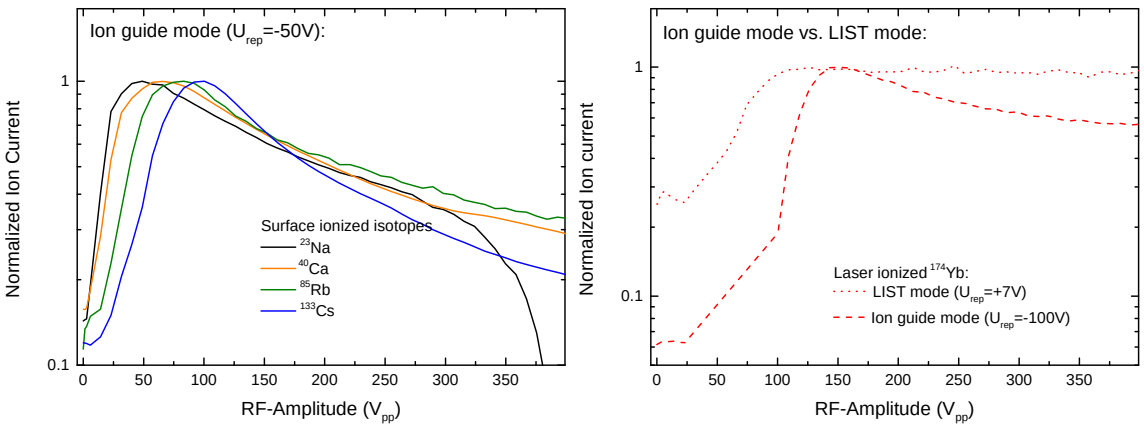

Figure 4.18: Measurements of the ion transmission through the LIST RFQ ion guide conducted at the ISOLDE off-line separator with LIST 2. The normalized ion current is given as a function of the RF voltage applied to the rods of the RFQ ion guide. Left: surface ionized ^{23}Na, ^{40}Ca, ^{85}Rb and ^{133}Cs in *ion guide mode* ($U_{\mathrm{rep}} = -50\,\mathrm{V}$).
Right: laser ionized ^{174}Yb in *LIST mode* ($U_{\mathrm{rep}} = +7\,\mathrm{V}$, dotted line) compared to *ion guide mode* ($U_{\mathrm{rep}} = -100\,\mathrm{V}$, dashed line).

the heavier of the studied isotopes, the available maximum RF-amplitude was not high enough to observe the limit of transmission. These curves clearly deviate from a transmission curve of an ideal RFQ ion guide, for which the ion current should remain stable over the full range of the stability diagram. The differences can be ascribed to the changes of the quadrupole potential compared to an ideal RFQ due to the finite and non-hyperbolic RF-rods and field disturbances due to the repeller voltage.
The difference in RF-amplitude dependence of laser ionized ^{174}Yb in *ion guide mode* and in *LIST mode* is shown in the right graph of Figure 4.18. In *ion guide mode*, the transmission curve is similar to the curves of the surface ionized ions. This is easily understandable since in *ion guide mode*, most atoms are ionized inside the hot cavity and the initial conditions of the ions are similar to those of the surface ionized isotopes. In contrast, the ion current in *LIST mode* remains constant for the full range of the applied RF-amplitudes after it reached its maximum ion current. This may be explained by the different initial conditions between ions created inside the hot cavity and inside the LIST RFQ and the different repeller voltage settings. The latter may also explain the disproportional shift of the maximum ion current between *LIST* and *ion guide mode*.
The dependency of the transmission through the LIST RFQ on the RF-amplitude, the repeller voltage and the mass of the ion therefore requires a careful determination of the optimal settings before studying the efficiency and performing any experiment. For radioactive isotopes, for which a scan of the RF-amplitude is difficult to perform, the optimal settings for the transmission through the RFQ need to be extrapolated from the values obtained with stable isotopes.

4.3.4 Surface ion suppression

Suppression: LIST 1

A *repeller scan* of ^{174}Yb measured off-line with the LIST 1 is shown in Figure 4.17 and revealed an *LSF* of about 400 (see Section 4.3.2). In contrast, Figure 4.19 shows a repeller scan, which was conducted for ^{48}Ti during the on-line test using LIST 1 in 2011. This measurement allowed the predefinition of the repeller voltages for *LIST mode* to $U_{\mathrm{rep}} = +7\,\mathrm{V}$ and for *ion guide mode* to $U_{\mathrm{rep}} = -50\,\mathrm{V}$. The overall suppression of ^{48}Ti was determined as $LSF = 4400$ by taking into account the Faraday cup background noise of $\approx 0.1\,\mathrm{pA}$. However, in contrast to the *repeller scan* of the surface ionized ^{174}Yb from Figure 4.17, the ion current increases for repeller voltages higher than the optimum LIST setting of $U_{\mathrm{rep}} = +7\,\mathrm{V}$ by more than one order of magnitude. A possible explanation of this is the poor vacuum condition related to the outgassing from the on-line target and electron impact ionization in this regime within the LIST structure.
Using the predefined repeller settings, ionization of radiogenic isotopes was studied using a tape station, which was equipped with a β- and γ-detector (see Chapter 3.4.1). For standard RILIS operation, a desired magnesium ion beam in this mass range may suffer from isobaric sodium and aluminum contamination. The suppression of the possible isobaric contaminants, ^{21,26}Na, was determined using the β-detector of the ISOLDE tape station, revealing a suppression of more than 3 orders of magnitude for both.

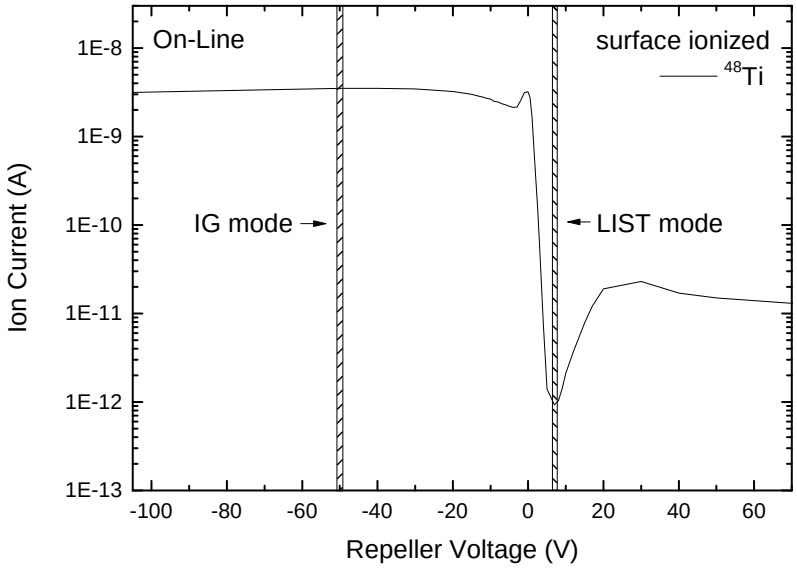

Figure 4.19: Surface ionized ^{48}Ti ion current as a function of the repeller voltage measured with LIST 1 under on-line conditions at ISOLDE. A suppression of 4400 is observed in *LIST mode* ($U_{rep} \approx 8\,V$) compared to *ion guide mode* ($U_{rep} \approx -50\,V$) with a strong increase of interfering contamination for a higher positive repeller potential.

An overview of the *LSF* of the studied isotopes obtained by the LIST is given in Table 4.1. For most isotopes, namely ^{21}Na, ^{23}Na, ^{26}Na, ^{48}Ti (off-line), and ^{174}Yb, the measurement of the actual LIST suppression factor was not possible since the ion intensity in *LIST mode* was indistinguishable from the background level of the detectors. In these cases, a lower limit for the suppression factor was calculated as the ion rate in *ion guide mode* divided by the statistical uncertainty $\sqrt{N}$ of the background measurement. However, this does not apply to ^{39}K, for which the absolute suppression factor was determined to only $LSF = 230$. In this case, the reduced suppression factor can be ascribed to additional ionization effects such as electron impact ionization as described above for ^{48}Ti. These isotope specific reductions of the *LSF* will be discussed in the next session in more detail. Using the individually determined *LSFs* from above, a conservative general value of $LSF > 1000$ can be expected.

Suppression: LIST 2

Figure 4.20 shows wide range mass scans for $20\,u < m < 75\,u$ and $125\,u < m < 180\,u$ taken at the off-line separator with LIST 2. The upper graph shows a mass scan in *ion guide mode* and the lower graph shows a mass scan in *LIST mode*. In *ion guide mode*, ^{23}Na, ^{27}Al, ^{39,41}K, ^{40}Ca, $^{46-50}$Ti, ^{52,53}Cr, ^{69,71}Ga, ^{133}Cs, $^{134-138}$Ba, and $^{168,170-174,176}$Yb are observed as well as titanium oxide (TiO) and some unidentified molecular ion beams in the mass region of 34 u to 45 u. In *LIST mode* only the alkaline elements sodium, potassium, cesium, and a reduced molecular ion signal around 34 u remain above the detection limit of the Faraday cup.

The reduced suppression factor for these ions can only be explained if one considers ionization mechanisms other than surface ionization, i.e. via electron impact. In agreement with the results from the studies with LIST 1, it appears that this effect is only observed if a large deposit of these atoms has condensed on the cold structures downstream of the hot cavity and is therefore enhanced by the extensive outgassing of the target in the initial conditioning phase or by contamination of the structures during production and assembly. The absence of this effect for radioactive alkaline isotopes supports this explanation.
Light radioactive isotopes with masses between 26 u and 46 u were measured by the β-detector of the tape station during the on-line run in 2012. Figure 4.21 shows the ion yields from β-decay of the surface ionized ^{26}Na and ^{46}K and laser ionized ^{30}Mg as a function of the repeller voltages. In *ion guide mode* ($U_{\mathrm{Rep}} = -50\,\mathrm{V}$), the surface ion rate is high, while in *LIST mode* ($U_{\mathrm{Rep}} = +7\,\mathrm{V}$), the ion rate drops by more than 3 orders of magnitude in case of ^{46}K and by more than four orders of magnitude in case of ^{26}Na and eventually falls below the detection limit. In contrast to the reduced suppression of stable sodium and potassium in the mass scans shown in Figure 4.20, the obtained suppression of ^{26}Na and ^{46}K of 3 to 4 orders of magnitude do agree well with the results obtained on-line for the LIST 1. The lower *LSF* for ^{30}Na of only 130 can be ascribed to the yield of this isotope and the high background measured by the β-detectors of the tape station during this measurement rather than a secondary ionization effect. The exact values of the ion intensities in *LIST* and *ion guide mode* and LIST suppression factors are given in Table 4.1.
For radioactive isotopes in the high mass range above 212 u, the suppression of francium isotopes was studied. These possible contaminants in RILIS ionized polonium ion beams were studied using the α-detector setup of the Windmill system from KU Leuven (see

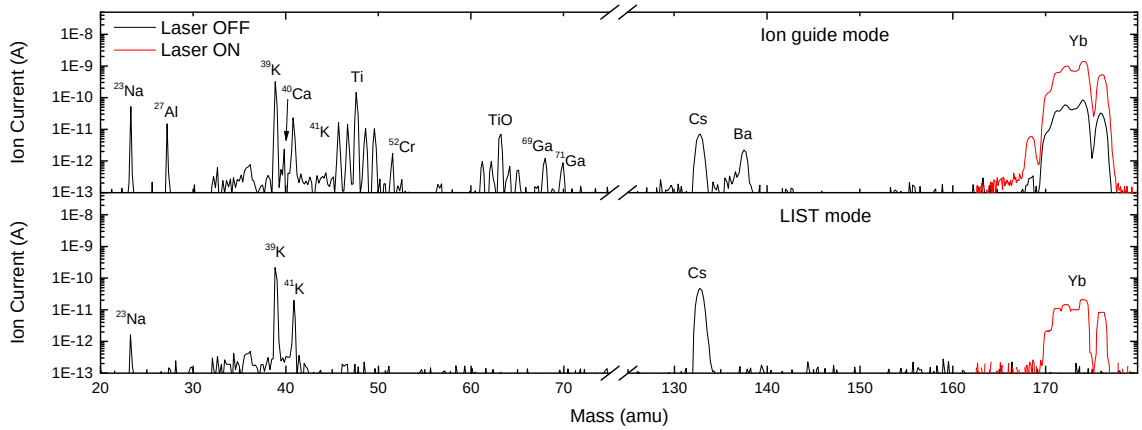

Figure 4.20: Wide range mass scans taken at the off-line separator with LIST 2 for 20 u $< m <$ 75 u and 125 u $< m <$ 180 u, in *ion guide mode* (upper graph) and *LIST mode* (lower graph). Surface ionized isotopes are suppressed to the noise level of the Faraday cup, except for the alkaline elements, which are assumed to be ionized by electron impact ionization behind the repeller. Laser ionized ytterbium (Yb) is visible in *LIST mode* with a loss factor of ≈ 50 with respect to *ion guide mode*.

Table 4.1: Ion intensities in *ion guide mode* and *LIST mode* and LIST suppression factors (*LSF*) of several stable and radioactive isotopes obtained by using LIST 1 (off-line, on-line) and LIST 2 (on-line). Half-lives of radioactive isotopes are given in brackets. Stable isotopes as well as ^{220}Fr were measured by a Faraday cup (FC) and ion intensities are given in pA. β-emitters were measured with the tape station (TS) and ion intensities are given in counts per µC protons, while α-emitters were measured by the α-detectors of the Windmill setup and ion intensities are given in counts / supercycle. If the ion intensity was below the background (bgnd) level of the Faraday cup detector system, a conservative value of the LIST ion intensity was estimated from the background fluctuations in case of the Faraday cup or the statistical uncertainty ($\sqrt{N}$, given in brackets) of the α or β counts. Values are implied with their significant numbers.

Isotope	**Detector**	$\mathbf{I_{IG}}$	$\mathbf{I_{LIST}}$	***bgnd***	**unit**	***LSF***
LIST 1						
Off-line						
^{23}Na	FC	75	0.4	0.08	pA	230
^{48}Ti	FC	145	0.08	0.08	pA	$\geq$ 1800
^{174}Yb	FC	3.15	0.08	0.08	pA	$\geq$ 300
On-line						
^{21}Na$_{(22.5\,\mathrm{s})}$	TS	$16000 \cdot 10^5$	100	100(10)	counts/µC	$\geq 1.6 \cdot 10^4$
^{23}Na	FC	85	0.4	0.1	pA	280
^{26}Na$_{(1.07\,\mathrm{s})}$	TS	$3900 \cdot 10^4$	100	100(10)	counts/µC	$\geq 3.9 \cdot 10^3$
^{39}K	FC	410	2	0.1	pA	230
^{48}Ti	FC	3500	0.9	0.1	pA	4400
LIST 2						
On-line						
^{26}Na$_{(1.07\,\mathrm{s})}$	TS	75000	50	50(7)	counts/µC	$\geq$ 10700
^{30}Na$_{(48\,\mathrm{ms})}$	TS	1437	125	125(11)	counts/µC	$\geq$ 130
^{46}K$_{(105\,\mathrm{s})}$	TS	13000	50	50(7)	counts/µC	$\geq$ 1850
^{205}Fr$_{(3.97\,\mathrm{s})}$	WM	63520	25	0	counts / supercycle	2540
^{212}Fr$_{(20.0\,\mathrm{min})}$	FC	80	2	0.85	pA	70
^{220}Fr$_{(27.4\,\mathrm{s})}$	WM	15379	412	412(20)	counts / supercycle	$\geq$ 770

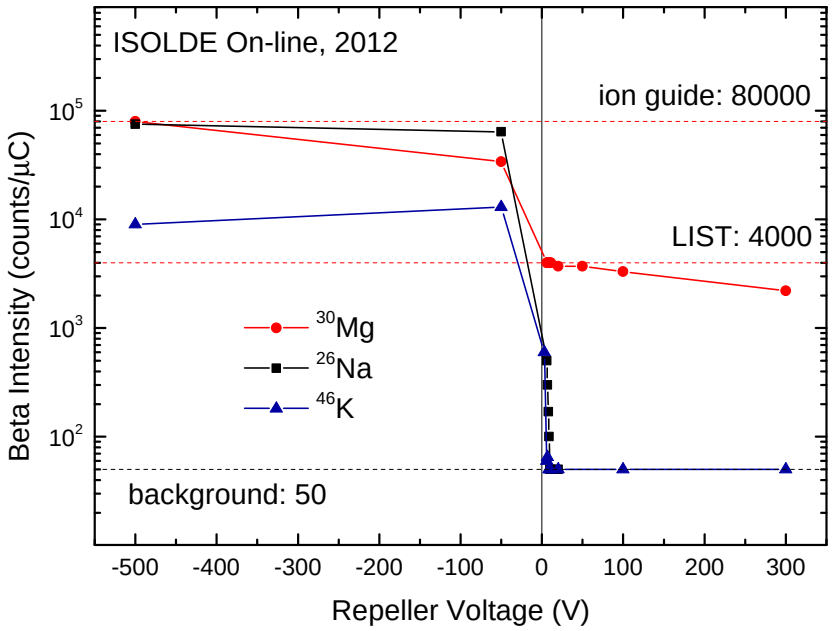

Figure 4.21: Ion rates of surface ionized ^{26}Na and ^{46}K and laser ionized ^{30}Mg as a function of the repeller voltage of the LIST 2 measured on-line at ISOLDE using a tape station. The background level was 50 counts per 1μC proton irradiation. If *LIST mode* is applied, the surface ion intensity drops below the detection limit, while the intensity of the laser ionized ions drops only by a factor of 20.

Chapter 3.4.1). Table 4.1 lists the results for the studied isotopes. While the LIST suppression factors of ^{205}Fr and ^{220}Fr agree well with the *LSFs* obtained for the lighter masses, an *LSF* of only 70 was measured for ^{212}Fr. Since the *LIST mode* ^{212}Fr intensity was above the α-detection limit, the low *LSF* for this particular francium isotope indicates that there is an isotope dependent ionization mechanism.
A suggested explanation is the presence of the ^{212}Fr ions inside the LIST RFQ ion guide due to the radioactive decay of precursors that have passed the repeller electrode as neutral atoms and condensed on the relatively cold structures of the LIST. In the case of ^{212}Fr, neutral ^{212}Ra is a possible predecessor, which may have decayed by β^+ decay (15% branching ratio) on the RF-rods inside the LIST RFQ. Also observed were weak, but detectable, ion beams of ^{216}At and ^{217}Rn which, due to their short half-lives ($<$ 1 ms), cannot be direct in-target reaction products, but similar to the case of ^{212}Fr be produced by the decay from precursors at the RFQ rods. The α-spectra of these isotopes and possible corresponding production mechanisms will be discussed in Chapter 7.4.1.
In summary, an absolute *LSF* measurement was only possible for ^{26}Na (10700), ^{205}Fr (2540) and ^{212}Fr (70). However, in the absence of secondary ionization mechanisms a minimum *LSF* of 1000 is obtained for LIST 2. This is similar to the results obtained by LIST 1, meaning that the repeller electrode of LIST 2, with a reduced distance of the repeller to the hot cavity of 2.5 mm, suppresses surface ions with the same efficiency as the repeller electrode of the LIST 1, with a distance of 5 mm.

4.3.5 Laser ionization efficiency

Laser ionization efficiency: LIST 1

At the off-line separator, the LIST 1 loss factor for ^{174}Yb was determined to be $LSF = 50$ by the *repeller scan* shown in Figure 4.17 and as it was discussed in Section 4.3.2.
For determination of the absolute laser ionization efficiency of ^{174}Yb in *LIST* and *ion guide mode* a calibrated mass marker of $6.9 \cdot 10^{14}$ atoms of natural ytterbium was used. Taking into account the 31.8 % abundance of ^{178}Yb, this corresponds to an atomic sample of ^{174}Yb of $2.2 \cdot 10^{14}$ atoms, or a maximum (100% efficient ionization) integrated ion current of 10 nAh. Figure 4.22 shows the ^{174}Yb ion current in *LIST mode* during the efficiency measurement as a function of time. The atoms were evaporated during a period of approximately 4 hours by stepwise increasing the mass marker temperature. The steps and spikes in the data-set correspond to occasional blocking of the lasers for background determination as well as for switching from *LIST* to *ion guide mode* for verifying the stability of the LIST's performance during the measurement.
The LIST 1 ionization efficiency was calculated by interpolating the ion current over the periods, when the LIST was in *ion guide mode* or when the lasers were blocked for background measurements. A total number of $4.4 \cdot 10^{11}$ was then compared to the original sample size to give a *LIST mode* ionization efficiency of $\epsilon_{\mathrm{LIST}} = 0.2\,\%$. This is about twice as high as obtained in previous studies on gallium at the RISIKO off-line separator in Mainz [151]. Multiplying by the LIST loss factor of $LLF = 50$ as extracted from Figure 4.22, the efficiency in *ion guide mode* reaches $\epsilon_{\mathrm{IG}} = 10\,\%$, which is in good agreement with the efficiency typically obtained for standard RILIS operation.
For verification, a similar procedure was implemented into the on-line test measurements of LIST 1 for the determination of the overall LIST ionization efficiency. A calibrated sample of $2.47 \cdot 10^{16}$ atoms of the stable magnesium (1100 nAh singly ionized ion current at 100% 1+ ionization efficiency) was released during a period of about 12 hours. Figure 4.23 shows the ^{24}Mg ion current as a function of time with the measurement predominantly performed in *ion guide mode*. Occasional measurements in *LIST mode* are visible in Figure 4.23 as sharp drops in the ion signal corresponding to the LLF. The measurement had to be stopped before the sample was fully evaporated due to time constraints. The gaps in the data-set correspond to the use of the ion beam by another experiment. To evaluate the integrated ion current, the latter was interpolated between the periods of data taking, once again with the assumption of an exponential decline of the ion rate with time.
1.5 hours at the start of the measurement, were required to optimize the lasers and the data acquisition system and data could not be taken. Therefore, the ion current was extrapolated by an exponential decay to the start of the measurement. In addition, a conservative extrapolation of the starting ion rate was made using a constant ion rate, which corresponds to the initially measured maximum value. The extrapolation beyond the measurement time was omitted. In this way, a lower limit of the ionization efficiency is $\epsilon_{\mathrm{IG}} = 2.5\,\%$ in *ion guide* and $\epsilon_{\mathrm{LIST}} = 0.08\,\%$ in *LIST mode*.
The fitted exponential decay curves depended on the background level. From the measured ion currents and the fitted curves it seems that the ion current does not drop to the background level of the Faraday cup. This excess is most likely due to atoms, which

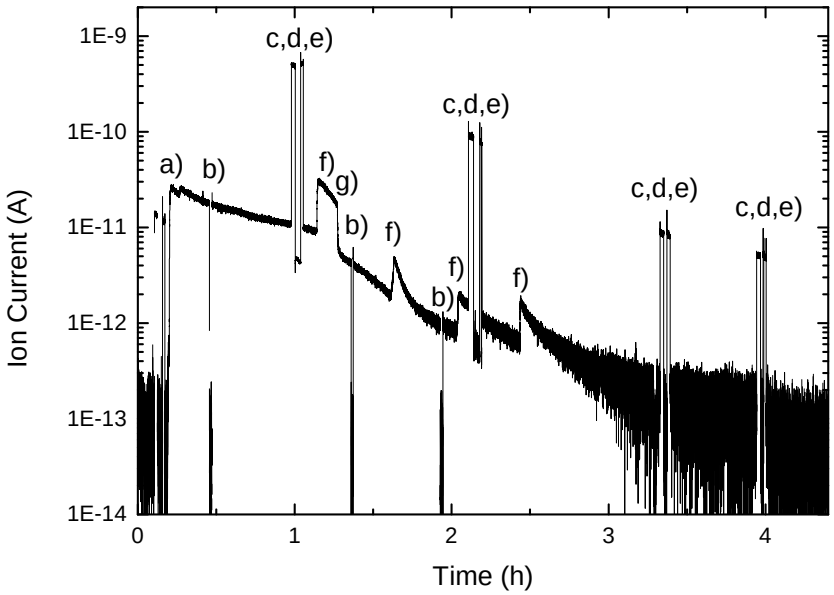

Figure 4.22: LIST 1 laser ionization efficiency measurement of a Yb-sample by full sample evaporation during 4 hours. The steps visible in the trace are due to the following actions: a) initial temperature increase of mass marker, b) laser blocking for Faraday cup background determination, c) switching to ion-guide mode for comparison, d) laser blocking in *ion guide mode* for surface ion background determination, e) return to *LIST mode*, f) mass marker temperature increase and g) intentional mass marker temperature decrease for test of reproducibility.

accumulated at a cold spot inside the target assembly. For the determination of the exponential decay curves of the ion current, the background levels were kept fixed for *LIST mode* and *ion guide mode* at 2.4 pA and 140 pA, respectively. These background ions do stem from the same sample and may explain the reduced laser ionization efficiency of magnesium obtained on-line, when compared to the laser ionization efficiency measurement of ytterbium at the ISOLDE off-line mass separator.
In Figure 4.23, a slight dependence of the loss factor on the ion current is evident with lower LIST loss factors of typically $LLF_1 = 33(1)$, measured for ion currents of almost 10 nA that were reached at the start of the measurement in *ion guide mode*. This is significantly smaller than the typical LIST loss factor, whereas later, when the ion current had reduced to below 1nA, a $LLF = 51(1)$ was measured. The evolution of the loss factor is documented in Table 4.2, with values corresponding to the LIST loss factors, LLF_1 to LLF_4, illustrated in Figure 4.23.
This is attributed to space charge effects that occur when the ion load in the hot cavity is high [89]. In this case, the laser ion density starts to screen the penetrating extraction voltage of the repeller electrode as well as the guiding RF field and reduces the ion transport accordingly. A reduction of the laser ionization efficiency is only observed in *ion guide mode*. In the case of high ion current, the obtained LIST loss factors are therefore unreliable. Correspondingly, the extracting negative repeller voltage should be chosen as

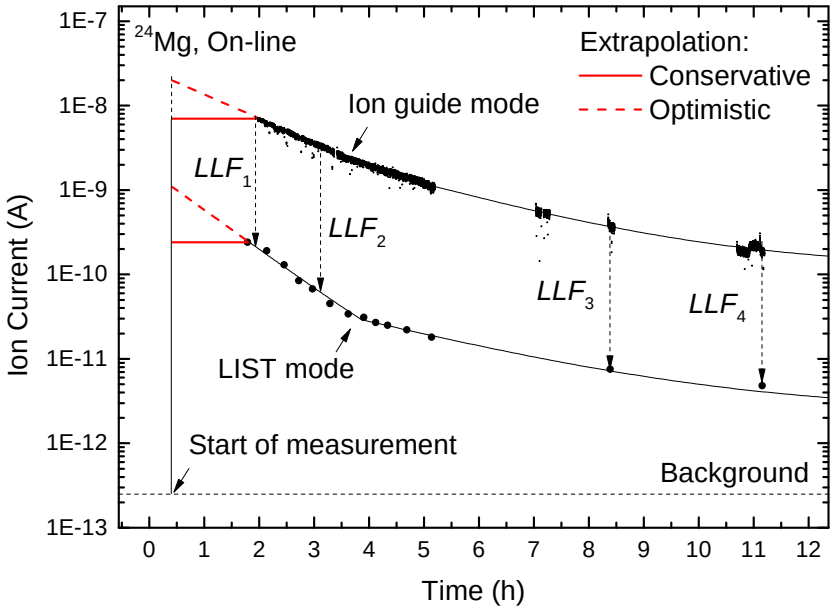

Figure 4.23: On-line measurement of the LIST 1 laser ionization efficiency in *ion guide mode* and *LIST mode* using a 0.11 µg sample of natural magnesium. The sample was evaporated over 12 h. Four different LIST loss factors, LLF_1 to LLF_4, were extracted at different times of the measurement and are listed in Table 4.2.

high as possible for efficient *ion guide mode* operation. This also applies in the case of a high ion load inside the cavity due to surface ionization and needs to be considered for the operation in *ion guide mode*.

Laser ionization efficiency: LIST 2

During the on-line run in 2012, the LIST loss factors of LIST 2 were measured with magnesium and polonium. As shown in the *repeller scan* of Figure 4.21, the laser ionized ^{30}Mg beam intensity drops only by an *LLF* of 20(1) from *ion guide mode* to *LIST mode*.
The ion intensity of laser ionized ^{208}Po was measured by the α-detectors of the KU Windmill for two different values of proton intensity: 0.3 μA and 1.1 μA. The LIST loss factor for ^{208}Po dropped from 10(1) to 4(1) at the higher proton current. This reduction can be explained similarly to the reduced loss factors obtained with ^{24}Mg observed for LIST 1 due to the reduced laser ionization efficiency in *ion guide mode* when there is a high ion load inside the hot cavity. Following these arguments, also the LIST loss factor of 10(1) is unreliable, when compared to the *LLF* of magnesium. Therefore, the LIST loss factor of the LIST 2 is conservatively estimated to $LFF \approx 20$, which corresponds to the value obtained for magnesium.
The measurement of the absolute laser ionization efficiency of the LIST 2 by the evaporation of a calibrated mass marker was not possible due to time constraints during the off-line preparatory tests and during the on-line run.

Table 4.2: LIST loss factors *LLFs* and laser ionization efficiencies ϵ measured for with LIST 1 and LIST 2. Ion intensities in *LIST* and *ion guide mode*, which were used for the calculation of the *LLFs* together with the detector type and the background levels are given. Half-lives of radioactive isotopes are noted next to the isotopes in brackets. ^{24}Mg, ^{174}Yb and ^{208}Po were measured with the Faraday cup (FC) ^{30}Mg with the tape station (TS) and results are given in pA and counts/μC, respectively. The four LIST suppression factors (LLF_1 to LLF_4) correspond to the LIST suppression factors, *LSFs*, illustrated in Figure 4.23. The proton intensities (I_p) for the the two ^{208}Po measurements are listed in the left column. Values are implied with their significant numbers.

Isotope	**Detector**	$\mathbf{I_{IG}}$	$\mathbf{I_{LIST}}$	***bgnd***	**unit**	***LLF***	$\boldsymbol{\epsilon_{IG}/\epsilon_{LIST}}$
LIST 1							
Off-line							
^{174}Yb	FC	1280	25	0.1	pA	51	10 / 0.2
On-line							
^{23}Mg$_{(11.3\,s)}$	TS	$1.0 \cdot 10^6$	$3.5 \cdot 10^3$	100	counts/μC	294	-
^{24}Mg	FC			0.1	pA		$\geq 2.5 / \geq 0.08$
LLF_1		7200	220			33	
LLF_2		3200	75			43	
LLF_3		360	7.4			49	
LLF_4		250	4.9			51	
^{27}Mg$_{(9.46\,min)}$	TS	$2.5 \cdot 10^6$	$4.5 \cdot 10^4$	100	counts/μC	56	-
LIST 2							
On-line							
^{30}Mg$_{(335\,ms)}$	TS	80000	4000	50		20	-
^{208}Po$_{(2.898\,y)}$	FC			-0.1	pA		-
I_p=0.3 μA		3	0.2			10	
I_p=1.1 μA		3	0.6			4	

Laser ionization efficiency: discussion

In total, absolute ionization efficiencies were determined for ^{24}Mg and ^{174}Yb and LIST loss factors were measured for ^{23,24,27}Mg, ^{174}Yb and ^{208}Po and the results are summarized in Table 4.2.
The absolute laser ionization efficiency of $\approx 10\,\%$ of ^{174}Yb in *ion guide mode* obtained at the off-line separator agrees with the expectation for a standard RILIS mode ionization efficiency. The slightly lower ionization efficiency for ^{24}Mg obtained on-line can be explained by the inability to completely evaporate the sample during the limited available measurement time. A series of ionization efficiency measurements is necessary to improve the statistics, but unfortunately, the scheduling restrictions of the testing facilities make this impractical and an increase of the reliance is based on regular checks of the LIST loss factor.
The results indicate that under optimal conditions and at low ion currents, the *ion guide efficiency* is comparable with the efficiency of the normal RILIS operation ($\approx 10\,\%$) and thus, the LIST loss factor can be also applied to compare the efficiency of the selective *LIST mode* to normal LIST operation.
The loss in *ion guide mode* efficiency at high ion loads is regained by increasing the extraction voltage, which is currently limited to $U_{rep} = -500\,V$ or by optimizing the design of the repeller electrode.
The LIST loss factors for lower ion currents were of the order of 50 for LIST 1 and around only 20 for LIST 2. The improvement can be ascribed to the reduced distance of the LIST 2 repeller electrode to the hot cavity of only 2.5 mm, which leads to an improved spatial overlap of the lasers and the free atoms inside the LIST RFQ. The overall efficiency of the LIST would benefit, if the distance of the repeller electrode to the hot cavity could be reduced further.

4.3.6 Selectivity

The LIST selectivity, defined in Equation (4.1), is difficult to determine exactly since it requires the simultaneous measurement of the ion intensities of the isotope of interest and the contaminant. A suitable pair of isotopes and corresponding detection system was not available during the on-line tests described here. Instead it was possible to assess the performance of each LIST using the LIST quality factor, defined in Equation (4.5), assuming that the *ion guide mode* efficiency is comparable to normal RILIS operation.
Table 4.3 summarizes the LIST parameters obtained in standard operation. The minimum LIST quality factor of LIST 1 is $LQF = 88$ and of LIST 2 is $LQF = 127$. These values were calculated by taking into account the absolute LIST suppression factor and the typical LIST loss factors. The results indicate that the selectivity was increased due to the improved laser ionization efficiency of the LIST 2.
However, the limited detection efficiency and high background levels made it difficult to determine the absolute suppression factor for some isotopes. Following the LIST suppression factors of at least 4 orders of magnitude in the case of ^{26}Na, a maximum LIST quality factor of the order of more than 200 can be expected with the LIST 1 and more than 500 with the LIST 2.

Table 4.3: Comparison of the different LIST parameters obtained on-line by LIST and LIST 2: minimum suppression factor ($LSF_{\mathbf{min}}$), maximum LIST loss factor ($LSF_{\mathbf{max}}$), representative LIST loss factor LLF, and corresponding minimum and maximum LIST quality factors ($LQF_{\mathbf{min}}$ and $LQF_{\mathbf{max}}$) are given. Values are implied with their significant numbers.

LIST	$\boldsymbol{LSF}_{\mathbf{min}}$	$\boldsymbol{LSF}_{\mathbf{max}}$	$\boldsymbol{LLF}$	$\boldsymbol{LQF}_{\mathbf{min}}$	$\boldsymbol{LQF}_{\mathbf{max}}$
LIST 1	4400	≥ 10000	50	88	≥ 200
LIST 2	2540	≥ 10000	20	127	≥ 500

4.3.7 Comparison of lineshapes of resonances obtained in LIST mode, ion guide mode and normal RILIS operation

The LIST is an important option for resonance ionization spectroscopy (RIS) (see Chapter 7). Any differences in terms of line-shape (width, asymmetry) and center frequencies of the observed atomic lines compared to those measured during in-source RIS in standard hot-cavity *RILIS mode* need to be examined. Therefore, several measurements of the resonance profile of the second step transition for ^{208}Po, which were taken during the experiments, were compared retrospectively. The profiles were obtained by scanning the

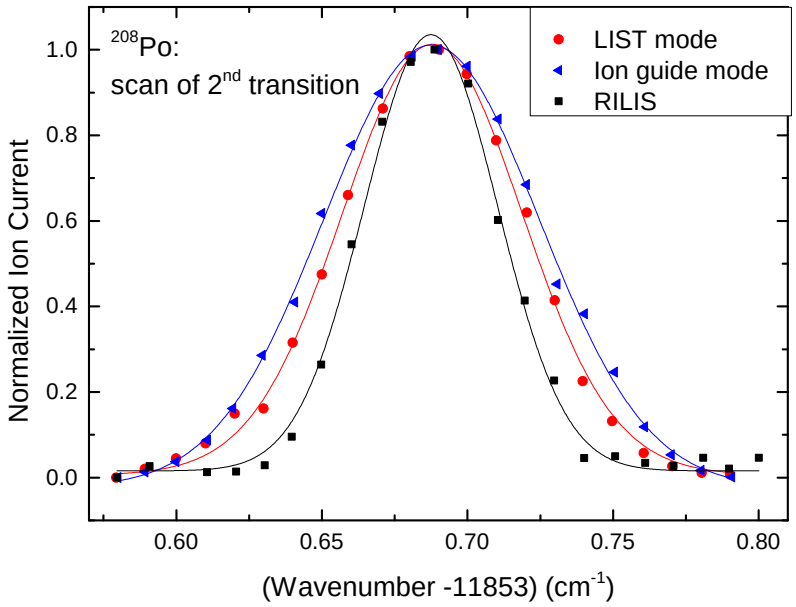

Figure 4.24: Comparison of the resonances of the second intermediate step of the polonium (Po) scheme (50934.89 cm^{-1}, $6p^3(^4S^\circ)7p$) obtained in *LIST mode*, *ion guide mode* and in *standard RILIS mode*, respectively. The transition was scanned by tuning a narrow band Ti:Sa laser across the resonance and fitted by a Voigt profile. Ion intensities were normalized for better comparison.

NB Ti:Sa laser (about 1 GHz linewidth, *WS7* wavemeter) for several operating modes: LIST 2 in *ion guide mode* (2 scans), LIST 2 in *LIST mode* (3 scans) and *standard RILIS mode* (4 scans during the measurement of the ionization potential of polonium during the following run at the HRS target. See Chapter 6.1). The laser power for the spectroscopic transition was attenuated to reduce the degree of saturation broadening.
The left graph in Figure 4.24 shows one of these resonances for each of the different modes of operation, *LIST mode*, *ion guide mode* and *standard RILIS mode*. By trend, it seems that the width of the resonance in normal RILIS operation ($FWHM = 0.053\,\mathrm{cm}^{-1} = 1.59\,\mathrm{GHz}$) is slightly narrower than in *LIST mode* ($FWHM = 0.073\,\mathrm{cm}^{-1} = 2.19\,\mathrm{GHz}$) and in *ion guide mode* ($FWHM = 0.086\,\mathrm{cm}^{-1} = 2.58\,\mathrm{GHz}$). In addition, no significant asymmetry nor shift in the frequency was obtained within the standard uncertainty of the wavemeter of $0.2\,\mathrm{cm}^{-1}$, but it is difficult to make conclusions about the comparison of the line widths and the centroid positions, since the measurement conditions (saturation, target temperature) were different. A more reliable comparison would require more statistics and better target control and is therefore best performed at an off-line separator facility.

4.3.8 Time structure of LIST ion bunches

The measurement of the time-structure of a pulsed ion source is an ideal probe for the understanding of the ionization process. The time-structure of the LIST bunches of laser ionized ^{24}Mg was measured during the first on-line run with the LIST 1. An MCP detector was installed about 18 m downstream within the ISOLDE beam line and the data was taken by a *Teledyne LeCroy Waverunner 104 Mxi scope*, which was synchronized to the 10 kHz laser pulses of the Nd:YAG pump laser. The time of flight was then measured with respect to the laser pulses for several seconds to provide enough statistics.
The time structure was measured for several positive repeller voltages, spanning the typical operation range of the LIST, namely 7 V, 10 V, 20 V, 30 V, 40 V, 70 V, 100 V, 120 V and 200 V. Figure 4.25 depicts the time structure for repeller voltages of 7 V, 10 V and 40 V. Three distinct structures are visible in each spectra:

Peak (A): a narrow, repeller-voltage independent peak at 29.725 µs.

Peak (B): an intense peak with a repeller voltage dependent position and width.

Tail (C): the long, flat tail of peak (B) for which the substructure is slightly dependent on the repeller voltage.

The width of peak (B) decreases from 3.43(7) µs for a repeller voltage of 7 V to 1.56(5) µs and 0.37(3) µs for a repeller voltage of 10 V and 40 V, respectively. For the maximum repeller voltage of 200 V the FWHM gets as small as 0.08(1) µs.
In order to understand the different features observed in Figure 4.25, the time structure of the LIST ion bunches was calculated . The following section discusses the mathematical model that was used for the calculations and the results will be discussed and compared to the experimental results in the last subsection.

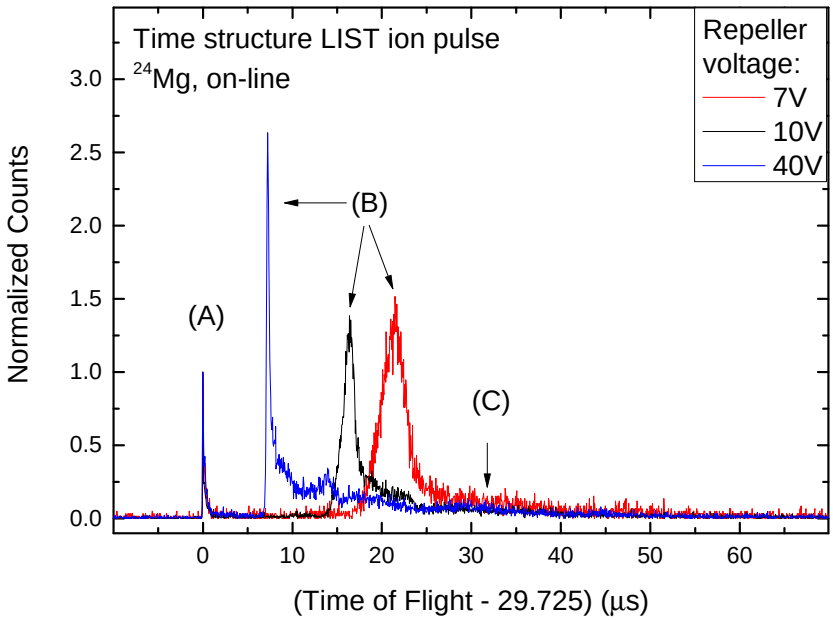

Figure 4.25: Time structure of LIST ion bunches of laser ionized ^{24}Mg for repeller voltages, 7 V (red line), 10 V (black line) and 40 V (blue line). Three distinct features are visible within each spectra: (A), a narrow, repeller-voltage independent peak; (B) a broader, more intense, repeller-voltage dependent peak; (C), the tail towards longer flight times. The time of flight is given with respect to peak (A) at 29.725 µs.

A model for the calculation of the LIST time structure

Prior to this work, simulations were performed using Monte-Carlo methods and the ion-tracking software SIMION© [150, 163]. For the work described in this thesis, a complementary approach was used that calculates the time of flight for ions with different initial conditions (position z_0, thermal velocity v_0) alongside the longitudinal potential inside the LIST. The potential was simulated by the *Charged Particle Optics*© (CPO©) software, a software for the accurate simulation of electrostatic potentials of ion optical elements using the *Boundary Element Method* [138]. For simplicity, the time-dependent potential of the RF-rods was not considered during the simulations. In turn, the calculation of the time of flights of the ions was implemented into a code that was written in the *Python* programming language. Figure 4.26 shows the overall shape of the calculated longitudinal potential for repeller voltages of 7 V and 40 V. Additional calculations were performed for repeller voltages of $U_{\mathrm{rep}} = 10$ V, 100 V and 200 V, which showed a similar behaviour.
For the calculation of the time of flights, the potential was approximated by purely empirical functions. Their purpose were merely to give an estimation of the longitudinal potential gradient inside the LIST that can be implemented into the calculations. Several different functions, e.g. exponential functions and polynomials, were tested. The best results for the description of the asymmetric shape of the potential close to the repeller electrode were obtained by hyperbolic tangent functions that were shifted to $z = 0$ and normalized to the calculated effective repeller voltage at $z = 0$ mm, $U_0(U_{\mathrm{rep}})$. The drop of

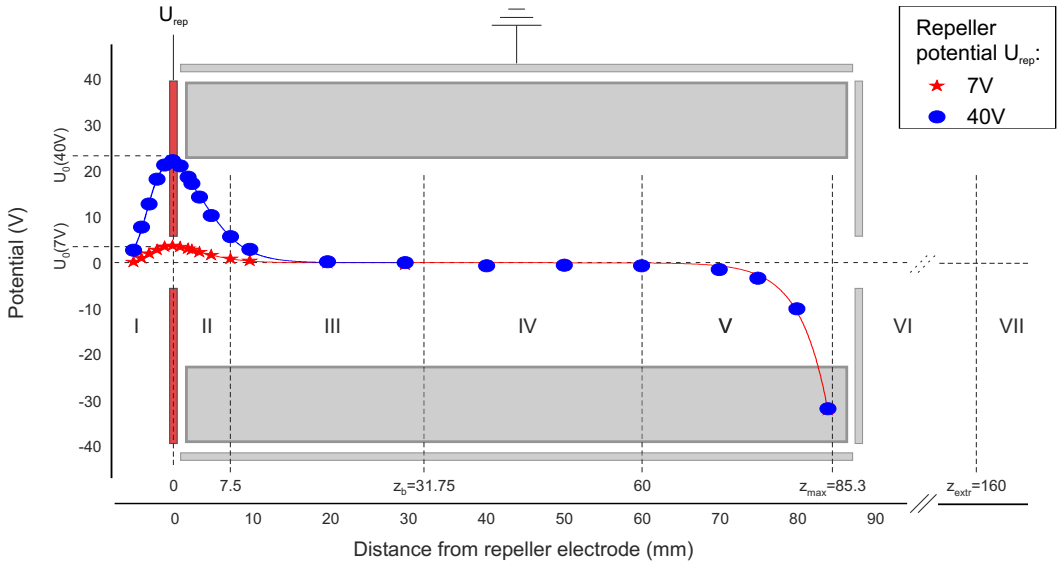

Figure 4.26: Longitudinal potential inside the LIST cavity as a function of the distance to the repeller electrode calculated by the CPO© program. Ranges on the longitudinal axis, which are discussed in the text, are indicated by the Roman numbers. The potential defined by Equation (4.6) is fitted to the simulated data

the potential close to the exit of the LIST could be approximated by an exponential function. The potential drop from $U = -50\,\mathrm{V}$ at $z_{\mathrm{max}} = -85.3\,\mathrm{mm}$ to the extraction electrode was approximated by a linear function and the potential behind the extraction electrode was assumed to be constant. The functions that were fitted to the repeller potentials of $U_{\mathrm{rep}} = 7\,\mathrm{V}$, $10\,\mathrm{V}$, $40\,\mathrm{V}$, $100\,\mathrm{V}$ and $200\,\mathrm{V}$ and that were used for the calculations are:

$$U(z) = \begin{cases} \dfrac{U_0(U_{\mathrm{rep}})}{1+\tanh(a)} \cdot (1+\tanh(b\cdot z+a)) & \text{for } z < 0 \\ \dfrac{U_0(U_{\mathrm{rep}})}{1+\tanh(c)} \cdot (1-\tanh(d\cdot z+c)) - B\cdot\exp(e\cdot(x-x_{\mathrm{b}})) & \text{for } 0 \le z < z_{\mathrm{max}} \\ U(z_{\mathrm{max}}) + (x-z_{\mathrm{max}}) \cdot \dfrac{U_{\mathrm{extr}}}{z_{\mathrm{extr}}-z_{\mathrm{max}}} & \text{for } z_{\mathrm{max}} \le z < z_{\mathrm{extr}} \\ U_{\mathrm{extr}} & \text{for } z > z_{\mathrm{extr}}\,, \end{cases} \tag{4.6}$$

where $z_{\mathrm{b}} = 31.75\,\mathrm{mm}$ is the position at which the potential drops to $0\,\mathrm{V}$, $z_{\mathrm{max}} = 85.3\,\mathrm{mm}$ is the position at which the potential reaches $-50\,\mathrm{V}$ and $z_{\mathrm{extr}} = 160\,\mathrm{mm}$ is the position of the extraction electrode operated at $U_{\mathrm{extr}} = -50\,\mathrm{kV}$ (see Figure 4.26 for an illustration). Only the effective repeller potential at $z = 0$, $U_0(U_{\mathrm{rep}})$, depends on the applied repeller voltage and this dependency was obtained by a linear fit to the $U_0(U_{\mathrm{rep}})$ for each repeller voltage:

$$U_0(U_{\mathrm{rep}}) = 0.575(1) \cdot U_{\mathrm{rep}}\,. \tag{4.7}$$

The constant parameters $a = 1.775$, $b = 0.565\,\mathrm{mm}^{-1}$, $c = 0.650$, $d = 0.185\,\mathrm{mm}^{-1}$, $e = 0.400\,\mathrm{mm}^{-1}$ and $B = 1.872{\cdot}10^{-8}\,\mathrm{V}$ are the averaged parameters of the fits of Equation (4.6) to the potential gradients of the different repeller voltages. Overall, the fits describe the longitudinal potential well and the representative fits to the repeller voltages of $U_{\mathrm{rep}} = 7\,\mathrm{V}$ and $U_{\mathrm{rep}} = 40\mathrm{V}$ are shown in Figure 4.26.
A simplified model of the atomic beam was used, where the atomic beam was assumed to evaporate divergently with a constant angle $\Theta = \textit{constant}$. The geometry is illustrated in Figure 4.27. For the calculations, the angle of the divergence was chosen to be $3.8\,^\circ$ according to the calculations for a hot cavity of 34 mm length described in [163]. For simplicity, the atom distribution within the cylindrical volume

$$V_{\mathrm{R}} = \pi \cdot R(z_0, \Theta)^2 \cdot \Delta z \tag{4.8}$$

for a given starting position z_0 and corresponding atomic beam radius $R(z_0, \Theta) = z_0 {\cdot} \tan\Theta$ was assumed to be uniform:

$$V_R \cdot \rho(z_0, \Theta) = \text{constant}\,, \tag{4.9}$$

where $\rho(z_0, \Theta)$ is the atomic density at z_0. Then, the number of atoms, N, which are ionized by the laser with radius r and ionization efficiency ϵ_{ion} in in the corresponding volume $V_r = \pi r^2 \Delta z$ can be calculated by:

$$N = N_0 \cdot \frac{V_r}{V_R} = N_0 \epsilon_{\mathrm{ion}} \cdot \frac{\pi r^2 \Delta z}{\pi R(z_0)^2 \Delta z} = N_0 \frac{r^2}{(z_0 \cdot \tan(\Theta))^2}\,, \tag{4.10}$$

where N_0 is the number of atoms within the volume V_R. With $r, \epsilon_{\mathrm{ion}}, \Theta = \text{constant}$, the number of atoms as a function of the initial position is then proportional to the square of the starting position (i.e. the distance to the hot cavity): $N \propto \frac{1}{z_0^2}$.
The time of flight was calculated for different starting positions, $-5\,\mathrm{mm} \leq z_0 \leq 85.3\,\mathrm{mm}$, with $\Delta z_0 = 0.01\,\mathrm{mm}$ between each starting position and different initial velocities, $5\mathrm{m/s} \leq v_0 \leq 3500\,\mathrm{m/s}$, increasing in steps of $\Delta v_0 = 5\,\mathrm{m/s}$. The velocity was weighted by the Maxwell velocity distribution given in Equation (2.40) and by an additional weighting factor* of $903/v_0\,\mathrm{m/s}$ to consider the higher probability of slower atoms to interact with the 10 kHz laser pulses before leaving the LIST RFQ.
To match the time of flight of the calculated values to the experimental values, it was necessary to introduce an off-set, ΔU_0, to the effective potential U_0:

$$U_0'(U_{\mathrm{rep}}) = 0.575(1) \cdot U_{\mathrm{rep}} + \Delta U_0\,. \tag{4.11}$$

The best overall agreement with the measured time of flights was obtained for a reduction of the effective potential of $\Delta U_0 = -2.1(1)$. Interestingly this offset is not dependent on the magnitude of the repeller voltage and its significance is not yet understood. A possible explanation are perturbations by the RF-potential, which were not considered for these calculations.

*903 m/s is the velocity, for which the atom is interacting with one laser pulse, when traveling from the hot cavity $z = -5\,\mathrm{mm}$ to the maximum allowed position $z_{\max} = 85.3\,\mathrm{mm}$

Calculated LIST time structure and comparison to the experiment

Figure 4.28 shows the calculated LIST time structure for $U_{\mathrm{rep}} = 7\,\mathrm{V}$, 10 V, 40 V with respect to peak (A). The countrate was normalized to the peak (A) similar to the measured time structure from Figure 4.25. Overall, the simulation reproduces the main features, peak (A), peak (B) and tail (C) of the measured time structure. The dependency of the position and the width of peak (B) on the repeller voltage are similar to the measured values. In contrast, the intensity of tail (C) and the background of the calculations are overestimated, but can be ascribed to the simplified model of the atomic beam, which does not take into account any angle-preference of the intensity nor the acceptance of the RFQ. The calculated strictly growing intensity of peak (A) for increasing repeller voltages was not observed in the measured time structures. This can be ascribed to a different statistic for each of these measurements and ion optics effects that depend on the initial energies (e.g. energy tolerance of the GPS magnet). The substructure observed in the tail (C) was not reproduced, but can be explained by perturbations of the potential along the longitudinal axis due to the influence of the RF-potential. The calculated positions of peak (B) with respect to peak (A) for different repeller voltages agree well with the experiment as shown in Figure 4.29. A small shift is observed for low repeller voltages, but can be explained by the unknown correction, ΔU_0, to the effective repeller voltage described by Equation (4.11).

The origin of the different features of the LIST time structure

In order to understand the features, peak (A), peak (B) and tail (C), observed in the spectra shown in Figure 4.25 and Figure 4.28, the time structure was calculated for 7 different ranges of starting positions, z_0, along the longitudinal axis, z. These ranges, denoted with Roman numbers, represent distinguishable features of the longitudinal potential as shown in Figure 4.26. The calculated time structures for the relevant ranges $I - V$ that allow for kinetic energies within the energy acceptance ± 50 of the GPS mass separator [70] are shown in Figure 4.30. Using the separate calculations of the time structure, peak (A), peak (B) and peak (C) can be understood as follows:

Range I, $-5\,\mathrm{mm} \leq z < 0\,\mathrm{mm}$: the longitudinal potential is rising from 0 V at the exit of the hot cavity ($z = -5\,\mathrm{mm}$) to the maximum potential at the position of the repeller electrode ($z = 0$). Only ions with sufficient initial velocities in forward direction can pass the repeller barrier. Ions created in range I contribute to peak (B).

Range II, $0\,\mathrm{mm} \leq z < 7.5\,\mathrm{mm}$: the longitudinal potential decreases rapidly by 75 % from its maximum value at the position of the repeller electrode $z = 0\,\mathrm{mm}$ to $z = 7.5\,\mathrm{mm}$. Assuming that the atomic beam is divergent, the atom density inside the LIST RFQ is highest in range I and thus most atoms are ionized close to the repeller electrode. The strong potential gradient and the drift time in the following ranges lead to a focusing and the formation of peak (B).

Range III, $7.5\,\mathrm{mm} \leq z < 31.75\,\mathrm{mm}$: the longitudinal potential decreases slowly from 25 % of its initial value at $z = 7.5\,\mathrm{mm}$ to 0 V at around $z = 31.75\,\mathrm{mm}$. Ions created

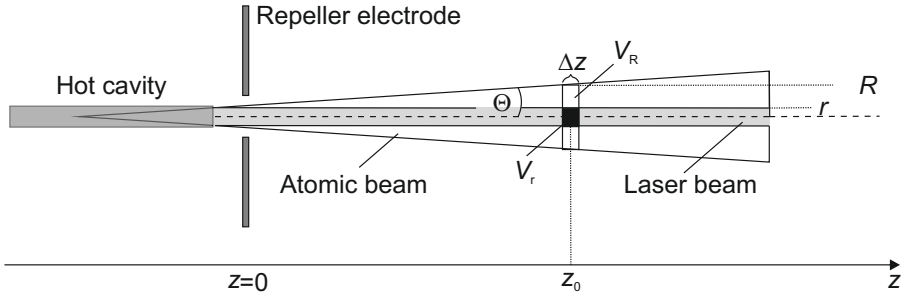

Figure 4.27: Simplified model of the diverging atomic beam with angle Θ. $V_r = \pi r^2 \Delta z$ is the volume in which the atoms at z_0 interact with the laser beam of radius r. $V_R = \pi R(z_0)^2 \Delta z$ is the corresponding volume of the total atomic beam with radius $R(z_0) = z_0 \cdot \tan(\Theta)$.

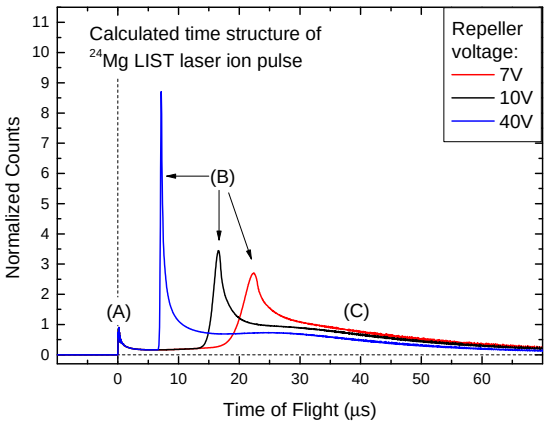

Figure 4.28: Calculated LIST time structure for $U_{rep} = 7\,V$, $10\,V$ and $40\,V$. The time of flight is given with respect to peak (A). The notation is similar to Figure 4.25.

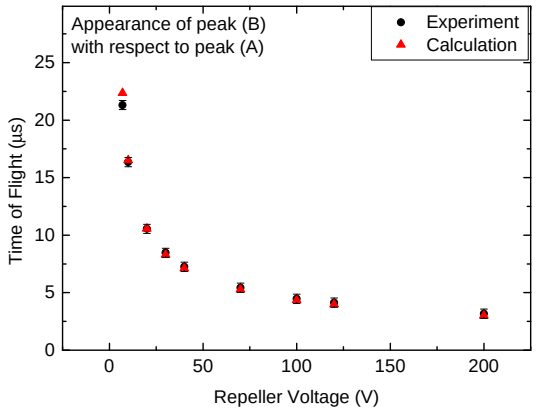

Figure 4.29: Comparison of the measured and calculated appearance of the main peak (peak (B)) in the LIST time structure with respect to peak (A).

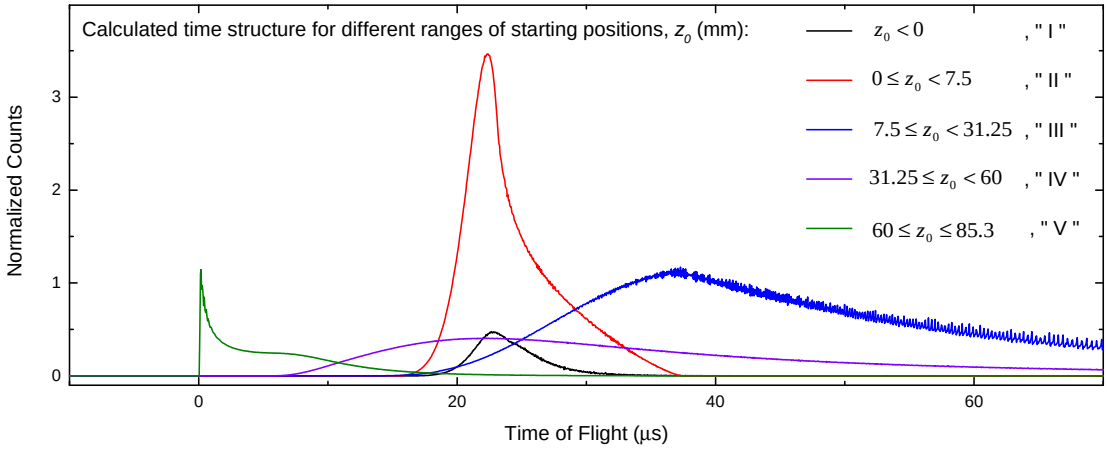

Figure 4.30: LIST ion bunch time structure for the repeller voltage of $U_{rep} = 7\,V$ for different ranges of starting positions z_0, corresponding to the ranges defined in Figure 4.26 and Section 4.3.8.

in range III form the tail (C).

Range IV, 31.75 mm $\leq z <$ 60 mm: the longitudinal potential is not affected by the repeller voltage or the extraction field of the extraction electrode on a high potential and the longitudinal potential is constant at around 0 V. The time of flight of the ions created in range III is therefore entirely defined by the initial conditions (position z_0, thermal velocity, ν_0).

Range V, 60 mm $\leq z <$ 85.3 mm: the longitudinal potential starts to drop due to the influence of the extraction potential of -50 kV at the extraction electrode at $z =$ 160 mm and a potential of -50 V is reached at $z = z_{\max} = 85.3$ mm. Ions created in range V form the peak (A) due to the strong potential gradient and the drift time towards the experiments.

Range VI, 85.3 mm $\leq z <$ 160 mm Ions created after $z = 85.3$ mm have an energy difference of more than 50 eV compared to ions created inside the LIST, which exceeds the acceptance of the GPS separator magnet and their contribution is therefore negligible. The potential drops by -50000 kV to the ground potential at the extraction electrode at $z = -160$ mm.

Range VII, $z \geq$ 160 mm: the potential remains constant after the extraction electrode and the ions drift to the experiment with the velocity corresponding to their kinetic energy.

In summary, peak (A) stems from the atoms ionized next to the exit of the LIST (range V), peak (B) are the ions produced close to the repeller electrode (range I and II), the tail (C) are the atoms ionized further away from the repeller electrode (range III) and the background is produced by ions produced in the nearly field free zone (range IV).
An important result of these calculations for the laser ionization efficiency of the LIST is that the dominant peak (B) stems mainly from ions created very close to the repeller electrode. Consequently, a reduction of the distance of the repeller electrode to the hot cavity should thus correlate with an increased laser ionization efficiency. This conclusion is supported by the improved ionization efficiency of a factor of 2,5 from LIST 1 to LIST 2, for which the distance was reduced by 2.5 mm.

4.3.9 Improving the selectivity of the Laser Ion Source and Trap

In the following, possibilities are discussed to improve the LIST selectivity for future applications at ISOLDE.

Improving the laser ionization efficiency

Improving the laser ionization efficiency increases directly the ratio of the intensity of the isotopes of interest over the intensity of the contaminants.

1. **Improvement of the laser/atom overlap:** a higher laser/atom overlap can be achieved by further reducing the distance of the LIST to the hot cavity. The reduction from 5 mm for LIST 1 to 2.5 mm for LIST 2 led to a significant improvement of the laser ionization efficiency of a factor of 2.5. This is also supported by the analysis and calculation of the time structure, which indicate that the atomic beam is densest close to the repeller. However, a further reduction is difficult to be mechanically constructed due to possible shortcuts with the heat shield of the hot cavity. One possibility could be to use the heat shield itself as a repeller, which would reduce the distance to about 1 mm, but possible complications need to be ruled out during long-term off-line tests.
   Additionally, the laser/atom overlap could be increased by improving the atom beam collimation by different hot cavity designs (e.g. increased length).

2. **Improvement of the laser ionization scheme:** if all steps would be strongly saturated, the laser beam radii could be expanded to interact with more atoms.

3. **Reducing the duty cycle:** atoms with the largest transverse velocity component may have a short ($< 100\,\mu s$) residence time inside the LIST laser interaction region. In this case an increased laser repetition rate would reduce duty cycle losses provided that the pulse energy stays the same, which is practically difficult.

Time dependence of laser ions

As it was discussed in Section 4.3.8, the laser ion pulse produced by the LIST has a distinct pattern with one dominant peak (B) corresponding to the ions produced close to the repeller electrode. For the standard repeller voltage setting of $I_{\mathrm{rep}} = 7\,V$, the FWHM was determined to be 3.43(7) µs. Using a beam gate could thus increases the selectivity significantly. For example, a gating time of 10 µs around peak (B) would allow $\approx 60\,\%$ of all ions to pass, whilst cutting of 90 %* of the pulse-independent contaminants leading to an overall selectivity gain of 6. Depending on the required laser ionization efficiency the gate could be increased at the cost of the reduction of the contamination and vice versa.

*The duty cycle for a 10 kHz laser is approximately 100 µs. With a gating time of only 10 µs, only the 10 % contaminants produced within this time interval could pass the beam gate.

Temperature dependency of contamination

Figure 4.31 shows that the ion rate of ^{212}Fr, which is a *LIST mode* contaminant of unknown origin*, has a stronger cavity temperature dependency than laser ionized ^{196}Po in *LIST mode* or the surface ionized ^{212}Fr in *ion guide mode*. It is therefore possible to improve the selectivity for *LIST mode* laser ionized ^{212}Po by a reduction of the hot cavity temperature. It should be noted that this method only applies to isotopes, which have a reasonable long lifetime to not be affected by the longer transport time through the hot cavity in case of lower temperatures. ^{196}Po has a half-live of $T_{1/2} = 5.8\,\mathrm{s}$ and an application for isotopes with similar half-lives should be feasible.
One possible future application is the resonance ionization spectroscopy of the polonium isomers ^{211m}Po and ^{211m}Po. Due to their relatively long half-lives of $T_{1/2} = 25.2\,\mathrm{s}$ and $T_{1/2} = 45.1\,\mathrm{s}$, respectively, the hot cavity temperature dependency of these isotopes is the same or even less than the hot cavity temperature dependency of ^{196}Po.

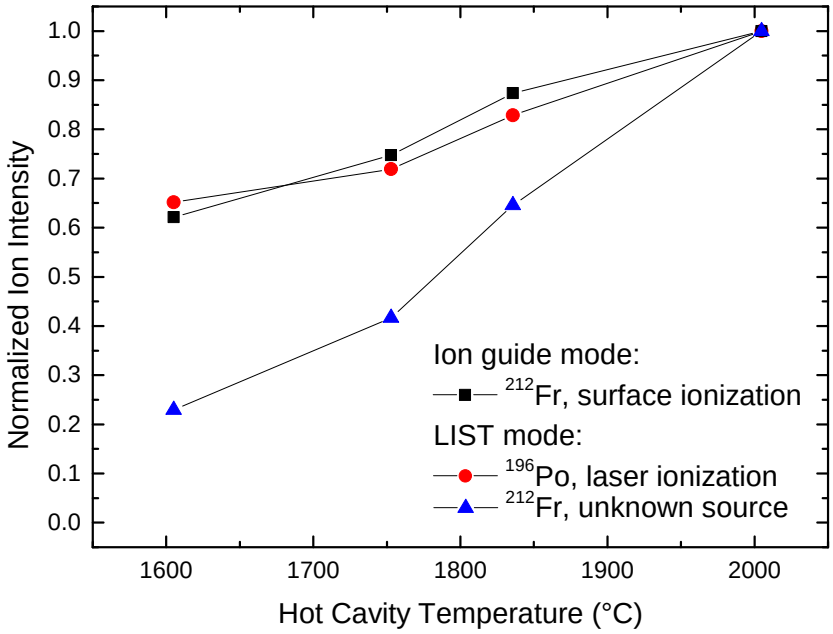

Figure 4.31: Ion intensity of ^{212}Fr ($T_{1/2} = 20\,\mathrm{min}$) in *ion guide mode* and *LIST mode* and ^{196}Po ($T_{1/2} = 5.8\,\mathrm{s}$) in *LIST mode* as a function of the hot cavity temperature. The ion intensity is normalized to the maximum intensity measured for each isotope at $T = 2000\,^{\circ}\mathrm{C}$. ^{196}Po was laser ionized and ^{212}Fr in *ion guide mode* was surface ionized. The exact source and ionization mechanism of ^{212}Fr in *LIST mode* is still unknown.

*In Chapter 4.3.4, the in-trap β-decay of neutral ^{212}Ra to ^{212}Fr at the RF-rods was discussed as a possible explanation for the contamination.

5 A new laser ionization scheme for calcium

More than 30 elements are currently available for the resonance laser ionization with the RILIS at ISOLDE and efforts are being continuously made to extend this further* [113]. For many laser ionization schemes, only non-resonant final steps have been applied and their relatively low ionization cross-sections of only $10^{-17}\text{cm}^2 - 10^{-19}\text{cm}^2$ require often a laser powers in excess of the power available from the Nd:YAG pump laser.
Thus, finding efficient autoionizing states (AIS) may improve the ionization efficiency. The general approach to improve the laser ionization schemes for elements with stable isotopes is to conduct this studies at off-line facilities such as the LARIS laboratory at CERN [115]. This allows for extended studies of the resonances without the scheduling constraints of the ISOLDE on-line facility. However, a very convenient and time-efficient alternative approach to improve existing laser ionization schemes is to perform the measurements during scheduled on-line runs at ISOLDE. The recent upgrade of the RILIS to a dual-RILIS system of 6 tunable lasers (see Chapter 3.3.1) has made opportunistic ionization scheme developments possible during the normal on-line operation of the system [143, 145].
Calcium (Ca) is one of those elements, which was ionized via a non-resonant last step during previous experiments [25, 127]. Figures 5.1 a,b show the existing laser ionization schemes: a) two-step scheme with one blue laser beam to the intermediate step and one UV laser beam for non-resonant ionization, and b), a three step scheme consisting of one blue laser beam, one infrared laser beam for the excitation to the intermediate steps and of one of the 532 nm pump lasers for the step above the ionization energy† of 49305.924 cm^{-1} [120]. Of these two laser ionization schemes, only the latter is applicable since the laser power provided by a UV laser beam is usually not sufficient to approach saturation in the case of non-resonant ionization.
Two calcium experiments were scheduled for 2012: Experiment IS529, "measurements of spins, moments and charge radii beyond 48Ca" by collinear laser spectroscopy with the COLLAPS experiment in April 2012 [11] and experiment IS532 for mass measurements of exotic calcium with the ISOLTRAP experiment in June 2012 [96], for which the results were recently published in *Nature* [177]. Both experiments relied on a high ionization efficiency for the study of very exotic calcium isotopes and thus, investigations towards an improvement of the existing calcium laser ionization scheme was integrated into the setup procedure and maintenance work of these two on-line runs.
In the following I report on the results of the resonance ionization spectroscopy study, the

*A RILIS web-database (http://riliselements.web.cern.ch) was recently developed to summarize and share the latest results of RILIS scheme developments at facilities worldwide [143].

†Transition energies and excitation energies are given in the unit of wavenumbers throughout this chapter.

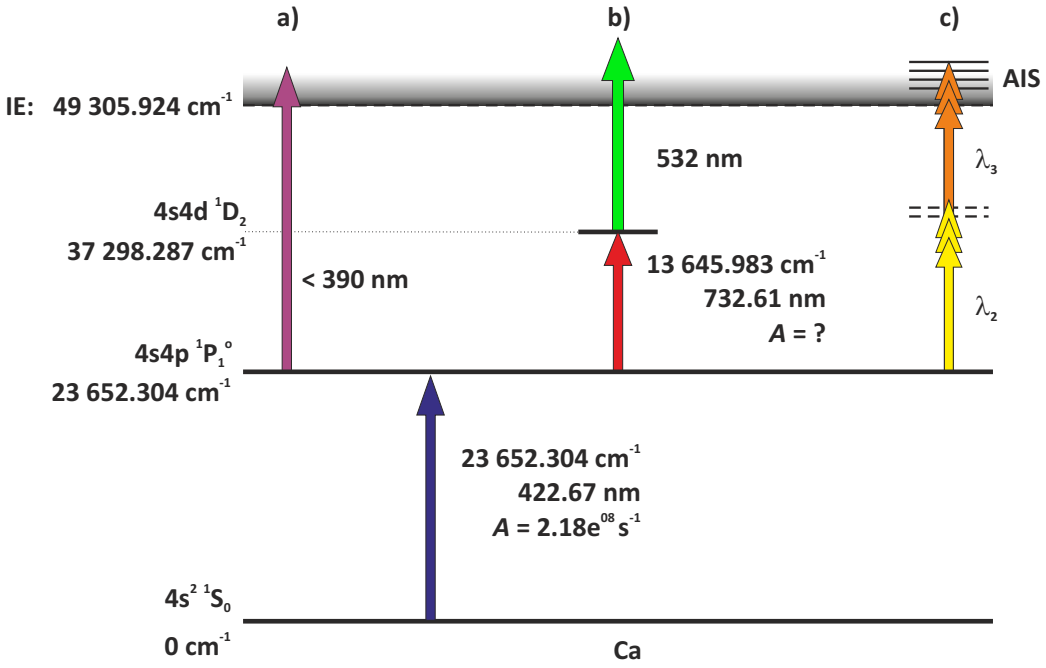

Figure 5.1: a) Two-step scheme using one resonant transition. b) Three-step scheme using two resonant transitions and one non-resonant ionization step. Both originally from [25, 127]. c) Illustration of the scanning regions for an alternative second intermediate step and the search for autoionizing states above the ionization region. The wavelengths are referred to as λ_2 and λ_3 for the second and third step, respectively.

analysis of the spectra and the discussion of possible new ionization schemes. It should be noted that these measurements aimed on the development of a new laser ionization scheme rather than a comprehensive and decisive study of the atomic spectrum of calcium. I therefore restrict the discussion to the relevant information such as relative peak heights, ion intensities, widths and saturation and refer to possible future experiments at off-line laser facilities for an in-depth study of the resonances and features in the spectra.

5.1 Experimental setup

The search for an alternative laser ionization scheme was performed during maintenance breaks of the IS529 experiment and during the laser setup and optimization procedure for the IS532 experiment. Experiment IS529 used a UC_x target (ISOLDE target # 471) with a hot cavity made of rhenium (Re) and experiment IS532 used a UC_x target (# 480) with a hot cavity made of tantalum. Typical target specifications and operation parameters are given in Figure 5.2.

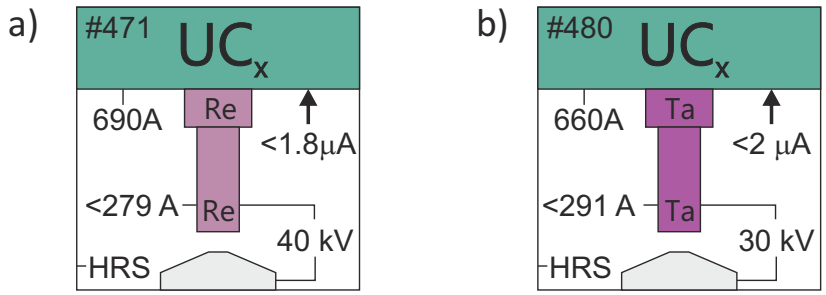

Figure 5.2: Target specifications of the targets used for the Ca-Spectroscopy. a) UC_x target # 471 with rhenium (Re) hot cavity for experiment IS529 and b) UC_x target # 480 with tantalum (Ta) hot cavity for experiment IS532. From top to bottom: target number, target material, typical target and hot cavity currents, proton intensities, extraction voltage and type of front-end. Note that these values represent maximum values and can differ for certain measurements. Design of schematics adopted from [143].

During the two experimental periods several scans of the calcium atomic spectrum were recorded. The scan ranges for the search of an alternative intermediate step and resonant last step are indicated in Figure 5.1 c with λ_2 and λ_3, respectively. For the search of alternative intermediate states, a dye laser, operated with a Rhodamin B (RB)-ethanol solution, was scanned from 16250 cm^{-1} to 17250 cm^{-1} (579.7 nm to 615.4 nm) from the first intermediate state $4s4p\,^1P_1^o$ at 23652.304 cm^{-1} , while a 532 nm Nd:Yag was used for the last step. Two levels were found in the range from 17030 cm^{-1} to 17070 cm^{-1}. Using these alternative intermediate levels, additional scans were performed with a dye-laser using a DCM*-ethanol solution in the range from 14700 cm^{-1} to 16300 cm^{-1} (613.5 nm to 680.2 nm). Various autoionizing states were observed and studied during several scans. Due to time constraints during the experiment IS529, the scans were repeated during the second experiment, IS532, where the setup was tuned from the beginning to the alternative intermediate steps and the autoionizing states.
In order to compensate possible frequency shifts due to time-delays in the DAQ-system, the scans for the relevant levels (intermediate levels, strongest autoionizing states) were performed in forward and backward direction as appropriate.

*DCM is the abbreviation for 4-dicyanomethylene-2-methyl-6-p-dimethylaminostyryl-4H-pyran.

5.2 Analysis of the spectra

Figure 5.3 shows the relevant segments of the scans: a) alternative second intermediate states; b) autoionizing states from the lower lying intermediate state ($3p^6 4s6s\,^1S_0$, denoted by the term symbol $^1S_0$); c) autoionizing states from the higher lying intermediate state ($3p^6 4p^2\,^1D_2$, denoted by the term symbol $^1D_2$); d) and e), zooms into the spectra of the autoionizing states reached from the two second intermediate steps, $^1S_0$ and $^1D_2$, respectively.

5.2.1 Alternative second intermediate states

The alternative second intermediate states were found in the energy range from 17035 cm^{-1} and 17080 cm^{-1} relative to the first intermediate state $3p^6 4s4p\,^1P_1^o$ at 23652.3 cm^{-1} as shown in Figure 5.3 a. The first structure appears at around 17037 cm^{-1} and the second structure is at around 17067 cm^{-1}. Both structures show unresolved substructures, which are due to strong saturation and the presence of additional laser frequency side bands.
To determine the transition energies E, a single Voigt-profile was fitted to the main resonance of the first structure and a superposition of two Voigt profiles was fitted to the second structure. The results from the forward and backward scans were averaged to calculate the final value of the transition energy, E. The transition energies were then added to the literature value for the first intermediate step $3p^6 4s4p\,^1P_1^o$ with energy 23652.3 cm^{-1} [94].
The statistical uncertainties of the fits are dominated by the uncertainty from the wavemeter of $\Delta E_{\mathrm{stat,WM}} = 0.02\,\mathrm{cm}^{-1}$ [79]. A systematic uncertainty arises from the wavemeter *WS7*, which was determined in [143] to $\Delta E_{\mathrm{sys,WM}} = 0.03\,\mathrm{cm}^{-1}$. Additionally, a systematic uncertainty of $\Delta E_{\mathrm{sys,WM}} = 0.3\,\mathrm{cm}^{-1}$ is conservatively added to resonance 1 because of the unresolved substructure.
Taking the systematic uncertainty of 0.33 cm^{-1} into account, the main resonance in the first structure with energy 40690.26(2) cm^{-1} can be assigned to the literature value at 40690.435(1) cm^{-1} with configuration $3p^6 4s6s\,^1S$. The highest lying resonance, resonance 2, in the second structure with energy 40719.87(2)cm^{-1} corresponds to the literature value of an atomic state at 40719.847 cm^{-1} with configuration $3p^6 4p^2\,^1D$ [94]. The peak in the lower energy flank of the main resonance with energy 40718.32(3) cm^{-1} is not known in literature. It is impossible that it can be assigned to an isotope shift of the second most abundant isotope ^{44}Ca, whose natural abundance of only 2 % does not correspond to the peak height. It is therefore likely to be a laser related effect as discussed above. The disappearance of this peak in a reduced power (close to saturation intensity) scan would confirm this but this was not feasible due to time constraints. The results for resonance 1 and resonance 2 are given in Table 5.1 and Table 5.2, respectively, together with the corresponding subsequent transitions to autoionizing states. The energy position of the two observed intermediate states enables a search for autoionizing states through the use of a visible dye laser for the third step in the ionization scheme.

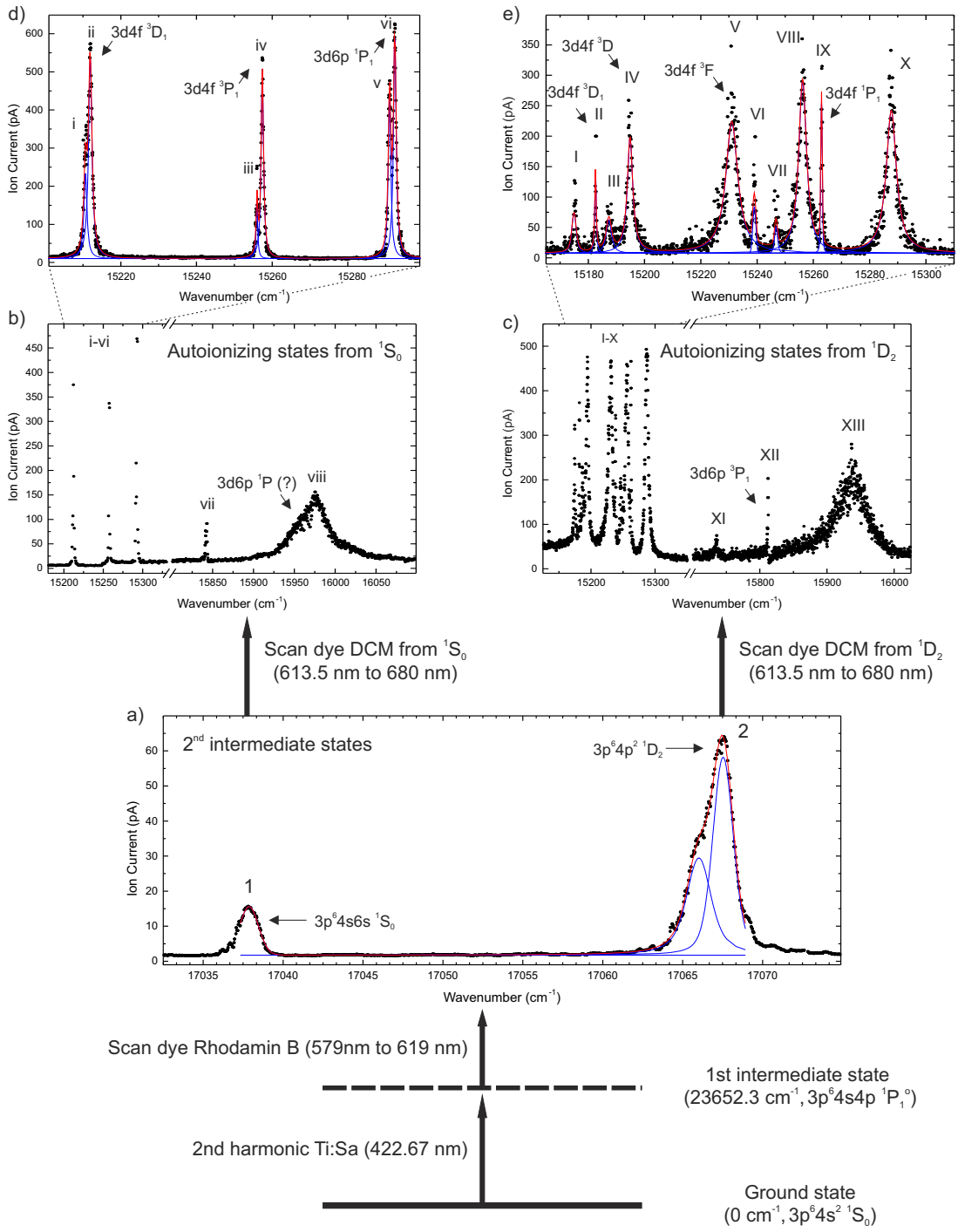

Figure 5.3: Overview of the different scans conducted for the search for a new laser ionization scheme for calcium: a) alternative second intermediate levels. b) and c), autoionizing states found in the scans from the second intermediate levels. d) and e): zooms to the most interesting resonances from the point of view of laser ionization efficiency in the spectra shown in b) and c), respectively, and the corresponding Voigt-fits (blue: individual line-shape; red: cumulative fit). Used dyes, scanning ranges and configurations, are given, if known from literature.

5.2.2 Excitation from the alternative intermediate state 1

A broad low-resolution scan ($0.7\mathrm{cm}^{-1}/\mathrm{s} \rightarrow 14\,\mathrm{measurements/cm}^{-1}$) over all observed transitions to autoionizing states from the $4p6s\,^1S_0$ state is shown in Figure 5.3 b. In total 8 resonances, denoted by small Roman number, could be identified for transition energies between $15175\,\mathrm{cm}^{-1}$ to $16100\,\mathrm{cm}^{-1}$. Of these, a pairing of the transitions i to vi was observed similar to the case of the resonance 2 observed in the scan for the search of the intermediate states described above. It is likely that these peaks are due to a similar laser side band, i.e. a saturation effect, as was discussed earlier.
A slower scan with higher resolution ($0.1\mathrm{cm}^{-1}/\mathrm{s} \rightarrow 100\,\mathrm{measurements/cm}^{-1}$) over the strongest lines (resonances i - vi) from $15200\,\mathrm{cm}^{-1}$ to $15300\,\mathrm{cm}^{-1}$ is shown in Figure 5.3 d). These resonances are highly symmetrical and were therefore fitted with Voigt fits as shown in Figure 5.3 d), where the individual fits are the solid blue lines and the cumulative fit is the red line. The Gaussian widths due to hot cavity temperature of $T \approx 2000\,^\circ\mathrm{C}$ (Doppler broadening) and the laser linewidth of 9 - 12 GHz of the broad-band Credo dye lasers[59, 113] was estimated to be $0.4\,\mathrm{cm}^{-1}$ and was kept fixed during the fits. The scan was performed with the maximum available laser power ($\approx 1\,\mathrm{W}$ in the source). The priority was given to maximizing the ionization efficiency, rather than extracting spectroscopic information, was made and thus, no attempt was made to reduce the degree of saturation and subsequent power broadening of the transitions. Similar to the transitions to the intermediate states, the statistical uncertainties are dominated by the statistical uncertainties of the wavemeter and are $0.02\,\mathrm{cm}^{-1}$. The results are listed in Table 5.1.

The two resonances, vii and viii, shown in Figure 5.3 b are less intense than the resonances, i to vi. Resonance vii is significantly narrower ($\approx 0.2\,\mathrm{cm}^{-1}$) than the resonances i-vi and shows a certain asymmetry and a further unresolved substructure. However, not enough data was available to study this structure precisely, but the excitation energy of the centroid of $W = 56531.98(20)\,\mathrm{cm}^{-1}$ (transition energy of $15841.55\,\mathrm{cm}^{-1}$) is close to an autoionizing state known in literature ($3p^6 3d6p\,^3P_1$) with energy $56532.6\,\mathrm{cm}^{-1}$ [94]. In contrast, the structure viii, for which no literature value is known, is extremely broad and significantly asymmetric. A Fano-fit (see Equation (3.17) in Chapter 3.2.3) was performed to resonance viii, to give the center of the resonance of $15977.12(50)(3)\,\mathrm{cm}^{-1}$ with a width of $23.5(3)\,\mathrm{cm}^{-1}$ (720 GHz). However, the asymmetry factor q depended on the choice of the background level and could not be determined unambiguously and the observed strong asymmetry could instead stem from an unresolved substructure. This idea is supported by a value known in literature with configuration $3d6p\,^1P$ and total excitation energy of 56651.0 [94], which would be observed at a transition energy of $15960.7\,\mathrm{cm}^{-1}$. This agrees well to the small perturbation of the left flank of resonance viii [94]. No corresponding states could be found in literature for the resonances i, v, and viii.
For the strongest resonances, ii, iv and vi, the ratio of the absolute height to the background due to surface ionization (Laser on/off) was determined in with all lasers in saturation for a realistic comparison to normal operation conditions.
For the strongest line ii, the overall gain in efficiency compared to surface ionization (Laser off) is 290. The slightly lower height of resonance ii in Figure 5.3 d), when compared to resonance vi, is misleading and can be explained by fluctuations of the laser power during the scan.

Table 5.1: Parameters of the transition to the first intermediate step, $4p6s\,^1S_0$ (resonance 1), and subsequent transitions to autoionizing states (resonances i-viii): number of resonance (Res.), transition energies E, total excitation energies from the ground-state W and corresponding literature values W_{lit}, electron configuration, term value and total angular momentum J, FWHM and relative ionization efficiency compared to surface ionization (Laser on/off). The literature values of the $3d4f\,^3P^o$ could not be unambiguously assigned to either resonance iii or iv and are marked with $(*)$. Statistical and systematic uncertainties of the measured transition energies E are given in the first and second parentheses, respectively, and are identical for the total excitation energy W. The other values are implied with their significant numbers.

Res.	$\boldsymbol{E}$ $\mathbf{cm^{-1}}$	$\boldsymbol{W}$ $\mathbf{cm^{-1}}$	$\boldsymbol{W}_{\mathrm{lit}}$ $\mathbf{cm^{-1}}$	**Config.**	**Term**	$\boldsymbol{J}$	**FWHM** $\mathbf{cm^{-1}/GHz}$	**Laser on/off**
1	17037.96(2)(33)	40690.26	40690.44	$3p^64s6s$	^1S	0		
i	15210.55(2)(3)	55900.99				1	0.3/8.8	
ii	15211.91(2)(3)	55902.35	55902.8	$3d4f$	$^3D^o$	1	0.9/28.1	290
iii	15256.00(2)(3)	55946.43	55946.6*	$3d4f$*	$^3P^o$*	1	0.4/11.9	
iv	15257.37(2)(3)	55947.80	55946.6*	$3d4f$*	$^3P^o$*	1	0.6/17.7	190
v	15290.95(2)(3)	55981.38				1	0.9/27.3	
vi	15292.33(2)(3)	55982.77	55982.3	$3d6p$	$^1P^o$	1	0.9/27.3	260
vii	15841.55(20)(3)	56531.98	56532.6	$3d6p$	$^3P^o$	1	$\approx 0.2/6$	
viii	15977.12(50)(3)	56667.55				1	$\approx 24/720$	

5.2.3 Excitation from the alternative intermediate state 2

The broad low-resolution scan ($0.5\mathrm{cm^{-1}/s} \rightarrow 20\,\mathrm{measurements/cm^{-1}}$) from the $4p^2\,^1D_2$ intermediate state at $40719.847\,\mathrm{cm^{-1}}$ [94] is shown in Figure 5.3 c). In total 13 resonances, denoted by capital Roman numbers, were found in the range from $15150\,\mathrm{cm^{-1}}$ to $16000\,\mathrm{cm^{-1}}$. The spectrum of autoionizing states shows some similarities to the spectrum explored from the $4p6s\,^1S_0$ intermediate state shown in Figure 5.3 b): several intense and rather narrow resonances at lower excitation energies, resonances I to X, and a very broad structure next to weaker resonances at higher excitation energies (between $15700\,\mathrm{cm^{-1}}$ and $16000\,\mathrm{cm^{-1}}$). In contrast to the spectrum of the excitation from the $4p6s\,^1S_0$ intermediate state, more peaks are visible. This can be explained by the higher $\boldsymbol{L}$- and $\boldsymbol{J}$-value of the $4p^2\,^1D_2$ intermediate, which allows for more possible transitions. Moreover, no systematic pairing of the peaks is visible.

The determination of the centroids of the resonances was similar to the analysis of the resonances found in the scan from the $4p6s\,^1S_0$ intermediate state described in the previous section: Voigt profiles were fitted with a fixed Gaussian linewidth of 0.4 GHz to the symmetrical resonances (I to X) and to the weak resonance XI and Fano-profiles to the higher excited resonances at higher energies $15700\,\mathrm{cm^{-1}}$ and $16000\,\mathrm{cm^{-1}}$ (resonance XII and res-

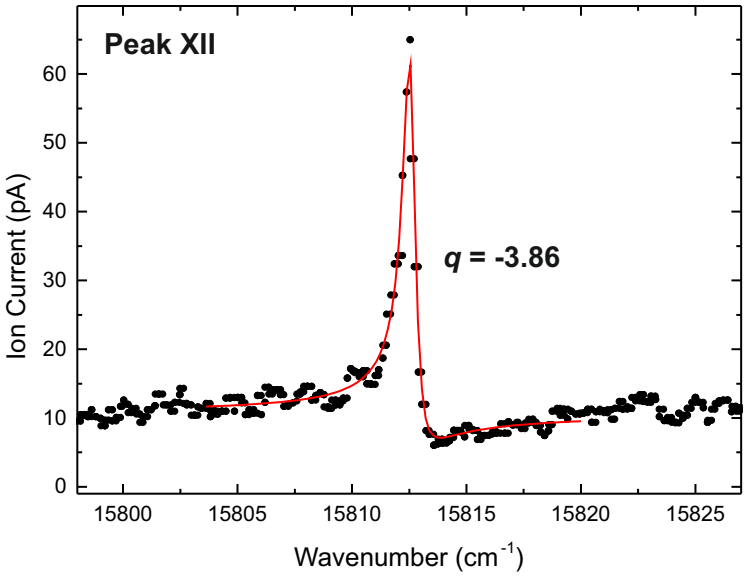

Figure 5.4: Resonance XII with transition energy 15812.89(3)(3) cm^{-1} (56532.76 cm^{-1} total excitation energy) accessed from the $4p^2\,{}^1D_2$ intermediate state. A Fano-profile was fitted (red solid line) to the asymmetric lineshape of the resonance.

onance XIII). Figure 5.3 e shows a scan with higher resolution 0.2cm^{-1}/s $\rightarrow$ 50 measurements/ cm^{-1} for the resonances I to X, together with individual fits (solid blue lines) and the cumulative fit (red line). It was difficult to resemble the peaks heights with the multi-peak Voigt fit, which can be explained by possible asymmetries of some of the peaks. Nevertheless, the transition energies could be determined and the fitting results for the backward and forward scan were averaged to obtain the transition energies.
Similar to the broad structure in the scan from the $4p6s\,{}^1S_0$ intermediate state, a fit with a Fano profile to the resonance XIII showed a strong dependency of the asymmetry factor q on the chosen fitting range and an unambiguous determination of q was not possible. A further discussion is therefore omitted. However, the strongly pronounced asymmetry in resonance XII is shown in figure 5.4 together with the fitted Fano profile (red solid line) and the corresponding Fano factor of $q = -3.86(8)$.
Center energies and widths of all resonances are given in Table 5.2 together with corresponding values and configurations of levels found in literature [66, 94] together with the relative intensities compared to surface ionization (Laser on/off) of the strongest lines, V, VIII, IX and X.. No corresponding states could be found for resonances I, III, VI-VIII, X, XI and XIII and are possibly newly discovered autoionizing resonances. Comparing the transitions from both intermediate steps listed in Table 5.1 and Table 5.2, each pair, ii and II, vi and IX and vii and XII correspond to the same autoionizing state. Of these transitions, resonance IX with configuration $3d6p\,{}^3P^o$ resulted in the highest recorded ionization efficiency with an overall gain in efficiency of a factor of 300 compared to surface ionization.

Table 5.2: Parameters of the transition to the second intermediate step, $3p^6 4p^2\,{}^1D_2$ (resonance 2), and subsequent transitions to autoionizing states (resonances I-XIII). The notation of the parameters is similar to those given in Table 5.1. Statistical and systematic uncertainties of the measured transition energies E are given in the first and second parentheses, respectively, and are identical for the total excitation energy W. The other values are implied with their significant numbers.

Res.	E **cm**$^{-1}$	W **cm**$^{-1}$	W_{lit} **cm**$^{-1}$	**Config.**	**Term**	J	**FWHM cm**$^{-1}$**/GHz**	**Laser on/off**
2	17067.56(2)(3)	40719.87	40719.85	$3p^6 4p^2$	^1D	2		
I	15175.00(2)(3)	55894.85				0	1.19/35.7	
II	15182.46(2)(3)	55902.30	55902.8	$3d4f$	$^3D^o$	1	0.62/18.5	
III	15187.17(2)(3)	55907.01				1,2,3	4.7/139.3	
IV	15194.79(2)(3)	55914.64	55915	$3d4f$	^3D	2.3	2.2/65.0	
V	15230.72(2)(3)	55950.56	55951	$3d4f$	^3F	1,2,3	4.5/142.1	240
VI	15238.84(2)(3)	55958.69				1,2,3	1.0/30.9	
VII	15246.76(2)(3)	55966.61				1,2,3	1.7/50.8	
VIII	15256.32(2)(3)	55976.17				1,2,3	3.5/105.0	275
IX	15262.93(2)(3)	55982.78	55982.3	$3d4f$	$^1P^o$	1	0.5/16.3	300
X	15287.56(2)(3)	56007.41				1,2,3	4.0/121.1	250
XI	15735.04(4)(3)	56454.89				1,2,3	0.3/8.8	
XII	15812.89(3)(3)	56532.74	56532.63	$3d6p$	$^3P^o$	1	0.3/8.8	
XIII	15933.51(30)(3)	56653.35				1,2,3	0.3/8.8	

5.3 The new laser ionization scheme for calcium

With the available dye laser power in the source of $P \approx 1\,\mathrm{W}$, many of the observed autoionizing states, namely ii, iv and vi from intermediate step $^1S_0^o$ and V, VIII, IX and X from intermediate step $^1D_2^o$, could serve as potential candidates for an efficient last step for a new calcium laser ionization scheme. However, of these, the transitions ii and IX were the easiest to saturate. Figure 5.5 shows the laser ionization schemes from the first intermediate step $4s4p\,^1P_1^0$ at 23652.304 cm^{-1} through a) the intermediate step $4s4p\,^1S_0$ at 40690 cm^{-1} to the autoionizing state ii ($3d4f\,^3D_1^o$, 55902.8 cm^{-1}) and through b) the intermediate step $4p^2\,^1D_2^o$ at 40719 cm^{-1} to the autoionizing state IX ($3d4f\,^1P^o$, 55982.3 cm^{-1}).

Saturation of the transitions

Figure 5.6 demonstrates the saturation for each transition shown in Figure 5.5 by showing the ion current as a function of the laser power inside the hot cavity. The latter was estimated based on simultaneous measurements of the laser power on the laser table. The ratio of the measured power to the laser power inside the hot cavity can be estimated by measuring the ratio to the 4 % reflection* of the laser beam at a quartz plate that is in the beam path at 50 % of the path length to the target. For the measurement of the saturation, the laser power was attenuated by inserting neutral density filters in the laser beam path. The other involved transitions were kept saturated during each measurement. The ion current IC as a function of the power P was then fitted by a saturation curve, defined by

$$IC = IC_0 + IC_{\mathrm{sat}} \cdot \frac{\frac{P}{P_{\mathrm{sat}}}}{\frac{P}{P_{\mathrm{sat}}} + 1}\,, \tag{5.1}$$

where IC_0 is the background of the ion current from the non-resonant ionization, I_{sat} is the maximum ion current in saturation and P_{sat} is the saturation parameter. The extracted saturation parameters are listed in Table 5.3 for each transition. The estimated typical available laser power in the hot cavity during the experiments IS529 and IS532 was about 175 mW for the first step provided by the frequency-doubled Ti:Sa output, 500 mW for the second step provided by the *Credo* dye filled with Rhodamin B and 1125 mW for the third steps provided by the Credo dye laser filled with DCM. The excess of the laser power available simplifies the maintenance of the RILIS performance because it makes the overall efficiency less sensitive to small changes of the power (aging of the dye, change of laser spot position) or small shifts of the wavelengths.

*The laser spot of the reflection at the quartz plate is usually used as the reference spot to observe the beam position during operation.

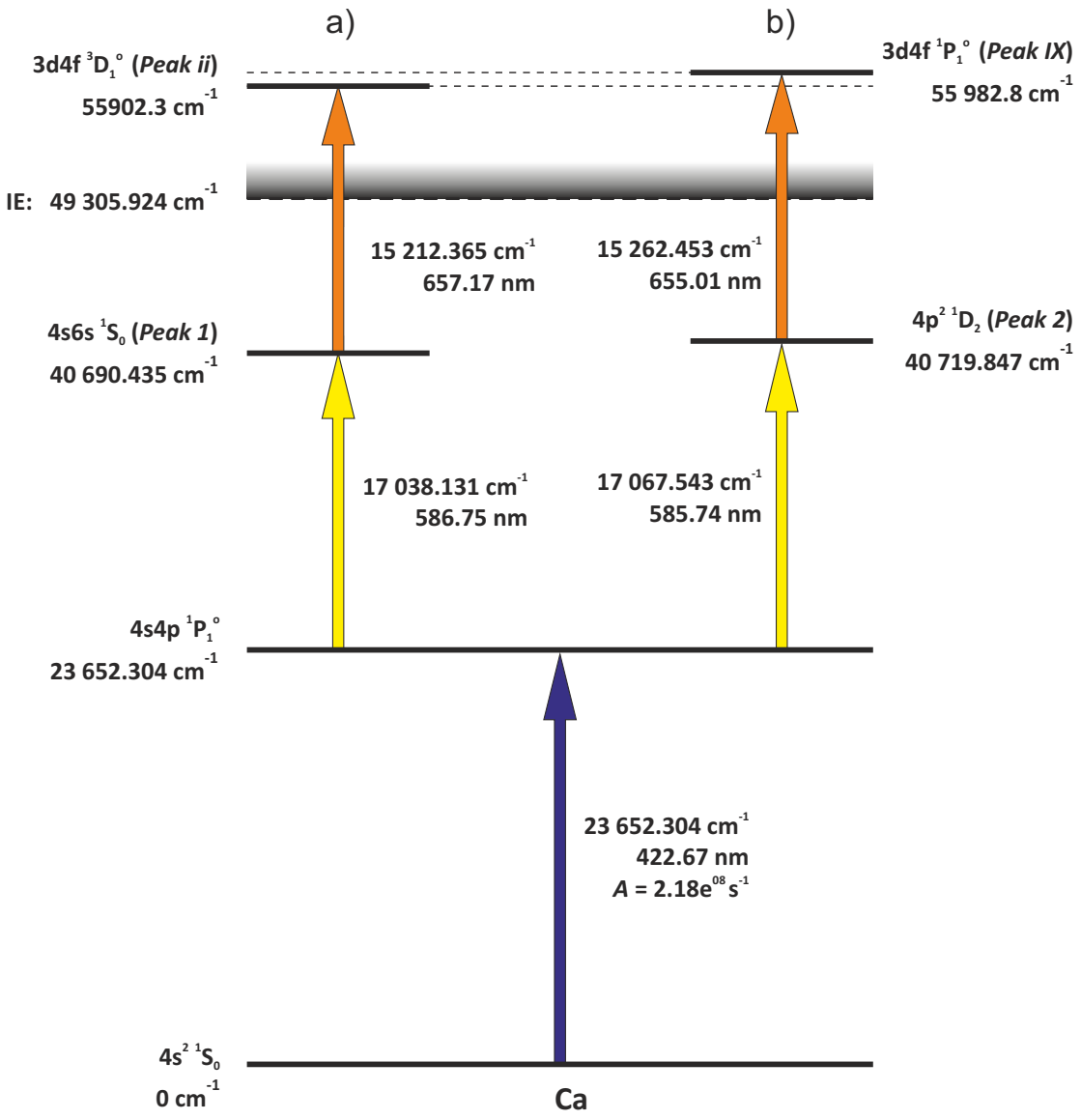

Figure 5.5: The new laser ionization schemes for calcium developed on-line at ISOLDE. From the first intermediate step at 23652 cm^{-1} with configuration $4s4p\,^1P_1^o$, two equally strong ionization schemes are accessible: a) via the second intermediate step 40690 cm^{-1} with configuration $4s4p\,^1P_1$ to the autoionizing state at 55902.8 cm^{-1} with configuration $3d4f\,^3D_1^o$ (resonance ii) and b) via the second intermediate step 40719.847 cm^{-1} with configuration $4p^2\,^1D_2$ to the autoionizing state at 55982.8 cm^{-1} with configuration $3d4f\,^1P^o$ (resonance IX). Excitation energies, transition energies and wavelengths are taken or calculated from values listed in [94]. Wavelengths are given for air. Peak numbers correspond to these defined in Figure 5.3.

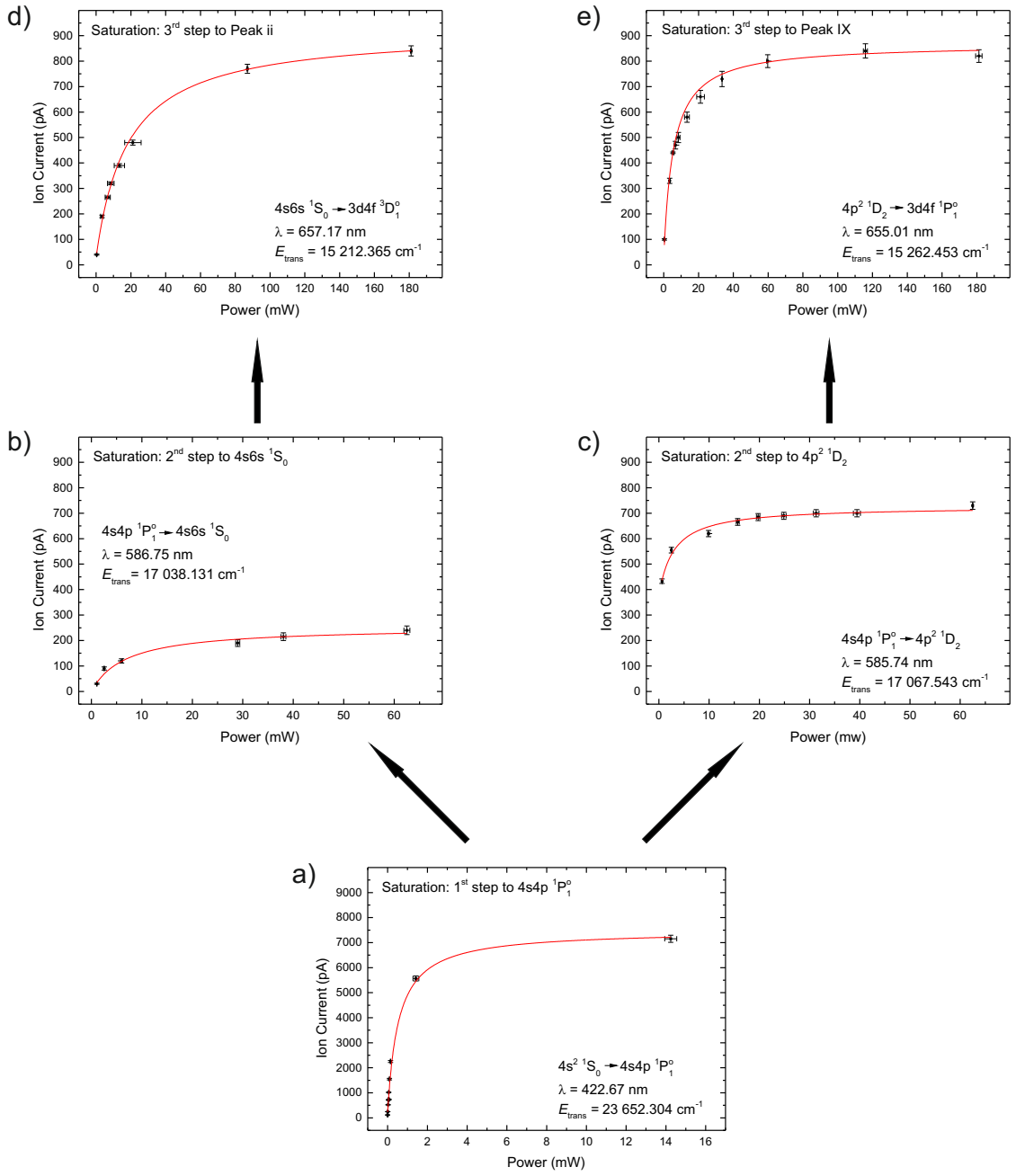

Figure 5.6: Saturation curves for the atomic transitions used in the new calcium schemes. The ion current of each involved transition is given as a function of the estimated laser power inside the hot cavity. a) transition to the first excited state $4s4p\,^1P_1^\circ$, b) second excited state $4s4p\,^1S_0$ (resonance 1), c) second excited state $4p^2\,^1D_2^\circ$ (resonance 2), d) to the autoionizing state $3d4f\,^3D_1^\circ$ (resonance ii) and e) to the autoionizing state $3d4f\,^1P^o$ (resonance IX). For each saturation measurement, the other involved transitions were saturated. Note that the saturation of the first transition was measured at a different time with different oven settings and thus, the total ion current differs from the other measurements.

Table 5.3: Saturation parameters, P_{sat}, of transitions of the new laser ionization schemes for calcium. Electron configuration of involved atomic levels of the transitions and wavelengths are given. The values correspond to the fits shown in Figure 5.6 and are organized following the two schemes to either the autoionizing state (AIS) *ii* ($3d4f\,^3D_1^\circ$) or to autoionizing state *IX* ($3d4f\,^1P_1^\circ$). Wavelengths are calculated from the literature values of the level energies listed in [94] and are implied with their significant numbers.

Step	**Transition**	**Wavelength (nm)**	$\boldsymbol{P_{\mathrm{sat}}}$ **(mW)**
1st	$4s^2\,^1S_0 \rightarrow 4s4p\,^1P_0^\circ$	422.67	0.5(1)
To AIS *ii*:			
2nd	$4s4p\,^1P_0^\circ \rightarrow 4s6s\,^1S_0$	586.75	9.6(29)
3rd	$4s6s\,^1S_0 \rightarrow 3d4f\,^3D_1^\circ$	657.17	18.2(11)
To AIS *IX*:			
2nd	$4s4p\,^1P_0^\circ \rightarrow 4p^2\,^1D_2$	585.74	0.5(1)
3rd	$4p^2\,^1D_2 \rightarrow 3d4f\,^1P_1^\circ$	655.0.1	5.5(2)

Conclusion

The saturation parameters of the transitions in the laser ionization scheme to the autoionizing state IX shown in Figure 5.5b are smaller than for the ionization scheme to the autoionizing state *ii* shown in Figure 5.5 a). Moreover, the autoionizing state IX with FWHM = 16 GHz is narrower than the autoionizing state *ii* with FWHM = 28.1 GHz. Thus, the ionization through the autoionizing state *IX* is the best candidate for a new calcium ionization scheme.

The laser ON/Off ratio for ionization through the autoionizing state IX was measured to about ≈ 300 for a hot cavity heating current of 279 A ($T \approx 2000\,^\circ$C) during the experiment IS532. Under similar conditions (hot cavity heating current of 279 A, $T \approx 2000\,^\circ$C) during experiment IS529, the laser on/off ratio for the previously used ionization scheme (Figure 5.1) was determined to about ≈ 14. This implies an overall improvement of the laser ionization efficiency of calcium of about ≈ 20 with the new calcium scheme. This is a remarkable improvement as it shortens the measurement time by at least* the same factor of 20 and surely the experiments at COLLAPS (IS529) and at ISOLTRAP (IS532) benefited greatly from the improved yields. Moreover, the newly developed laser ionization scheme for calcium will enable future experiments on highly exotic calcium isotopes far away from stability due to the higher ion yield, which were not possible prior to this work.

The experiments illustrate the necessity of a highly efficient ionization scheme for the study of exotic isotopes. At ISOLTRAP, the masses of the exotic calcium isotopes, ^{53,54}Ca, were measured using a newly developed multi-reflection time-of-flight (MR-TOF) mass separator [181] leading to the discovery of a shell closure at neutron number $N = 32$ [177].

*The reduction of the measurement time depends on the measurement conditions. For a background dominated measurement, the reduction of the measurement time can be even stronger.

These isotopes have extremely low production yields, e.g. in the case of ^{54}Ca the ion count rate was only a few ions per second. In this case, one measurement cycle took more than one hour even with the newly developed ionization scheme for calcium. The measurement would not have been possible within the allocated time period without the efficiency improvement of the new ionization scheme.

Part III

In-source laser spectroscopy of polonium

6 Precision measurement of the ionization energy of polonium

The *ionization energy** (IE) is one of the most important parameters of an element. It determines chemical properties such as the reactivity and the stability of its bonds within a chemical compound.
Polonium (Po) is one of the rarest elements in the Earth's crust and mainly appears in uranium ores as an intermediate product of the ^{238}U decay chain (also called the *uranium-* or *radium series*). The amount of ^{210}Po in these ores is estimated to be as little as 0.1 µg per ton [154], which makes the study of naturally occurring polonium extremely challenging. A more effective source of polonium for study by experiments is artificial production at radioactive isotope production facilities such as ISOLDE.
Thus, only very few experiments have investigated the atomic spectrum of polonium so far [31, 32, 93]. A first prediction for the ionization energy of polonium was given by *W. Finkelnburg* and *F. Stern* [61]. They estimated the IE of polonium to be 8.4 ± 0.3 eV by taking into account the regularities of the screening constant $s = Z - Z_{\text{eff}}$ in the periodic table and interpolating the ionization energy between the neighboring elements. *Charles et al.* [31, 32] confirmed this value by semi-empirical calculations following the method of *Russel* [147] and by trying to associate some few lines in the spectra to Rydberg series. This allowed for calculating the ionization energy by applying the Rydberg-Ritz formulas from Equation (2.7) and Equation (2.10). Sansonetti *et al.* lists a literature value of the polonium ionization energy of $\text{IE}_{\text{lit}} = 67860(30)\,\text{cm}^{-1}$, which is the averaged value of the values given in [32] and [31]. Additionally, several theoretical predictions for the ionization energy of polonium have been published with values ranging from 7.90 eV to 8.575 eV [99, 133, 141, 155, 182]. A summary of the experimental and theoretical values can be found in Table 6.1. However, these values are not within close agreement and a determination of the ionization energy of polonium down to a precision of few or below $1\,\text{cm}^{-1}$ had not been achieved.
A very precise method of determining the ionization energy is the spectroscopy of a high-lying series of Rydberg levels, which in turn allows the precise calculation of the ionization energy by fitting the Rydberg-Ritz formulas to the obtained members of these series. At ISOLDE, this method has been recently applied to determine the ionization energy of astatine for the first time [144].
A series of Rydberg levels in the spectrum of polonium has been measured at ISOLDE by resonance ionization spectroscopy using the RILIS. The obtained value of the ionization energy is over two orders of magnitude more precise than that listed in [149].
The following chapter describes the experimental setup, the data taking, and the analysis of these Rydberg levels and the determination of the IE of polonium. The newly obtained

*In literature it is often alternatively referred to as the ionization potential (IP)

Table 6.1: Experimental values and theoretical predictions for the first ionization energy of polonium available prior to the work described in this thesis. If not stated otherwise, the uncertainties are implied by the significant figures.

Author	**Year**	**Method**	**Ionization Energy**	
			(eV)	$\mathbf{(cm^{-1})}$
Finkelnburg *et al.* [61]	1949	Interpolation	8.4 (3)	67750(2500)
Charles *et al.* [32]	1955	Semi-empirical [147]	8.43	67980
Charles *et al.* [31]	1966	Rydberg-Ritz	8.417	67885.3
		Semi-empirical [147]	8.411	67840.0
Seijo [155]	1995	Theoretical	7.90	637000
Peterson *et al.* [133]	2003	Theoretical	8.575	69160
Roos *et al.* [141]	2004	Theoretical	8.29	66900
Sansonetti *et al.* [149]	2005	Evaluation of lit. values [149]	8.414(4)	67860 (30)
Zeng *et al.* [182]	2010	Theoretical	8.271	66710
Laury *et al.* [99]	2012	Theoretical	8.473	68340

value for the ionization energy of polonium is then discussed and compared to the existing literature values, to the experimental results obtained simultaneously at the TRIUMF facility, and to recent theoretical calculations.

6.1 Experimental setup

The target was installed at the HRS separator frontend with a standard RILIS UC_X-target (target #490, 71.5 g/cm^3 UC_X, 14.5 g/cm^3 C, tantalum hot cavity).
As it was discussed in in Chapter 4, polonium beams may be contaminated with a critical amount of isobaric francium. Therefore, a process called *"pseudo off-line measurement"* was used to produce an intense isobar free, quasi-DC* ion current of ^{208}Po [36]. Prior to our measurements, the target was irradiated for several days while being used for another experiment (IS 479). A ^{208}Po ($T_{1/2}$ = 2.898 years) source had been accumulated in the target by direct proton induced spallation and through the proton induced production of its mother nucleus ^{208}At ($T_{1/2}$ = 1.63 h). After the protons were turned off, ^{208}Fr ($T_{1/2}$ = 59.1 s), a possible isobaric contaminant, decayed rapidly because of its much shorter half-life. Shortly after, only ^{208}Po was released at mass $A = 208$ with ion currents of the order of pA from the target matrix due to its long lifetime.
A further advantage of this method for resonance ionization spectroscopy is the absence of noise in the spectrum due to proton induced fluctuations and instabilities of the ion signal (see appendix of [143]). The atoms were then ionized by the RILIS lasers producing

*Stable ion current with relatively low fluctuations.

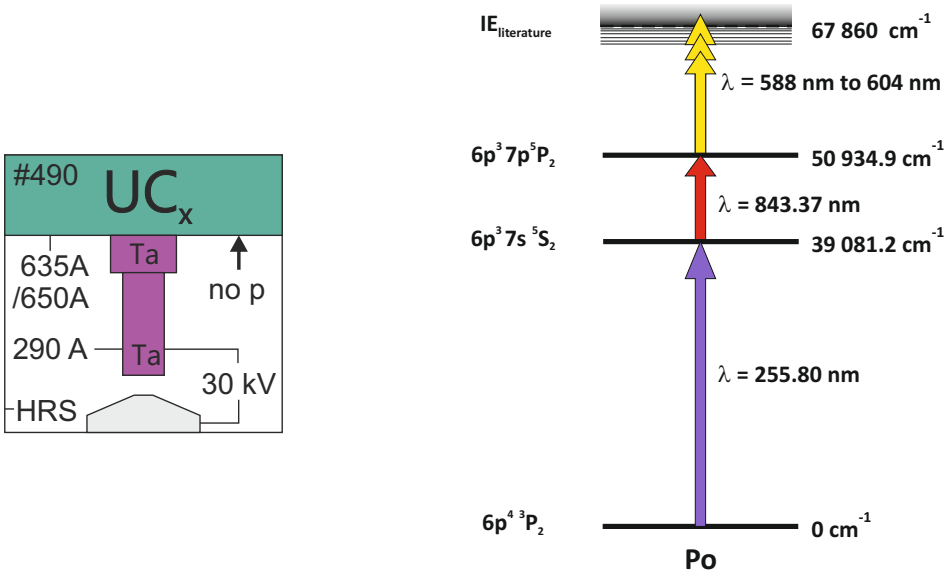

(a) (b)

Figure 6.1: a) Operational parameters of the ISOLDE target used during the measurements of the ionization energy. Design of schematics adopted from [143]. b) Ionization scheme for polonium as used for the Rydberg spectroscopy. The first step was provided by a frequency-tripled dye-laser, the second step by the fundamental output of a Ti:Sa laser and the region around the ionization energy was scanned by a tunable dye laser operated with R6G in ethanol.

an ion current, which was stable over the whole measurement period and which was high enough to be measured directly by the Faraday cup ($\geq 0.1\,\mathrm{pA}$).
Figure 6.1b shows the ionization scheme of polonium as used for the measurement. The intermediate steps are the same as those described in Chapter 4.2.3 and [41]: the first step ($\lambda = 255.80\,\mathrm{nm}$) was provided by a frequency-tripled dye-laser (dye: *styryl 8*, $P \approx 40\,\mathrm{mW}$ in the hot cavity) and the second intermediate step ($\lambda = 843.37\,\mathrm{nm}$) by the fundamental beam of a Ti:Sa laser ($P \approx 1\,\mathrm{W}$ in the hot cavity). The ionizing step, which is usually provided by the 532 nm output of a Nd:YAG pump laser, was replaced by a tunable dye-laser (dye: *rhodamine 6G* (R6G)) for scanning across the expected ionization energy at $67860\,(30)\,\mathrm{cm}^{-1}$ [149]. The laser was scanned over a range of 585 nm - 605 nm ($16530\,\mathrm{cm}^{-1}$ to $17100\,\mathrm{cm}^{-1}$, respectively), equivalent to a scan across the ionization threshold from $67460\,\mathrm{cm}^{-1}$ to $68030\,\mathrm{cm}^{-1}$. The wavelength was measured by the WS7 wavemeter [79].
The power output power of the dye laser is wavelength-dependent and thus, the intensity of the ion signal varies while scanning along the tuning range of the dye. This affects the relative intensities of the different Rydberg levels and has to be considered when comparing the relative heights of the peaks.
The background signal at the Faraday cup HRS.FC690 was of the order of -0.08 pA. This negative offset is due to the decay of radioactive isotopes, which are deposited on the Faraday cup.

For each Rydberg scan, the last step was scanned by the control program of the commercial dye laser, while the wavelength and the Faraday cup current were recorded by the LabVIEW based RILIS control system [142]. This leads to a systematic *DAQ delay* for which the data needs to be corrected (see Section 6.4.1).

6.2 Rydberg scans

Three Rydberg scans around the ionization energy ($W_{\mathrm{lim,lit}} = 67860\,\mathrm{cm}^{-1}$ [149]) were performed during one on-line shift of 8 hours at ISOLDE and the results are shown in Figure 6.2, where the ion current is given as a function of the excitation energy from the second intermediate step at $50934.89(1)\,\mathrm{cm}^{-1}$ ($6p^3(^4S^o)7p$) [31]. Correspondingly, energy ranges and energy levels are given as the excitation energy from the second intermediate state*, W''_{n}, in the following. This simplifies the analysis and allows for the correction of the literature values of the intermediate steps, if necessary. Transitions to Rydberg levels were observed in the range from about $16550\,\mathrm{cm}^{-1}$ to $16975\,\mathrm{cm}^{-1}$, which corresponds to laser wavelengths from 589 nm to 605 nm, respectively.
The three Rydberg scans differ in the scanning direction and speed to allow for correction of the shifts caused by the DAQ-system (*DAQ-shifts*). The scanning speed was reduced by a factor of two for each subsequent scan. The results, together with the estimated resolution, are given in Table 6.2.

Table 6.2: Scanning speeds of the obtained Rydberg spectra and estimated resolution. The uncertainties are implied by the significant figures.

Scan	**Scanning speed (cm^{-1}/s)**	**Resolution (data-points/cm^{-1})**
1	-0.56	3
2	0.28	7
3	-0.14	15

In the spectra presented in Figure 6.2, the general structure of the observed Rydberg series is reproduced but the relative peak heights. This is due to fluctuations in the experimental conditions such as laser power and beam position that occurred during the measurement period. For the data-taking it was preferable to acquire a complete scan with no external corrective action, than to attempt continuous ion-rate optimization during the scans. However, it is thus difficult to draw conclusions about the relative intensities observed in different scans. It is possible that the use of some Rydberg-levels might improve the efficiency of the laser ionization scheme for polonium [36], but this would require a careful comparison of the two ionization methods and time restriction did not allow this.

*In the following, a double-primed value always refers to an observable, which is given relative to the second intermediate state.

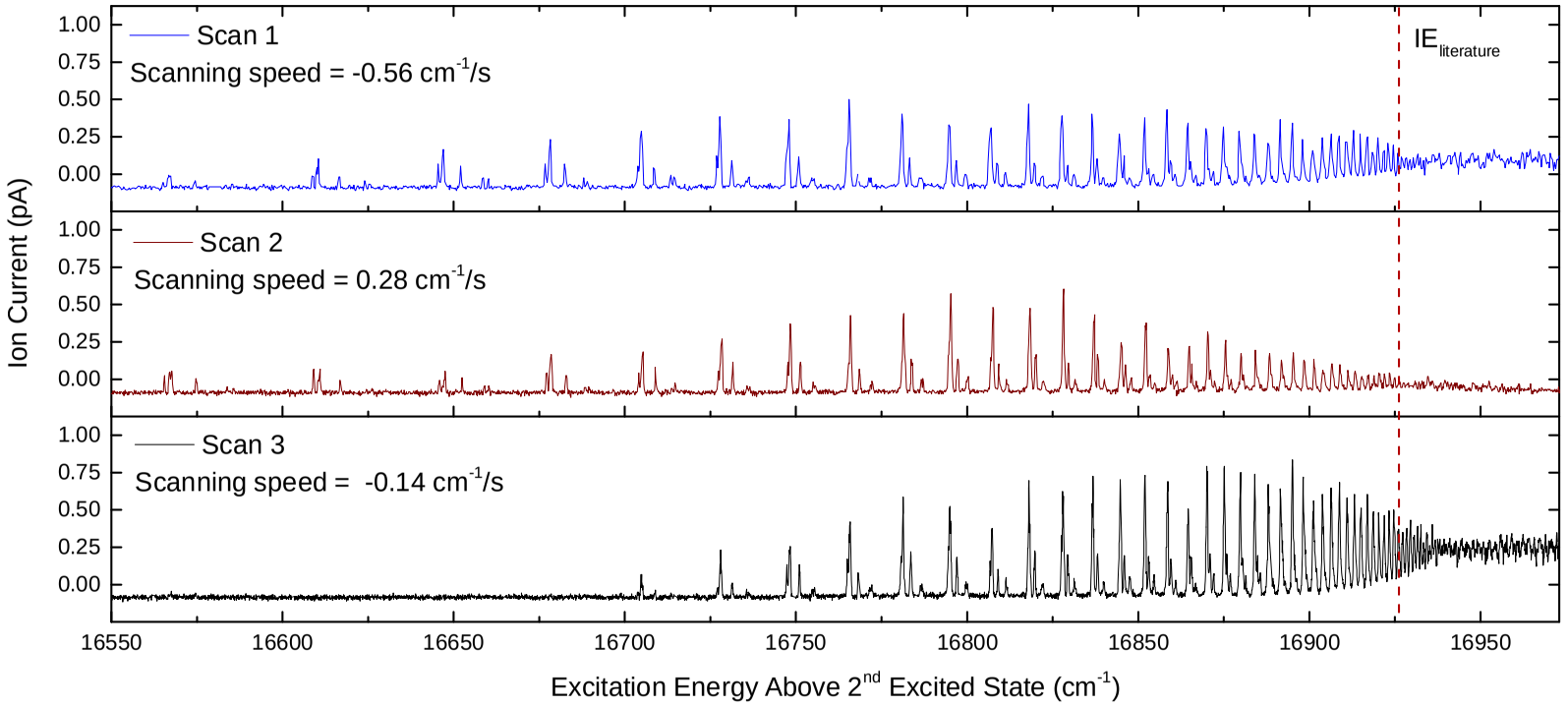

Figure 6.2: The three Rydberg scans of ^{208}Po, which were obtained during the measurement campaign. The wavenumbers correspond to the energy from the last intermediate step at 50934.9 cm^{-1} with configuration $6p^3(^4S^o)7p$ [31]. The first and the third Rydberg scans covered a region which crossed the literature value of the ionization energy of 67860 cm^{-1} (16925.1 cm^{-1} from the second step) to well below the ionization energy [149]. Scan 2 was scanned in the opposite direction. The scanning speed of all three scans differed from each other, which led to a different resolution. Variations in peak heights during a scan may originate from the change in laser beam position inside the cavity. Differences between the scans indicate slightly different conditions of the RILIS or the ISOLDE target.

6.3 Analysis of the Rydberg spectra

Each obtained Rydberg spectrum was analyzed individually. In the following the procedure is explained using Rydberg scan 3 as an example, but Rydberg scans 1 and 2 were analyzed similarly. Figure 6.3 a shows the detailed structure of scan 3. In total 93 peaks could be resolved. The spectrum contains a repetitive substructure of 5 peaks, each belonging to a separate Rydberg series. These subseries converge eventually to the center of gravity of the group for higher energies towards the ionization energy. The five peaks, which all have the same principal quantum number n, are referred to as one group (g).

6.3.1 Identification of the subseries and peaks in the Rydberg scans

Figure 6.3 b shows a zoom into the spectrum of a low-lying group ($g = 7$) of Rydberg states from 16746 cm^{-1} to 16757 cm^{-1}. Each peak is well-resolved and belongs to one of the five subseries. The labeling with arbitrary names from the lowest-lying series to the highest lying series is as follows: Π, Θ, Σ, Ω, and Φ. Within one group, the second subseries Θ is the strongest and the first subseries Π and the isolated subseries Ω in the middle of the group are about half as strong as subseries Θ. The fourth subseries Ω and the fifth subseries Φ are much weaker than the others.
These subseries converge towards higher energies and become unresolved in an enveloping peak, which are then treated as a new individual subseries. The different stages of the merging of the subseries are shown in Figure 6.3 b-d: in Figure 6.3 c, the first two subseries and the last two subseries become indistinguishable and are denoted as $\overline{\Pi\Theta}$ and $\overline{\Omega\Phi}$; then, the third subseries Σ merges with the first two subseries to become subseries $\overline{\Pi\Theta\Sigma}$; Figure 6.3 c shows the subseries very close to the ionization energy; all series converge eventually to the center of gravity of the group, which is then denoted as the subseries $\overline{\Pi\Theta\Sigma\Omega\Phi}$.
The point from which the subseries start to merge depends on the resolution of the scan and consequently more Rydberg levels were resolved for scan 3 since it has the highest resolution due to the slow scanning speed.
In total 97 resonances were resolved in scan 1 and 93 resonances were resolved in scan 2 and scan 3. In scan 1 and scan 2, the peaks belong to 39 identified groups and in scan 3 to 48 identified groups. Each group is numbered, starting with $g = 1$ for the lowest-lying Rydberg group of scan 1 and 2 visible in Figure 6.2. Correspondingly the lowest lying group visible in scan 3 is $g = 6$.

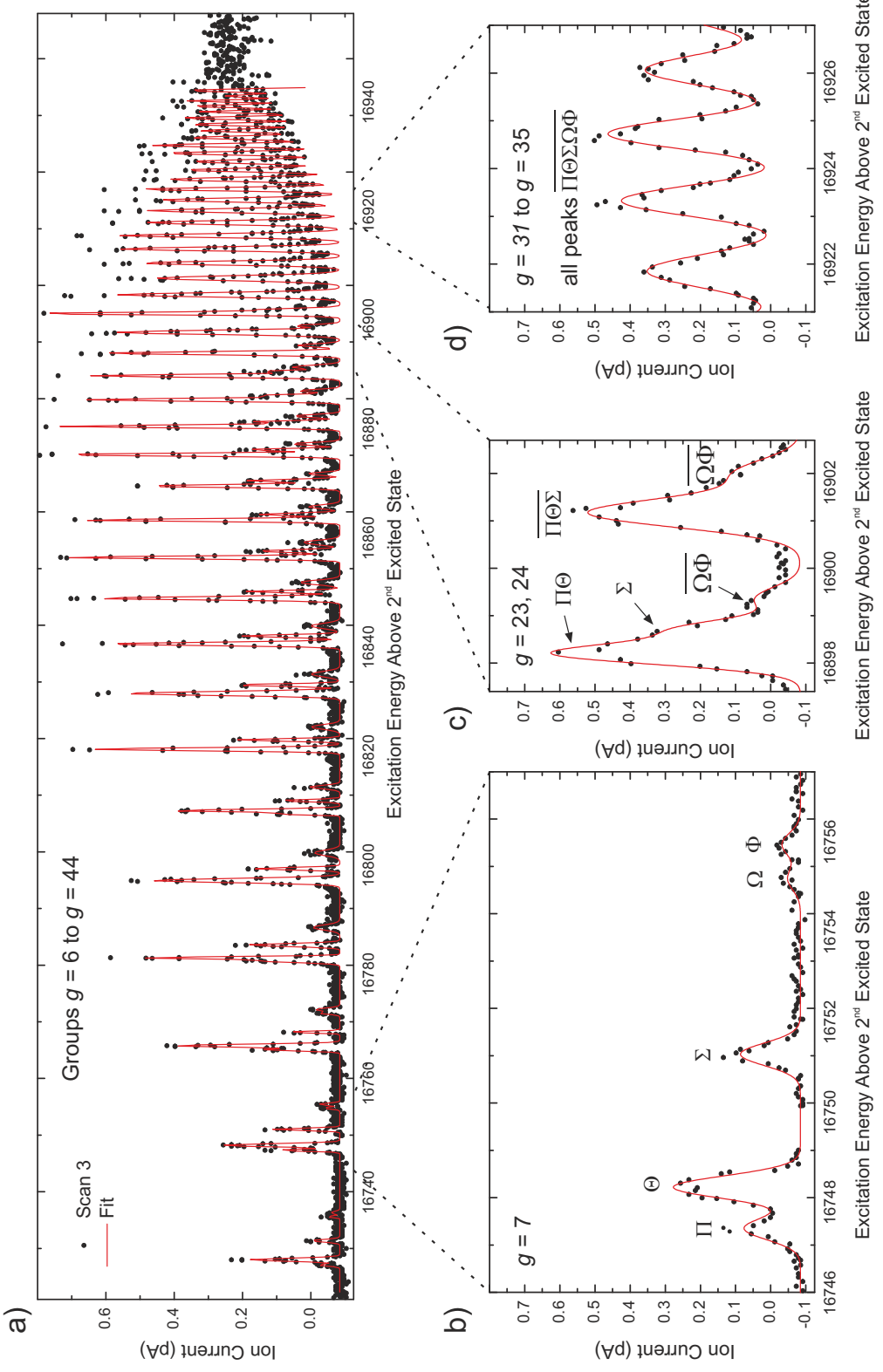

Figure 6.3: a) Rydberg spectrum recorded in scan 3 with the multi-peak fit to all well-resolved peaks. 88 resonances (93 resonances in all three scans) could be unambiguously resolved and were fitted by overlapping Gaussian line-shapes. b) Zoom from 16746 cm^{-1} to 16757 cm^{-1} into the energy region of group $g = 7$: the Rydberg series denoted as Π, Θ, Σ, Ω, and Φ are well-resolved. c) Zoom from 16897 cm^{-1} to 16903 cm^{-1}: Π and Θ converged and are denoted as $\overline{\Pi\Theta}$. Σ is still distinguishable in group $g = 23$, but converges in group $g = 24$ to $\overline{\Pi\Theta\Sigma}$. Ω and Φ converged to $\overline{\Omega\Phi}$ in both groups. d) Zoom from 16921 cm^{-1} to 16927 cm^{-1}: the individual subseries are no longer resolved in groups $g = 31$ to $g = 35$. The subseries converged to the center of gravity of the main series, which is denoted as $\overline{\Pi\Theta\Sigma\Omega\Phi}$.

6.3.2 Fitting

The fitting was performed using the *Origin Pro © 9.0* analysis software. To determine the center of each well-resolved peak, one or more groups were fitted simultaneously with a multipeak fit of superposed Gaussians for each scan. The equation describing this is:

$$F(\tilde{\nu}) = y_0 + \sum_{i=1}^{N} \frac{A_i}{w_i\sqrt{\pi/2}} \cdot e^{-2\frac{\left(\tilde{\nu}-\tilde{\nu}_{c,i}\right)^2}{w_i^2}}, \tag{6.1}$$

where y_0 is the FC background level, which is kept constant for each scan, A_i is the area under the i^{th} peak, $w_i = 2\sigma_i$ is the peak width, and $\tilde{\nu}_{c,i}$ is the wavenumber of the center of peak i. The common background level y_0 was determined for each scan before the multipeak fit by fitting a straight line to the background signal well below the ionization energy and was then kept fixed during the actual fitting. The peak width of the well-resolved resonances was on average FWHM $\approx 0.4\,\text{cm}^{-1}$. This was taken as a lower limit and, for a single fully resolved peak, it corresponds to the expected Doppler broadening in the hot cavity. No upper limit was set in order to take into account the merging of the subseries and the corresponding broadening.
The groups below $16740\,\text{cm}^{-1}$ (see Figure 6.2) were considered to be independent of the neighboring groups and were fitted individually by a multipeak fit. All groups from $16740\,\text{cm}^{-1}$ to about $16940\,\text{cm}^{-1}$ were fitted by one multi-peak fit to take potential superpositions of the peaks of neighboring groups into account. For these cases, the high number of fitting parameters made it necessary to fit in several stages: first, the wavenumbers of the peak centers were initialized and the width was shared for all peaks during the first fit. Then, the width was fitted freely with a lower limit of $0.4\,\text{cm}^{-1}$. If necessary, centroids and widths were slightly varied until the fit converged by X^2-minimization. The overall uncertainty of each peak centroid is between $0.01\,\text{cm}^{-1}$ and $0.1\,\text{cm}^{-1}$ depending on the statistics and how well resolved the individual peak is. Table 6.3 gives an overview about the most important parameters of the analysis.
Note that the obtained values for the centroid of the peaks show a systematic shift between the scans due to the different scanning speeds caused by a delay in the DAQ system.

Table 6.3: Characteristics of the three different Rydberg scans and the fitting results: peaks and groups that were identified, Faraday cup background levels and wavenumbers of the first and the last identified peak. The levels are not yet corrected for the systematic shift of the spectra due to the DAQ delay.

Scan	**# peaks**	**Range groups** g_{min}-g_{max}	**Background (pA)**	**First peak (cm^{-1})**	**Last peak (cm^{-1})**
1	97	1 – 39	−0.0896 (6)	16565.09 (9)	16924.54 (3)
2	93	1 – 39	−0.0895 (6)	16565.49 (2)	16924.91 (6)
3	93	6 – 48	−0.0847 (2)	16703.86 (6)	16934.41 (2)

6.4 Evaluation of Rydberg peak position

6.4.1 Correction for the systematic shift of the spectra due to the DAQ delay

A systematic shift of the peak positions is observed between the different scans. This is illustrated in Figure 6.4a which shows the Rydberg state series Σ in group $g = 7$. The peak position of scan 1 is shifted towards lower wavenumbers compared to scan 3, while the peak position of scan 2 is shifted towards higher wavenumbers compared to scan 3. It is furthermore observed that the lineshape broadens slightly for faster scan speeds (see Figure 6.4a). Both effects can be explained by the different acquisition speeds of the wavemeter and the Faraday cup: while the wavenumber is measured about 28 times per second, the Faraday-cup DAQ integrates the ion current over a half a second and thus measures only 2 values per second. This results in a systematic shift of the measured wavenumber. Additionally, the lineshape is broadened due to the increased ion current that is recorded on rising and falling peak flanks.
The overall systematic DAQ-shift of the peaks was determined by calculating the weighted average of the systematic shifts of several well-resolved and undisturbed peaks of series Σ,

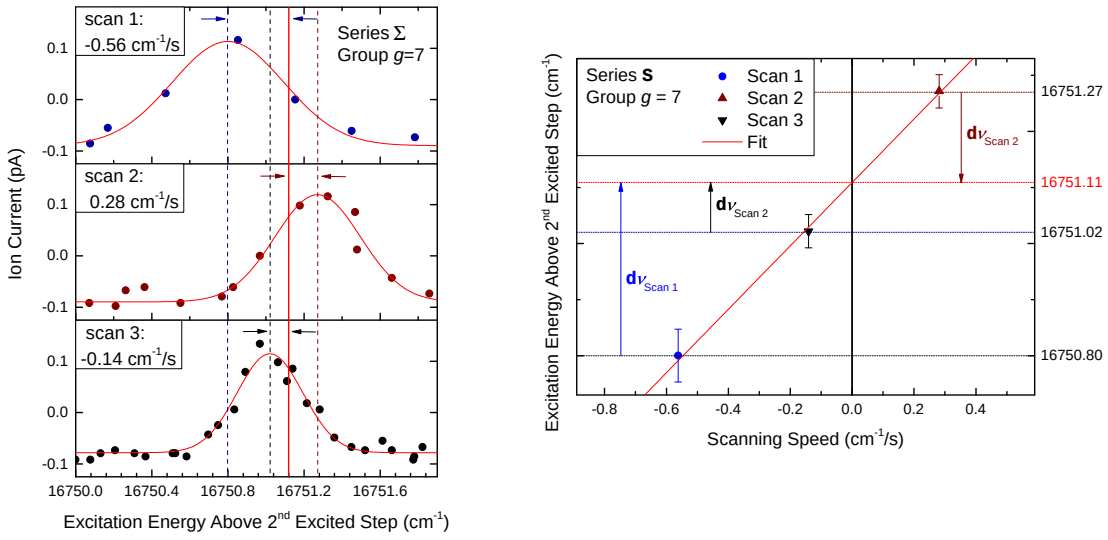

(a) (b)

Figure 6.4: A representative example of the determination of the systematic shift due to the DAQ delay, conducted for the resonance of series Σ in group $g = 7$. a) Plot and fit of the resonance of series for the three Rydberg scans. The estimated real position of the peak is given by the red solid line and the shifts to the measured peak positions are indicated with the arrows. b) The peak position as a function of the scanning speed and a fit to the data (red solid line). The real position of the centroid is defined as the intercept of the straight line with the abscissa (scanning speed of $0\,\mathrm{cm}^{-1}/\mathrm{s}$).

for which it was certain that no superposition with neighboring series could disturb the peak. In total, 13 of such resonances ($g = 7$ to $g = 19$) appear in each scan.
As shown in Figure. 6.4b, the systematic shift, $\delta\tilde{\nu}$, of the peaks is proportional to the scanning speed. This allows for the determination of the real peak position at a scanning speed of $0\,\mathrm{cm}^{-1}/\mathrm{s}$ by fitting a straight line to the data and interpolating to the intercept. This procedure was repeated for the other 12 undisturbed peaks of the series Σ and the results of all fits are given in Table A.1 in the Appendix A. No systematic wavenumber-dependent trend in the DAQ-shifts was observed. The correction factor was then determined by calculating the weighted average of all the individual DAQ-shifts, for which the fitting uncertainty was taken as the weighting factor. The uncertainty of the systematic DAQ-shift was obtained by calculating the standard deviation of the scans to the weighted average. Table 6.4 lists the systematic DAQ-shifts of the peaks obtained for each scan.

Table 6.4: Details of the systematic shift due to the time delay in the DAQ. Different frequency steps, measured scanning speeds and corresponding systematic DAQ-shift, $\delta\tilde{\nu}$ obtained by the fit and the uncertainty of the DAQ-shift, $\Delta\delta\tilde{\nu}$.

Scan	**Steps size** ($\mathbf{cm^{-1}}$)	**Scanning speed** ($\mathbf{cm^{-1}/s}$)	$\boldsymbol{\delta\tilde{\nu}}$ ($\mathbf{cm^{-1}/s}$)	$\boldsymbol{\Delta\delta\tilde{\nu}}$ ($\mathbf{cm^{-1}/s}$)
1	0.02	-0.56	-0.275	0.073
2	0.01	0.28	0.138	0.047
3	0.005	-0.14	-0.074	0.045

6.4.2 Evaluation procedure for the determination of the peak positions

The final values of the transition wavenumbers to the Rydberg levels were calculated by correcting the measured peak values in each scan for the systematic DAQ-shift and averaging the results from the individual analysis of the three Rydberg scans. The procedure is summarized in the following and the final results for each observed level can be found in Table B.1 in Appendix B.1.

Correction of the fit results for the systematic DAQ-shift due to the DAQ delay: In order to obtain the DAQ-shift corrected centroids $\tilde{\nu}'_{i,j,k}$, the DAQ-shifts $\delta\tilde{\nu}_k$ of each Rydberg scan given in Table 6.4 were added to each centroid $\tilde{\nu}_{i,j,k}$ (i: Rydberg series, j: group number, k: scan number):

$$\tilde{\nu}'_{i,j,k} = \tilde{\nu}_{i,j,k} - \delta\tilde{\nu}_k \tag{6.2}$$

Calculation of the uncertainties of the DAQ-shift corrected peaks: The statistical error of the DAQ-shift corrected centroid is given by the uncertainty of the multipeak fit and the statistical uncertainty of the wavemeter $\Delta\mathrm{WM} = 0.02\,\mathrm{cm}^{-1}$ [79]. In addition, a systematic error due to the DAQ-shift $\Delta\delta\tilde{\nu}_k$ needs to be added. The systematic error of the wavemeter will be added later to the final combined values

of the centroids and to the uncertainty of the evaluated ionization energy since this systematic is a property of the combined values of all three scans. Thus, the total error of the DAQ-shift corrected centroids calculates to:

$$\Delta\tilde{\nu}'_{i,j,k} = \sqrt{(\Delta\tilde{\nu}_{i,j,k})^2 + (\Delta\mathrm{WM})^2} + \Delta\delta\tilde{\nu}_k \tag{6.3}$$

The position of the Rydberg levels: The calculation of the final value of the combined centroids depends on the number of scans in which the individual Rydberg level was resolved. Most peaks were resolved in at least two or three scans ($N = 2, 3$). In these cases, the final values of the Rydberg levels were obtained by calculating the weighted mean for each Rydberg level $W''_{i,j}$:

$$W''_{i,j} = \frac{\sum_{k=1}^{N=k} \tilde{\nu}'_{i,j,k} w_{i,j,k}}{\sum_{k=1}^{N=k} w_{i,j,k}} \quad \text{with} \quad w_{i,j,k} = \frac{1}{\Delta\tilde{\nu}'_{i,j,k}}\,, \tag{6.4}$$

where $w_{i,j,k}$ is the weighting factor. If a Rydberg level was only resolved in one scan ($N = 1$), the DAQ-shift corrected value from Equation (6.2) was taken:

$$W''_{i,j} = \tilde{\nu}'_{i,j,k}\,. \tag{6.5}$$

The excitation energy of the Rydberg level with respect to the ground state is then given by

$$W_{i,j} = W'' + W''_{i,j}\,, \tag{6.6}$$

where W'' is the total excitation energy with respect to the energy of the second excited state in the ionization scheme.

Final error of Rydberg levels: In case the Rydberg state $W''_{i,j}$ was observed in at least two Rydberg scans ($N \geq 2$), the final statistical uncertainty is given by the standard deviation $\sigma_{i,j}$ of the DAQ-shift corrected fit values $\tilde{\nu}'_{i,j,k}$ around the weighted mean of the Rydberg level $W''_{i,j}$. If a Rydberg level was only resolved in one peak ($N = 1$), the error of the DAQ-shift corrected value $\Delta\tilde{\nu}'_{i,j,k}$ was taken. In order to treat the errors conservatively, a lower limit for the statistical uncertainty of the Rydberg level was estimated by calculating the average standard deviation, $\bar{\sigma} = 0.06\,\mathrm{cm}^{-1}$, of all Rydberg levels. This can be summarized by:

$$\Delta W_{i,j} = \begin{cases} \sigma_{i,j} & \text{if } N \geq 2 \text{ and } \sigma_{i,j} > \bar{\sigma} \\ \Delta\tilde{\nu}'_{i,j,k} & \text{if } N = 1 \text{ and } \Delta\tilde{\nu}'_{i,j,k} > \bar{\sigma}\,. \\ \bar{\sigma} = 0.06\,\mathrm{cm}^{-1} & \text{if } \sigma_{i,j}, \Delta\tilde{\nu}'_{i,j,k} \leq \bar{\sigma} \end{cases} \tag{6.7}$$

For the final values $W_{i,j}$ of all observed Rydberg levels (see Table B.1 in Appendix B.1) the systematic uncertainty of the wavemeter was added.

6.5 Detailed analysis of the ionization energy of polonium

The ionization energy of polonium was calculated by fitting the Rydberg formula (Equation (2.7)) and Rydberg-Ritz formula (Equation (2.10)) to the final values of the Rydberg level from Table B.1.
For practical reasons, the ionization energy is calculated with respect to the second excited state $W''_{\mathrm{lit}} = 50934.89\,\mathrm{cm}^{-1}$ [31] throughout the rest of the chapter and will be denoted as W''_{lim}. This allows for a simpler correction of the total ionization energy W_{lim}, in case the literature value of the second step is measured more precisely in the future. The ionization energy can then be calculated by:

$$W_{\mathrm{lim}} = W''_{\mathrm{lit}} + W''_{\mathrm{lim}}\,. \tag{6.8}$$

Using the conventions defined in Chapter 2.1.2 for the excitation energy W_n and the energy E_n of an intermediate atomic level, $W_n = E_n - E_0$, the excitation energies W''_n of the Rydberg levels can then be calculated to the first order by using the Rydberg formula (Equation (2.7)) and setting the charge to $\zeta = 1$ for a singly ionized ion:

$$W''_{\mathrm{n}} = W''_{\mathrm{lim}} - \frac{R_M}{(n^*)^2} = W''_{\mathrm{lim}} - \frac{R_M}{(n-\delta_{n,l})^2}\,, \tag{6.9}$$

where n^* is the effective quantum number, n the principal quantum number and $\delta_{n,l}$ the quantum defect. The reduced-mass Rydberg constant for ^{208}Po is calculated to $R_M = 109737.0262385\,(8)$ by Equation (2.5) using the values for the Rydberg constant and electron mass recommended in CODATA [121] and the mass of ^{208}Po given in the AME2012 [173].
If the ionization energy W''_{lim} is known, the effective quantum number n^* can be calculated from Equation (6.9) by

$$n^* = \sqrt{\frac{R_M}{W''_{\mathrm{lim}} - W''_n}}\,. \tag{6.10}$$

In the case of a dependency of the quantum defect on the principal quantum number n as described in Chapter 2.1.2, the ionization energy is calculated to second order using the Rydberg-Ritz formula (Equation (2.10)):

$$W''_{\mathrm{n}} = W''_{\mathrm{lim}} - \frac{R_M}{\left(n - A + \frac{B}{(n-A)^2}\right)^2}\,. \tag{6.11}$$

The ionization energy, W''_{lim}, with respect to the excitation energy of the second excited state, W''_{lim}, is obtained by a fit of Equation (6.9) or Equation (6.11) to a series of Rydberg levels.

6.5.1 Substitution of principal quantum number and quantum defect

In practice it can be difficult to assign the real principle quantum number n to high-lying Rydberg levels. An unambiguous allocation of a principal quantum number to each Rydberg level is only possible, if the head* of the Rydberg series, or other members of the same Rydberg series, are described in the literature. A possible assignment of the principle quantum numbers to the Rydberg levels will be discussed in Chapter 6.5.5.
However, to keep the following calculation and discussions free from speculations on the real principal quantum number, the principal quantum number n and the quantum defect δ are substituted in the following:

$n \to n'$: The principal quantum number n must be larger than the effective quantum number $n^* = n - \delta$ since $\delta > 0$. Hence, n is substituted by the minimum value for the principal quantum number n', which can be expressed by:

$$n' = \text{int}\,[n^*] + 1\,. \tag{6.12}$$

Alternatively, n' can be defined by introducing an integer Δn, which is the difference between n' and the principal quantum number n:

$$n' := n - \Delta n\,. \tag{6.13}$$

$\delta \to \delta'$: The quantum defect δ can be substituted by the *remainder of the quantum defect* δ', which is calculated by:

$$\begin{aligned} \delta' &= \text{mod}_1\,[\delta] \\ &= \text{mod}_1\,[n - n^*] \\ &= \text{mod}_1\,[-n^*]\,. \end{aligned} \tag{6.14}$$

Similar to n', δ' can be alternatively defined using an integer $\Delta\delta$, which is the difference between the remainder of the quantum defect δ' and the quantum defect δ:

$$\delta' := \delta - \Delta\delta\,. \tag{6.15}$$

It can be easily verified that $\Delta n \equiv \Delta\delta$:

$$\begin{aligned} \delta' &= n' - n^* && |\delta' = \delta - \Delta\delta,\ n' = n - \Delta n \\ \delta - \Delta\delta &= n - \Delta n - n^* && |-n \\ \delta - \Delta\delta - n &= -\Delta n - n^* && |n^* = n - \delta \\ \Delta\delta &\equiv \Delta n\,. \end{aligned} \tag{6.16}$$

Once it is possible to allocate the data unambiguously, this approach allows for a simple correction to the obtained values of n' and δ' for Δn and $\Delta\delta$, respectively.
The calculation of the value of the ionization energy by Equation (6.9) and Equation (6.11) is independent of the choice of the principal quantum number and the quantum defect.

*Low-lying members of a Rydberg series, for which the principal quantum number n is known.

6.5.2 Visualization of the Rydberg series

The different subseries can be visualized by plotting the remainder of the quantum defect δ' as a function of the minimum principal quantum number n'. This allows for first conclusions about the relative weight of one subseries in a merged series and the dependency of the quantum defect on the principal quantum number and simplifies the further discussion.
In order to obtain δ' and n', a first fit of the ionization energy was performed by fitting the Rydberg formula (Equation (6.9)) to the members of series Σ ($g = 1$ to $g = 21$) and by substituting n with their group number g. The Rydberg fit and the fit residuals are shown in Figure 6.5a. This approach leads to a first determination of the ionization energy with respect to the second excited state, W'', of polonium of

$$W''_{\mathrm{lim},\Sigma} = 16961.42(1)\,.$$

This first iteration is precise enough to calculate δ' and n' by Equation (6.9), Equation (6.12) and Equation (6.14) for the visualization of the series. The uncertainties of δ' are calculated with an error propagation of the uncertainties by taking into account the fit uncertainties of the centroids ΔW_{n}, the fit uncertainty of the second step ionization energy $\Delta W''_{\mathrm{lim},\Sigma}$ and the uncertainty of the reduced Rydberg constant of Polonium ΔR_M.

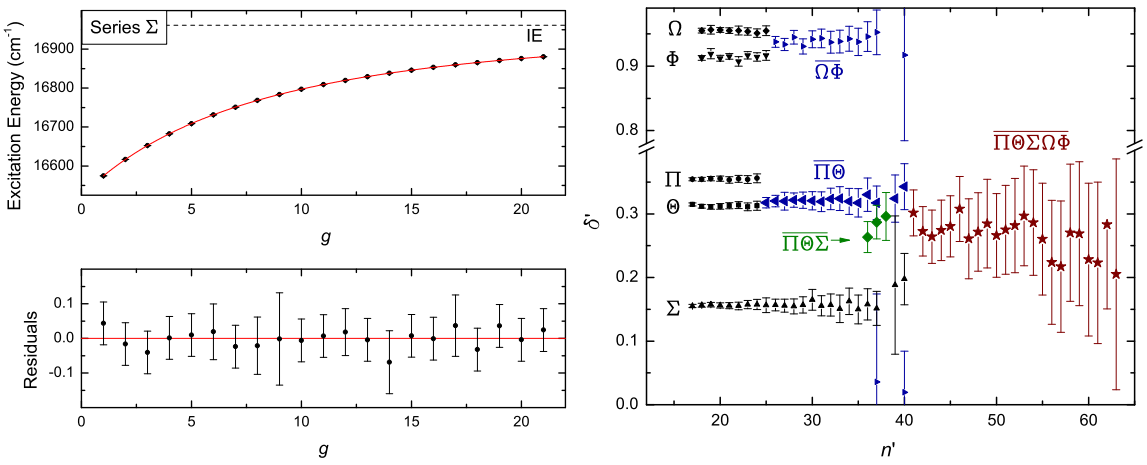

(a) (b)

Figure 6.5: a) Top: the excitation energy of the well-resolved peaks of series Σ as a function of the group number g. The red solid line is a fit of the Rydberg formula to the data. Bottom: the residuals of the fit values show no trend and also no distortions. b) Remainder of the quantum defect δ' as a function of the minimum principle quantum number n' calculated from the results of the fit shown in (a).

The corresponding n'-δ' plot for the observed Rydberg levels is shown in Figure 6.5b. Each subseries and merged series are distinguishable by comparing the corresponding δ'-values. The δ' of the lower n' do not change significantly, when compared to the δ' of the resonances with higher principal quantum numbers, n.
For some resonances, δ', differs slightly to the overall trend of the corresponding series. This mainly occurs for peaks in which the individual subseries are visible, but not clearly resolved from the neighboring series and thus, these peaks were omitted from the fit.

6.5.3 Determination of the ionization energy with respect to the second excited state

The final value of the ionization energy with respect to the second excited state at $W'' = 50934.89(1)\,\mathrm{cm}^{-1}$ was determined by three different methods:

Method 1: Rydberg fit to only the strongest peaks of each group.

Method 2: Individual Rydberg fits for all resolved Rydberg series and merged series. W''_{lim} was calculated by the weighted average.

Method 3: Global fit to all Rydberg series with the ionization energy as a shared fitting parameter.

For each method, the Rydberg formula Equation (6.9) and the Rydberg-Ritz formula of second order in Equation (6.11) were fitted. However, the fits with the Rydberg-Ritz formula led to an unrealistic value for the parameter B with uncertainties as large or larger than the value. Additionally, the ionization energy showed a dependency on the parameter B. Therefore, a further use of the Rydberg-Ritz formula was omitted and only the Rydberg formula was used for the calculation of the ionization energy in the following.

Method 1: Rydberg fit to strongest peaks

As shown in Figure 6.5b, the strongest observed peaks in each group are the members of the subseries Θ and the corresponding merged series $\overline{\Pi\Theta}$. The full range of the Rydberg scan is then covered by Θ, $\overline{\Pi\Theta}$ and the center of gravity series $\overline{\Pi\Theta\Sigma\Omega\Phi}$ for a combined Rydberg fit with the Rydberg formula as shown in Figure 6.6.
With method 1, the ionization energy with respect to the second excited state is $W''_{\mathrm{lim,M1}} = 16961.45(1)$ and the common remainder of the quantum defect is $\delta' = 0.3149(9)$. This value differs slightly to the one obtained from the fit of the well-resolved peaks of series Σ.
However, the residuals are not uniformly continuous and show jumps of up to $0.2\,\mathrm{cm}^{-1}$ between the individual series. This illustrates the need of an individual fit with a free δ for each subseries, as it was performed for method 2 and method 3.

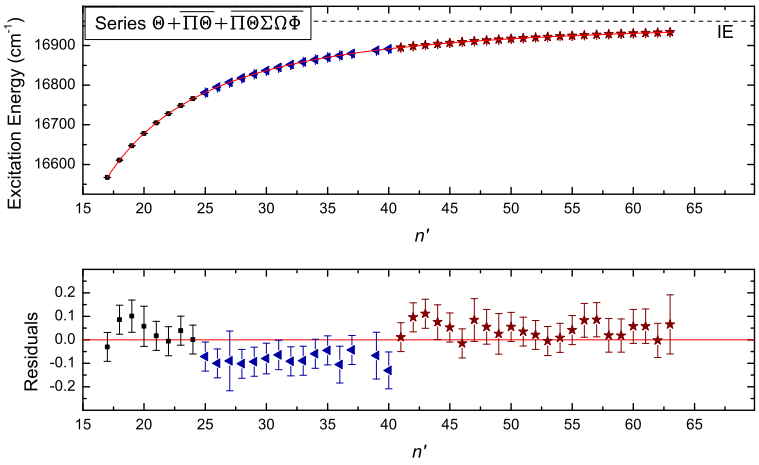

Figure 6.6: The fit of the Rydberg formula to the combined series of Θ, $\overline{\Pi\Theta}$ and $\overline{\Pi\Theta\Sigma\Omega\Phi}$ from method 1. The symbols used for the individual series are the same as introduced in Figure 6.5b. Jumps of the residuals are visible where a new series begins.

Method 2: weighted mean of individual fits to all series.

In a second approach, each subseries was analyzed separately and the final value of the ionization energy was determined by calculating the weighted average of all individually obtained ionization energies, for which the fit uncertainties were taken as weighting factors. The results are given in Table 6.5.
It should be noted that not all the peaks of each series were used, since peaks, which were not fully resolved or for which the residuals were diverging from the fit were not taken into account. Table 6.5 gives the range of the corresponding n'-values for the Rydberg

Table 6.5: Results of the separate Rydberg fits to each individual Rydberg series and weighted average of the ionization energy.

Series	**Range *n'***	**δ' (cm^{-1})**	**W''_{lim} (cm^{-1})**
Π	17 - 24	0.3544(8)	16961.41(2)
Θ	17 - 24	0.3145(17)	16961.47(5)
Σ	17 - 37	0.1559(5)	16961.42(1)
Ω	18 -21, 23 - 25	0.9580(16)	16961.50(4)
Φ	18, 20, 21, 23 - 25	0.9113(29)	16961.33(5)
$\overline{\Pi\Theta}$	25 - 37, 39, 40	0.3165(19)	16961.38(2)
$\overline{\Omega\Phi}$	26 - 37	0.9331(45)	16961.37(4)
$\overline{\Pi\Theta\Sigma\Omega\Phi}$	41 - 65	0.30153(11)	16961.47(2)
Weighted average			**16961.415(7)**

resonances, which were used. The uncertainty was determined by calculating the standard deviation of the difference of the individual results of each series to the weighted average. The obtained ionization energy with respect to the second excited state of $W"_{\mathrm{lim,M2}} = 16961.415\,(7)\,\mathrm{cm}^{-1}$ agrees with the value from method 1 within the uncertainties. The uncertainty however, is significantly higher due to the scattering of the individual values, but the uncertainty of Method 1 is most likely underestimated.

Method 3: global fit to all individual series.

In a third attempt, the Rydberg formula was globally fitted to the individual Rydberg series, where the ionization energy with respect to the second excited state, W''_{lim}, was a shared parameter. Only the remainder of the quantum defect δ' was an individual fitting parameter. The ranges of the n' of the used Rydberg levels correspond to the ranges used in method 2.
This approach has the advantage that it uses all the available statistics in one fit for the determination of the ionization energy, while taking into account the different quantum defects of each individual subseries. Table 6.6 lists the fit results for δ' and Figure 6.7 shows the residuals for each Rydberg series. The residuals are stable for the whole range of Rydberg levels and the obtained ionization energy with respect to the second excited state obtained by the global fit is:

$$W''_{\mathrm{lim,M3}} = 16961.420(8)\,\mathrm{cm}^{-1}.$$

This value agrees well with the result from method 2, but differs from the result obtained by method 1.

Table 6.6: Quantum defects obtained by the global fit of the Rydberg formula to all series with a shared ionization energy with respect to the second excited state, $W''_{\mathrm{lim,global}}$.

Series	**Range *n'***	***δ'***
Π	17 - 24	0.3548(87)
Θ	17 - 24	0.3130(5)
Σ	17 - 37	0.1561(5)
Ω	18 -21, 23 - 25	0.9548(7)
Φ	18, 20, 21, 23 - 25	0.9145(7)
$\overline{\Pi\Theta}$	25 - 37, 39, 40	0.3204(15)
$\overline{\Omega\Phi}$	26 - 37	0.9384(14)
$\overline{\Pi\Theta\Sigma\Omega\Phi}$	41 - 65	0.3204(15)

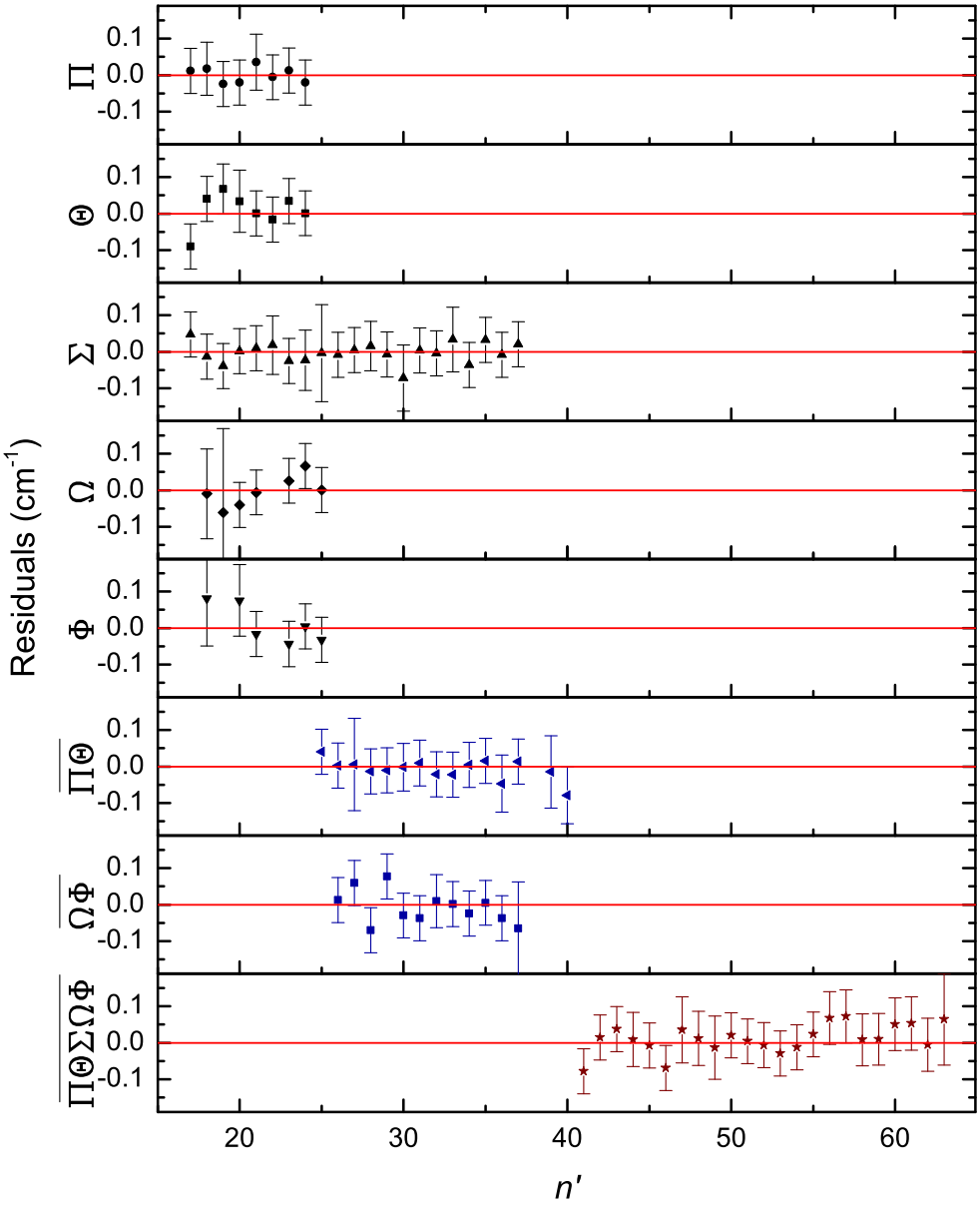

Figure 6.7: Residuals for each Rydberg series obtained by the global fit of method 3: a global fit to all series for which the ionization energy with respect to the second excited state was a shared fit parameter.

6.5.4 Final result of the ionization energy of polonium

The total ionization energy of polonium from the ground-state, W_{lim}, is given by the excitation energy of the second excited state, W'', and the ionization energy with respect to the second excited state, W''_{lim}:

$$W_{\mathrm{lim}} = W'' + W''_{\mathrm{lim}} \,. \tag{6.17}$$

The second step, $W'' = 50934.89(1)\,\mathrm{cm}^{-1}$, was taken from [31] and the result of method 3 for the ionization from the second state, $W_{\mathrm{lim,M3}} = 16961.420(8)\,\mathrm{cm}^{-1}$ was taken for the final value since it combines the advantage of taking the whole data set in one fit into account and no shifts of residuals.
Several uncertainties have to be considered in the calculation of the total ionization energy:

Statistical uncertainties: The uncertainty of the literature value of the second excited step is of the order of $\Delta W''_{\mathrm{lit}} = 0.01\,\mathrm{cm}^{-1}$ according to [31] an the fit uncertainty of the ionization energy with respect to the second excited state is $\Delta W''_{\mathrm{lim}} = 0.008\,\mathrm{cm}^{-1}$. The overall statistical uncertainty then calculates by error propagation to $\Delta W_{\mathrm{lim,stat}} = 0.012\,\mathrm{cm}^{-1}$.

Systematic uncertainty: Systematic uncertainties arise from the wavemeter and the DAQ system. The systematic uncertainty of the *HighFinesse WS7* wavemeter was estimated to $\Delta\tilde{\nu}_{\mathrm{WM}} = 0.03\,\mathrm{cm}^{-1}$ in [143] by comparing the output of wavemeter *WS7* to the output of wavemeter *WS6*.

The final result of the ionization energy of polonium is therefore given by:

$$\begin{aligned} W_{\mathrm{lim}} &= W''_{\mathrm{lit}} + W''_{\mathrm{lim}} \\ &= 50934.89(1)\,\mathrm{cm}^{-1} + 16961.420(8)(30)\,\mathrm{cm}^{-1} \\ &= 67896.310(13)(30)\,\mathrm{cm}^{-1}\,. \end{aligned} \tag{6.18}$$

In alternative units, the ionization energy of polonium can be written as

$$\begin{aligned} W_{\mathrm{lim}} &= 67896.310(13)(30)\,\mathrm{cm}^{-1} \\ &= 8.418069(2)(4)\,\mathrm{eV} \\ &= 147.28341(3)(7)\,\mathrm{nm}\,. \end{aligned} \tag{6.19}$$

6.5.5 Assignment of subseries

It is possible to allocate the members of a Rydberg series to a specific principal quantum number by comparing the quantum defect of similar homologous elements. For this purpose, the quantum defects of the literature values of the known atomic levels of sulphur (S) [116], selenium (Se) [123] and tellurium (Te) [27, 124, 146] were calculated.
The second intermediate state of the polonium excitation scheme has the configuration $6p^3 7p^5 P_2$. Excitation from the second intermediate state is therefore only possible to an s-state ($l = 0$) or a d-state ($l = 2$). Therefore, odd-parity s- or d-states of sulphur, selenium or tellurium were taken into account for the comparison of the quantum defects. In

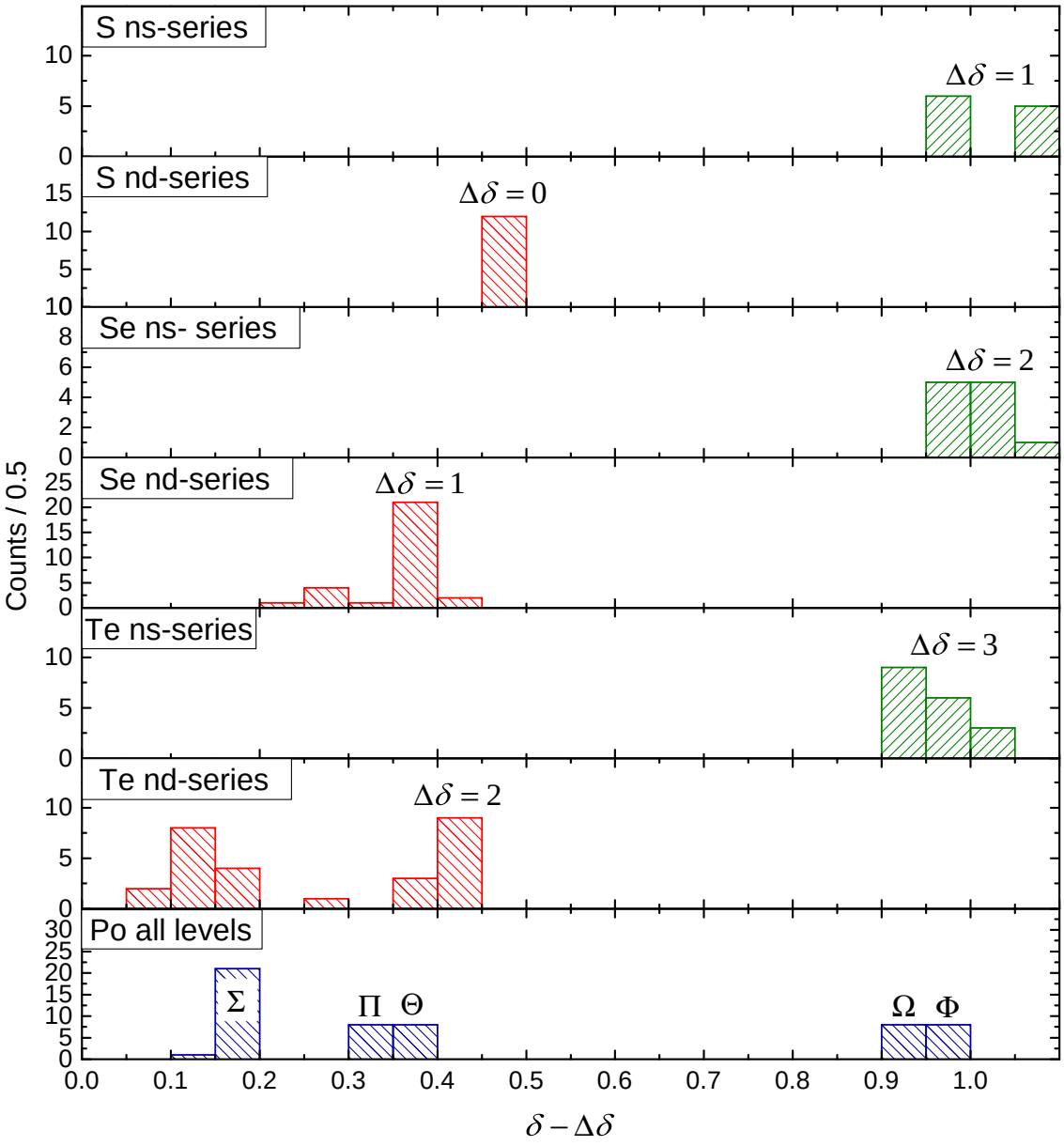

Figure 6.8: Histograms of the distributions of the quantum defects of the Rydberg levels of polonium (Po) and the electron levels found in literature for sulphur (S), selenium (Se) and tellurium (Te). The quantum defects are substituted by $\delta - \Delta\delta$ for a better comparison and the calculated $\Delta\delta$-values are given in the corresponding histograms. For Rydberg levels, $\delta - \Delta\delta$ values can be identified with the δ'-values: $\delta_{\mathrm{Po}} - \Delta\delta_{\mathrm{Po}} \equiv \delta'_{\mathrm{Po}}$. A general trend is observed that $\delta - \Delta\delta$ values of the ns-series (green) tend to be ≈ 1, while the $\delta - \Delta\delta$ values of nd-series (red) tend to accumulate between 0.05 and 0.5. Correspondingly, it can be thus assumed that the Rydberg series Ω and Φ of polonium are *ns*-series and Σ, Π and Θ of polonium are *nd*-series. The $\Delta\delta$ values increase by $+1$ from sulphur to selenium and to tellurium following the increase of the periods of the homologous elements. Polonium *ns*-levels should thus have $\Delta\delta = 4$ and polonium *nd*-levels should have $\Delta\delta = 3$.

addition, only quantum defects for levels with high n were taken into account for which the quantum defects don't show any dependency on the principal quantum number.
In contrast to polonium, the configurations and quantum numbers of the levels of sulphur, selenium and tellurium were known and therefore, $\Delta\delta$ could be extracted for each of the s- and d-levels individually and subtracted from the total quantum defect: $\delta - \Delta\delta$. These resulting values where then compared to the remainder of the quantum defect of the polonium isotopes, for which $\delta' \equiv \delta - \Delta\delta$.
Figure 6.8 shows the histograms of the $\delta - \Delta\delta$ values. The distribution of the quantum defects of the s-levels (green) and d-levels (red) of sulphur, selenium and tellurium are clearly separated. The s-states tend to be in the range $\delta - \Delta\delta \approx 0.9 - 1.1$, while the d-states scatter between 0.05 and 0.5. Based on these assumptions, the series Ω and Φ of polonium are identified as transitions to s-states, while Σ, Π and Θ are transitions to d-states.
Following the evolution of the $\Delta\delta$ values of sulphur, selenium and tellurium and adding one additional electron shell for Po, it becomes conclusive that $\Delta\delta_s(\mathrm{Po}) = 4$ and $\Delta\delta_d(\mathrm{Po}) = 3$. These results are nicely confirmed by a comparison with the 7 atomic states with odd parity found in [31], of which the listed ns states have quantum defects ranging from 4.9 to 5.05 like the series Ω and Φ and the listed np-values have quantum defects scattering around 3.3 like the series Π. The latter might also be valid for the series Θ since the quantum defects of lower lying members of a Rydberg series have slightly different quantum defects due to the stronger interaction with the nucleus. No corresponding levels were found for the series Σ, but this is most likely due to the low number of known levels in literature. For the ns-states, it is even possible to conclude that the series Σ corresponds to states with $J = 1$ and the series Φ corresponds to states with $J = 2$.
The values of $\Delta\delta \equiv \Delta n$ can then be added to the n' and δ' values obtained in Chapter 6.5.3 and an estimation for the n and δ values for the polonium series can be made. Table B.1 in Appendix B lists the complete list of the observed transitions to Rydberg states together with the corresponding excitation energies and the suggested quantum numbers.

6.5.6 Summary and discussion

In this work, the ionization energy of polonium has been determined by fitting the Rydberg formula (Equation (2.7)) to a set of Rydberg series, which led to final value of:

$$IE_{\mathrm{Po}} = 67896.310(13)(30)\,\mathrm{cm}^{-1} \tag{6.20}$$
$$= 8.418069(2)(4)\,\mathrm{eV}\,. \tag{6.21}$$

This value is more than 50 times more precise than the literature value of $67860(30)\,\mathrm{cm}^{-1}$ given in [149]. Moreover, the ionization energy determined in this work differs by more than $10\,\mathrm{cm}^{-1}$ from the value of $67885.3\,\mathrm{cm}^{-1}$, which was obtained by a Rydberg-Ritz analysis in [31]. However, in [31], only 3 low-lying levels were allocated to a Rydberg series, which limits the accuracy of the determination. Additionally, 93 new resonances in the polonium spectra were observed, of which 57 resonances could be assigned to unambiguously resolved atomic states as listed in Table B.1 in the Appendix B.

At the same time of the measurements of the polonium Rydberg series at ISOLDE in September 2012, a team at the *Tri University Meson Facility* (TRIUMF) in Vancouver, Canada, measured Rydberg series of polonium with the TRILIS setup [134]. Here, an alternative two-step ionization scheme was used: a frequency-tripled Ti:Sa UV-laser beam with wavelength of 245.08 nm to the first intermediate step at 39081.19 cm^{-1} ($6p^3(^4S°)7s\ ^5S^o_2$) and a frequency-doubled tunable Ti:Sa laser for the scan of the region around the ionization energy.
These measurements provided a complementary determination of the polonium ionization energy with different Rydberg series of levels with even parity in contrast to these measurements, for which Rydberg levels with odd parity were measured. The measurements at TRIUMF led to a value for the ionization energy of polonium of IE=67896.35(17)(20) cm^{-1} [136], which is in excellent agreement with the value measured in this work. In addition, a new theoretical value of 67790(129) cm^{-1} has been calculated by A. Borschevsky [22], which also agrees well with the new experimental values. The new value for the ionization energy of polonium obtained by Rydberg spectroscopy at ISOLDE and TRIUMF and the results from the theoretical calculations by A. Borschevsky will be published in a joint article [137]. An overview of the values obtained in this work, at TRIUMF and by new theoretical calculations are given in Table 6.7 and compared to the literature values.

Table 6.7: Comparison of the ionization energy of polonium obtained during the work on this thesis, at TRIUMF and by recent theoretical calculations with the literature values. Values indicated with * should be taken as preliminary. The values given in [31, 32] are implied with significant numbers.

Origin	**Method**	**Ionization energy**	
		(eV)	**(cm^{-1})**
This work	Rydberg analysis	8.418069(2)(4)	67896.310(13)(30)
S. Raeder *et al.* [136]	Rydberg analysis	8.418074(21)(25)*	67896.35(17)(20)*
A. Borschevsky [22]	Theoretical	8.405(16)*	67790(129)*
Charles *et al.* [32]	Semi-empirical [147]	8.43	67980
Charles *et al.* [31]	Rydberg-Ritz	8.417	67885.3
	Semi-empirical [147]	8.411	67840.0
Sansonetti *et al.* [149]	Evaluation of lit. values	8.414(4)	67860 (30)

7 First experiments with the LIST: laser spectroscopy of neutron-rich polonium

During the LIST on-line run in 2012 at ISOLDE, the mean square charge radii and hyperfine-structures of neutron-rich polonium ($A > 210$) isotopes were studied by in-source laser resonance spectroscopy using the LIST for the suppression of the strong francium contamination in this mass region. The goal was to fill the gaps in the isotope chain visible in Figure 7.1 and to investigate the properties of the odd-A neutron-rich polonium isotopes. Due to the remaining contamination of ^{212}Fr (see Chapter 4.3.4), a measurement of the polonium isotopes near the shell-closure $N = 126$ was omitted. However, the isotope shift and the hyperfine-structure of ^{217}Po were successfully measured for the first time together with the neighboring isotopes ^{216,218}Po as reference isotopes. In addition, a first glimpse into the hyperfine-structure of ^{219}Po was possible, demonstrating the feasibility of the LIST for the study of this isotope.
A brief review over the physics around the closed proton shell at $Z = 82$ and a summary of the previous experiments on polonium at ISOLDE will put the work described in here into context, before the experiment and the results will be discussed.

7.1 A brief review of the physics around the closed proton shell at Z=82

The isotopes of elements close to the magic proton and neutron numbers (see Figure 1.1 in Chapter 1) are of particular interest for nuclear structure studies. Fundamental properties*, such as the binding energies of the nucleons or the changes in the mean square charge radii, $\delta\langle r^2\rangle_{A,A_{\mathbf{ref}}}$, are sensitive to the interactions of few nucleons around an inert core. The region around the closed proton shell $Z = 82$ of lead (Pb) is no stranger to this and unveils a variety of interesting phenomena. It hosts for example the stable doubly-magic ($Z = 82$, $N = 126$) isotope ^{208}Pb, which consequently is the heaviest stable isotope found in nature (ignoring "virtually" stable nuclei, such as ^{209}Bi, which has a half-live of $1.9(2) \cdot 10^{19}$ years [46]). Close to the neutron shell closure at $N = 126$, the ground-state shapes of lead-isotopes ($\boldsymbol{I^{\pi}} = 0^+$) are observed as spherical [39]. Further away from the shell-closure to the neutron-deficient side an effect called *shape-coexistence* was observed close to the ground states of mid-shell *isotones* (nuclei with same number of neutrons, but different proton numbers) of $N = 104$. Shape-coexistence occurs when different quantum configurations give rise to states with distinct nuclear shapes within

*In order to keep this discussion concise, I refer to the dedicated literature and text books. An overview of nuclear structure can be found in [29, 95]. For the discussion of the charge radii and moments, I refer to [128].

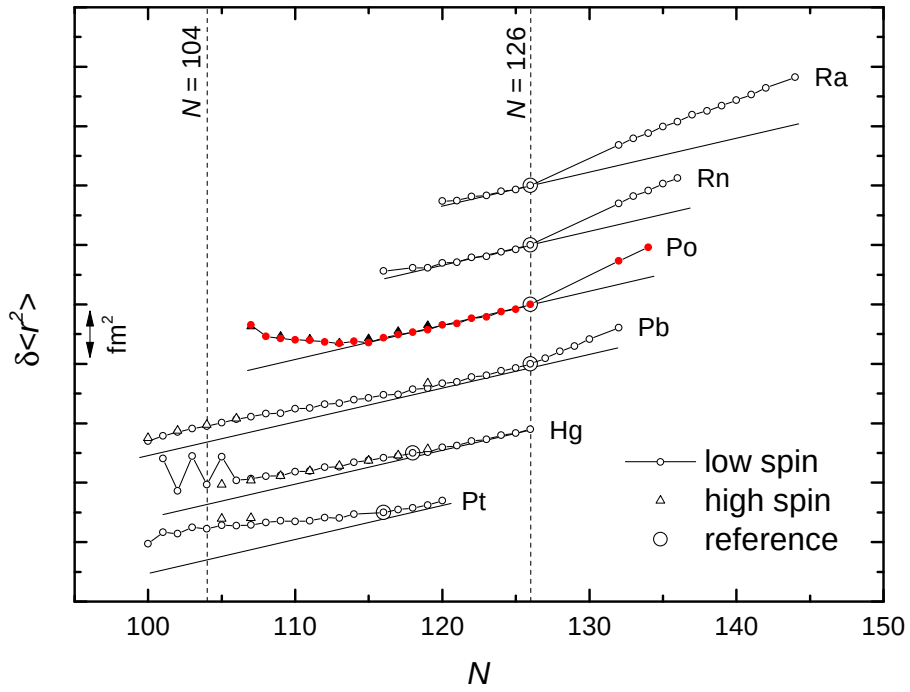

Figure 7.1: Changes in mean square radii, $\delta\langle r^2\rangle_{A,A'}$, for even-$Z$ isotopes in the lead-region ($Z = 82$): platinum ($_{78}$Pt) [101], mercury ($_{80}$Hg) [171], lead ($_{82}$Pb) [6, 47, 50, 53], polonium ($_{84}$)Po [39, 159], radon ($_{86}$Rn) and radium ($_{88}$Ra) [64]. The reference isotopes are indicated by the large circles.

the same energy range and the same spin and parity. The proximity of those quantum configurations may result in configuration mixing, whereby the shape of the state becomes difficult to determine. A remarkable example is ^{186}Pb, which was found to have the three lowest states in a $\boldsymbol{I}^{\pi} = 0^{+}$ configuration within a range of 700 keV and its shape was interpreted as a mixing of the corresponding spherical-, oblate-, and prolate shapes [5]. Shape-coexistence was also found for the neutron-deficient isotopes of platinum (Pt) [101] and mercury (Hg) [171]. For the latter, also a specifically large *odd-even staggering* in the mean square charge radii was observed, where the odd-N nuclei have a systematically larger mean square charge radii than the trend set out by the even-N isotopes. This can be interpreted by a systematically stronger deformation of the odd-A nuclei. Figure 7.1 shows these mean square charge radii.
On the neutron-rich side of the shell closure ($N > 126$), it is of particular interest to map the existence of *octupolar deformation** and *inverted odd-even staggering* as observed for isotopes of radon (Rn) [20], francium (Fr) [35] and radium (Ra) [67]. The inverted odd-even staggering refers to the odd-A isotopes being systematically smaller than the trend for the even-A isotopes and is considered to be a fingerprint for octupolar deformation. Additionally, a kink in the mean square charge radii was observed departing from the neutron shell closure for lead, radon and radium [64] as shown in Figure 7.1.

*Octupolar deformed nuclei have pear-like shapes. An illustration can be found in [67]

During the last years, the systematics in the lead region were studied at ISOLDE by the means of the *in-source resonance ionization spectroscopy*. This technique enables to determine the isotope shift and the hyperfine structure and thus allows the determination of the changes of the mean square charge radii and the electric dipole and magnetic quadrupole moments, respectively. So far, lead- [47, 157, 158], bismuth- (Bi) [112], and polonium-isotopes (Po) [39, 159] were studied. This list was recently extended to isotopes of thallium (Tl), gold (Au) and astatine (At) [114, 143].

7.2 Status of the ISOLDE experiment IS456: "Study of polonium ground state properties by simultaneous atomic- and nuclear-spectroscopy"

The experiment described in here is part of the IS456 experiment [38] aimed at the "Study of polonium ground state properties by simultaneous atomic- and nuclear-spectroscopy". Polonium has $Z = 84$ protons and is the first even-Z element being above the magic proton shell-closure with $Z = 82$ and having no stable isotopes. Prior to experiment IS456, evidence for shape coexistence close to the mid-shell at $N = 104$ arose from α-decay spectroscopy of radon and polonium [10, 175] and from in-beam studies [86]. However, the extent and onset of the ground-state deformation was still unknown until the neutron-deficient polonium isotopes were studied during two on-line runs at ISOLDE in 2007 and 2009 [39, 159]. The results are shown in Figure 7.1. An astonishing result was the early deviation from the spherical shape compared to the mercury or the platinum chain [39]. A comparison of the even isotopes to the odd isotopes did not show any pronounced odd-even staggering as observed for mercury [159]. On the neutron-rich side, a kink of the mean charge radii is visible, starting for isotopes heavier than ^{210}Po with the neutron magic number $N = 126$, similar to the neutron-rich lead, radon and radium isotopes [64].
However, the overwhelming contamination of the beam with francium above $N > 126$ and the very short half-lives made the study of most isotopes on the neutron-rich side impossible during the first two runs. ^{212,213}Fr and ^{220,222}Fr are the strongest contaminants in the polonium chain. The latter leaked into the beams of the lower masses due the asymmetric shape of the mass peaks after the GPS mass separator [52] and were observed down to the mass $A = 216$. Only ^{216}Po and ^{218}Po could be measured on the neutron-rich side using the *"pseudo off-line measurement"* method described in [36] and in Chapter 6.1. The neutron-rich odd-A polonium isotopes remain still unstudied and the measurements described in here aim at shedding light on the unknown border of octupolar deformation in this region, colloquially called "the island of octupolar deformation".

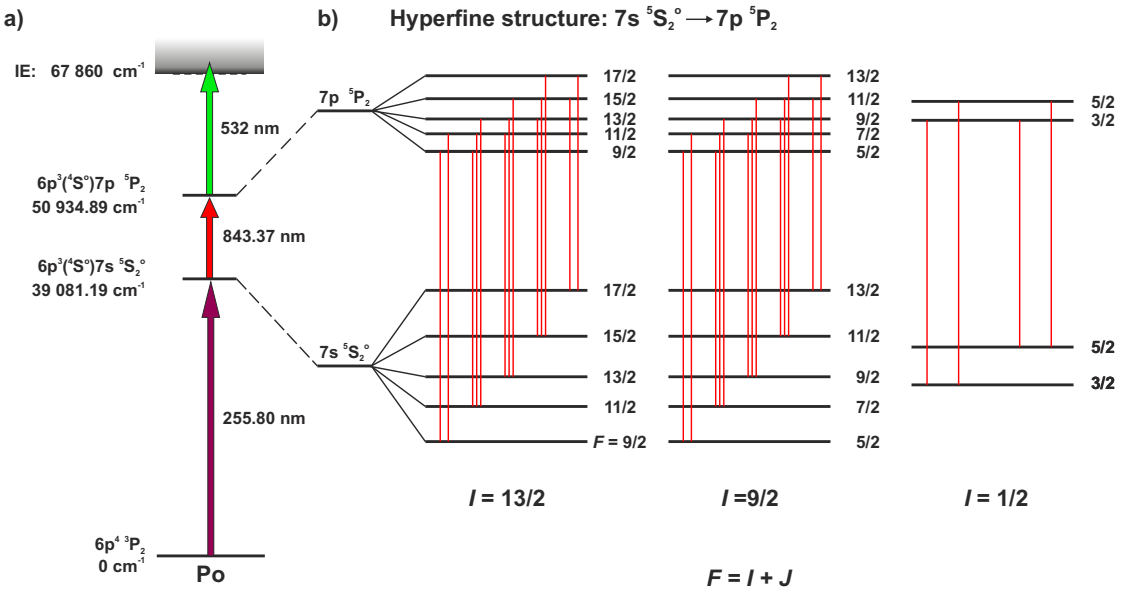

Figure 7.2: a) Three-step laser ionization scheme for polonium. b) Zoom on the possible hyperfine levels for nuclear spins $I^\pi = 13/2^+, 9/2^+, 1/2^-$ with total angular momentum F and corresponding transitions (red solid lines) for the studied transition from the $7s\,^5S_2^\circ$ state to the $7p\,^5P_2$ state. The hyperfine structure is not to scale.

7.3 Experimental setup and data taking

The polonium isotopes with mass $A > 210$ were produced* at ISOLDE in the spallation reaction of ^{238}U induced by the impingement of a 1.4 GeV proton of typically 1.1 µA intensity from the CERN PS-Booster onto a LIST-UC$_x$ target (ISOLDE target #488, 50 g/cm^2). The reaction products effused into the tantalum transfer line and the hot cavity, both kept on a temperature of $T \approx 2300$ K and enter the LIST. Surface ionized contaminants, such as francium isotopes were separated from the neutral atomic beam by the repeller electrode of the LIST operating on a positive potential of typically 7 V. Polonium was then element-selectively ionized inside the LIST RFQ structure by a three-step laser ionization scheme [41]. It consisted of a frequency-tripled dye laser of 255.8 nm ($P \approx 20$ mW) for the transition to the $6p^3(4S^\circ)7s\,^5S_2^\circ$ first state, a tunable 0.8 GHz narrowband (NB) Ti:Sa laser of ≈ 843.37 nm ($P \approx 3$ mW) for the scan of the transition to the $6p^3(^4S^\circ)7p\,^5P_2$ second state and the 532 nm ($P > 10$ W) second harmonic output of a Nd:YAG pump laser for the non-resonant transition over the ionization energy into the continuum. The output power of the NB-Ti:Sa for the second transition was reduced to avoid power broadening. Figure 7.2 shows the laser ionization scheme together with possible transitions between hyperfine levels of the $7s\,^5S_2^\circ$ first state to the $7p\,^5P_2$ second state for different nuclear spins $I = 13/2, 9/2, 1/2$. After leaving the LIST RFQ, the ions were then accelerated to

*For a detailed description of the nuclear reactions, the target specifications, the laser setup and the technical aspects of the LIST, I refer to the corresponding sections in Chapter 3 and Chapter 4.

50 keV, mass separated by the GPS dipole magnet and sent to the KU Leuven "Windmill" detector setup [55, 160], where the ions were implanted into one of the 10 carbon foils (10 mm diameter, 20 $\mu g/cm^2$, from the GSI target laboratory) [106]) mounted on a rotating wheel. The 10 foils are divided into two sets of 5 foils so that different sets were used for different isotopes. Two passivated implanted planar silicon (PIPS) detectors, C1 and C2 (see Figure 3.12 in Chapter 3.4.1), surround the carbon foil and are placed into the ion beam axis, whereas C1 is placed in front of the foil and has an 8 mm aperture for beam transport to the foil and C2 is placed behind the carbon foil. Together, these detectors cover 51% of the total angular solid angle. After each implantation and data acquisition (DAQ) cycle, the rotating wheel was turned and a fresh carbon foil was moved between the detectors into the axis of the ion beam. Once the narrow band scanning laser was set to a new wavelength, a new measurement cycle could begin.

7.3.1 Measurement cycle

The control systems of the setup and data acquisition of the RILIS (tunable NB-laser and corresponding wavemeters) and the "Windmill" (Implantation and DAQ) were combined and synchronized to the proton bunches of the proton supercycle (SC).
A measurement cycle was started once the desired laser frequency was set and stabilized and the "Windmill" setup was ready. Figure 7.3 shows a simplified logical sequence for the initialization of a measurement cycle: once, the operational state of the RILIS lasers and the DAQ of the Windmill were confirmed, the system was waiting for a trigger signal of the proton supercycle to start the new measurement cycle. An additional clock is introduced to take into account for the time delay of 535 ms [36] between the trigger signal and the arrival of the first bunch of the proton supercycle.
The total measurement cycle for one scan over the studied transition is shown in Figure 7.4a. As soon as, the new laser frequency was set and the "Windmill"-setup was ready (set-up time of typically a fraction $m = 0.3$ of proton supercycle) data were taken and integrated over a fraction $n = 0.7$ of a proton supercycle. Figure 7.4b shows a typical measurement cycle: The sequence of 9 proton bunches out of the total proton supercycle (39 proton bunches, spaced by 1.2 s) were sent to the ISOLDE target. The overall proton sequence adds up to an average proton current of $\approx 1.02\,\mu A$, which was identical for each measurement presented in this chapter. Of these 9 proton pulses, 7 fall into the time of the data taking. Figure 7.4c illustrates the measurement sequence between each proton pulse. Elements with a fast release from the target matrix and isotopes with very short half-lives will see their production peak shortly after the proton impact on the target. This is the case of the francium contaminants [109], while the polonium beams have a more gradual release profile [41]. Thus, the beam-gates were closed for 100 ms during and after the proton pulse.
Laser frequency scans were recorded for the GPS mass separator and set to mass $A = 217$ and mass $A = 218$. Due to the relatively broad energy acceptance of the GPS separator magnet (≈ 50 eV), ^{216}Po was observed simultaneously in the scans for mass $A = 217$, making a specific scan for mass $A = 216$ unnecessary. A further advantage of having two isotopes in one mass spectra is that it allows a direct measurement of the isotope shifts

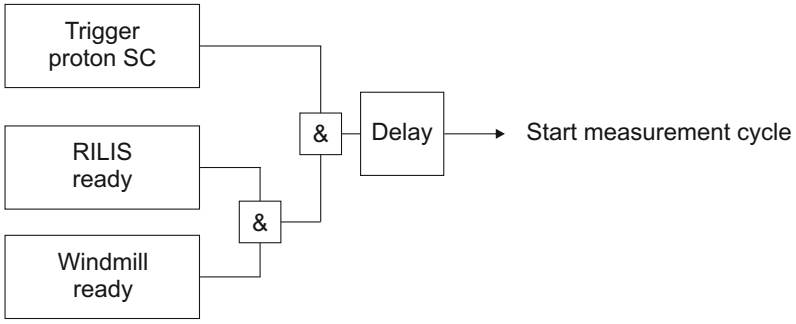

Figure 7.3: Sequence of logical steps to validate the start of the measurement cycle with the RILIS lasers and the "Windmill" α-detector setup.

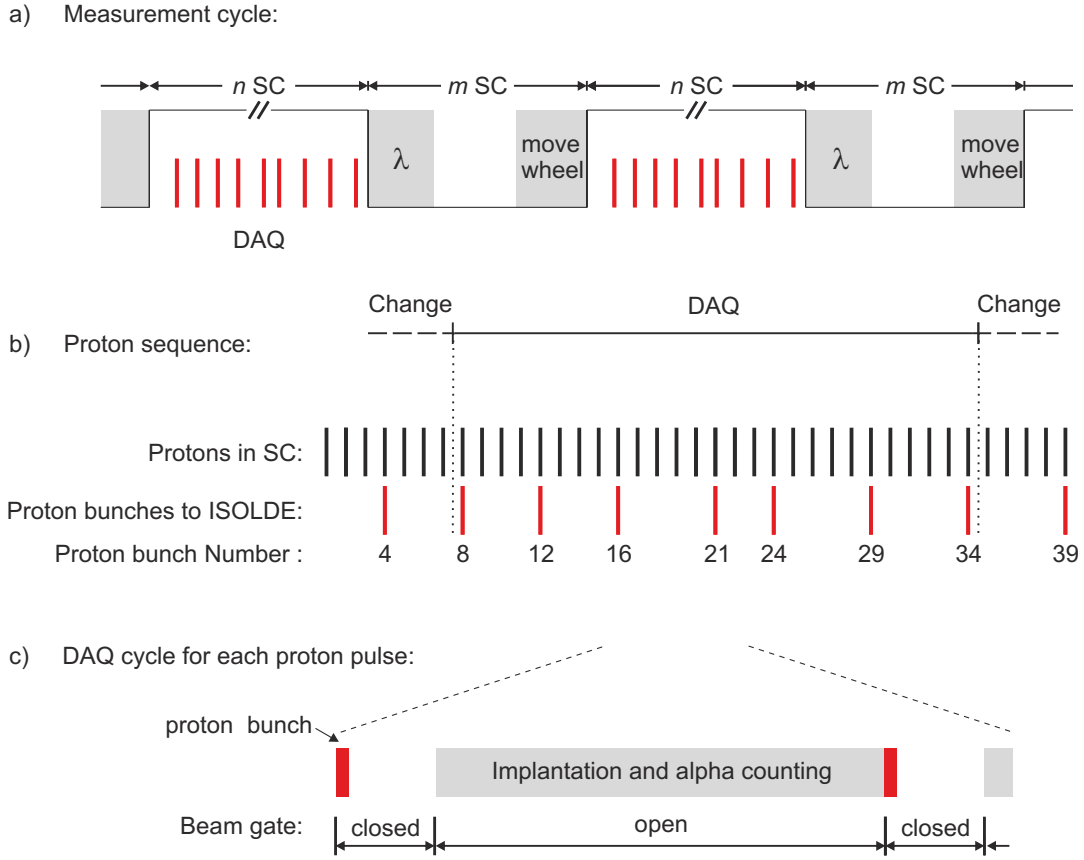

Figure 7.4: a) Total measurement cycles for one isotope. For each frequency step, data is taken and integrated over n proton supercycles (SC). In between the measurements, the laser frequency is changed and the "Windmill" wheel moves a fresh carbon foil into the beam axis. Proton pulses are shown as red bars. b) Proton delivery to ISOLDE. c) Measurement sequence for each proton pulse.

of these two isotopes in one scan under the same conditions. In this case, ^{216}Po serves as a reference isotope without possible laser related shifts or systematic uncertainties due to the DAQ system. One scan was performed for mass $A = 219$ but time constraints did not allow to accumulate enough statistics to extract information about the isotope shift and the hyperfine structure and thus, ^{219}Po is not further discussed. However, the decay energy spectra revealed an unknown α-line, which is assigned to ^{219}Po. This represents the first information about the decay properties and the lifetime of ^{219}Po and will be subject of a separate publication [40].
Using these measurement routines, a specific α-decay energy spectrum can now be assigned to each set laser wavelength and the laser scan is constructed plotting the integral of the gated α-spectrum for each scan step.

7.4 The alpha-decay energy spectra

Figure 7.5 shows one representative α-decay energy spectrum obtained by the C2-silicon detector of the Windmill (see Figure 3.12 in Chapter 3.4.1) for a) mass $A = 217$ and for b) mass $A = 218$. The insets are zoomed to the peaks of the polonium isotopes and the corresponding energy ranges (red lines), which represent the gate that is applied for evaluating the polonium counts for each laser wavelength position. The structure of the α-decay energy spectra obtained by the C1-silicon detector is similar but the wide low-energy tails of the α-decay peaks, which arises from the straggling of the α-particles through the carbon foil, is less pronounced. This is because the isotopes are implanted in the first 25 mm of the 90 mm-thick-foil. The discrepancy between C1 and C2 in this experiment are greater than in previous studies of the neutron-rich polonium isotopes [49]. C1 and C2 were therefore analyzed separately and their data were combined later during the off-line analysis.
Despite the selectivity enhancement provided by the LIST, additional α-decay energy lines were observed in the spectra. These non-laser related contaminants are discussed* in the following sections for each mass separately. Nevertheless, a significant consequence of the LIST operation is the absence of ^{213,220,221}Fr α-decay lines in the α-decay energy spectra at $A = 217$ and $A = 218$, in contrast to the previous experiments [36].

7.4.1 Alpha-decay energy spectrum for mass A=217

The α-decay energy spectrum for mass $A = 217$ is shown in Figure 7.5a. The two strongest lines belong to laser-ionized ^{217}Po ($E_\alpha = 6536(4)$ keV) and ^{216}Po ($E_\alpha = 6778.2(5)$ keV). The next significant peak is ^{217}At ($E_\alpha = 7069.9(15)$ keV), which is produced by β^--decay (5 % branch) from ^{217}Po. In the same decay-chain, ^{213}Po ($E_\alpha = 8375.9(25)$ keV) is produced from ^{217}At $\xrightarrow{\alpha}$ ^{213}Bi $\xrightarrow{\beta}$ ^{213}Po or by ^{217}Po $\xrightarrow{\alpha}$ ^{213}Pb $\xrightarrow{\beta}$ ^{213}Bi $\xrightarrow{\beta}$ ^{213}Po.
Traces of ^{217}Rn ($E_\alpha = 7741(2)$ keV) and ^{216}At ($E_\alpha = 7802(3)$ keV) are also visible. In contrast to ^{217}At and ^{213}Po, which stem from the decay of ^{217}Po in the carbon foils, ^{216}At and ^{217}Rn are not daughter products of the ion beam components and their presence indicates that these isotopes were extracted as low intensity ion beams (0.1 counts/s).

*The energies of the α-lines are taken from the *WWW table of radioactive isotopes* database [34].

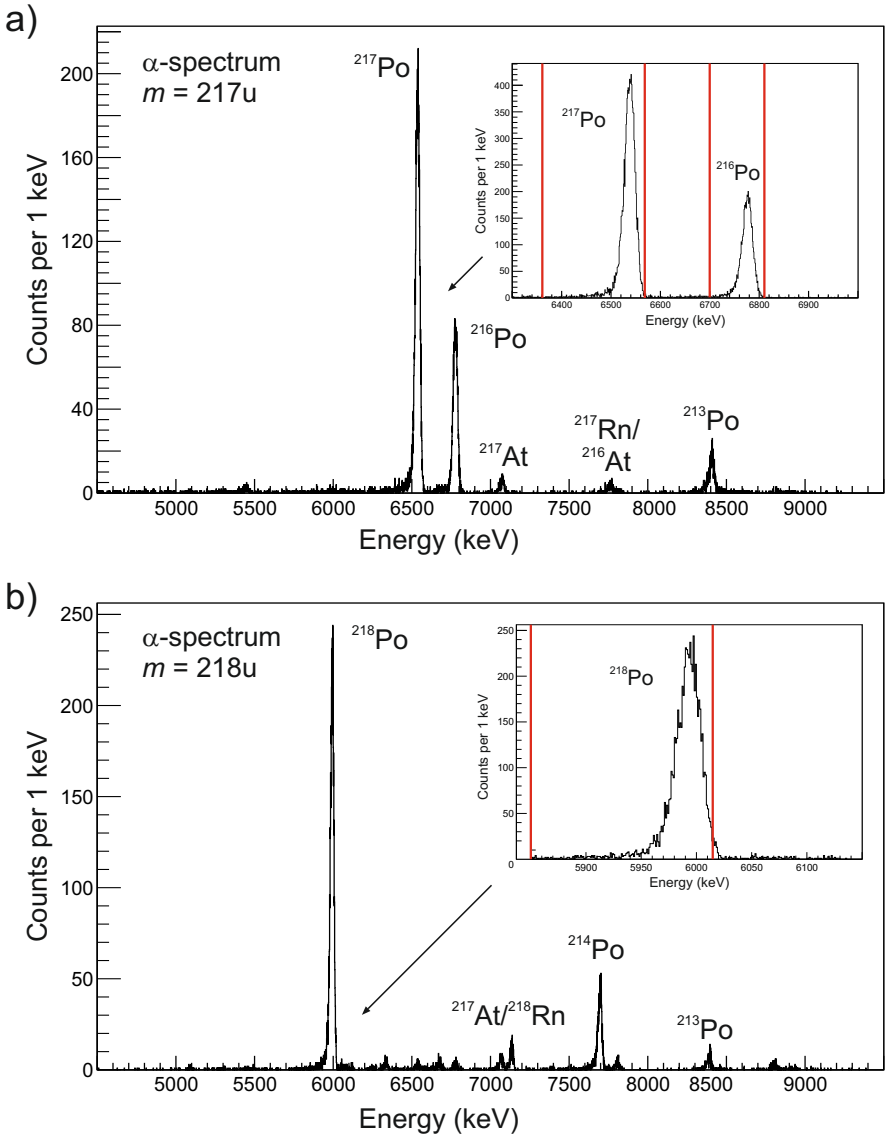

Figure 7.5: α-decay energy spectra (countrate per 1 keV bin) for a) mass $A = 217$ and b) mass $A = 218$ obtained by the C2-silicon detector of the Windmill and integrated over all frequency steps of the laser scan for ^{216,217}Po and ^{218}Po, respectively. The small graphs show the alpha-energy gating that was applied for determining the polonium counts at each scan step.

Given the sub-millisecond lifetime of these, in-target production is an unlikely source due the typical release time from the target of $> 100\,\text{ms}$ [52]. A possible explanation is the production by radioactive decay inside the LIST RFQ from precursor nuclei, which passed the repeller electrode as neutral atoms and condensed to the RF-rods. A similar scenario was discussed for ^{212}Fr in Chapter 4.3.4, where the high intensity in *LIST mode* was ascribed to β-decay of ^{212}Ra inside the LIST RFQ. Possible processes for the production of ^{217}Rn are α-decay of ^{221}Ra or β-decay ($< 0.01\,\%$ β^--decay branch) of ^{217}At*, originating from the α-decay of ^{221}Fr. The only possible production process for ^{216}At is α-decay of ^{220}Fr. However, the recoil energy of ^{216}At ($\approx 145\,\text{keV}^\dagger$) from the α-decay would exceed the trapping potential of the LIST ($\approx 10\,\text{eV}$) and the acceptance of the mass separator. The exact nature of this process is therefore not understood and will be studied during future on-line experiments with the LIST. One should note that prior to this observation, the shortest lived ion beam that was measured at ISOLDE was ^{14}Be, with a half-life of 4.35 ms [84].
Apart from the rather weak peaks of ^{213}Po, ^{216,217}At and ^{217}Rn, no further dominant lines are visible and the peaks of ^{216}Po and ^{217}Po are well isolated.

7.4.2 Alpha-decay energy spectrum for mass A=218

Figure 7.5b shows the α-decay energy spectrum for mass $A = 218$ recorded by the C2 silicon detector with a well-isolated peak of ^{218}Po ($E_\alpha = 6002.35(9)\,\text{keV}$). The second strongest peak arises from α-decay of ^{214}Po ($E_\alpha = 7686.82(7)\,\text{keV}$), which is produced in the carbon foils in the direct decay chain of ^{218}Po: $^{218}\text{Po} \xrightarrow{\alpha} {}^{214}\text{Pb} \xrightarrow{\beta} {}^{214}\text{Bi} \xrightarrow{\beta} {}^{214}\text{Po}$. In contrast, ^{213}Po ($E_\alpha = 8375.9(25)\,\text{keV}$) is left-over contamination from the laser scans of mass $A = 217$ and the decay-chains of ^{217}At and ^{217}Po as described in previous subsection. Within these decay-chains ^{213}Bi serves as a waiting point due to its relatively long half-life of 45.59 min. The weaker peaks, ^{217}At ($E_\alpha = 7066.9(1)\,\text{keV}$) and ^{218}Rn ($E_\alpha = 7129.2(12)\,\text{keV}$), are most likely produced inside the LIST RFQ by β-decay from ^{217}Po and ^{218}At, respectively. Additionally, traces of ^{216}Po ($E_\alpha = 6778.2(5)\,\text{keV}$), ^{218}At ($E_\alpha = 6693(3)\,\text{keV}$) and ^{217}Po ($E_\alpha = 6536(4)\,\text{keV}$) are observed between ^{217}Po and ^{217}At.

*It should be mentioned that this is no indication for β^--decay inside the carbon foils as the intensity ratio between ^{217}At and ^{217}Rn is far too small and does not reflect the β^--decay branch.

†The recoil energy is calculated by considering the conservation of the momentum. This leads to a kinetic energy, $E_{\text{kin,rec.}}$, of the recoiled nucleus with mass m_{rec} of $E_{\text{kin,rec.}} = \frac{m_\alpha}{m_{\text{rec}}} \cdot E_\alpha$. Using $m_{\text{rec}} \approx 216\,\text{u}$ for ^{216}At and $m_\alpha \approx 4\,\text{u}$, this calculates to $E_{\text{kin,rec.}} \approx 145\,\text{keV}$.

7.5 Laser resonance spectra and fitting

Integrating the counts in the determined energy ranges for every laser frequency step reveals the laser spectrum. Figure 7.6 shows the laser resonance spectra for the neutron-rich polonium isotopes ^{216,217,218,219}Po. ^{219}Po was analyzed by T.E. Cocolios [40] and is only shown for completeness. The even-even isotopes, ^{216,218}Po, show the single resonance for the ground-state configuration $\boldsymbol{I} = 0^+$ and a clear isotope shift with respect to each other, while the even-odd isotopes, ^{217,219}Po, show a rich hyperfine structure. Even though the statistics for ^{219}Po is not sufficient for a further analysis, the visible structure in the spectra of ^{219}Po indicates the feasibility of the LIST for laser spectroscopy of ^{219}Po in future experiments provided that more beam time is available.
The frequency of each hyperfine component, $\nu_0^{F,F'}$ (or alternatively the wavenumber, $\tilde{\nu}_0^{F,F'} = \nu_0^{F,F'}/c$, where c_n is the speed of light.) is defined relative to the central transition frequency of the transition $7s\,^5S_2^0 \rightarrow 7s\,^5P_2^0$:

$$\nu_0^{FF'} = \nu_0 + \Delta\nu^{FF'} \tag{7.1}$$

where ν_0 is the center of gravity of the hyperfine structure and $\Delta\nu^{F,F'} = \Delta\nu^{F'} - \Delta\nu^{F}$ the overall shift of the lower level, $\Delta\nu^{F}$, and the upper level, $\Delta\nu^{F'}$ with total angular momentum $\boldsymbol{F} = \boldsymbol{I} + \boldsymbol{J}$ and $\boldsymbol{F'} = \boldsymbol{I} + \boldsymbol{J'}$, respectively. Using Equation (2.22) from Chapter 2.2.2, the centroid can be calculated by:

$$\begin{aligned}\nu^{FF'} &= \nu_0 + \frac{A'}{2}\cdot C' + B'\cdot\frac{\frac{3}{4}C'\left(C'+1\right) - I\left(I+1\right)J'\left(J'+1\right)}{2\left(2I-1\right)\left(2J'-1\right)I\cdot J'} \\ &\quad -\frac{A}{2}\cdot C - B\cdot\frac{\frac{3}{4}C\left(C+1\right) - I\left(I+1\right)J\left(J+1\right)}{2\left(2I-1\right)\left(2J-1\right)I\cdot J}\end{aligned} \tag{7.2}$$

where A and B are the magnetic dipole and electric quadrupole hyperfine constants, respectively and $C = F\left(F+1\right) - J\left(J+1\right) - I\left(I+1\right)$. The primed parameters belong to the upper level.
The fitting of the spectra was performed by M.D. Seliverstov of the Petersburg Nuclear Physics Institute in Gatchina, Russia [156]. The fitting routine that was applied is specially adapted to in-source resonance ionization spectroscopy using the RILIS lasers and wavemeters and is described in detail in [39, 157, 160, 179]. In summary, each laser scan was fitted by a superposition of the individual lineshapes of the resonances. In turn, each individual lineshape consists of a Gaussian Doppler profile and a deformed Lorentzian profile, which takes into account the asymmetry of the laser lineshape. The Doppler width was calculated for a hot-cavity temperature of $T \approx 2300\,\mathrm{K}$ and is fixed during the fitting (see Equation (2.43)). The degree of saturation of the three transitions of the ionization scheme (shown in Figure 7.2) was taken into account by solving the rate equations following the method discussed in [7]. During the fitting process, $\tilde{\nu_0}$, A and B were free parameters, while the ratios for the hyperfine constants, A'/A and B'/B were fixed [160]. The final fits are shown together with the data in Figure 7.6.

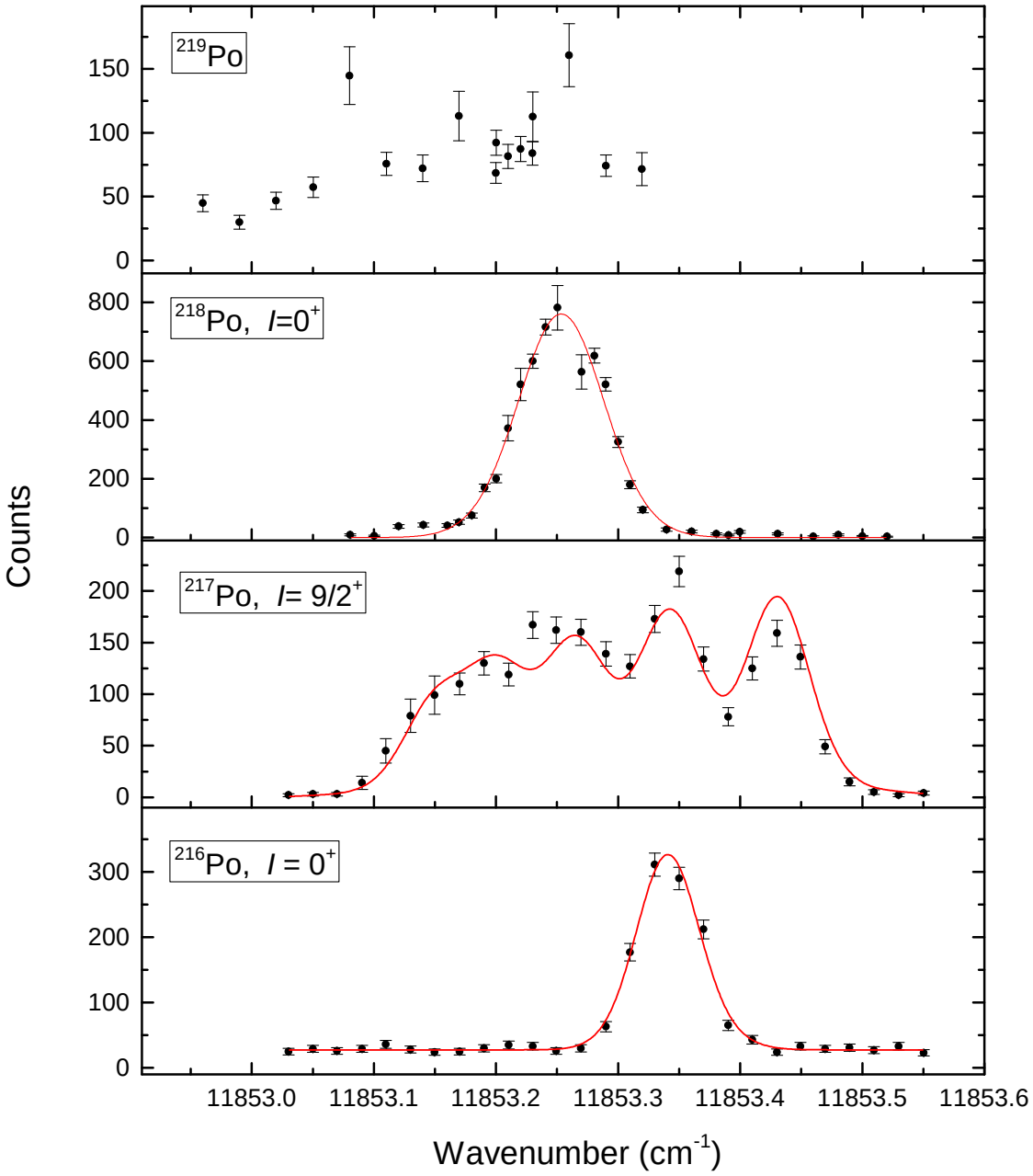

Figure 7.6: Laser spectra of the neutron-rich ^{116,117,118,119}Po isotopes. Uncertainties are given by the standard deviation. The red curves are the fits to the data [156]. The spectrum of ^{219}Po was analyzed by T.E. Cocolios [40].

7.6 Results and discussion

7.6.1 Isotope shifts and mean square charge radii

The simultaneous measurement of ^{216}Po and ^{217}Po allows the determination of the isotope shift of ^{217}Po, without any systematic uncertainties from a possible wavemeter drift or from the DAQ system. The individual results of each scan were averaged to give the final value: $\delta\nu_{217,216} = -1.060(150)$ GHz. For comparison with the data obtained during previous runs, the isotope shift of ^{217}Po to the reference mass ^{210}Po, the isotope shift $\delta\nu_{217,210}$, was calculated using the isotope shift of ^{216}Po, $\delta\nu_{216,210} = -8.820(110)$ GHz, from [39]. In the case of ^{218}Po, the isotope shift was first calculated relative to ^{216}Po, $\delta\nu_{218,216}$, and then relative to ^{210}Po in the same manner as described for ^{217}Po. An overview of the results is given in Table 7.1 together with the corresponding values from [39]. The slightly higher statistical uncertainties compared to the values from the previous measurements arise from the combined statistical uncertainty of ^{217}Po and of the reference isotope ^{216}Po. The small shift to the previous measurements is within the statistical uncertainties, but could stem from a drift in the wavemeter calibration. The changes in the mean square charge radii with respect to ^{210}Po, $\delta\langle r^2\rangle_{A,210}$, were extracted from the isotope shifts by the formulae discussed in Chapter 2.2.1 and by using the same parameters used for the analysis of previous ISOLDE runs on polonium [39, 159]. The electronic factor, F, for the studied transition and the constant of the specific mass shift, K_{SMS} were calculated by large-scale atomic calculations for polonium to $F = -12.786\,(1900)$ GHz/fm^2 and $K_{\mathrm{SMS}} = -51\,(13)$, respectively [33, 39]. The corrections for the higher moments were 0.932 (see Equation (2.19)) [169]. Table 7.1 gives an overview of the changes in the mean square radii from this experiment and from the previous runs [39].
The left graph in Figure 7.7 shows the changes in the mean square charge radii of ^{217}Po and the polonium isotopes measured during the previous runs at ISOLDE [39, 159]. Here, the mean square charge radii are compared to the predictions from the *droplet model* (DM) [172], calculated by the second parametrization from [8] and the theoretical predictions of a SKk4 from a *Skyrme-Hartree-Fock model* with the *skl4-parametrization*, which was recently benchmarked for the neutron-rich even lead and polonium isotopes [71, 72]. The

Table 7.1: Isotope shifts and mean square radii of ^{216,217,218}Po. The results for ^{216,218}Po from the previous runs are shown for comparison [36]. Statistical uncertainties are given in parentheses and systematic uncertainties originating from the are given in the curly brackets.

		Previous runs [39]		**This work**	
Isotope	I^{π}	$\delta\nu_{A,210}$ **GHz**	$\delta\langle r^2\rangle_{A,210}$ **fm²**	$\delta\nu_{A,210}$ **GHz**	$\delta\langle r^2\rangle_{A,210}$ **fm²**
^{216}Po	0^+	-8.820(110)	0.733(10){5}		-
- ^{217}Po	$9/2^+$	-	-	-9.880(200)	0.821(17){8}
^{218}Po	0^+	-11.524(125)	0.958(10){7}	-11.406(150)	0.948(10){7}

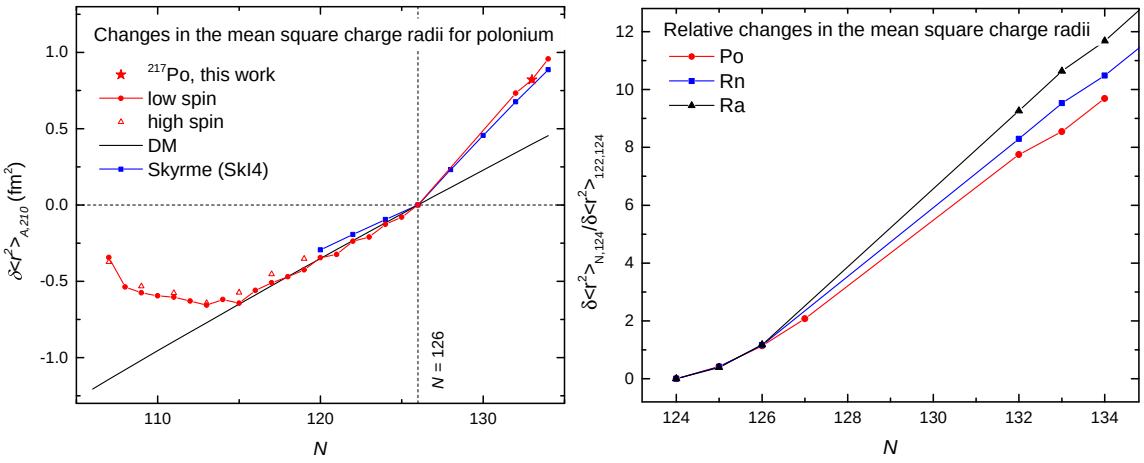

Figure 7.7: Left: changes in mean square charge radii, $\delta\langle r^2\rangle_{\mathrm{A},210}$, for polonium isotopes with respect to the reference isotope, ^{210}Po. ^{217}Po (star) is shown among the other isotopes (low spin, circle; high spin, triangle) measured during the previous runs at ISOLDE [39, 159]. The predictions from the droplet model (DM) [8] and the SkI4-parametrization of the Skyrme-Hartree-Fock model [71, 72] are given by the black line and the blue squares, respectively. Right: comparison of the relative changes in the mean square charge radii, $\delta\langle r^2\rangle_{\mathrm{N},124}/\delta\langle r^2\rangle_{122,124}$, of Po (this work and [39, 159]), Rn, and Ra [64]. The connections between the data are to guide the eyes only.

changes in the mean square charge radii, $\delta\langle r^2\rangle_{\mathrm{A},210}$, do only agree with the predictions of the FRDM for $115 \leq N \leq 126$. The departure from sphericity for light polonium isotopes ($107 \leq N \leq 115$) was discussed in detail in [39] and was explained by shape-coexistence. The reproduction of the kink at the closed neutron shell of $N = 126$ by the SkI4-parametrization of the Skyrme-Hartree-Fock model was ascribed to the occupancy of the $1i_{11/2}$ neutron orbital, which invokes a change in the evolution of the charge radii systematics [72].

The right graph in Figure 7.7 shows the comparison of the relative changes in the mean square charge radii, $\delta\langle r^2\rangle_{\mathrm{N},126}/\delta\langle r^2\rangle_{122,124}$, of polonium (this work and [39, 159]), radon, and radium [64]. $\delta\langle r^2\rangle_{\mathrm{N},126}/\delta\langle r^2\rangle_{122,124}$ was calculated according to the formalism described in [26, 80] by and normalizing the $\delta\langle r^2\rangle_{\mathrm{N},124}$ in each isotopic chain to $\delta\langle r^2\rangle_{122,124}$. ^{217}Po clearly reveals the normal odd-even staggering. This can be quantified with a modified odd-even staggering parameter, γ, [157, 168] for ^{217}Po of $\gamma_{217} = 1 - \frac{2\delta\langle r^2\rangle_{216,217}}{\delta\langle r^2\rangle_{216,218}} = 0.22(10)$, for which in general, a higher modified odd-even staggering parameter refers to a stronger staggering. The normal odd-even staggering of ^{217}Po is in contrast to the reversed odd-even staggering, which was observed for the even-Z elements radon and radium isotopes of the same N [20, 35] shown in the right graph of Figure 7.7 and for neutron-rich francium [35]. Thus, polonium marks a lower limit of the end of the region of inverted odd-even staggering.

7.6.2 Electromagnetic moments

From the fits, the hyperfine-structure constants of ^{217}Po, were determined to $A = -0.437(20)$ GHz and $B = 0.10(40)$ GHz. These values enable the extraction of the magnetic dipole moment, μ, and the spectroscopic electrical quadrupole moment, Q_S, using scaling relations to the reference isotope ^{207}Po derived from Equations (2.23) and (2.24) and by disregarding any hyperfine anomaly:

$$\mu = \frac{A \cdot I \cdot \mu_0}{A_0 \cdot I_0}\,; \quad Q_S = \frac{B \cdot Q_{S0}}{B_0} \tag{7.3}$$

with the corresponding values of ^{207}Po of $I_0 = 5/2$, $A_0 = 564(1)$ MHz, $B_0 = 367(7)$ MHz, $\mu_0 = 0.793(55)$ n.m. and $Q_{S0} = 0.28(3)$ e·b [31, 93]. The latter needs to be corrected for the *Sternheimer effect* by $Q_S^{\mathrm{corr}} = \frac{Q_S^{nl}}{1-R_{nl}}$ with an estimation of the quadrupole shielding factor of $R_{6p} = 0.20(5)$ [160].
The spin-assignment of ^{217}Po is controversial. From the α-decay spectroscopy of ^{221}Rn, ^{217}Po was first believed to be octupolar deformed as is its mother nuclide with a corresponding nuclear spin assignment of $\boldsymbol{I^{\pi}} = 11/2^+$ [105]. Later, the same authors refined their conclusion and suggested a spherical $\boldsymbol{I^{\pi}} = 9/2^+$ groundstate, based on the study of the α-decay of ^{217}Po to ^{213}Pb. The octupolar deformed $\boldsymbol{I^{\pi}} = 11/2^+$ state is instead believed to be a low-lying excited state with excitation energy of only 9.5 keV or 19.8 keV [104]. It should be noted that the nuclear spin cannot be unambiguously determined in our experiment from the analysis from the hyperfine-structure due to a low resolution.
However, the magnetic dipole and electric quadrupole moments for the spin-assignment of $9/2^+$ are $\mu = -1.106(50)\{40\}$ n.m. and $Q_S = 0.06(30)\{2\}$, respectively. The magnetic moment μ agrees well with the magnetic moment of ^{211}Po of $\mu(^{211}\mathrm{Po}) = -1.196(58)$ n.m. [49, 160] with a spin-assignment of $9/2^+$. This shows that ^{217}Po and ^{211}Po have similar quantum configurations, supporting the spin-assignment of $9/2^+$ made in [104]. In turn, this leads to the conclusion about the absence of octupole deformation, which is in agreement with the observed "normal" odd-even staggering, contradictory to the expected inverted odd-even staggering, which would be a fingerprint for octupolar deformation. Polonium thus marks the end of the "island of octupolar deformation".
This debate would benefit greatly from future studies on the relative positions of the $9/2^+$ state with respect to the $11/2^+$ state in the ^{217}Po isotope.

8 Summary and outlook

This work comprises various aspects of the *Resonance Ionization Laser Ion Source* (RILIS) at the radioactive ion beam facility ISOLDE at CERN, ranging from the development of new techniques for the improvement of the selectivity, to experiments in atomic and nuclear physics by the means of the in-source resonance ionization spectroscopy.

To tackle the problem of unwanted isobaric contamination in RILIS beams, a new device, the *Laser Ion Source and Trap* (LIST), was successfully implemented into the ISOLDE framework, operated on-line and further developed to optimize the performance. This was achieved due to successfully addressing the many pre-requisites for on-line operation of the LIST: thorough testing with a realistic off-line laser ion source setup; preparation of the LIST for compatibility with the harsh conditions at the target frontend of ISOLDE through the use of radiation-hard and heat-resistant materials; a dedicated transport and remote control system for the electronic signals (repeller voltage, RF-signal).
Throughout the course of this thesis, two off-line and two on-line runs were conducted. The latter, conducted in 2012, was the first ISOLDE physics experiment to use the LIST. The LIST was characterized extensively in terms of suppression of contaminants, laser ionization efficiency and selectivity. A surface-ion suppression of at least three to four orders of magnitude was observed. In its final configuration (LIST 2), a loss of the laser ionization efficiency of $LSF = 20(1)$ compared to normal RILIS operation was determined; an improvement of a factor of 2.5 compared to the first tests. A LIST quality factor, i.e. the improvement of the LIST selectivity over the RILIS selectivity, was conservatively estimated to be 50, but higher values of up to 500 can be expected.
The feasibility of the LIST as a tool for in-source resonance ionization spectroscopy was demonstrated. The temporal profile of the LIST ion bunches were measured on-line and described by a mathematical model that reproduces the main features of the time structure. Several possibilities for the further improvement of the selectivity of the LIST were proposed. In conclusion, the LIST is now an established ion-source option at ISOLDE and further on-line experiments are expected.

The ionization efficiency for calcium was improved by developing a new laser ionization scheme. Alternative intermediate and ionizing steps were explored and characterized. Several autoionizing states were observed that were unknown in the literature. Using the strongest observed transitions, a 20-fold improvement of the laser ionization efficiency was achieved. During the ISOLDE on-line period in 2012, the increased ionization efficiency allowed the ISOLTRAP experiment to measure the masses of ^{53,54}Ca for the first time [177]. These measurements demonstrated the new opportunities enabled by the recent upgrade of the RILIS laser system [143] to perform ionization scheme developments as an integrated part of the tuning and maintenance routine of ongoing on-line experiments.

For polonium, a rich spectrum of Rydberg resonances close to the ionization threshold were measured in an on-line experiment. These enabled the first precise determination of the first ionization energy. The resonances were classified and five separate Rydberg series could be identified. Possible spin assignments of these individual Rydberg series were discussed by comparing the remainders of the quantum defects to the homologous elements sulphur, selenium and tellurium. It was shown that these subseries belong to *ns* and *nd*-series, which is supported by the analysis of polonium levels found in literature. Fitting the Rydberg formula globally to these individual subseries led to a final value of the ionization energy of $IE_{\mathrm{Po}} = 67896.310(13)(30)\,\mathrm{cm}^{-1}$. This is more than two orders more precise than the literature value [149] and is shifted by more than $10\,\mathrm{cm}^{-1}$ from the value reported in [31]. The new value is in excellent agreement with complementary measurements that were performed at the TRIUMF facility in Vancouver, Canada [136] and will be published together with theoretical calculations [22] in a joint publication [137].

Finally, and this is where we return to the first on-line application of the LIST, the groundstate properties of ^{216,217,218,219}Po were investigated by the means of in-source resonance ionization spectroscopy. Due to the strong suppression of francium isotopes by the LIST, the isotope shift and the hyperfine structure of ^{217}Po were measured for the first time. This enabled the determination of the change in the mean-square charge radii with respect to ^{210}Po and the electromagnetic moments to $\delta\langle r^2\rangle_{\mathbf{A,210}} = 0.821(17)\,\mathrm{cm}^{-1}$, $\mu = -1.106(50)\{40\}$ n.m. and $Q_S = 0.06(30)\{2\}$ e·b, respectively. The observation of normal odd-even staggering and the strongly suggested $9/2^+$spin assignment leads to the conclusion of the absence of octupolar deformation, in contrast to the neutron-rich isotopes of radon, francium and radium. Polonium thus marks the end of the "island of octupolar deformation".

Future activities concerning the LIST will focus on a further improvement of the LIST selectivity as well as a reduction of the LIST loss factor. Several possibilities, such as the improvement of the laser ionization schemes, the laser/atom overlap and the gating on the LIST ion pulses were discussed in Chapter 4.3.9. The best possible LIST efficiency requires the minimum possible gap between the LIST RFQ and the hot cavity exit. This can be realized if the hot cavity itself can act as an ion repeller by operating with an inverted, but easily switchable, resistive heating polarity. This option is currently under investigation and would benefit from a successful outcome of the ongoing tests of high resistance cavity materials and novel heating methods.
Laser ionization scheme development is an ongoing process and a lot of effort is currently made at off-line laboratories to further extend the list of the elements available for RILIS. This could be accompanied by complementary on-line laser ionization scheme development work, as it was demonstrated for calcium in this thesis.
In-source laser resonance spectroscopy and laser-assisted α-spectroscopy will continue to be an essential part of the atomic and nuclear physics program at ISOLDE. Experiments in the near future may aim to the study of the *electron affinity** of astatine and polonium

*The electron affinity is the energy required to attach an electron to a neutral atom

[143].
In nuclear physics, the program to map the nuclear properties in the lead region will be continued. Many ion beams of isotopes in this region are highly contaminated by surface ionized contaminants such as francium isotopes. In these cases, the Laser Ion Source and Trap would be the ideal tool to enable the measurements. In the case of polonium, the debate about the ground state spin-assignment of ^{217}Po would benefit greatly of a future experiment, for which the LIST would be an essential part of the setup. In addition, the feasibility of the study of ^{219}Po and other exotic isotopes with similar experimental challenges was demonstrated using the LIST.

Appendices

A Fit results for the analysis of the systematic shift of the Rydberg scans due to the DAQ delay

Table A.1: List of the fit results for the analysis of the systematic DAQ-shift of the Rydberg scans from Chapter 6.4.1 of the linear fits to the centroids of members of series Σ with group numbers ranging from $g = 7$ to $g = 19$ as a function of the scanning speed (Scan 1: -0.56 cm^{-1}/s, scan 2: 0.28 cm^{-1}/s, scan 3: -0.15 cm^{-1}/s). The calculated real position of the centroid is found at scanning speed 0 cm^{-1}/s (intercept). The centroid positions of each scan, the intercept with the abscissa and the slope of the linear fit are given.

	scan 1		**scan 2**		**scan 3**					
g	**Centroid** cm^{-1}	**ΔCentroid** cm^{-1}	**Centroid** cm^{-1}	**ΔCentroid** cm^{-1}	**Centroid** cm^{-1}	**ΔCentroid** cm^{-1}	**Intercept** cm^{-1}	**Δ Intercept** cm^{-1}	**Slope** cm^{-1}/s	**Δ Slope** cm^{-1}/s
7	16750.80	0.05	16751.27	0.03	16751.02	0.03	16751.11	0.01	0.57	0.02
8	16768.10	0.10	16768.54	0.04	16768.19	0.14	16768.38	0.03	0.55	0.11
9	16783.18	0.04	16783.84	0.03	16783.55	0.03	16783.63	0.02	0.77	0.07
10	16796.83	0.04	16797.26	0.03	16797.03	0.03	16797.11	0.01	0.51	0.03
11	16808.81	0.05	16809.32	0.04	16809.05	0.03	16809.14	0.01	0.60	0.03
12	16819.69	0.05	16820.06	0.03	16819.76	0.03	16819.89	0.05	0.52	0.18
13	16829.31	0.05	16829.61	0.03	16829.45	0.03	16829.51	0.01	0.37	0.02
14	16837.97	0.05	16838.21	0.02	16838.10	0.03	16838.13	0.01	0.28	0.02
15	16845.82	0.03	16846.27	0.03	16845.95	0.03	16846.08	0.05	0.51	0.14
16	16852.95	0.07	16853.37	0.05	16853.09	0.03	16853.19	0.03	0.54	0.13
17	16859.48	0.05	16859.96	0.05	16859.58	0.03	16859.72	0.08	0.54	0.25
18	16865.33	0.05	16865.70	0.03	16865.51	0.03	16865.57	0.01	0.44	0.01
19	16870.84	0.16	16871.19	0.04	16871.00	0.03	16871.06	0.01	0.44	0.02

B Table of observed Rydberg levels of polonium

Table B.1: A table of the parameters of all observed peaks in the spectra obained during the Rydberg scans discussed in Chapter 6: minimum value of the principal quantum number n', series notation used throughout this thesis, energy of the observed transition W" to the Rydberg states from the second step at 39081.19 cm^{-1} , total excitation energy of the resonance W and corresponding statistical uncertainty, estimated quantum defect δ and corresponding statistical uncertainty and estimated term configuration for the unambiguously identified atomic states. The statistical uncertainty of the transition energies $\Delta W''$ is the same of the statistical uncertainty of the total excitation energy ΔW. An additional systematic uncertainty of 0.3 cm^{-1} caused by the wavemeter must be taken into account for the transition energies and the total excitation energies.

n'	**Series**	$\boldsymbol{W}$" [$\mathbf{cm}^{-1}$]	$\boldsymbol{W}$ [$\mathbf{cm}^{-1}$]	$\boldsymbol{\Delta W}$ [$\mathbf{cm}^{-1}$]	δ	$\Delta\delta$	**Configuration**
17	Π	16565.36	67500.25	0.06	3.354	0.002	$6p^3(^4S)\,20d$
17	Θ	16567.24	67502.13	0.06	4.315	0.002	$6p^3(^4S)\,20d$
17	Σ	16574.68	67509.57	0.06	4.155	0.003	$6p^3(^4S)\,20d$
18	Φ	16583.71	67518.60	0.12	4.955	0.004	$6p^3(^4S)\,22s\,^5S_2$?
18	Ω	16585.58	67520.47	0.13	4.913	0.004	$6p^3(^4S)\,22s\,^3S_1$?
18	Π	16608.99	67543.88	0.07	3.354	0.003	$6p^3(^4S)\,21d$
18	Θ	16610.67	67545.56	0.06	4.312	0.003	$6p^3(^4S)\,21d$
18	Σ	16616.76	67551.65	0.06	4.156	0.003	$6p^3(^4S)\,21d$
19	Φ	16624.36	67559.25	0.23	4.957	0.007	$6p^3(^4S)\,23s\,^5S_2$?
19	Ω	16625.75	67560.64	0.27	4.919	0.008	$6p^3(^4S)\,23s\,^3S_1$?
19	Π	16645.74	67580.63	0.06	3.355	0.003	$6p^3(^4S)\,22d$
19	Θ	16647.24	67582.13	0.07	4.311	0.004	$6p^3(^4S)\,22d$
19	Σ	16652.34	67587.23	0.06	4.157	0.004	$6p^3(^4S)\,22d$
20	Φ	16658.84	67593.73	0.06	4.956	0.004	$6p^3(^4S)\,24s\,^5S_2$?
20	Ω	16660.23	67595.12	0.10	4.912	0.004	$6p^3(^4S)\,24s\,^3S_1$?
20	Π	16677.06	67611.95	0.06	3.355	0.004	$6p^3(^4S)\,23d$

Continued on next page

Table B.1 – *Continued from previous page*

n'	**Series**	$\boldsymbol{W}$" [$\mathbf{cm}^{-1}$]	$\boldsymbol{W}$ [$\mathbf{cm}^{-1}$]	$\Delta\boldsymbol{W}$ [$\mathbf{cm}^{-1}$]	δ	$\Delta\delta$	**Configuration**
20	Θ	16678.32	67613.21	0.09	4.312	0.005	$6p^3(^4S)\,23d$
20	Σ	16682.75	67617.64	0.06	4.156	0.004	$6p^3(^4S)\,23d$
21	Φ	16688.31	67623.20	0.06	4.955	0.004	$6p^3(^4S)\,25s\,^5S_2$?
21	Ω	16689.39	67624.28	0.06	4.915	0.004	$6p^3(^4S)\,25s\,^3S_1$?
21	Π	16703.99	67638.88	0.08	3.353	0.005	$6p^3(^4S)\,24d$
21	Θ	16705.00	67639.89	0.06	4.313	0.005	$6p^3(^4S)\,24d$
21	Σ	16708.85	67643.74	0.06	4.156	0.005	$6p^3(^4S)\,24d$
22	Φ	16713.64	67648.53	0.13	4.955	0.007	$6p^3(^4S)\,26s\,^5S_2$?
22	Ω	16714.77	67649.66	0.14	4.907	0.007	$6p^3(^4S)\,26s\,^3S_1$?
22	Π	16727.19	67662.08	0.06	3.355	0.005	$6p^3(^4S)\,25d$
22	Θ	16728.08	67662.97	0.06	4.314	0.005	$6p^3(^4S)\,25d$
22	Σ	16731.46	67666.35	0.08	4.155	0.006	$6p^3(^4S)\,25d$
23	Φ	16735.64	67670.53	0.06	4.954	0.006	$6p^3(^4S)\,27s\,^5S_2$?
23	Ω	16736.40	67671.29	0.06	4.917	0.006	$6p^3(^4S)\,27s\,^3S_1$?
23	Π	16747.44	67682.33	0.06	3.354	0.006	$6p^3(^4S)\,26d$
23	Θ	16748.25	67683.14	0.06	4.311	0.006	$6p^3(^4S)\,26d$
23	Σ	16751.11	67686.00	0.06	4.157	0.006	$6p^3(^4S)\,26d$
24	Φ	16754.86	67689.75	0.06	4.951	0.007	$6p^3(^4S)\,28s\,^5S_2$?
24	Ω	16755.52	67690.41	0.06	4.914	0.007	$6p^3(^4S)\,28s\,^3S_1$?
24	Π	16765.12	67700.01	0.06	3.356	0.007	$6p^3(^4S)\,27d$
24	Θ	16765.84	67700.73	0.06	4.313	0.007	$6p^3(^4S)\,27d$
24	Σ	16768.38	67703.27	0.08	4.158	0.008	$6p^3(^4S)\,27d$
25	Φ	16771.62	67706.51	0.06	4.955	0.007	$6p^3(^4S)\,29s\,^5S_2$?
25	Ω	16772.22	67707.11	0.06	4.917	0.007	$6p^3(^4S)\,29s\,^3S_1$?
25	ΠΘ	16781.29	67716.18	0.06	4.318	0.008	
25	Σ	16783.62	67718.51	0.13	4.156	0.012	$6p^3(^4S)\,28d$
26	ΦΩ	16786.72	67721.61	0.06	4.937	0.008	
26	ΠΘ	16795.01	67729.90	0.06	4.320	0.009	
26	Σ	16797.11	67732.00	0.06	4.157	0.009	$6p^3(^4S)\,29d$
27	ΦΩ	16799.91	67734.80	0.06	4.934	0.009	

Continued on next page

Table B.1 – *Continued from previous page*

n'	**Series**	$\boldsymbol{W}$" [$\mathbf{cm}^{-1}$]	$\boldsymbol{W}$ [$\mathbf{cm}^{-1}$]	$\Delta\boldsymbol{W}$ [$\mathbf{cm}^{-1}$]	δ	$\Delta\delta$	**Configuration**
27	ΠΘ	16807.26	67742.15	0.13	4.320	0.014	
27	Σ	16809.14	67744.03	0.06	4.156	0.010	$6p^3(^4S)\,30d$
28	ΦΩ	16811.50	67746.39	0.06	4.945	0.011	
28	ΠΘ	16818.18	67753.07	0.06	4.322	0.011	
28	Σ	16819.89	67754.78	0.07	4.155	0.012	$6p^3(^4S)\,31d$
29	ΦΩ	16822.14	67757.03	0.06	4.931	0.012	
29	ΠΘ	16827.99	67762.88	0.06	4.322	0.013	
29	Σ	16829.51	67764.40	0.06	4.157	0.013	$6p^3(^4S)\,32d$
30	ΦΩ	16831.46	67766.35	0.06	4.942	0.013	
30	ΠΘ	16836.84	67771.73	0.07	4.321	0.014	
30	Σ	16838.14	67773.03	0.09	4.165	0.016	$6p^3(^4S)\,33d$
31	ΦΩ	16839.95	67774.84	0.06	4.943	0.015	
31	ΠΘ	16844.84	67779.73	0.06	4.319	0.016	
31	Σ	16846.07	67780.96	0.06	4.156	0.016	$6p^3(^4S)\,34d$
32	ΦΩ	16847.69	67782.58	0.07	4.937	0.017	
32	ΠΘ	16852.05	67786.94	0.06	4.324	0.017	
32	Σ	16853.20	67788.09	0.06	4.157	0.017	$6p^3(^4S)\,35d$
33	ΦΩ	16854.67	67789.56	0.06	4.938	0.018	
33	ΠΘ	16858.64	67793.53	0.06	4.324	0.019	
33	Σ	16859.72	67794.61	0.09	4.151	0.022	$6p^3(^4S)\,36d$
34	ΦΩ	16861.00	67795.89	0.06	4.942	0.019	
34	ΠΘ	16864.68	67799.57	0.06	4.320	0.020	
34	Σ	16865.58	67800.47	0.06	4.162	0.021	$6p^3(^4S)\,37d$
35	ΦΩ	16866.84	67801.73	0.06	4.937	0.021	
35	ΠΘ	16870.19	67805.08	0.06	4.317	0.022	
35	Σ	16871.07	67805.96	0.06	4.150	0.023	$6p^3(^4S)\,38d$
36	ΦΩ	16872.12	67807.01	0.06	4.946	0.023	
36	ΠΘ	16875.17	67810.06	0.08	4.330	0.026	
36	Σ	16876.00	67810.89	0.06	4.158	0.025	$6p^3(^4S)\,39d$
37	ΦΩ	16876.97	67811.86	0.13	4.952	0.035	

Continued on next page

Table B.1 – *Continued from previous page*

n'	**Series**	$\boldsymbol{W}$" [$\mathbf{cm}^{-1}$]	$\boldsymbol{W}$ [$\mathbf{cm}^{-1}$]	$\Delta\boldsymbol{W}$ [$\mathbf{cm}^{-1}$]	δ	$\Delta\delta$	**Configuration**
37	ΠΘ	16879.87	67814.76	0.06	4.317	0.026	
37	Σ	16880.60	67815.49	0.06	4.151	0.027	$6p^3(^4S)\,40d$
37	ΦΩ	16881.11	67816.00	0.59	5.036	0.138	
38	ΠΘΣ	16884.15	67819.04	0.06	4.314	0.029	
39	ΦΩ	16885.43	67820.32	0.48	4.999	0.122	
39	ΠΘ	16888.06	67822.95	0.10	4.324	0.037	
39	Σ	16888.57	67823.46	0.40	4.188	0.109	$6p^3(^4S)\,42d$
40	ΦΩ	16889.58	67824.47	0.48	4.917	0.133	
40	ΠΘ	16891.64	67826.53	0.08	4.343	0.036	
40	Σ	16892.15	67827.04	0.10	4.198	0.040	$6p^3(^4S)\,43d$
40	ΦΩ	16892.77	67827.66	0.20	5.019	0.065	
41	ΠΘΣΦΩ	16895.17	67830.06	0.06	4.302	0.036	
42	ΠΘΣΦΩ	16898.40	67833.29	0.06	4.273	0.039	
43	ΠΘΣΦΩ	16901.33	67836.22	0.06	4.264	0.042	
44	ΠΘΣΦΩ	16904.02	67838.91	0.07	4.274	0.047	
45	ΠΘΣΦΩ	16906.55	67841.44	0.06	4.280	0.048	
46	ΠΘΣΦΩ	16908.86	67843.75	0.06	4.308	0.051	
47	ΠΘΣΦΩ	16911.19	67846.08	0.09	4.261	0.063	
48	ΠΘΣΦΩ	16913.25	67848.14	0.07	4.272	0.062	
49	ΠΘΣΦΩ	16915.18	67850.07	0.09	4.285	0.070	
50	ΠΘΣΦΩ	16917.05	67851.94	0.06	4.266	0.066	
51	ΠΘΣΦΩ	16918.77	67853.66	0.06	4.275	0.070	
52	ΠΘΣΦΩ	16920.39	67855.28	0.06	4.282	0.074	
53	ΠΘΣΦΩ	16921.91	67856.80	0.06	4.297	0.078	
54	ΠΘΣΦΩ	16923.38	67858.27	0.06	4.286	0.083	
55	ΠΘΣΦΩ	16924.80	67859.69	0.06	4.260	0.088	
56	ΠΘΣΦΩ	16926.15	67861.04	0.07	4.224	0.097	
57	ΠΘΣΦΩ	16927.39	67862.28	0.07	4.217	0.103	
58	ΠΘΣΦΩ	16928.49	67863.38	0.07	4.270	0.108	
59	ΠΘΣΦΩ	16929.61	67864.50	0.07	4.269	0.113	

Continued on next page

Table B.1 – *Continued from previous page*

n'	**Series**	$\boldsymbol{W}$" [$\mathbf{cm}^{-1}$]	$\boldsymbol{W}$ [$\mathbf{cm}^{-1}$]	$\Delta\boldsymbol{W}$ [$\mathbf{cm}^{-1}$]	δ	$\Delta\delta$	**Configuration**
60	ΠΘΣΦΩ	16930.70	67865.59	0.07	4.228	0.120	
61	ΠΘΣΦΩ	16931.71	67866.60	0.07	4.223	0.127	
62	ΠΘΣΦΩ	16932.61	67867.50	0.07	4.283	0.133	
63	ΠΘΣΦΩ	16933.59	67868.48	0.13	4.205	0.181	

Bibliography

[1] G. Alkhazov, L. Batist, A. Bykov, V. Vitman, V. Letokhov, V. Mishin, V. Panteleyev, S. Sekatsky, and V. Fedoseyev. Application of a high efficiency selective laser ion source at the IRIS facility. *Nucl. Instrum. Meth. A*, 306:400 – 402, 1991.

[2] G. D. Alkhazov, V. S. Letokhov, V. I. Mishin, V. N. Panteleyev, V. I. Romanov, S. K. Sekatskii, and V. Fedoseyev. High-performance z-selective photoionization of atoms in hot metal cavity with following electrostatic ion retention. *Pis'ma Zh. Tekhn. Fiz.*, 15:63–67 (in Russian), 1989.

[3] G. Alton. Semi-empirical mathematical relationships for electropositive adsorbate induced work function changes. *Surf. Sci.*, 175:226 – 240, 1986.

[4] G. Alton. Ion sources for accelerators in materials research. *Nucl. Instrum. Meth. B*, 73:221 – 288, 1993.

[5] A. N. Andreyev, M. Huyse, P. Van Duppen, L. Weissman, D. Ackermann, J. Gerl, F. Hessberger, S. Hofmann, A. Kleinbohl, G. Munzenberg, S. Reshitko, H. Schlegel, C. Schaffner, P. Cagarda, M. Matos, S. Saro, A. Keenan, C. Moore, C. D. O'Leary, R. D. Page, M. Taylor, H. Kettunen, M. Leino, A. AU Lavrentiev, and K. Wyss, R. Heyde. A triplet of differently shaped spin-zero states in the atomic nucleus ^{186}Pb. *Nature*, 405:430, 2000.

[6] M. Anselment, W. Faubel, S. Göring, A. Hanser, G. Meisel, H. Rebel, and G. Schatz. The odd-even staggering of the nuclear charge radii of Pb isotopes. *Nucl. Phys. A*, 451:471 – 480, 1986.

[7] H. Backe, A. Dretzke, S. Fritzsche, R. Haire, P. Kunz, W. Lauth, M. Sewtz, and N. Trautmann. Laser spectroscopic investigation of the element fermium (Z = 100). *Hyperfine Interact.*, 162:3–14, 2005.

[8] D. Berdichevsky and F. Tondeur. Nuclear core densities, isotope shifts, and the parametrization of the droplet model. *Z. f. Phys. A*, 322:141–147, 1985.

[9] I. Beterov, D. Tretyakov, I. Ryabtsev, V. Entin, A. Ekers, and N. Bezuglov. Ionization of Rydberg atoms by blackbody radiation. *New J. Phys.*, 11:013052, 2009.

[10] N. Bijnens, P. Decrock, S. Franchoo, M. Gaelens, M. Huyse, H. Y. Hwang, I. Reusen, J. Szerypo, J. von Schwarzenberg, J. Wauters, J. G. Correia, A. Jokinen, and P. Van Duppen. Intruder states and the onset of deformation in the neutron-deficient even-even polonium isotopes. *Phys. Rev. Lett.*, 75:4571, 1995.

[11] M. Bissell, K. Blaum, I. Budincevic, N. Frömmgen, R. Garcia Ruiz, C. Geppert, M. Hammen, M. Kowalska, K. Kreim, P. Lievens, R. Neugart, G. Neyens, W. Nörtershäuser, J. Papuga, M. Rajabali, and D. Yordanov. Spins, moments and charge radii beyond ^{48}Ca. Technical Report CERN-INTC-2011-049. INTC-P-313, CERN, 2011.

[12] K. Blaum, B. A. Bushaw, W. Nörtershäuser, and K. Wendt. High-resolution, three-step resonance ionization mass spectrometry of gadolinium. *AIP Conf. Proc.*, 584:141–144, 2001.

[13] K. Blaum, J. Dilling, and W. Nörtershäuser. Precision atomic physics techniques for nuclear physics. *Phys. Scrip.*, T152:014017, 2013.

[14] K. Blaum, C. Geppert, H.-J. Kluge, M. Mukherjee, S. Schwarz, and K. Wendt. A novel scheme for a highly selective laser ion source. *Nucl. Instrum. Meth. B*, 204:331 – 335, 2003.

[15] K. Blaum, C. Geppert, P. Müller, W. Nörtershäuser, E. Otten, A. Schmitt, N. Trautmann, K. Wendt, and B. Bushaw. Properties and performance of a quadrupole mass filter used for resonance ionization mass spectrometry. *Int. J. Mass Spectrom.*, 181:67 – 87, 1998.

[16] K. Blum. *Density Matrix Theory and Applications*, volume 64 of *Springer Series on Atomic, Optical and Plasma Physics*. Springer-Verlagand Berlin Heidelberg, 2012.

[17] Y. Blumenfeld. Radioactive ion beam facilities in Europe. *Nucl. Instrum. Meth. B*, 266:4074 – 4079, 2008.

[18] Y. Blumenfeld, T. Nilsson, and P. V. Duppen. Facilities and methods for radioactive ion beam production. *Physi. Scrip.*, 2013:014023, 2013.

[19] N. Bohr and V. Weisskopf. The influence of nuclear structure on the hyperfine structure of heavy elements. *Phys. Rev.*, 77:94–98, Jan 1950.

[20] W. Borchers, R. Neugart, E. Otten, H. Duong, G. Ulm, and K. Wendt. Hyperfine structure and isotope shift investigations in $^{202-222}$Rn for the study of nuclear structure beyond $z = 82$. *Hyperf. Interact.*, 34:25, 1987.

[21] C. Borgmann. Private communication, 2013.

[22] A. Borschevsky. *Private communication*, 2013.

[23] E. Bouquerel, R. Catherall, M. Eller, J. Lettry, S. Marzari, T. Stora, and I. the collaboration. Purification of a Zn radioactive ion beam by alkali suppression in a quartz line target prototype. *Eur. J. Phys. Spec. Top.*, 150:277–280, 2007.

[24] B. Bushaw, W. Nörtershäuser, K. Blaum, and K. Wendt. Studies of narrow autoionizing resonances in gadolinium. *Spectrochim. Act. B*, 58:1083, 2003.

[25] B. Bushaw, W. Nörtershäuser, and K. Wendt. Lineshapes and optical selectivity in high-resolution double-resonance ionization mass spectrometry. *Spectrochim. Acta B*, 54:321 – 332, 1999.

[26] P. Campbell, J. Billowes, J. Behr, G. Gwinner, G. Sprouse, and F. Xu. Isotope shifts of the neutron-deficient bismuth isotopes: charge radii systematics across the $z = 82$ shell closure. *Phys. Lett. B*, 346:21, 1995.

[27] A. Cantú, M. Mazzoni, and Y. Joshi. Rydberg series in the absorption spectrum of Te I limiting on $5s^2\,5p^3\,{}^4S^o_{3/2}$ ionization limit. *Phys. Scr.*, 27:261, 1983.

[28] H. Casimir. *On the interaction between atomic nuclei and electrons.* Archives du musée Teyler. F. Bohn, 1936.

[29] R. F. Casten. *Nuclear Structure from a Simple Perspective.* Oxford University Press, USA, 1990.

[30] CERN, 2013.

[31] G. Charles. Spectra of ^{208}Po and the hyperfine structure of ^{209}Po. *J. Opt. Soc. Am.*, 56:1292–1297, 1966.

[32] G. W. Charles, D. Hunt, G. Pish, and D. Timma. Preliminary description and analysis of the spectrum of polonium. *J. Opt. Soc. Am.*, 45:869–872, 1955.

[33] B. Cheal, T. E. Cocolios, and S. Fritzsche. Laser spectroscopy of radioactive isotopes: Role and limitations of accurate isotope-shift calculations. *Phys. Rev. A*, 86:042501, 2012.

[34] S. Chu, L. Ekström, and R. Firestone. WWW table of radioactive isotopes, 2013.

[35] A. Coc, C. Thibault, F. Touchard, H. Duong, P. Juncar, S. Liberman, J. Pinard, J. Lermé, J. Vialle, S. Büttgenbach, A. Mueller, and A. Pesnelle. Hyperfine structures and isotope shifts of $^{207-213,220-228}$Fr; possible evidence of octupolar deformation. *Phys. Lett. B*, 163:66 – 70, 1985.

[36] T. Cocolios. *Single-particle and collective properties around closed shells probed by in-source laser spectroscopy.* PhD thesis, Katholieke Universiteit Leuven and Groep Wetenschap & Technologie and Arenberg Doctoraatsschool, 2010.

[37] T. Cocolios. Private communication, 2013.

[38] T. Cocolios, A. Andreyev, A. Barzakh, J. Billowes, D. Fedorov, V. Fedosseev, S. Franchoo, G. Huber, M. Huyse, A. Ionan, U. Köster, Y. Kudryavtsev, F. L. Blanc, S. Lesher, B. Marsh, I. Mukha, M. Seliverstov, J. V. de Walle, P. V. Duppen, and Y. Volkov. Study of polonium isotopes ground state properties by simultaneous atomic- and nuclear-spectroscopy. Technical Report CERN-INTC-2007-003. INTC-P-222, CERN, 2007.

[39] T. Cocolios, W. Dexters, M. Seliverstov, A. Andreyev, S. Antalic, A. Barzakh, B. Bastin, J. Büscher, I. Darby, D. Fedorov., V. Fedosseyev, K. Flanagan, S. Franchoo, S. Fritzsche, G. Huber, M. Huyse, M. Keupers, U. Köster, Y. Kudryavtsev, E. Mané, B. Marsh, P. Molkanov, R. Page, A. Sjoedin, I. Stefan., J. V. de Walle, P. V. Duppen, M. Venhartv, S. Zemlyanoy, M. Bender, and P.-H. Heenen. Early onset of ground state deformation in neutron deficient polonium isotopes. *Phys. Rev. Lett.*, 106:052503, Feb 2011.

[40] T. Cocolios, D. Fink, A. Andreyev, S. Antalic, A. Barzakh, B. Bastin, K. Blaum, D. Fedorov, V. Fedosseev, K. Flanagan, L. Ghys, A. Gottberg, M. Huyse, N. Lecesne, K. Lynch, B. Marsh, D. Pauwels, E. Rapisarda, S. Richter, S. Rothe, M. Seliverstov, A. Sjödin, C. V. Beveren, P. V. Duppen, and K. Wendt. First decay spectroscopy of ^{219}Po with the LIST. In preparation, 2014.

[41] T. Cocolios, B. Marsh, V. Fedosseev, S. Franchoo, G. Huber, M. Huyse, A. Ionan, K. Johnston, U. Köster, Y. Kudryavtsev, M. Seliverstov, E. Noah, T. Stora, and P. V. Duppen. Resonant laser ionization of polonium at RILIS-ISOLDE for the study of ground- and isomer-state properties. *Nucl. Instrum. Meth. B*, 266:4403 – 4406, 2008.

[42] R. Cowan. *The theory of atomic structure and spectra*. University of California Press and Ltd. and Berkeley and Los Angeles, 1919.

[43] P. Dawson. Performance characteristics of an r.f.-only quadrupole. *Int. J. Mass Spectrom. and I. Proc.*, 67(3):267 – 276, 1985.

[44] P. Dawson. *Quadrupole Mass Spectrometry and Its Applications*. American Vacuum Society Classics. American Inst. of Physics, 1997.

[45] P. Dawson and N. Whetten. Non-linear resonances in quadrupole mass spectrometers due to imperfect felds. ii. the quadrupole mass filter and the monopole mass spectrometer. *Int. J. Mass Spectrom. Ion. Phys.*, 3:1, 1969.

[46] P. de Marcillac, N. Coron, G. Dambier, J. Leblanc, and J.-P. Moalic. Experimental detection of α-particles from the radioactive decay of natural bismuth. *Nature*, 422:876, 2003.

[47] H. De Witte, A. N. Andreyev, N. Barré, M. Bender, T. E. Cocolios, S. Dean, D. Fedorov, V. N. Fedoseyev, L. M. Fraile, S. Franchoo, V. Hellemans, P. H. Heenen, K. Heyde, G. Huber, M. Huyse, H. Jeppessen, U. Köster, P. Kunz, S. R. Lesher, B. A. Marsh, I. Mukha, B. Roussière, J. Sauvage, M. Seliverstov, I. Stefanescu, E. Tengborn, K. Van de Vel, J. Van de Walle, P. Van Duppen, and Y. Volkov. Nuclear charge radii of neutron-deficient lead isotopes beyond $N = 104$ midshell investigated by in-source laser spectroscopy. *Phys. Rev. Lett.*, 98:112502, 2007.

[48] W. Demtröder. *Atoms, Molecules and Photons: an Introduction ao Atomic-and Molecular- and Quantum-Physics*. Springer Verlagand Berlin, 2006.

[49] W. Dexters. Neutron-rich polonium isotopes studied with in-source laser spectroscopy. Master's thesis, Katholieke Universiteit Leuven, 2010.

[50] U. Dinger, J. Eberz, G. Huber, R. Menges, S. Schröder, R. Kirchner, O. Klepper, T. Kühl, D. Marx, and G. Sprouse. Nuclear moments and change in the charge-radii of neutron deficient lead isotopes. *Z. Phys. A*, 328:253, 1987.

[51] P. V. Duppen. Laser ion sources for on-line isotope separators. *Nucl. Instrum. Meth. B*, 126:66, 1997.

[52] P. V. Duppen. Isotope separation on line and post acceleration. *Lect. Notes Phys*, 700:37–77, 2006.

[53] S. Dutta, R. Kirchner, O. Klepper, T. Kühl, D. Marx, G. Sprouse, R. Menges, U. Dinger, G. Huber, and S. Schröder. Measurement of isotope shift and hyperfine splitting of ^{190,191,193,197}Pb isotopes by collinear laser spectroscopy. *Z. Phys. A*, 341:39–45, 1991.

[54] A. Einstein. Zur Quantentheorie der Strahlung. *Physikalische Z.*, 18:121 – 128, 1917.

[55] J. Elseviers, A. N. Andreyev, M. Huyse, P. Van Duppen, S. Antalic, A. Barzakh, N. Bree, T. E. Cocolios, V. F. Comas, J. Diriken, D. Fedorov, V. N. Fedosseev, S. Franchoo, L. Ghys, J. A. Heredia, O. Ivanov, U. Köster, B. A. Marsh, K. Nishio, R. D. Page, N. Patronis, M. D. Seliverstov, I. Tsekhanovich, P. Van den Bergh, J. Van De Walle, M. Venhart, S. Vermote, M. Veselský, and C. Wagemans. β-delayed fission of ^{180}tl. *Phys. Rev. C*, 88:044321, 2013.

[56] U. Fano. Effects of configuration interaction on intensities and phase shifts. *Phys. Rev.*, 124:1866–1878, 1961.

[57] V. Fedoseev, Y. Kudryavtsev, V. Letokhov, V. Mishin, H. Ravn, S. Sundell, H. Kluge, and F. Scheerer. A laser ion-source for on-line isotope separation. In *Proceedings of the Fifth International Symposium on Resonance Ionization Spectroscopy and its Applications, RIS -90, Varese, Italy*, 1990.

[58] V. Fedosseev, Y. Kudryavtsev, and V. Mishin. Resonance laser ionization of atoms for nuclear physics. *Phys. Scripta*, 85:058104, 2012.

[59] V. N. Fedosseev, L.-E. Berg, D. V. Fedorov, D. Fink, O. J. Launila, R. Losito, B. Marsh, R. E. Rossel, S. Rothe, M. D. Seliverstov, A. M. Sjödin, and K. D. A. Wendt. Upgrade of the resonance ionization laser ion source at ISOLDE on-line isotope separation facility: New lasers and new ion beams. *Rev. Sci.. Instrum.*, 83:02A903, 2012.

[60] D. Fink, S. Richter, B. Bastin, K. Blaum, R. Catherall, T. Cocolios, D. Fedorov, V. Fedosseev, K. Flanagan, L. Ghys, A. Gottberg, N. Imai, T. Kron, N. Lecesne, K. Lynch, B. Marsh, T. Mendonca, D. Pauwels, E. Rapisarda, J. Ramos, R. Rossel, S. Rothe, M. Seliverstov, M. Sjödin, T. Stora, C. V. Beveren, and K. Wendt. First application of the laser ion source and trap (LIST) for on-line experiments at ISOLDE. *Nucl. Instrum. Meth. B*, 317, Part B:417 – 421, 2013.

[61] W. Finkelnburg and F. Stern. Electron screening and ionization potentials of neutral and singly ionized atoms. *Phys. Rev.*, 77:303–303, 1950.

[62] E. Fischer. Die dreidimensionale Stabilisierung von Ladungsträgern in einem Vierpolfeld. *Z. Phys.*, 156:1, 1959.

[63] G. Focker, F. Hoekemeijer, O. Jonsson, E. Kugler, and H. Ravn. The beam observation system of the ISOLDE facility. *AIP Conf. Proc.*, 333:196, 1995.

[64] G. Fricke and K. Heilig. *Nuclear Charge Radii*. Springer Berlin-Heidelberg, 2005.

[65] S. Fritzsche. Large-scale accurate structure calculations for open-shell atoms and ions. *Physica Scripta*, T100:37, 2002.

[66] J. Gaardsted, T. Andersen, H. Haugen, J. Hansen, and N. Vaeck. Multiphoton spectroscopy of doubly excited autoionizing states of Ca. *J. Phys. B*, 24:4363, 1991.

[67] L. P. Gaffney, P. A. Butler, M. Scheck, A. B. Hayes, F. Wenander, M. Albers, B. Bastin, C. Bauer, A. Blazhev, S. Bönig, N. Bree, J. Cederkäll, T. Chupp, D. Cline, T. E. Cocolios, T. Davinson, H. De Witte, J. Diriken, T. Grahn, A. Herzan, M. Huyse, D. G. Jenkins, D. T. Joss, N. Kesteloot, J. Konki, M. Kowalczyk, T. Kröll, E. Kwan, R. Lutter, K. Moschner, P. Napiorkowski, J. Pakarinen, M. Pfeiffer, D. Radeck, P. Reiter, K. Reynders, S. V. Rigby, L. M. Robledo, M. Rudigier, S. Sambi, M. Seidlitz, B. Siebeck, T. Stora, P. Thoele, P. Van Duppen, M. J. Vermeulen, M. von Schmid, D. Voulot, N. Warr, K. Wimmer, K. Wrzosek-Lipska, C. Y. Wu, and M. Zielinska. Studies of pear-shaped nuclei using accelerated radioactive beams. *Nature*, 497:199, 2013.

[68] T. F. Gallagher, S. A. Edelstein, and R. M. Hill. Radiative lifetimes of the s and d Rydberg levels of Na. *Phys. Rev. A*, 11:1504, 1975.

[69] P. Ghosh. *Ion Traps*. Oxford science publications. Oxford University Press, Incorporated, 1995.

[70] T. Giles. *Private communication*, 2013.

[71] P. M. Goddard. *Private communication*, 2013.

[72] P. M. Goddard, P. D. Stevenson, and A. Rios. Charge radius isotope shift across the n=126 shell gap. *Phys. Rev. Lett.*, 110:032503, 2013.

[73] M. Goeppert-Mayer. Nuclear configurations in the Spin-Orbit Coupling Model. I. empirical evidence. *Phys. Rev.*, 78:16, 1950.

[74] T. Gottwald. Messung der Emittanz der Laserionenquellenfalle LIST am RISIKO Massenseparator. Master's thesis, Johannes Gutenberg-Universität Mainz, 2007.

[75] P. G. Hansen. Experiments with beams of rare isotopes: A fifty-year perspective 1951-2001. *Nucl Phys. News*, 11:31, 2001.

[76] K. Heilig and A. Steudel. Changes in mean-square nuclear charge radii from optical isotope shifts. *Atomic Data and Nuclear Data Tables*, 14:613 – 638, 1974.

[77] F. Herfurth, J. Dilling, A. Kellerbauer, G. Bollen, S. Henry, H.-J. Kluge, E. Lamour, D. Lunney, R. Moore, C. Scheidenberger, S. Schwarz, G. Sikler, and J. Szerypo. A linear radiofrequency ion trap for accumulation, bunching, and emittance improvement of radioactive ion beams. *Nucl. Instrum. Meth. A*, 469:254, 2001.

[78] HighFinesse GmbH. *WS6 product sheet*, 2013.

[79] HighFinesse GmbH. *WS7 product sheet*, 2013.

[80] R. J. Hull and H. H. Stroke. Nuclear moments and isotope shifts of Tl^{199}, Tl^{200}, Tl^{201}, Tl^{202}, and Tl^{204} - isotope shifts in odd-odd nuclei. *Phys. Rev.*, 122:1574, 1961.

[81] G. S. Hurst, M. G. Payne, S. D. Kramer, and J. P. Young. Resonance ionization spectroscopy and one-atom detection. *Rev. Mod. Phys.*, 51:767, 1979.

[82] R. Janssens. Unexpected doubly magic nucleus. *Nature*, 459:1069, 2009.

[83] R. Jastrow. On the Rydberg-Ritz formula in quantum mechanics. *Phys. Rev.*, 73:60–67, 1948.

[84] H. Jeppesen, U. Bergmann, M. Borge, J. Cederkäll, V. Fedoseyev, H. Fynbo, V. Hansper, B. Jonson, K. Markenroth, V. Mishin, T. Nilsson, G. Nyman, K. Riisager, O. Tengblad, and K. Rolander. Search for beta-delayed charged particles from the halo nucleus ^{14}Be. *Nucl. Phys. A*, 709:119, 2002.

[85] B. Jonson and A. Richter. More than three decades of ISOLDE physics. *Hyperf. Interact.*, 129:1, 2000.

[86] R. Julin, K. Helariutta, and M. Muikku. Intruder states in very neutron-deficient Hg, Pb and Po nuclei. *J. Phys. G*, 27:R109, 2001.

[87] S. Kaufman. High-resolution laser spectroscopy in fast beams. *Optics Commun.*, 17:309 – 312, 1976.

[88] W. King. *Isotope shifts in atomic spectra*. Plenum Press and New York and London, 1984.

[89] R. Kirchner. On the thermoionization in hot cavities. *Nucl. Instrum. Meth. A*, 292:203, 1990.

[90] H.-J. Kluge, F. Ames, W. Ruster, and K. Wallmeroth. Laser ion sources. In L. Buchmann and J. D'Auria, editors, *Proceedings of the Accelerated Radioactive Beams Workshop*, page 119. TRIUMF Proceedings TRI-85-1, Canada, 1985.

[91] O. Kofeod-Hansen and K. O. . Nielsen. Measurements on short-lived radioactive krypton isotopes from fission after isotopic separation. *Dan. Mat. Fys. Medd.*, 56-7:1, 1951.

[92] U. Köster. Resonance ionization laser ion sources. *Nucl. Phys. A*, 701:441, 2002.

[93] D. Kowalewska, K. Bekk, S. Göring, A. Hanser, W. Kälber, G. Meisel, and H. Rebel. Isotope shifts and hyperfine structure in polonium isotopes by atomic beam laser spectroscopy. *Phys. Rev. A*, 44:R1442, 1991.

[94] A. Kramida, Y. Ralchenko, J. Raeder, and N. A. TEAM. NIST Atomic Spectra Database (version 5.1), Thursday, 26 September 2013.

[95] K. Krane. *Introductory Nuclear Physics*. Wiley, 1987.

[96] S. Kreim. Seeking the purported magic number $N = 32$ with high-precision mass spectrometry. Technical Report CERN-INTC-2011-053. INTC-P-317, CERN, 2011.

[97] M. Kronberger, A. Gottberg, T. Mendonca, J. Ramos, C. Seiffert, P. Suominen, and T. Stora. Production of molecular sideband radioisotope beams at CERN-ISOLDE using a Helicon-type plasma ion source. *Nucl. Instrum. Meth. B*, 317, Part B:438 – 441, 2013.

[98] I. Langmuir and K. Kingdon. Thermionic effects caused by vapours of alkali metals. *Proc. R. Soc. Lond. A*, 107:61, 1925.

[99] M. Laury and A. Wilson. Examining the heavy p-block with a pseudopotential-based composite method: Atomic and molecular applications of rp-ccCA. *J. Chem. Phys.*, 137:214111, 2012.

[100] J. Lawson. Particle beams and plasmas. *CERN Report*, 76-09:1–93, 1976.

[101] F. Le Blanc, D. Lunney, J. Obert, J. Oms, J. Putaux, B. Roussière, J. Sauvage, S. Zemlyanoi, J. Pinard, L. Cabaret, H. T. Duong, G. Huber, M. Krieg, V. Sebastian, J. E. Crawford, J. K. P. Lee, M. Girod, S. Péru, J. Genevey, and J. Lettry. Large odd-even radius staggering in the very light platinum isotopes from laser spectroscopy. *Phys. Rev. C*, 60:054310, 1999.

[102] V. Letokhov. *Laser photoionization spectroscopy*. Academic Press, Orlando, 1987.

[103] V. Letokhov and V. Mishin. Laser photoionization pulsed source of radioactive atoms. In *Abstracts from the Workshop on the ISOLDE programme: on-line in 1985 and Beyond, Zinal, Switzerland*, 1984.

[104] C. Liang, P. Paris, R. Sheline, and P. Alexa. Alpha decay of ^{221}Rn and ^{217}Po; level structure of ^{217}Po and the ^{213}Pb ground state. *Czech. J. Phys*, 54:189–198, 2004.

[105] C. F. Liang, P. Paris, and R. K. Sheline. Level structure of ^{217}Po and the spin of the previously proposed ^{213}Pb ground state. *Phys. Rev. C*, 56:2324, 1997.

[106] B. Lommel, W. Hartmann, B. Kindler, J. Klemm, and J. Steiner. Preparation of self-supporting carbon thin films. *Nucl. Instrum. Meth. A*, 480:199 – 203, 2002.

[107] W. Lotz. An empirical formula for the electron-impact ionization cross-section. *Z. Phys.*, 206:205–211, 1967.

[108] R. Luis, J. Marques, T. Stora, P. Vaz, and L. Zanini. Optimization studies of the CERN-ISOLDE neutron converter and fission target system. *Eur. J. Phys. A*, 48:90, 2012.

[109] S. Lukić, F. Gevaert, A. Kelić, M. Ricciardi, K.-H. Schmidt, and O. Yordanov. Systematic comparison of ISOLDE-SC yields with calculated in-target production rates. *Nucl. Instrum. Meth. A*, 565:784 – 800, 2006.

[110] F. Major, V. Gheorghe, and G. Werth. *Charged Particle Traps: Physics and Techniques of Charged Particle Field Confinement*. Charged Particle Traps. Springer, 2005.

[111] E. Mané, J. Billowes, K. Blaum, P. Campbell, B. Cheal, P. Delahaye, K. Flanagan, D. Forest, H. Franberg, C. Geppert, T. Giles, A. Jokinen, M. Kowalska, R. Neugart, G. Neyens, W. Nörtershäuser, I. Podadera, G. Tungate, P. Vingerhoets, and D. Yordanov. An ion cooler-buncher for high-sensitivity collinear laser spectroscopy at ISOLDE. *Nucl. Instrum. Meth. A*, 42:503–507, 2009.

[112] B. Marsh. *In-Source Laser Resonance Ionization at ISOL Facilities*. PhD thesis, The University of Manchester, 2007.

[113] B. Marsh. Resonance ionization laser ion sources. In *CERN accelerator school*, 2013.

[114] B. Marsh, B. Andel, A. Andreyev, S. Antalic, D. Atanasov, A. Barzakh, B. Bastin, C. Borgmann, L. Capponi, T. Cocolios, T. D. Goodacre, M. Dehairs, X. Derkx, H. D. Witte, D. Fedorov, V. Fedosseev, G. Focker, D. Fink, K. Flanagan, S. Franchoo, L. Ghys, M. Huyse, N. Imai, Z. Kalaninova, U. Köster, S. Kreim, N. Kesteloot, Y. Kudryavtsev, J. Lane, N. Lecesne, V. Liberati, D. Lunney, K. Lynch, V. Manea, P. Molkanov, T. Nicol, D. Pauwels, L. Popescu, D. Radulov, E. Rapisarda, M. Rosenbusch, R. Rossel, S. Rothe, L. Schweikhard, M. Seliverstov, S. Sels, A. Sjödin, V. Truesdale, C. V. Beveren, P. V. Duppen, K. Wendt, F. Wienholtz, R. Wolf, and S. Zemlyanoy. New developments of the in-source spectroscopy method at RILIS/ISOLDE. *Nucl. Instrum. Meth. B*, 317, Part B:550 – 556, 2013.

[115] B. Marsh, L.-E. Berg, D. Fedorov, V. Fedosseev, O. Launila, M. Lindroos, R. Losito, F. Österdahl, T. Pauchard, I. Pohjalainen, U. Sassenberg, M. Seliverstov, A. Sjödin, and G. Tranströmer. The ISOLDE RILIS pump laser upgrade and the LARIS Laboratory. *Hyperf. Interact.*, 196:129–141, 2010.

[116] W. Martin, R. Zalubas, and A. Musgrove. Energy levels of sulfur, S i through S XVI. *J. Phys. Chem. Ref. Data*, 19:821, 1990.

[117] S. Marzari. *Private communication*, 2013.

[118] N. McLachlan. *Theory and application of Mathieu functions*. Clarendon Press, Oxford, 1947.

[119] V. Mishin, V. Fedoseyev, H.-J. Kluge, V. Letokhov, H. Ravn, F. Scheerer, Y. Shirakabe, S. Sundell, and O. Tengblad. Chemically selective laser ion-source for the

CERN-ISOLDE on-line mass separator facility. *Nucl. Instrum. Meth. B*, 73:550 – 560, 1993.

[120] M. Miyabe, C. Geppert, M. Kato, M. Oba, I. Wakaida, K. Watanabe, and K. Wendt. Determination of ionization potential of calcium by high-resolution resonance ionization spectroscopy. *J. Phys. Soc. Jpn.*, 75:034302, 2006.

[121] P. Mohr, B. Taylor, and D. Newell. The 2010 CODATA recommended values of the fundamental physical constants, 2011.

[122] L. Monz, R. Hohmann, H.-J. Kluge, S. Kunze, J. Lantzsch, E. Otten, G. Passler, P. Senne, J. Stenner, K. Stratmann, K. Wendt, K. Zimmer, G. Herrmann, N. Trautmann, and K. Walter. Fast, low-level detection of strontium-90 and strontium-89 in environmental samples by collinear resonance ionization spectroscopy. *Spectrochim. Act. B*, 48:1655 – 1671, 1993.

[123] C. Moore. Atomic energy levels as derived from the analysis of optical spectra - chromium through niobium. *Nat. Stand. Ref. Data Ser.*, 11:230, 1971.

[124] C. Morillon and J. Vergès. Observation et classification du spectre d'arc du tellure (Te) entre 3678 et 11761 cm^{-1}. *Phys. Scr.*, 12:129, 1975.

[125] M. Mukherjee. *The mass of ^{22}Mg and a concept for a novel laser ion source trap.* PhD thesis, Karl Ruprecht-Universität Heidelberg, 2004.

[126] A. Müller, E. Salzborn, R. Frodl, R. Becker, H. Klein, and H. Winter. Absolute ionisation cross sections for electrons incident on O^+, Ne^+, Xe^+ and Ar^+ (i=1,...,5) ions. *J. Phys. B*, 13:1877, 1980.

[127] W. Nörtershäuser, N. Trautmann, K. Wendt, and B. Bushaw. Isotope shifts and hyperfine structure in the $4s^2\ ^1S_0 \rightarrow 4s4p\ ^1P_1 \rightarrow 4s4d\ ^1D_2$ transitions of stable calcium isotopes and calcium-41. *Spectrochim. Acta B*, 53:709 – 721, 1998.

[128] E. Otten. *Spectra, radii and moments of unstable isotopes.* Springer Verlag and Berlin, 1989.

[129] W. Paul. Electromagnetic traps for charged and neutral particles. *Rev. Mod. Phys.*, 62:531–540, 1990.

[130] W. Paul and M. Raether. Das elektrische Massenfilter. *Z. Phys.*, 140(3):262–273, 1955.

[131] W. Paul, H. Reinhard, and U. Zahn. Das elektrische Massenfilter als Massenspektrometer und Isotopentrenner. *Z. Phys.*, 152:143–182, 1958.

[132] W. Paul and H. Steinwedel. Ein neues Massenspektrometer ohne Magnetfeld. *Z. Naturforschung A*, 8:448, 1953.

[133] K. A. Peterson. Systematically convergent basis sets with relativistic pseudopotentials. I. correlation consistent basis sets for the post-d group 13–15 elements. *J. Chem. Phys.*, 119:11099–11112, 2003.

[134] E. Prime, J. Lassen, T. Achtzehn, D. Albers, P. Bricault, T. Cocolios, M. Dombsky, F. Labrecque, J. Lavoie, M. Pearson, T. Stubbe, N. Lecesne, C. Geppert, and K. Wendt. TRIUMF resonant ionization laser ion source. *Hyperf, Interact.*, 171:127–134, 2006.

[135] T. Procter and K. Flanagan. First on-line results from the CRIS (Collinear Resonant Ionisation Spectroscopy) beam line at ISOLDE. *Hyperfine Interactions*, 216:89–93, 2013.

[136] S. Raeder. *Private Communication*, 2013.

[137] S. Raeder, D. Fink, A. Borschevsky, et al. Preliminary title: The first ionization energy of polonium. In preparation, 2014.

[138] F. Read, A. Adams, and J. Soto-Montiel. Electrostatic cylinder lenses i: Two element lenses. *J. Phys. E.*, 4:625, 1971.

[139] S. Richter. The setup of the laser ion source and trap. to be published as a technical note, 2013.

[140] S. Richter. PhD thesis, University of Mainz, to be submitted, 2014.

[141] B. Roos, R. Lindh, P. Malmqvist, V. Veryazov, and P. Widmark. Main group atoms and dimers studied with a new relativistic ANO basis set. *J. Phys. Chem.*, 108:2851–2858, 2004.

[142] R. Rossel, V. Fedosseev, B. Marsh, D. Richter, S. Rothe, and K. Wendt. Data acquisition, remote control and equipment monitoring for ISOLDE RILIS. *Nucl. Instrum. Meth. B*, 317, Part B:557 – 560, 2013.

[143] S. Rothe. *An all-solid state laser system for the laser ion source RILIS and in-source laser spectroscopy of astatine at ISOLDE, CERN*. PhD thesis, Johannes Gutenberg-Universität Mainz, 2012.

[144] S. Rothe, A. Andreyev, S. Antalic, A. Borschevsky, L. Capponi, T. Cocolios, H. D. Witte, E. Eliav, V. F. D.V. Fedorov and, D. Fink, S. Fritzsche, L. Ghys, M. Huyse, N. Imai, U. Kaldor, Y. Kudryavtsev, U. Köster, J. Lane, J. Lassen, V. Liberati, K. Lynch, B. Marsh, K. Nishio, D. Pauwels, V. Pershina, L. Popescu, T. Procter, D. Radulov, S. Raeder, M. Rajabali, E. Rapisarda, R. Rossel, K. Sandhu, M. Seliverstov, A. Sjödin, P. V. den Bergh, P. V. Duppen, M. Venhart, Y. Wakabayashi, and K. Wendt. Measurement of the first ionization potential of astatine by laser ionization spectroscopy. *Nat. Commun.*, 4:1835, 2013.

[145] S. Rothe, B. Marsh, C. Mattolat, V. Fedosseev, and K. Wendt. A complementary laser system for ISOLDE RILIS. *J. Phys. Conf. Ser.*, 312:052020, 2010.

[146] J. E. Ruedy. Series and term values in the arc spectrum of tellurium. *Phys. Rev.*, 41:588–594, 1932.

[147] H. Russel. The arc and spark spectra of gadolinium. *J. Opt. Soc. Am.*, 40:550–554, 1950.

[148] M. Saha. Ionization in the solar chromosphere. *Pli. Mag. Ser. 6*, 40:472, 1920.

[149] J. Sansonetti and W. Martin. Handbook of basic atomic spectroscopic data. *J. Phys. Chem. Ref. Data*, 34:1559, 2005.

[150] F. Schwellnus. *Entwicklung von Ionenquellen zur Optimierung von Selektivität und Effizienz bei der resonanten Laserionisation.* PhD thesis, Johannes Gutenberg-Universität Mainz, 2010.

[151] F. Schwellnus, K. Blaum, R. Catherall, B. Crepieux, V. Fedosseev, T. Gottwald, H.-J. Kluge, B. Marsh, C. Mattolat, S. Rothe, T. Stora, and K. Wendt. The laser ion source trap for highest isobaric selectivity in online exotic isotope production. *Rev. Sci. Instrum.*, 81:02A515, 2010.

[152] F. Schwellnus, K. Blaum, C. Geppert, T. Gottwald, H.-J. Kluge, C. Mattolat, W. Nörtershaeuser, K. Wies, and K. Wendt. The laser ion source and trap (LIST): A highly selective ion source. *Nucl. Instrum. Meth. B*, 266:4383 – 4836, 2008.

[153] F. Schwellnus, R. Catherall, B. Crepieux, V. Fedosseev, B. Marsh, C. Mattolat, M. Menna, F. Österdahl, S. Raeder, T. Stora, and K. Wendt. Study of low work function materials for hot cavity resonance ionization laser ion sources. *Nucl. Instrum. Meth. B*, 267:1856 – 1861, 2009.

[154] J. Sedlet. *Actinium, Astatine, Francium, Polonium, and Protactinium*, volume 6 of *Treatise on analytical chemistry. Part II: Analytical chemistry of the elements.* Wiley & Sons, USA, 1964.

[155] L. Seijo. Relativistic ab initio model potential calculations including spin–orbit effects through the Wood–Boring Hamiltonian. *J. Chem. Phys.*, 102:8078–8088, 1995.

[156] M. Seliverstov. *Private communication*, 2013.

[157] M. Seliverstov, A. Andreyev, N. Barré, A. Barzakh, S. Dean, H. De Witte, D. Fedorov, V. Fedoseyev, L. Fraile, S. Franchoo, J. Genevey, G. Huber, M. Huyse, U. Köster, P. Kunz, S. Lesher, B. Marsh, I. Mukha, B. Roussière, J. Sauvage, I. Stefanescu, K. Van de Vel, P. Van Duppen, and Y. Volkov. Charge radii and magnetic moments of odd-A $^{183-189}$Pb isotopes. *Eur. Phys. J. A*, 41:315–321, 2009.

[158] M. Seliverstov, A. Andreyev, N. Barré, H. Witte, D. Fedorov, V. Fedoseyev, S. Franchoo, J. Genevey, G. Huber, M. Huyse, U. Köster, P. Kunz, S. Lesher, B. Marsh, B. Roussière, J. Sauvage, P. Duppen, and Y. Volkov. Study of the neutron deficient $^{182-190}$Pb isotopes by simultaneous atomic- and nuclear-spectroscopy. *Hyperf. Interact.*, 171:225–231, 2006.

[159] M. Seliverstov, T. Cocolios, W. Dexters, A. Andreyev, S. Antalic, A. Barzakh, B. Bastin, J. Büscher, I. Darby, D. Fedorov, V. Fedoseyev, K. Flanagan, S. Franchoo, S. Fritzsche, G. Huber, M. Huyse, M. Keupers, U. Köster, Y. Kudryavtsev, B. Marsh, P. Molkanov, R. Page, A. Sjödin, I. Stefan, J. V. de Walle, P. V. Duppen, M. Venhart, and S. Zemlyanoy. Charge radii of odd-A $^{191-211}$Po isotopes. *Phys. Lett. B*, 719:362 – 366, 2013.

[160] M. Seliverstov, T. Cocolios, W. Dexters, A. Andreyev, S. Antalic, A. Barzakh, B. Bastin, J. Büscher, I. Darby, D. Fedorov, V. Fedoseyev, K. Flanagan, G. Huber, M. Huyse, M. Keupers, U. Köster, Y. Kudryavtsev, B. Marsh, P. Molkanov, R. Page, A. Södin, I. Stefan, J. V. de Walle, P. V. Duppen, M. Venhart, and S. Zemlyanoy. Electromagnetic moments of odd-a $^{191-211}$Po isotopes. *in preparation*, 2014.

[161] E. C. Seltzer. K X-ray isotope shifts. *Phys. Rev.*, 188:1916–1919, Dec 1969.

[162] B. Shore and P. Berman. Theory of coherent atomic excitation. *Phys. Today*, 44:71, 1991.

[163] V. Sonnenschein. Untersuchung zum Abdampf- und Atomisationsverhalten verschiedener Elemente zur Steigerung der Effizienz bei HR-RIMS und LIST. Master's thesis, Johannes Gutenberg-Universität Mainz, 2008.

[164] R. Stebbings and F. Dunning. *Rydberg states of atoms and molecules*. Cambridge University Pressand Cambridge, 1983.

[165] D. Steppenbeck, S. Takeuchi, N. Aoi, P. Doornenbal, M. Matsushita, H. Wang, H. Baba, N. Fukuda, S. Go, M. Honma, J. Lee, K. Matsui, S. Michimasa, T. Motobayashi, D. Nishimura, T. Otsuka, H. Sakurai, Y. Shiga, P.-A. Soderstrom, T. Sumikama, H. Suzuki, R. Taniuchi, Y. Utsuno, J. J. Valiente-Dobon, and K. Yoneda. Evidence for a new nuclear 'magic number' from the level structure of ^{54}Ca. *Nature*, 502:207, 2013.

[166] P. Suominen. *Private communication*, 2013.

[167] A. Thorne, U. Litzíen, and S. Johansson. *Spectrophysics: Principles and Applications*. Springer Verlagand Berlin, 1999.

[168] W. Tomlinson and H. Stroke. Nuclear moments and isotope and isomer shifts of neutron-deficient mercury isotopes 195, 195^m, 194, 193, 193^m and 192. *Nucl. Phys.*, 60:614 – 633, 1964.

[169] G. Torbohm, B. Fricke, and A. Rosén. State-dependent volume isotope shifts of low-lying states of group-II a and -II b elements. *Phys. Rev. A*, 31:2038–2053, 1985.

[170] M. Turek, A. Droździel, K. Pyszniak, D. Maczka, and B. S. owiński. Simulations of ionization in a hot cavity surface ion source. *Rev .Sci. Instrum.*, 83:023303, 2012.

[171] G. Ulm, S. Bhattacherjee, P. Dabkiewicz, G. Huber, H.-J. Kluge, T. Kühl, H. Lochmann, E.-W. Otten, K. Wendt, S. Ahmad, W. Klempt, and R. Neugart.

Isotope shift of ^{182}Hg and an update of nuclear moments and charge radii in the isotope range ^{181}Hg-^{206}Hg. *Z. Phys. A*, 325:247, 1986.

[172] C. von Weizsäcker. Zur Theorie der Kernmassen. *Z. Phys.*, 96:431–458, 1935.

[173] M. Wang, G. Audi, A. Wapstra, F. Kondev, M. MacCormick, X. Xu, and B. Pfeiffer. The AME2012 atomic mass evaluation. *Chinese Phys. C*, 36:1603, 2012.

[174] D. Warner. Not-so-magic numbers. *Nature*, 430:517, 2004.

[175] J. Wauters, P. Dendooven, M. Huyse, G. Reusen, P. Van Duppen, and P. Lievens. α-decay properties of neutron-deficient polonium and radon nuclei. *Phys. Rev. C*, 47:1447, 1993.

[176] K. Wendt, K. Blaum, K. Brueck, C. Geppert, H.-J. Kluge, M. Mukherjee, G. Passler, S. Schwarz, S. Sirotzki, and K. Wies. A highly selective laser ion source for bunched, low emittance beam release. *Nucl. Phys. A*, 746:47 – 53, 2004.

[177] F. Wienholtz, D. Beck, K. Blaum, C. Borgmann, M. Breitenfeldt, R. Cakirli, S. George, F. Herfurth, J. Holt, M. Kowalska, S. Kreim, D. Lunney, V. Manea, J. Menendez, D. Neidherr, M. Rosenbusch, L. Schweikhard, A. Schwenk, J. Simonis, J. Stanja, R. Wolf, and K. Zuber. Masses of exotic calcium isotopes pin down nuclear forces. *Nature*, 498:346, 2013.

[178] K. Wies. *Entwicklung des Laserionenquellen- und fallenprojekts LIST für Ultraspurendetektion und Grundlagenforschung.* PhD thesis, Johannes Gutenberg-Universität Mainz, 2006.

[179] H. D. Witte. *Probing the nuclear structure along the Z=82 closed shell: decay- and laser spectroscopic studies of exotic Pb, Bi and Po nuclei.* PhD thesis, Katholieke Universiteit Leuven, 2004.

[180] J. Wiza. Microchannel plate detectors. *Nucl. Instrum. Meth.*, 162:587 – 601, 1979.

[181] R. Wolf, D. Beck, K. Blaum, C. Böhm, C. Borgmann, M. Breitenfeldt, F. Herfurth, A. Herlert, M. Kowalska, S. Kreim, D. Lunney, S. Naimi, D. Neidherr, M. Rosenbusch, L. Schweikhard, J. Stanja, F. Wienholtz, and K. Zuber. On-line separation of short-lived nuclei by a multi-reflection time-of-flight device. *Nucl. Instrum. Meth. A*, 686:82 – 90, 2012.

[182] T. Zeng, D. Fedorov, and M. Klobukowski. Multireference study of spin-orbit coupling in the hydrides of the 6p-block elements using the model core potential method. *J. Chem. Phys.*, 132:074102, 2010.

Acknowledgements

Being amongst all the *modern alchemists** at ISOLDE for the last few years, I finally feel able to consider myself to be one of them. It has been a challenging, but also a very exciting time (although, for the sake of my blood pressure, I would not have minded a little less excitement during the on-line runs). There is no doubt that the successful outcome of this thesis was entirely dependent on the help of numerous people and I want to express my gratitude to:

My university supervisor *Professor Klaus Blaum* for offering me the opportunity to work with him on this interesting project at ISOLDE, for the scientific advice, for all the practical and financial support throughout the project and for always lending an ear to my smaller and bigger problems.

My local supervisor at CERN, *Bruce Marsh*, whose initiatives in the lab and the *MacGyver-like* problem-solving capabilities were key to the success of my Ph.D. project. I am especially grateful for all the discussions, the exceptional help with the manuscript and the fun at the various conferences.

The whole RILIS team, which I had the pleasure to be part of: section leader *Valentin Fedosseev* for giving me the opportunity to be a part of his team, for the financial support and for the scientific advice; *Sebastian Rothe* for the unofficial co-supervision, the fruitful discussions and the great time in Japan; *Ralph Rossel* for help with the electronics and the remote control system; *Maxim Seliverstov* for the help with fitting of the polonium laser scans; and *Dmitry Fedorov*, *Thomas Day Goodacre*, *Nobuaki Imai*, and *Pavel Molanov* for the various discussions and the good times in the labs.

The *LARISSA* working group of the University of Mainz for the close collaboration for the LIST project and in particular: the LIST project leader *Professor Klaus Wendt* for allowing me to coordinate the LIST project at CERN, the financial support of the project, and the scientific advice and discussions; *Sven Richter* for the coordination of the LIST developments at the University of Mainz, the technical drawings and construction of the LIST and transducer box, and the great team-work before, during and after the off-line and on-line experiments; and of course the former and present members of the team that supported the LIST project during my time: *Tobias Kron*, *Christoph Mattolat*, *Sebastian Raeder*, *Fabian Schneider* and *Fabio Schwellnus* and let me not forget to mention the rest of the team for the fun during my stays in Mainz and at the various conferences.

*Although modern alchemist (i.e. scientists at ISOLDE) possess the power to synthesize gold, their intentions are purely scientific.

The members of the ISOLDE technical and target team that contributed to the LIST project in various ways: *Ermanno Barbero*, *Richard Catherall*, *Tim Giles*, *Matthias Kronberger*, *Stefano Marzari*, *Tania Mendonca*, *Michael Owen*, *Emiliano Piselli*, *Joao Ramos*, *Erwin Siesling*, *Thierry Stora*; and in particular *Bernard Crepieux* for the technical support at the off-line mass separator and with the targets; *Alexander Gottberg* for our successful day-and-night debugging session at ISOLDE that saved the second LIST on-line run; and *Pekka Suominen* for the design of the coaxial copper line.

The mechanical workshop of the University of Mainz physics institute for machining the LIST and *Michael Boessenecker* and *Herr Lenk* for the construction of the LIST transducer box.

All members of the *IS456* collaboration that contributed to the second LIST on-line run. Of all these, I would like to especially thank: *Thomas Cocolios* for arranging the first on-line application of the LIST, the supervision of the data analysis and discussion of the results; *Elisa Rapisarda* for the personal ROOT course; and *Anatoly Barzakh* for input to the discussion of the results.

The *German doctoral student programme at CERN* (*Wolfgang-Gentner scholarships*) of the *Deutsches Bundesministerium für Bildung und Forschung*, supervised by *Michael Hauschild*, for financial support.

My friends, whether they are in Geneva, Mundelsheim, Zürich or in another corner of the world for reminding me that there is a life besides working on a Ph.D. thesis and for not giving up on contacting me. I hereby promise I'll become a social animal again. I hope we'll ride the mountains again sooner rather than later, *Christoph.*

Der Familie, meinen Eltern *Judith* und *Burghard* und meiner Schwester *Bigna.* Eure mentale und praktische Unterstützung war in jeder Hinsicht super. Auch an die Unterstützung von *Helga* möchte ich mich da noch einmal erinnern.

Min siste takk går til den utrolige kvinnen, som ikke bare fant Higgs-bosonet og klatret i Himalaya, men som også er kvinnen jeg ble kjent med den første dagen jeg begynte på doktorgraden, og som nå er min fantastiske kjæreste. Din tålmodighet og ro var en stor styrke og hjelp i avslutningen av prosjektet. Du inspirerer meg hver dag.

... "*For(;;){printf("Takk!");}* til *Lillian*!"

Cartman:	Stan, don't you know the first law of physics?
	Anything that's fun costs at least eight dollars!

from *South Park* (season 9, episode 12)